CONTROL OF LEADING EDGE VORTEX AND THREE-DIMENSIONAL SURFACE SEPARATION ON A NON-SLENDER DELTA WING USING PASSIVE AND ACTIVE TECHNIQUES

A THESIS SUBMITTED TO
THE GRADUATE SCHOOL OF NATURAL AND APPLIED SCIENCES
OF
MIDDLE EAST TECHNICAL UNIVERSITY

BY

CENK ÇETİN

IN PARTIAL FULFILLMENT OF THE REQUIREMENTS
FOR
THE DEGREE OF DOCTOR OF PHILOSOPHY
IN
MECHANICAL ENGINEERING

NOVEMBER 2024

Approval of the thesis:

CONTROL OF LEADING EDGE VORTEX AND THREE-DIMENSIONAL SURFACE SEPARATION ON A NON-SLENDER DELTA WING USING PASSIVE AND ACTIVE TECHNIQUES

submitted by **CENK ÇETİN** in partial fulfillment of the requirements for the degree of **Doctor of Philosophy in Mechanical Engineering Department, Middle East Technical University** by,

Prof. Dr. Naci Emre Altun
Dean, Graduate School of **Natural and Applied Sciences** _____

Prof. Dr. Serkan Dağ
Head of Department, **Mechanical Engineering** _____

Prof. Dr. Mehmet Metin Yavuz
Supervisor, **Mechanical Engineering, METU** _____

Examining Committee Members:

Prof. Dr. Cüneyt Sert
Mechanical Engineering, METU _____

Prof. Dr. Mehmet Metin Yavuz
Mechanical Engineering, METU _____

Prof. Dr. Murat Kadri Aktaş
Mechanical Engineering, TOBB ETU _____

Assoc. Prof. Dr. Özgür Uğraş Baran
Mechanical Engineering, METU _____

Assist. Prof. Dr. Onur Baş
Mechanical Engineering, TEDU _____

Date:19.11.2024

I hereby declare that all information in this document has been obtained and presented in accordance with academic rules and ethical conduct. I also declare that, as required by these rules and conduct, I have fully cited and referenced all material and results that are not original to this work.

Name, Surname: Cenk Çetin

Signature :

ABSTRACT

CONTROL OF LEADING EDGE VORTEX AND THREE-DIMENSIONAL SURFACE SEPARATION ON A NON-SLENDER DELTA WING USING PASSIVE AND ACTIVE TECHNIQUES

Çetin, Cenk
Ph.D., Department of Mechanical Engineering
Supervisor: Prof. Dr. Mehmet Metin Yavuz

November 2024, 214 pages

In line with the progress achieved in unmanned aerial vehicle (UAV) technologies in recent decades, interest in the control of flow structures over delta wing planforms, which constitute the baseline for such vehicles, has significantly increased. As product phases advance from conceptual design to operational prototypes, performance, efficiency, and stability targets have become the focus for the industry. To benefit from the advantages of delta wing planforms, the control of flow structures has been a major concern for researchers and industry, allowing for the expansion of the operational envelopes of such platforms, particularly where high angles of attack and lift forces are required.

In the present study, the effects of passive bleeding and active periodic blowing flow control techniques on flow physics over a $\Lambda = 45^{\circ}$ swept delta wing with a thickness-to-chord ratio of $t/C = 5.9$ were experimentally investigated.

For the passive bleeding technique, an innovative nozzle-type bleeding geometry design aimed at increasing the bleeding momentum was studied using surface pressure, force, and particle image velocimetry measurements. The results suggest that the

nozzle-type bleeding design is quite effective in altering the flow structure and aerodynamic coefficients. Additionally, a bleeding momentum estimation method was developed based on surface pressure measurements by utilizing the Bernoulli equation and a loss coefficient calibrated with in-situ hot wire measurements.

For the periodic blowing technique, a comprehensive active flow control system based on fast-switching actuators was built and characterized prior to aerodynamic measurements, using in-situ hot-wire measurements. Characterization results indicated that a full investigation of such systems provides valuable calibration schemes, which are crucial for assessing the aerodynamic benefits and developing possible closed-loop flow control systems. The effect of periodic blowing actuation in the form of regular and burst-modulated square waves, applied through the leading edges, was examined using surface pressure and force measurements. Results showed that periodic actuation is quite effective in improving and recovering the suction pressure coefficient, particularly at high angles of attack, which was associated with an improvement in stall behavior, as evidenced by force measurements.

Keywords: Experimental Aerodynamics, Non-slender Delta Wing, Three Dimensional Surface Separation, Passive Flow Control, Bleeding Momentum, Active Flow Control, Periodic Blowing, In-Situ Calibration

ÖZ

DÜŞÜK OK AÇILI DELTA KANATLAR ÜZERİNDEKİ HÜCUM KENARI GİRDAPLARININ VE ÜÇ BOYUTLU YÜZEY AKIŞ AYRILMALARININ PASİF VE AKTİF TEKNİKLER İLE KONTROLÜ

Çetin, Cenk
Doktora, Makina Mühendisliği Bölümü
Tez Yöneticisi: Prof. Dr. Mehmet Metin Yavuz

Kasım 2024 , 214 sayfa

Son yıllarda insansız hava aracı (İHA) teknolojilerinde kaydedilen ilerlemeler doğrultusunda, bu tür araçlar için temel teşkil eden delta kanat planformları üzerindeki akış yapılarını kontrol etme konusundaki ilgi önemli ölçüde artmıştır. Ürün aşamaları kavramsal tasarımdan operasyonel prototiplere doğru ilerledikçe, performans, verimlilik ve kararlılık hedefleri sektörün odak noktası haline gelmiştir. Akış yapılarının kontrolü, delta kanat planformlarının avantajlarından yararlanmak için araştırmacılar ve endüstri için ana konulardan biri olmaktadır. Akış kontrolü özellikle yüksek hücum açıları ve kaldırma kuvvetlerinin gerektiği durumlarda, bu tür platformların operasyonel zarflarını genişletmeyi mümkün kılabilecek bir yaklaşımdır.

Bu çalışmada, $t/C = 5.9$ kalınlık-veter oranına sahip, $\Lambda = 45^\circ$ süpürme açılı delta kanat üzerindeki pasif akıtma ve aktif periyodik üfleme akış kontrol tekniklerinin akış fiziği üzerindeki etkileri deneysel olarak incelenmiştir.

Pasif akıtma tekniği için, akıtma momentumunu artırmayı amaçlayan yenilikçi bir

lüle tipi geometrisi tasarımı, yüzey basıncı, kuvvet ve parçacık görüntülemeli hız ölçüm teknikleri kullanılarak incelenmiştir. Sonuçlar, lüle tipi tasarımının akış yapısını ve aerodinamik katsayıları değiştirmede oldukça etkili olduğunu göstermektedir. Ayrıca, Bernoulli denklemi ve yerinde sıcak tel ölçümleriyle kalibre edilen yüzey basıncı ölçümlerine dayanan bir pasif akıtma momentum öngörüm yöntemi geliştirilmiştir.

Periyodik üfleme tekniği için, hızlı anahtarlamalı eyleyicilere dayanan kapsamlı bir aktif akış kontrol sistemi kurulmuştur ve aerodinamik ölçümlerden önce yerinde sıcak tel ölçümleri kullanılarak karakterize edilmiştir. Karakterizasyon sonuçları, bu tür sistemlerin kapsamlı olarak incelenmesinin, aerodinamik avantajları değerlendirmek ve olası kapalı döngü akış kontrol sistemlerini geliştirmek için değerli kalibrasyon şemaları sağladığını göstermiştir. Hücum kenarları boyunca uygulanan düzenli ve modülasyonlu kare dalgalar biçimindeki periyodik üfleme profillerinin etkisi, yüzey basıncı ve kuvvet ölçümleri kullanılarak incelenmiştir. Sonuçlar, periyodik tahriklemenin özellikle yüksek hücum açılarında emme basınç katsayısını iyileştirmede ve geri kazanmada oldukça etkili olduğunu göstermiştir ve kuvvet ölçümlerinden elde edilen bulgular da perdövites durumundaki taşıma ve kararlılık iyileşmeleri ile bunu doğrulamıştır.

Anahtar Kelimeler: Deneysel Aerodinamik, Düşük Ok Açılı Delta Kanat, Üç Boyutlu Yüzey Ayrımı, Pasif Akış Kontrolü, Akıtma Momentumu, Aktif Akış Kontrolü, Periyodik Üfleme, Yerinde Kalibrasyon

To My Wife and Family

ACKNOWLEDGMENTS

I would like to extend my heartfelt gratitude to everyone who has contributed their time, effort, and support throughout my research journey. First and foremost, I am deeply indebted to my supervisor, Prof. Dr. Mehmet Metin Yavuz, for his unwavering support and guidance during my graduate years. His belief in our research and the opportunity to conduct my studies as a member of the Yavuz Research Group (YRG) have been invaluable. The experiences and knowledge I gained in this environment have greatly enriched my academic journey.

I also thank my thesis monitoring committee members, Prof. Dr. Cüneyt Sert and Prof. Dr. Murat Kadri Aktaş, for their insightful guidance and constructive criticism. The suggestions and comments made by Assoc. Prof. Dr. Özgür Uğraş Baran and Assist. Prof. Dr. Onur Baş to improve the quality of the dissertation are greatly acknowledged. I am grateful for the funding provided by Middle East Technical University (METU), Turkish Aerospace Industries, Inc. (TA), and the Scientific Research Projects (BAP) Coordination of METU under grant number BAP TEZ-D-302-2023-11057, as well as the BAP fund of TA.

My sincere thanks go to the Turkish Aerospace BAP committee members. I also express my acknowledgements to my former and current chiefs and managers, Aydın Birol Akdemir, Volkan Kargın, Ercan Ürek, Özge Kapulu Gülbağ, and Haydar Efdal Tarhan, for their continuous support and confidence in me. I am grateful to be part of the Gökbey product team, and I appreciate the support and encouragement from my colleagues.

I am eternally grateful to my colleague, teammate, and friend Göktuğ Koçak for his valuable knowledge, insights, and moral support throughout this study. His contributions in all aspects have been immensely appreciated. I greatly acknowledge Yavuz Research Group members; Oğuzhan Yılmaz, Diren Dikbaş, Osman Ohtaroğlu, Ahmet Emin Sürücü, and Erdoğan Güneş for their continuous support and assistance

with experiments. Our collaborative spirit and the unforgettable moments we shared in the Fluid Mechanics Lab made this journey truly enjoyable. I also wish to express my gratitude to all my friends who stood by me during my PhD journey: Mert Nizamı Işık, Hüseyin Toprak, Yağmur Toprak, Güney Görgün, Tufan Akba, Arda Çalışkan, Ilgaz Doğa Okcu, Emre Zengin, Tuğrul Akpolat, and Gökay Günacar. Your support has meant a lot to me.

I express my heartfelt gratitude to my family, whose unwavering support has been the foundation of my academic journey. To my parents, Nebahat and Abdurrahman Çetin, your endless love and sacrifices have shaped who I am today. I am especially thankful to my brother, Remzi Çetin, for his steadfast support and encouragement.

Most importantly, I owe my deepest appreciation to my wonderful wife, Suna Güçyılmaz Çetin. Your love, understanding, and unwavering support have been my guiding light throughout this journey. Your patience during the countless hours I have spent on my research has been remarkable. Together, we have created a beautiful journey, and I look forward to the adventures that lie ahead.

TABLE OF CONTENTS

LIST OF TABLES

TABLES

LIST OF FIGURES

FIGURES

LIST OF ABBREVIATIONS

SYMBOLS

a, b	First and second coefficients for the linear fit
A	Planform surface area [m^2]
A_{bleed}	Bleed slot cross-sectional area [m^2]
A_h	Blowing hole exit cross-sectional area [m^2]
C	Chord length [mm]
C_D	Drag coefficient
C_L	Lift coefficient
C_M	Pitching moment coefficient
C_p	Pressure coefficient
C_μ	Momentum coefficient
$C_{\mu,\text{eff}}$	Effective momentum coefficient
d	Bleed slot end diameter [mm]
d	Blowing hole outlet diameter [mm]
DC_c	Carrier duty cycle [%]
DC_m	Modulating duty cycle [%]
F	Force [N]
F_D	Drag Force [N]
F_L	Lift Force [N]
E	CTA Voltage [V]
f	Frequency [Hz]
f_c	Carrier excitation frequency [Hz]
f_m	Modulating frequency [Hz]
g	Gravitational acceleration [m/s^2]

i	Bleed slot number
k_{across}	Across bleed slot pressure loss coefficient
l, l_p, l_s	Bleed slot length on pressure and suction sides of the wing [mm]
L	Characteristic length
M	Moment [Nm]
M_y	Pitching moment [Nm]
$\bar{p}$	Mean pressure designation for surface pressure [Pa]
p_∞	Static pressure of the freestream [Pa]
p_{dyn}	Dynamic pressure of the freestream [Pa]
Q	Calibration supply flow rate [lit/min]
R	Measured variable
Re	Reynolds number of the freestream
Re_b	Reynolds number of the calibration bleed air supply velocity
Q	Calibration bleed air supply flow rate [l/min]
s	Wing half span [mm]
s_p	Bleed slot spacing on pressure side [mm]
s_s	Bleed slot spacing on suction side [mm]
S	Wingspan [mm]
St	Strouhal number
T	Torque, Moment
T_w	Pulse Width Duration [sec]
u, v, w	x, y, z velocity components [m/s]
u_R	Relative uncertainty of measured variable
U_∞	Freestream velocity [m/s]
U_{blow}	Blowing velocity [m/s]
$U_{blow,rms}$	Root mean square of the valve on state mean blowing velocity profile [m/s]

V_{bleed}	Bleed slot exit velocity [m/s]
$V_{bleed,supply}$	Calibration bleed air supply velocity [m/s]
V_{ent}	Bleed slot entrance velocity [m/s]
w	Bleed slot thickness [mm]
α	Angle of attack [deg]
Δp	Across bleed slot pressure difference [Pa]
Λ	Sweep angle
θ	Bleed slot forward back angle [deg]
θ'	Bleed slot rear back angle [deg]
ν	Kinematic viscosity of the fluid [m^2/s]
ρ	Density of the fluid [kg/m^3]
Ψ	Streamlines
ω_R	Uncertainty estimate of measured variable
ω_z	Vorticity in normal direction [1/s]

SUBSCRIPTS

b	Body coordinate system
w	Wind coordinate system
p	Pressure side
s	Suction side
x	x-axis
y	y-axis
z	y-axis

ABBREVIATIONS

CR	Contraction ratio
CTA	Constant temperature anemometry
DAQ	Data acquisition
FFT	Fast Fourier transform

FS	Full Scale
LEV	Leading edge vortex
PIV	Particle image velocimetry
PSD	Power spectral density
RMS	Root mean square
SLS	Selective Laser Sintering
UAV	Unmanned aerial vehicle

CHAPTER 1

INTRODUCTION

Control of flow structures using advanced techniques on non-slender delta wing models, typically with a sweep angle (Λ) of less than 55 degrees, has gained significant attention in recent decades [1]. These models represent the simplified planforms of micro air vehicles, unmanned combat air vehicles, and unmanned air vehicles designed for both commercial and military applications. Such planforms generate complex and unsteady flow patterns during steady flight or predefined maneuvers, which significantly affect their stability and performance characteristics. To quantify the effectiveness of the applied flow control methods, it is essential to accurately identify both inherent and manipulated flow structures [2], [3].

Delta wings are classified based on their sweep angles into slender ($\Lambda > 55$ degrees) and non-slender ($\Lambda < 55$ degrees) categories. For both types, the flow field is characterized by vortical structures. The flow over sharp-edged delta wings separates from the windward side of the leading edges and rolls up into a coherent primary vortex structure, which is continuously fed by discrete vortices shedding from the leading edge [4]. As a result, these wings experience complex flow features including vortex breakdown, shear layer instabilities, and fluid-structure interactions. The principal coordinate orientation, along with the representation of the sweep angle (Λ) and separation lines, is illustrated in Figure 1.1 [3].

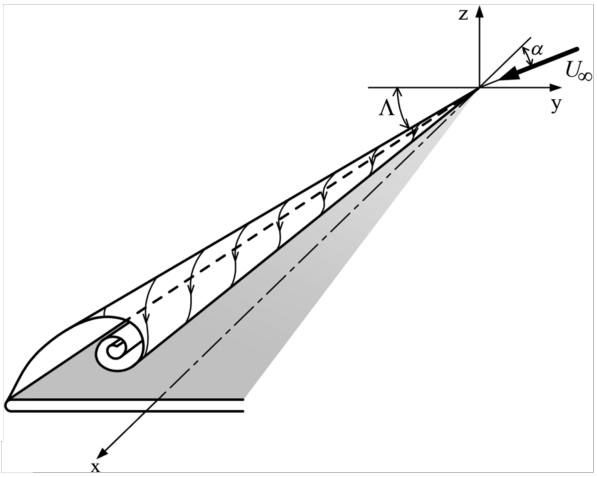

Figure 1.1: Designation of delta wing leading edge vortex formation; principal axis, sweep angle [3].

The strong suction regions created by high axial core velocities, which may reach up to 4–5 times the airspeed, generate an additional lift component [5]. Compared with slender delta wings, the vortices over non-slender delta wings appear closer to the wing surface and exhibit lower strength characteristics [6]. This proximity causes an interaction between the boundary layer and the primary vortex, resulting in the formation of a second primary vortex of the same sign, known as the "dual vortex" [7], [8]. Consequently, vortex-induced lift is more limited over non-slender wings compared to slender ones. Additionally, considering the buffet loading on non-slender wings, the shear layer reattachment is the essential source of fluid-structure interaction in pre-stall regions due to the high-velocity fluctuations along the reattachment line [9], rather than the existence of vortex breakdown. The control of leading edge vortex systems over non-slender delta wings encompasses a broad range of structures and parameters, including vortex location and strength and inherent instabilities such as shear layer reattachment, vortex breakdown, and three-dimensional surface separation/stall. Therefore, each of these phenomena may require different approaches, and a single approach may not be effective for all. Given the drawbacks associated with the flow over non-slender delta wings, significant effort has been directed towards various control techniques. This includes the development of new and novel approaches as well as the implementation and characterization of existing techniques for the first time.

1.1 Motivation and Problem Definition

In recent decades, there has been a significant increase in studies focusing on the characterization of flow structures over delta wings with a sweep angle (Λ) of less than 55 degrees. These planforms provide valuable data for the advanced design of Unmanned Aerial Vehicles (UAVs), Unmanned Combat Aerial Vehicles (UCAVs), and Micro Aerial Vehicles (MAVs). It is also anticipated that in the near future, such delta wing geometries will serve as baseline models for manned aircraft, given their growing popularity in recent years.

Delta wings offer several advantages, including high maneuverability, agility, and a low structural-weight-to-take-off-weight ratio. As the transition from conceptual design to operational vehicles accelerates, concerns regarding performance, efficiency, and stability have become central to the community. These planforms may experience aerodynamic performance degradation due to complex flow physics during critical flight phases such as landing, takeoff, and maneuvering at high pitch and yaw rates. These phases often involve high angles of attack and sideslip, where delta wing planforms exhibit deteriorated performance due to unsteadiness and three-dimensional surface separation. Despite the complexity of these flow structures, there are still relatively few studies investigating the flow physics of non-slender wings. A detailed understanding of the flow field and the estimation of aerodynamic load characteristics are crucial for documenting comprehensive performance. Such an approach could also help identify potential flow control solutions to address design concerns for both researchers and the industry.

Recent studies have shown that, among various passive and active flow control approaches, passive bleeding and periodic blowing can effectively control flow structures on non-slender delta wings. These methods particularly focus on eliminating three-dimensional surface separation, enhancing the leading edge vortex, and delaying stall. However, there are still very few studies investigating the comprehensive impact of passive bleeding techniques on vortex-dominated aerodynamic surfaces. Innovative bleeding geometries could enhance effectiveness in terms of aerodynamic performance and stability. Despite the increased popularity of periodic excitation techniques on non-slender delta wings, their impacts need further investigation, par-

ticularly concerning multi-control parameter sensitivity and the assessment of aerodynamic loads and stability.

In addition to documenting the effectiveness of these sophisticated flow control strategies, quantifying their individual momentum contributions is essential to relate the achieved aerodynamic and stability benefits. Most existing studies have characterized proposed flow control actions in isolation. A detailed investigation into the quantification of these flow control approaches may help researchers more accurately estimate aerodynamic benefits. Additionally, a well-established sensor relationship could facilitate the development of real-time closed-loop control architectures using on-off valve actions at different flight regimes, based on the results of parametric passive and open-loop active control studies.

1.2 Aim of the Study

The aim of the present study is to control the complex flow structures over a delta wing with a sweep angle (Λ) of 45 degrees using passive and active techniques, specifically passive bleeding and periodic blowing. This experimental work was conducted in a low-speed wind tunnel facility at the Fluid Mechanics Laboratory of the Mechanical Engineering Department at Middle East Technical University. The experiments were performed at Reynolds numbers ranging from $3.5x10^4 \leq$ Re $\leq$ 1 x 10^5 and angles of attack from $0^o \leq \alpha \leq 30^o$, using the experimental techniques of surface pressure, force balance, hot wire anemometry, and near-surface particle image velocimetry measurements.

For the passive technique, the study investigated the effect of a novel bleeding geometry design with a nozzle cross-section aimed at increasing the bleeding momentum. Four different nozzle wing models were tested in comparison to a baseline delta wing model for the defined nozzle bleed geometry parameter namely a contraction ratio of CR = 1:0.5 and CR = 1:0.75. To broaden the scope of comparison, force measurements were also conducted for the Back Bleed wing configuration previously studied by Çelik et al. [10]. Additionally, a method for estimating the passive bleeding momentum coefficient was developed and presented based on surface pressure

measurements, utilizing the Bernoulli equation and loss coefficient. In-situ hot wire measurements were performed to characterize the technique, allowing to extract of the pressure loss coefficient across the bleed slot.

For the periodic blowing technique, the effect of square wave type actuation applied through the leading edges with a jet angle parallel to the bevel surface was studied. Two main configurations were tested: regular signal and burst modulated signal, using an in-house active blowing flow control system. A detailed matrix was developed to assess the sensitivity of the active flow control parameters. For the regular square wave periodic blowing actuation, an excitation frequency range of $1 \leq f_c \leq 64$ Hz was tested for two different duty cycle settings of $DC_c = 25\%$ and 50%, at a maximum momentum coefficient value of $C_{\mu,max} = 1\%$. For the burst modulated square wave cases, experiments were performed for a carrier frequency range of $4 \leq f_c \leq 64$ Hz with carrier duty cycle settings of $DC_c = 25\%$ and 50%, and a modulating frequency range of $1 \leq f_m \leq 4$ Hz with modulating duty cycle settings of $DC_m = 50\%$. For comparison purposes, steady blowing actuation was also tested at a maximum momentum coefficient range of $0.25\% \leq C_{\mu,max} \leq 1\%$ In addition, prior to aerodynamic measurements, a comprehensive characterization of the flow control system was conducted using in-situ approaches to test and construct calibration charts for each control parameter.

1.3 The Outline of the Thesis

This thesis is organized into eight main chapters. Chapter 1 provides introductory remarks, an overview of flow structures over delta wings, and the impact of passive and active flow control applications, as well as the motivation and objectives of the study.

Chapter 2 presents a detailed examination of flow physics and its control using various techniques, in line with the associated literature.

Chapter 3 describes the technical aspects of the experimental system, including measurement techniques, methodology, uncertainty estimates, and the experimental matrix.

Chapter 4 proposes a calibration scheme for estimating the bleed momentum coefficient, with a detailed discussion of the results obtained using this technique. Chapter 5 reports on the results of passive bleeding control using nozzle-type slots.

Chapter 6 details the comprehensive characterization of the in-house active blowing flow control setup, utilizing an in-situ calibration scheme. Chapter 7 discusses the results of the periodic blowing flow control experiments.

Finally, Chapter 8 presents the principal findings and conclusions of the present work.

CHAPTER 2

LITERATURE SURVEY

In this chapter, the fundamental flow physics over delta wings, particularly those focusing on non-slender types, and the associated active and passive flow control applications are summarized. The outcomes of reported flow control applications on similar planforms are discussed in terms of manipulating complex flow features, including leading-edge vortices, flow reattachment, vortex breakdown, and three-dimensional surface separation.

2.1 Flow Over Delta Wings

The flow over delta wings is characterized by flow separation along the leading edge. The separated shear layers roll up into a coherent vortex structure, fed by discrete vortices emanating from the leading edge towards the leeward side of the wing, forming what is known as the primary vortex [4]. The strong suction areas associated with negative pressure zones created by the high axial velocities across the vortex core can significantly increase the lift coefficient [11]. There are fundamental differences in the vortical structures of slender and non-slender delta wings, which are highly dependent on the sweep angle [12]–[14]. The steady and unsteady aspects of flow over slender delta wings have been investigated in detail in the open literature [15]–[18]. In contrast, foundational knowledge regarding non-slender delta wings has grown extensively in recent decades.

To provide a comprehensive understanding, it is reasonable to present the flow physics of non-slender wings alongside that of slender wings. In Figure 2.1, the principal schematic of the flow over the suction side (a), a closer look at the separated shear

layer (b) [19], and the spectral distribution of the unsteady nature (c) [20] are provided. Breitsamter [21] summarized a correlation representing the leading-edge vortex (LEV) development as a function of the sweep angle ($\Lambda = 45° - 85°$) and the angle of attack ($\alpha = 0° - 40°$) in a progressive manner for sharp leading-edge wing models.

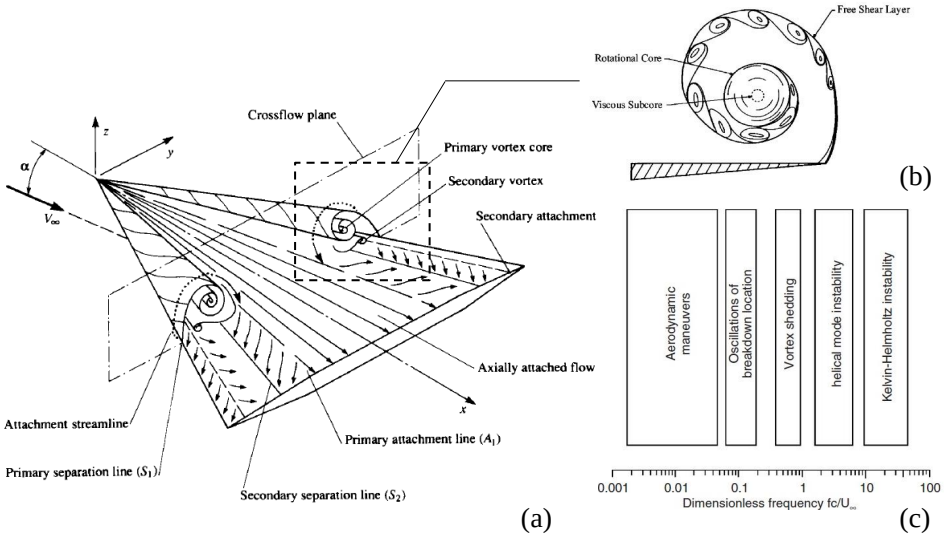

Figure 2.1: Summary of delta wing aerodynamics, (a) flow field (Courtesy of John Stollery, Cranfield Institute of Technology, England.), (b) schematic of separated of shear layer [19], (c) unsteady flow spectrum [20].

As illustrated in Figure 2.2, at sufficiently high angles of attack, separation initially occurs at the rear part of the wing, creating the primary vortex. As the angle of attack increases further, the separation point moves towards the apex, leading to a fully developed vortex for slender delta wings with $\Lambda > 55° - 60°$. This behavior may not be observed in non-slender delta wings, resulting in a lower onset of vortex burst and three-dimensional surface separation, which affects critical aerodynamic performance.

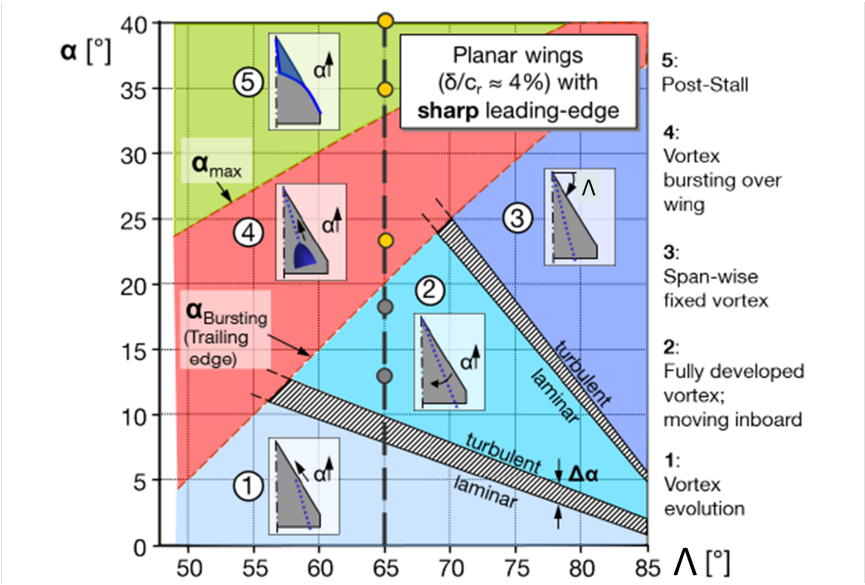

Figure 2.2: Progression of the vortex flow as a function of Λ and α, adapted from [21].

The presence of the primary vortex leads to velocity and associated pressure gradients, as evidenced by numerous studies in the literature. A sample distribution velocity distribution for a slender delta wing [22] is shown in Figure 2.3 and sample dimensionless pressure distributions are represented in Figure 2.4 for a non-slender [10]. The pressure gradient across the suction peak and leading edge may trigger a secondary vortex separation in the opposite direction, with the primary vortex located near the leading edge.

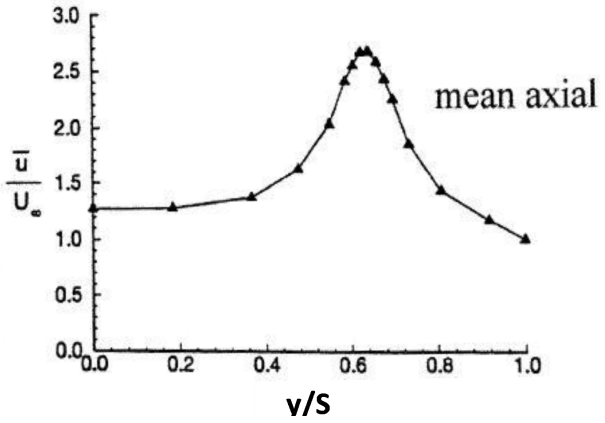

Figure 2.3: Sample velocity distribution across slender wing primary vortex [22].

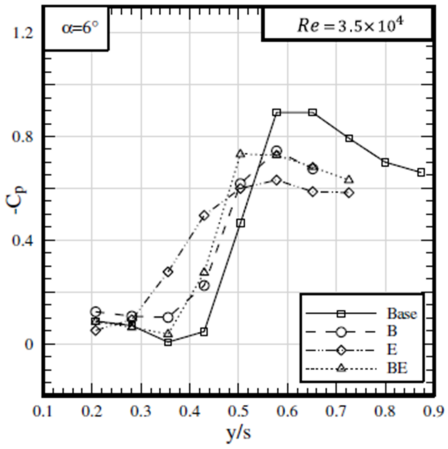

Figure 2.4: Sample dimensionless surface pressure distribution over non-slender delta wings [10].

Compared to slender delta wings, vortices over non-slender delta wings form closer to the wing suction surface [6], leading to an interaction between the boundary layer and the vortex [7]. This interaction may result in the formation of a second primary vortex of the same sign, creating a "dual vortex" structure, which has been observed both computationally [7] and experimentally [8]. The schematic of dual vortex formation [23] is provided in Figure 2.5.

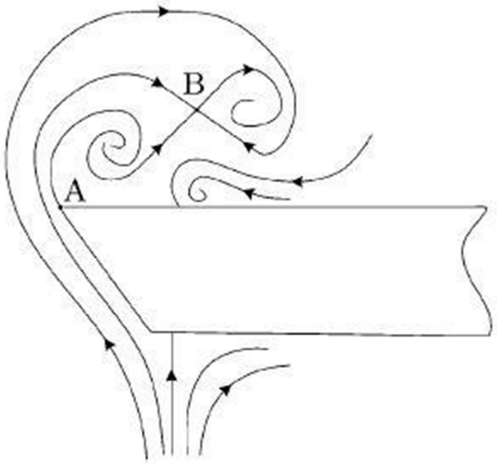

Figure 2.5: Illustration of the dual vortex formation [23].

These structures are most evident in low Reynolds number and low angle of attack regimes. The mean axial core velocity can increase up to 4-5 times the freestream velocity for slender delta wings, whereas this increase is around twice for non-slender wings, which may be attributed to the presence of distinct vortical structures. The baseline aerodynamic performance of non-slender delta wings is generally less promising compared to slender delta wings, as illustrated by the lift distribution comparison [24] in Figure 2.6. This unfavorable characteristic will be a key motivation for implementing flow control techniques.

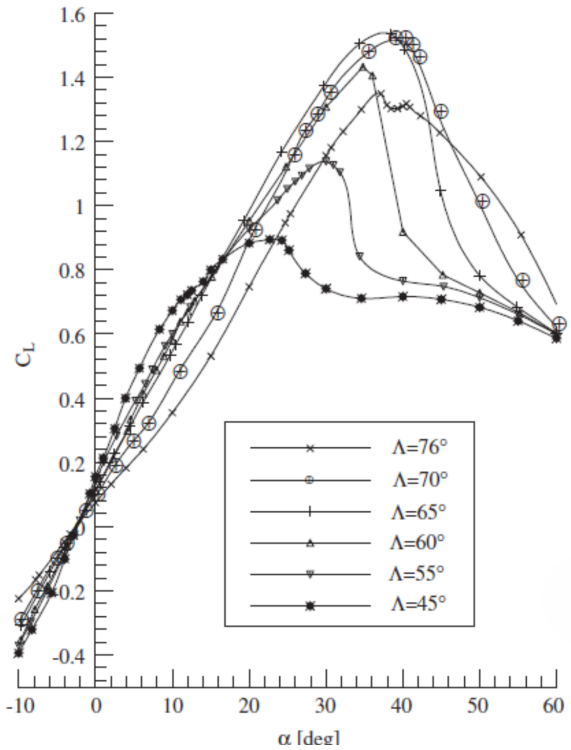

Figure 2.6: Lift distribution as a function of Λ and α [24].

Another significant difference is the shear layer reattachment process. For non-slender delta wings, reattachment of the separated primary shear layers is observed even after vortex breakdown, whereas this phenomenon is only present at low angles of attack for slender delta wings. The schematic representation of the reattachment process for both types [25] is shown in Figure 2.7.

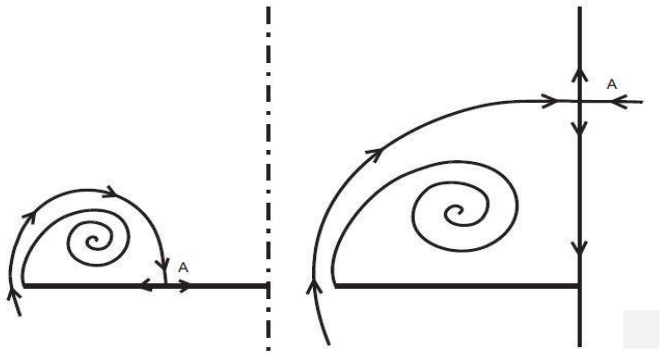

Figure 2.7: Flow reattachment process: Non-slender (left) and slender (right) wings [25].

For non-slender delta wings, this process, along with high velocity fluctuations on the reattachment line, is considered a major source of wing buffeting [19], rather than the vortex breakdown itself. Sample flow measurement results for controlled vortex flow over a 50° non-slender wing [26], with clear indications of the reattachment regions, are shown in Figure 2.8. For slender wings, promoting reattachment in the post-stall regime benefits aerodynamic performance, though manipulating this process presents a challenging issue [5].

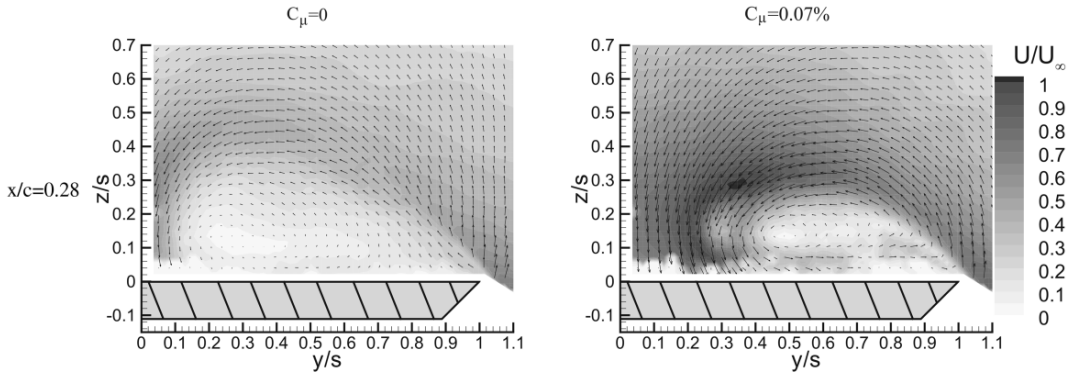

Figure 2.8: Cross flow PIV results for a sample controlled vortex flow [26].

2.1.1 Unsteady Nature of the Flow Field

The flow over delta wing planforms exhibits complex and unsteady flow patterns, including shear layer instabilities, vortex breakdown, oscillation of the vortex break-

down location, vortex shedding, and vortex wandering, while performing steady flight or defined maneuvers. The occurrence spectrum of these phenomena is shown in Figure 2.1 (c).

In the larger magnitude and broadband region, Kelvin-Helmholtz (K-H) type instability, commonly observed for slender wings, is also evident in non-slender wings at lower angles of attack. The periodic formation of discrete vortices on the shear layer is attributed to K-H instability. These structures continuously feed the primary vortex structure. Sample discrete vortex occurrence for a slender delta wing ($\Lambda = 60°$) are presented in Figure 2.9 [27]. Such structures were also evidenced for non-slender delta wings as represented in Figure 2.10 ($\Lambda = 50°$). Due to its spectral distribution, K-H type instability serves as an inspiration for high-frequency excitation flow control applications [25].

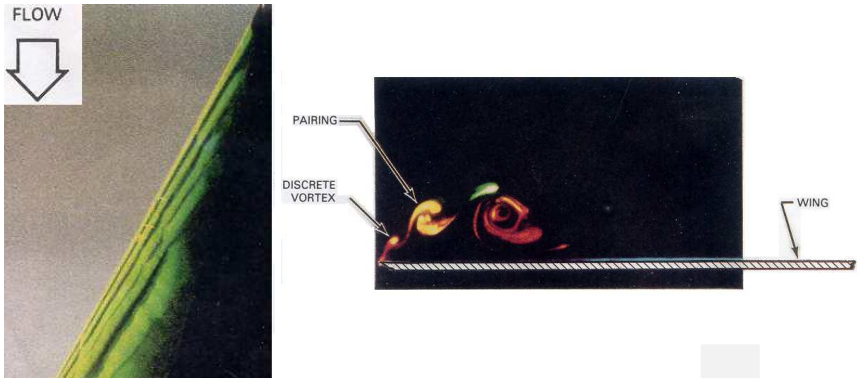

Figure 2.9: Sample discrete vortex formation for a slender delta wing with $\Lambda = 60°$ at $\alpha = 10°$ [27].

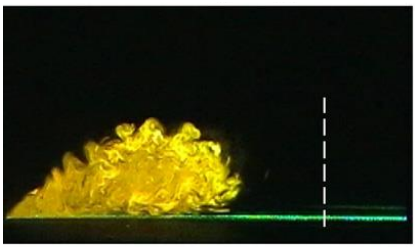

Figure 2.10: Sample discrete vortex formation for a non-slender delta wing with $\Lambda = 50°$ at $\alpha = 15°$ [25].

Prior to vortex breakdown formation, a significant unsteady random movement of the vortex core, known as vortex wandering, can be observed for both slender and non-slender wings. This phenomenon has been primarily reported in relation to shear layer instabilities, particularly Kelvin-Helmholtz (K-H) type instabilities [28]. The adapted root mean square (RMS) velocity distribution for the vortex core over a slender delta wing [22] is presented in Figure 2.11.

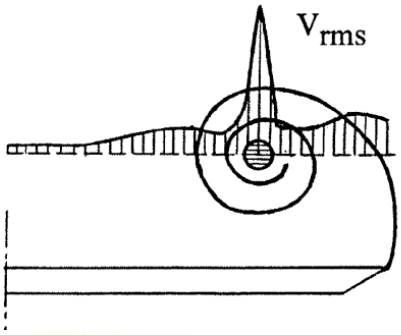

Figure 2.11: Representative cross flow plane vortex core RMS velocity distribution for a slender delta wing [22]

This phenomena was also characterized over a non-slender delta wing with $\Lambda = 38.7°$ sweep angle for which a sample vorticity and RMS of axial velocity [29] are shown in Figure 2.12. Additional discussions indicate that vortex wandering is sensitive to Reynolds number, with velocity fluctuations increasing with Reynolds number, as shown in Figure 2.13 [30] and Figure 2.14 [20].

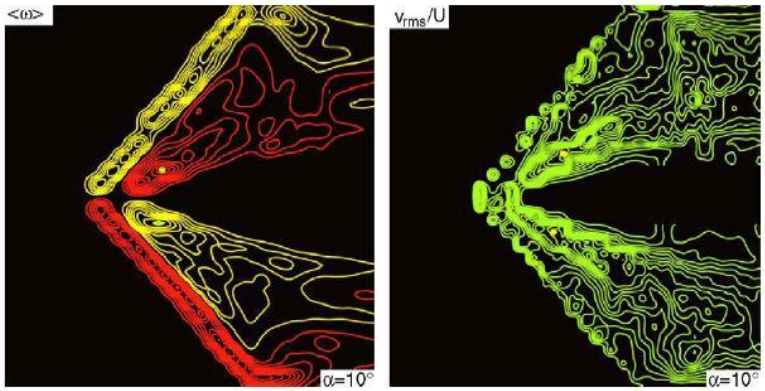

Figure 2.12: Near surface RMS velocity representations for a non-slender delta wing with $\Lambda = 38.7°$ at $\alpha = 10°$ [29].

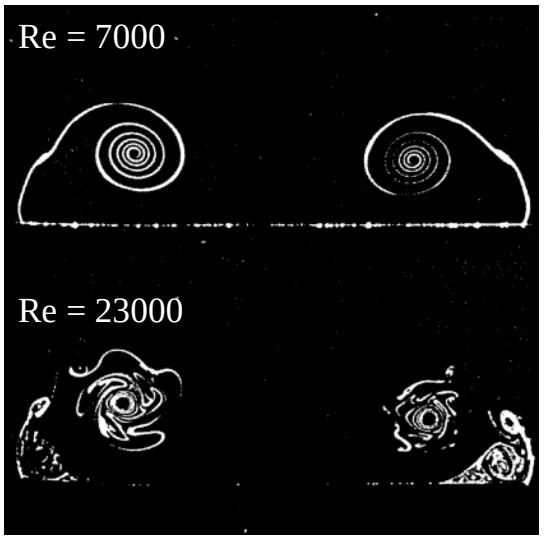

Figure 2.13: Steady v.s. unsteady shear layer on a slender delta wing with $\Lambda = 70^\circ$ at $\alpha = 20^\circ$ [30].

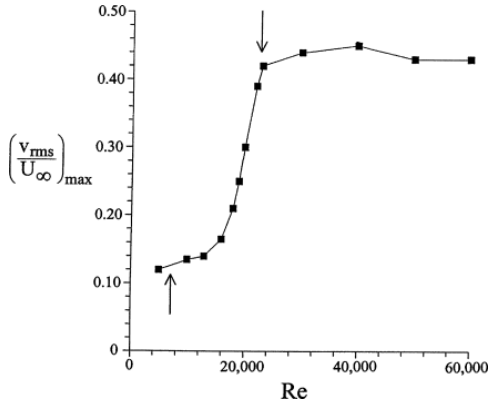

Figure 2.14: RMS of lateral velocity as a function of Reynolds number [28].

Compared to the aforementioned instabilities, another significant mechanism called vortex shedding can occur at smaller frequencies, specific to very high angle of attack regimes. This phenomenon develops once the vortex breakdown reaches the apex of the wing. Vortex shedding has been studied in detail in the literature, with a review for slender wings provided by Gürsül [20]. Periodical separation of leading-edge shear layers may occur in symmetric or antisymmetric modes across a broad Reynolds number range. Schematic representations of the shedding mechanism for slender delta wings are shown in Figure 2.15 [31].

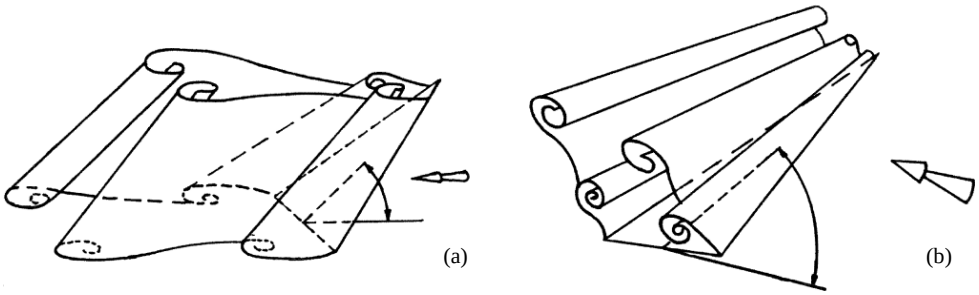

Figure 2.15: Schematic representation of the vortex shedding mechanism: (a) Symmetric formation, (b) Axisymmetric formation [31].

2.1.2 Vortex Breakdown

In the absence of the aforementioned instabilities, the vortical flow structure over a delta wing, in its well-organized state, exhibits a cylindrical and stable formation with well-defined longitudinal, axial, and azimuthal velocity components. Delery [32] provided a critical review of vortex breakdown across various conditions, summarizing the criteria leading to vortex breakdown in terms of velocity components and swirl parameters. Our discussion will focus specifically on vortex breakdown mechanisms over delta wings. As the angle of attack increases, the jet-like longitudinal core flow decelerates and eventually stagnates due to the adverse pressure gradient. In this condition, the azimuthal velocity component becomes comparable to the longitudinal velocity component, transforming the structure into a wake-like condition due to viscous forces, which diminishes its strength and vortex characteristics. The commonly observed types of vortex breakdown include bubble, helix, and spiral formations, as shown in Figure 2.16 (a), (b), and (c), respectively [33]. Vortex breakdown phenomena can occur over both slender (Figure 2.17 (b)) and non-slender (Figure 2.17 (c)) delta wings, with commonly observed formations including bubble and spiral types (Figure 2.17 (a)).

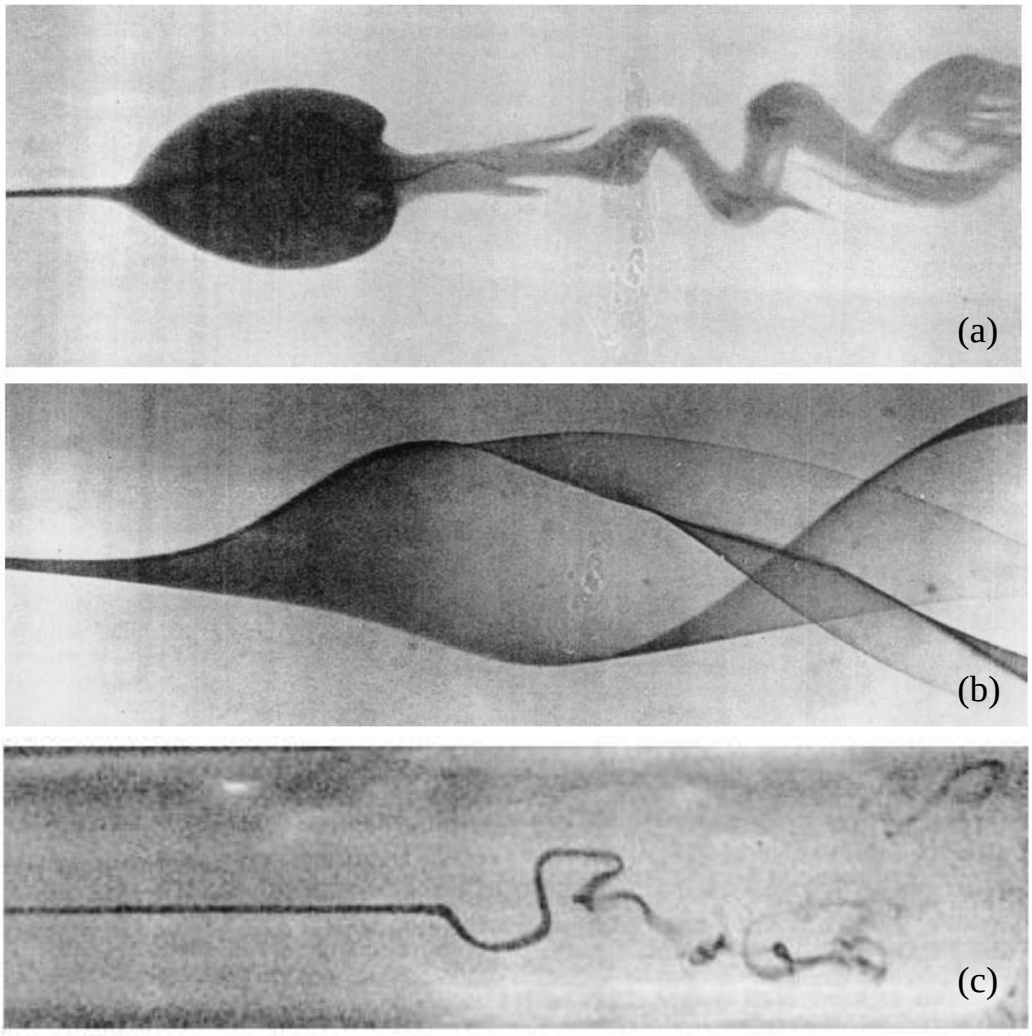

Figure 2.16: Vortex breakdown types: (a) Bubble, (b) Helix, and (c) Spiral formations [33].

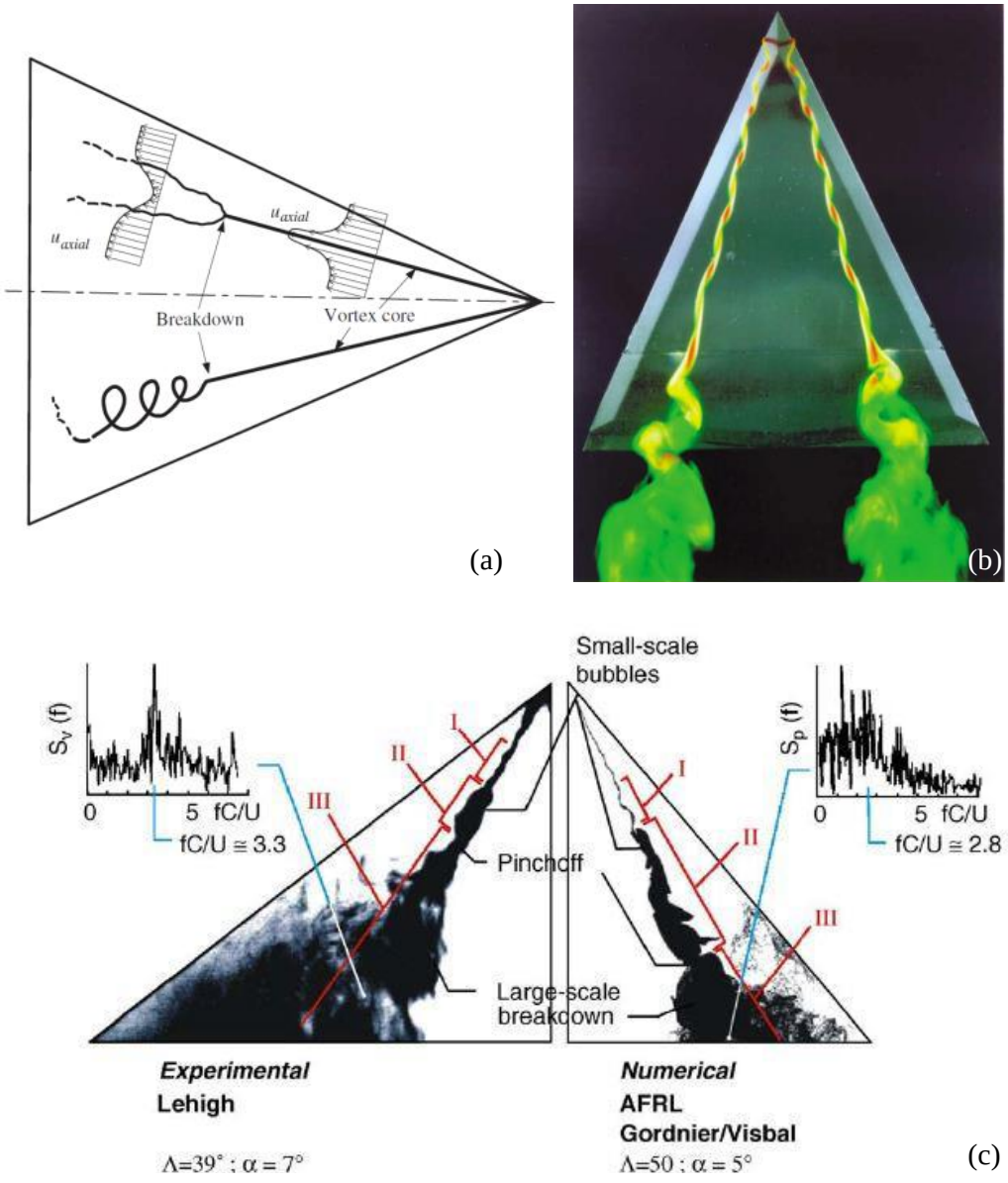

Figure 2.17: Vortex breakdown formation: (a) Sketch of bubble and spiral types [3], (b) Visualization over a slender delta wing [34], (c) Visualization over non-slender delta wings adapted from Gürsül et al. [1].

Considering the leading-edge vortices, the effective parameters such as swirl level and pressure gradient are also dependent on the sweep angle, in addition to the angle of attack. Gürsül [25] presented the boundaries of these phenomena in relation to the flow reattachment concept, as shown in Figure 2.18, which is similar to the sketch provided by Breitsamter [21] in Figure 2.2.

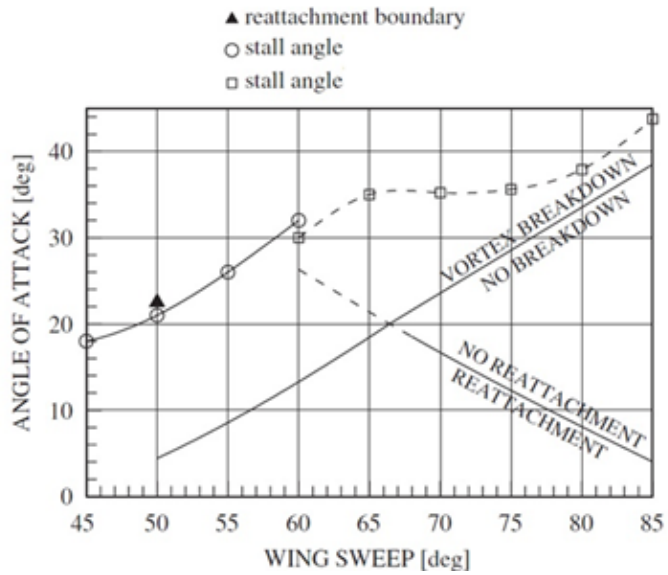

Figure 2.18: Boundaries of vortex breakdown and flow reattachment as a function of angle of attack and sweep angle [25].

In contrast to non-slender delta wings, vortex breakdown is considered a major source of wing buffeting for slender delta wings, in addition to being the predominant mechanism for lift loss. Consequently, for slender delta wings, vortex breakdown, or vortex bursting, becomes the primary focus of flow control strategies. In this context, the flow downstream of vortex breakdown becomes a major concern, as it typically exhibits hydrodynamic instability, leading to helical mode instability and quasi-steady pressure fluctuations over the wing surface. For more detailed explanations of vortex breakdown, readers are referred to the important results and review studies cited above.

2.1.3 Flow Reattachment

Flow reattachment is a characteristic feature of non-slender delta wings, and as mentioned earlier, it is also observed in slender delta wings, albeit limited to lower angles of attack. The region where flow reattachment occurs is typically associated with velocity fluctuations. Once reattachment is established over the wing, its spanwise location tends to move inboard with increasing incidence. Figure 2.19 (a) presents Particle Image Velocimetry (PIV) results obtained by Taylor and Gürsül [35] for a

2 mm thick aluminum flexible non-slender delta wing with $\Lambda = 50°$, showing the formation of the reattachment line and its inboard movement with increasing angle of attack (Figure 2.19 (b)). They reported that maximum r.m.s. velocity fluctuations occur adjacent to the reattachment line, with frequency content similar to that observed in slender wings, indicating that the buffeting response is primarily related to the reattachment phenomena. Additionally, Figure 2.19 (b) and (c) show that when reattachment is completely inboard, stalled wing conditions are also reached, as evidenced by aerodynamic coefficients. Due to the fact that flow reattachment over slender delta wings is limited to lower angles of attack, manipulating this phenomenon on slender wings becomes more challenging compared to non-slender delta wings.

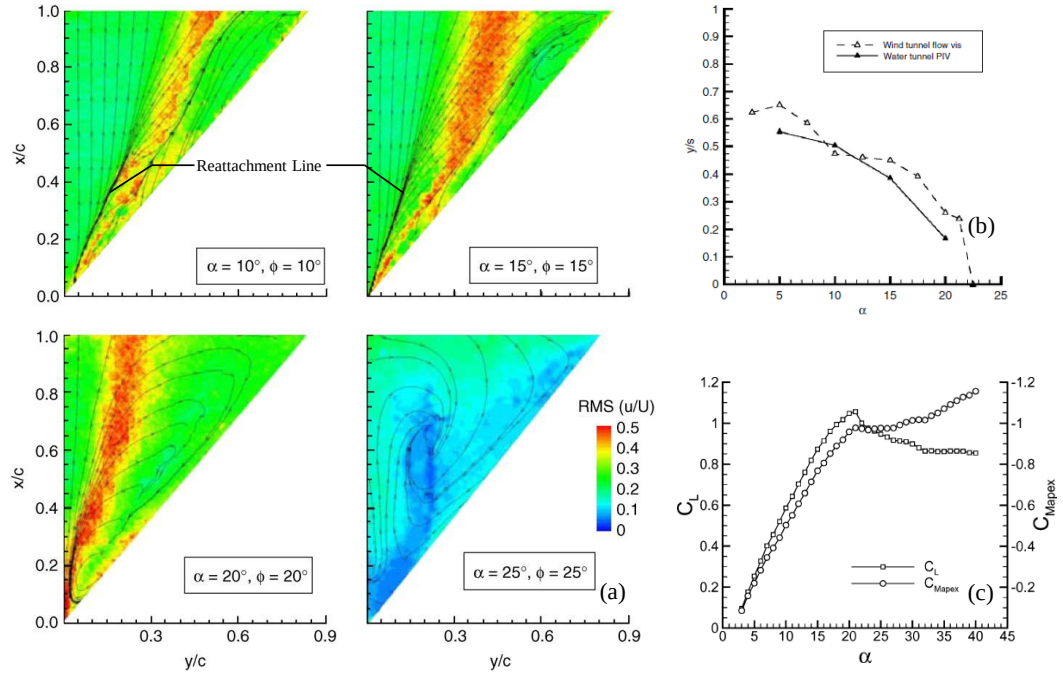

Figure 2.19: (a) Surface PIV measurement for a non-slender delta wing with $\Lambda = 50°$, (b) Variation of spanwise reattachment line location with incidence, and (c) Force measurement results [35].

2.1.4 Three - Dimensional Surface Flow Separation

Viscous flow theory suggests that an adverse pressure gradient induces flow separation, a phenomenon observed over delta wings just before reaching stall conditions.

Streamline structures over delta wings, including flow reattachment and separated flow with a "whorl" feature, manifest at different angles of attack. At sufficiently high incidences, the vortical structure around the delta wing loses its characteristics and is replaced by a large-scale, inward-swirling surface streamline structure, a key indicator of three-dimensional separation [36]. Further increases in incidence lead to stall, characterized by the appearance of the "whorl." During stall, shear layer reattachment becomes impossible, lift over the wing decreases, and velocity near the planform converges to near stagnation [37].

In addition to numerical methods, extensive experimental studies have documented these phenomena using techniques such as oil flow visualization, particle image velocimetry (PIV), and laser Doppler anemometry (LDA). Moreover, Miau et al. [38] investigated flow patterns on a wing with a 50° sweep angle, focusing on the consequences of the leading-edge profile. Gordinier and Visbal [7] numerically computed the instantaneous and averaged flow structure on a delta wing with a 50° sweep angle. Taylor et al. [8] used dye techniques and PIV to visualize vortex cores on wings with a low sweep angle of 50°. Their studies demonstrated that at low angles of attack, a dual primary vortex system exists, which transitions to a single, larger-scale vortex at higher angles of attack. Yaniktepe and Rockwell [13] examined a wing with a sweep angle of 38.7° using PIV, identifying an elongated vorticity layer reattaching to the wing surface. Yaniktepe and Rockwell [39] further explored flow structures at the trailing edge of low sweep diamond and lambda planforms, while Yavuz et al. [29] studied near-surface topology for a wing with a 38.7° sweep angle using PIV.

Understanding these separation mechanisms is crucial for optimizing delta wing designs, as controlling or delaying flow separation can significantly improve lift and overall aerodynamic performance of the aircraft.

2.2 Flow Control

In recent decades, efforts to manipulate flow instabilities on non-slender wings, including localized flow separation, separated shear layers, vortex formation, flow reattachment, and vortex breakdown, have exhibited significant growth [25]. Gad-El-Hak

[40] reviewed flow control classifications under two schemes: passive and active. The former is defined as a control device requiring no auxiliary power input or control loop, often referred to as flow management. In contrast, the latter requires energy input of any kind and a control loop, either predetermined or reactive. While passive flow control techniques have the advantage of being efficient with no energy cost, a significant drawback is that since the modification is permanently employed on the wing structure, they might induce undesired flow characteristics under different flight conditions.

Among the aerodynamic community focusing on the control of tip and edge vortices, passive flow control techniques are mostly associated with geometric and material modifications, including edge modifications [41]–[46], thickness-to-chord ratio [47], [48], static control surfaces [49]–[52], and bleeding [10], [53]. Considering the active flow control techniques in the literature, most studies have relied on predetermined active flow control methods. The most common predetermined control methods include steady blowing and/or suction [54]–[60], unsteady excitations, including small-large amplitude perturbations [13], [61], periodic blowing and/or suction [27], [62]–[68], and plasma actuators [69], [70].

In the following sections, the targets and results of selected studies from the aforementioned techniques are given and discussed accordingly for both slender and non-slender delta wings.

2.2.1 Passive Flow Control Techniques

2.2.1.1 Edge Modifications

Edge modifications appear as a widely investigated technique. The leading-edge shape, in terms of edge contour such as rounded profiles and beveled profiles, as well as thickness-to-chord (t/C) ratio values, have become significant factors in delta wing flows. At first glance, such modifications may not seem like distinct flow control approaches. However, one can argue that any improvement or deterioration might make the leading edge selection a preliminary vortex conditioner over delta wings, thus affecting the shear layer separation direction and strength. Some samples for the

leading-edge profiles and results from the literature are represented in Figures 2.20 and 2.21. Wang and Lu [41] studied the effects of bevel direction and angles for $\Lambda = 50^\circ$ non-slender planforms (see Figure 2.20). Sample results show that, in the post-stall regime, lift can be considerably enhanced using a windward beveled leading edge, whereas in the post-stall region, a leeward beveled wing exhibits superior performance in terms of lift. McClain et al. [42] compared beveled and rounded leading edges in different configurations (see Figure 2.21) for $\Lambda = 50^\circ$ non-slender planforms to evaluate their effect on roll response. They also reported the lift coefficient distributions of the wing models where sharp leading edges represent better characteristics in the pre-stall region, whereas the opposite is observed in the post-stall regime.

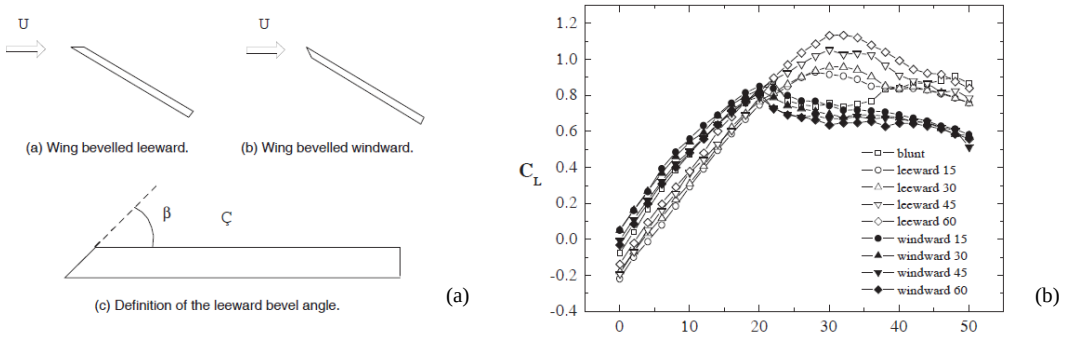

Figure 2.20: Effect of bevel direction and angle [41] for $\Lambda = 50^\circ$ non-slender delta wing: (a) schematic of edge modifications, (b) lift coefficient distributions.

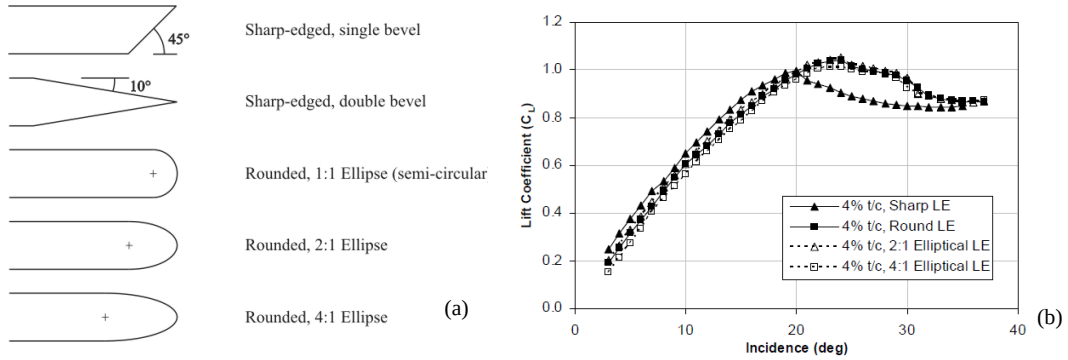

Figure 2.21: comparison of beveled and rounded leading edge shapes [42] for $\Lambda = 50^\circ$ non-slender delta wing: (a) schematic of edge modifications, (b) lift coefficient distributions.

Gülsaçan et al. [47] studied the effect of the thickness-to-chord ratio on a low-swept delta wing with $\Lambda = 35°$. Based on the PIV, surface pressure measurements, and flow visualization results, they concluded that the t/C ratio is highly effective in transforming flow structures in different phases. Some major concluding remarks include the following: the thickness of the region bounded by the primary shear layer is inherently correlated with wing thickness, and the lowest t/C ratio might be more resistant to pre-stall and stall conditions. Figure 2.22 represents the comparison for the lowest and the highest t/C values investigated for $\alpha = 10°$, indicating the results for the aforementioned conclusions.

An interesting technique that has gained popularity is the implementation of sinusoidal edge profiles among airfoil studies; however, there are comparatively limited studies on delta wings, mostly on non-slender planforms [43], [44]. This technique is inspired by the bio-mimicking of the humpback whale fin. Major findings from reference studies reveal observations such as multiple vortices forming weaker in strength [45], an increase in turbulence kinetic energy in axial flow, postponement of vortex breakdown, favoring reattachment, and delay in stall [44]. Similarly, Çelik and Yavuz [46] qualitatively tested non-slender planforms inspired by dolphin fluke geometry at moderate Reynolds numbers to explore potential improvements in stall performance and breakdown characteristics. Figure 2.23 shows sample results for different Reynolds numbers at $\alpha = 10°$. Despite maintaining the effective sweep angle, the leading and trailing edge modifications significantly altered the flow structure. However, compared to the base wing model, significant deteriorations were observed with modified geometries in terms of earlier occurrence of three-dimensional surface separations, particularly at moderate angles of attack $\alpha = 10°$ and $12°$. Recently, Tan et al. [71] investigated the impact of short flexible flags attached to the leading edges of two non-slender delta wings with sweep angles of $\Lambda = 40°$ and $\Lambda = 50°$. Their study demonstrated promising post-stall aerodynamic improvements attributed to the oscillations of the flags. Through flow field measurements, they showed that the flag oscillations caused the separated shear layer to roll up closer to the wing surface, resulting in a smaller separated region compared to the clean wing case.

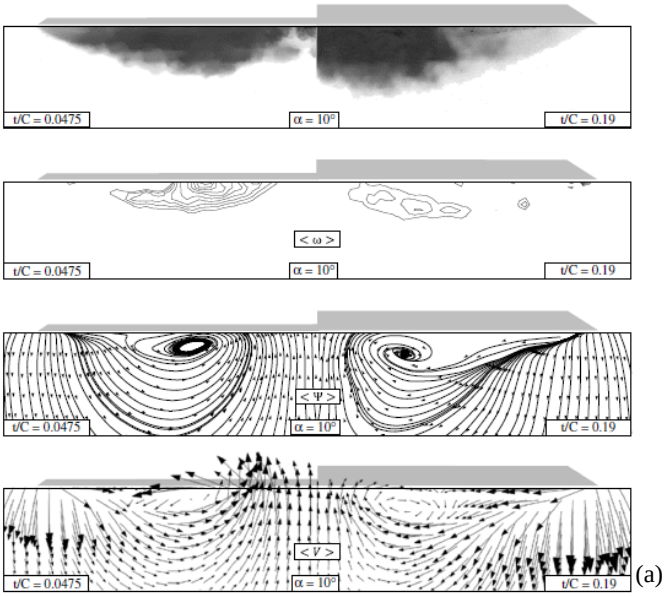

Figure 2.22: Effect of t/C ratio for $\Lambda = 50°$ and $\alpha = 10°$: (a) cross flow visualization and PIV results, (b) surface pressure measurement results [47].

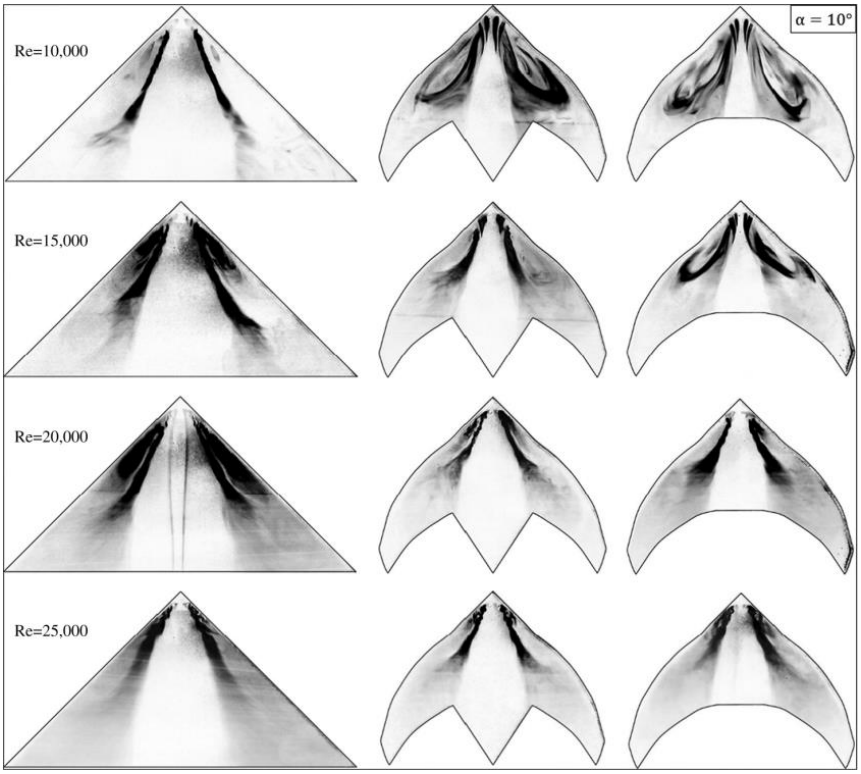

Figure 2.23: Surface flow visualizations, comparison with bio-inspired geometries [46].

2.2.1.2 Static Control Surfaces

Static control surfaces, including winglets, vortex generators, trailing edge flaps, Gurney flaps, and T-strips, are widely utilized in airfoil-shaped static surfaces and dynamic direction control surfaces. Some of these have also become a focus of interest in delta wing studies.

Early research on the implementation of leading edge and trailing edge flaps, as well as plain and Gurney flaps, primarily involved slender delta wings [49], where lift enhancement could be achieved with certain configurations without significant drawbacks to longitudinal stability. Suction side leading edge flaps have been shown to delay the location of vortex breakdown. The schematic of the implemented control surfaces, along with some selected results, is presented in Figure 2.24. The reported discrepancies include an increase in nose-down pitching with Gurney flaps and a reduction in the lift-to-drag ratio with leading edge fences compared to Gurney flaps.

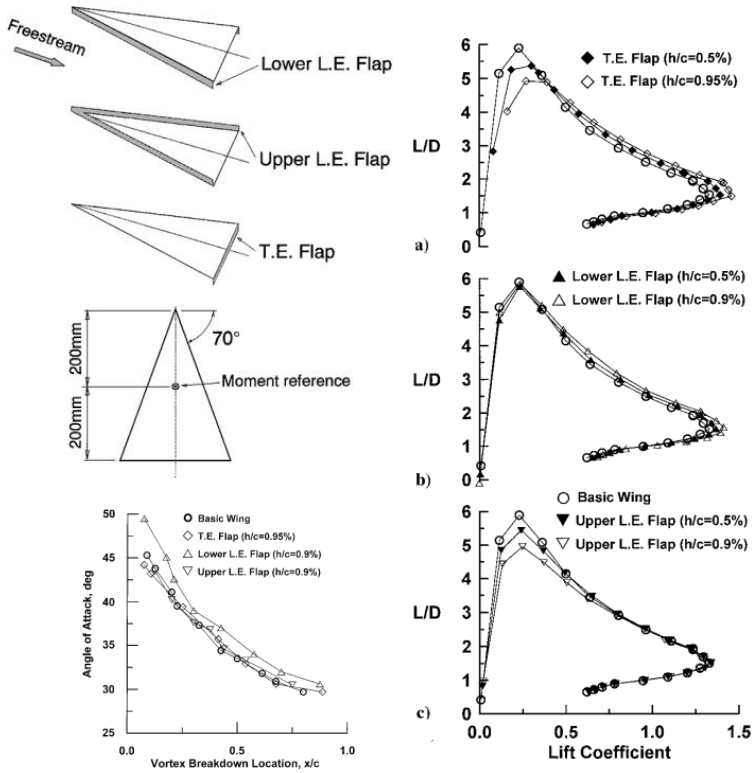

Figure 2.24: Schematic of control surface implementation on a slender delta wings [49].

Greenwell parametrically studied the effect of the trailing edge Gurney flap on slender and non-slender delta wings, demonstrating a significant reduction in induced drag. However, this reduction in drag is accompanied by higher form drag penalties and reduced control capabilities due to the aft shift of the aerodynamic center [51]. Recently, Traub [72] investigated the effects of plain flaps, trailing edge flaps, and Gurney flaps on a non-slender delta wing with a sweep angle of $\Lambda = 55^{\circ}$. Consistent with previous studies on slender wings, the benefits in terms of lift and penalties in terms of drag were found to be similar for both trailing edge and Gurney flaps. It is important to note that, although these studies primarily serve as a basis for the design of active flow control systems for delta wing planform-based aircraft, they are considered passive flow control applications in the context of the current proposal, as they involve modifications to the planform geometries alone.

2.2.1.3 Passive Bleeding

Among the simpler passive flow control alternatives, passive bleeding utilizes the inherent pressure difference across the pressure and suction sides of an aerodynamic surface, allowing the flow to be transferred across simple slots. Despite its simplicity, there were very few studies investigating the performance of passive bleeding on delta wing planforms until the late 2010s. Çelik et al. [10] first implemented passive bleeding slots parallel to the leading edges of a $\Lambda = 45^{\circ}$ non-slender delta wing, reporting the effect of slot orientation in terms of body alignment toward leading and trailing edges with a set of pressure and cross-flow particle image velocimetry measurements and flow visualizations. Three different slot orientations were tested: Back (B), Edge (E), and Back-Edge (BE). For the Back bleed wing, slots were oriented such that forward and rear surfaces were aligned towards the trailing edge with a back orientation angle (θ), whereas for the Edge bleed wing, inboard and outboard surfaces were aligned towards the leading edge with the bevel angle. The Back-Edge bleed wing was constructed using both back and edge angles simultaneously. The geometric details of the proposed approach are shown in Figure 2.25.

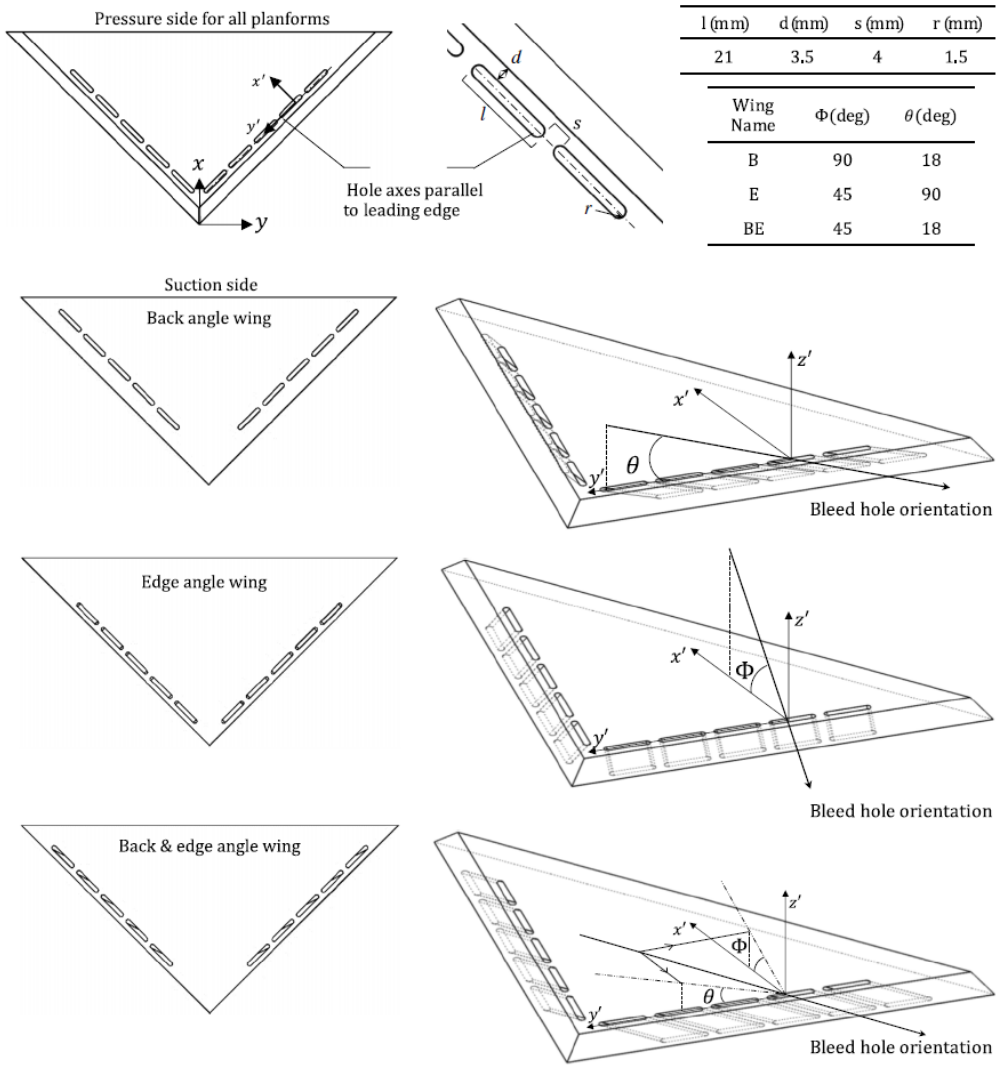

l (mm)	d (mm)	s (mm)	r (mm)
21	3.5	4	1.5

Wing Name	Φ (deg)	θ (deg)
B	90	18
E	45	90
BE	45	18

Figure 2.25: The geometric details of the passive bleeding configurations over a non-slender delta wing with $\Lambda = 45^\circ$ [10].

Being among the first studies applied to delta wings, the concluding remarks obtained from the study are as follows: with proper bleeding configuration, significant improvements in the overall flow pattern can be achieved. A comprehensive comparison between the base and back angle bleed wing models, in terms of surface and cross-flow visualizations, axial vorticity contours, and surface pressure measurements, is represented in Figure 2.26 at an attack angle of $\alpha = 16^\circ$. The pronounced surface separation is evident for the base delta wing model from the surface flow visualization, with no indication of flow reattachment and low vorticity contours. When

the flow is induced to the suction side by means of the bleeding, there is a recovery of the vortical structures with a clear indication of flow reattachment.

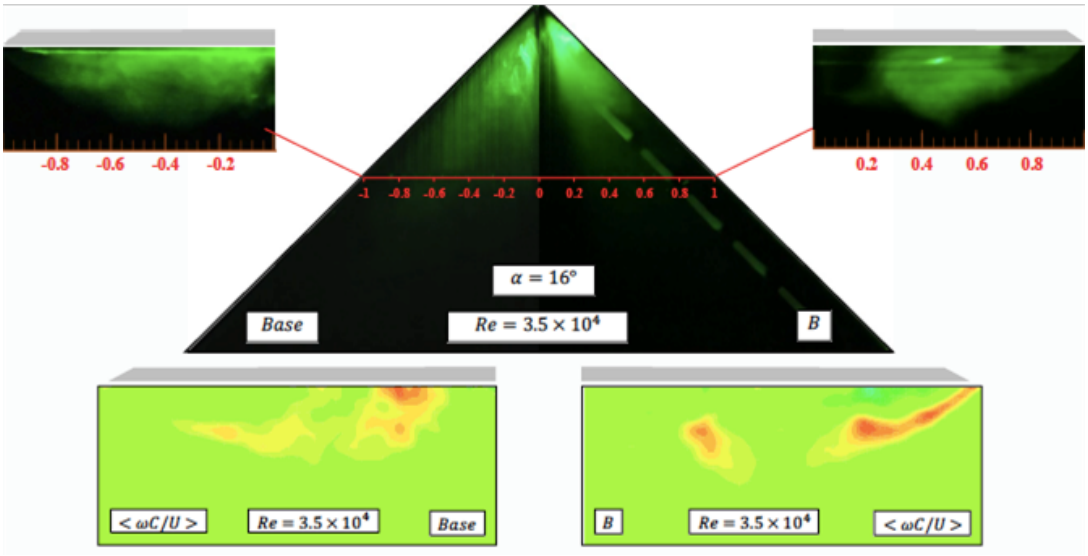

Figure 2.26: Comparison between base (left) and B (right) planforms with surface and cross-flow visualizations, axial vorticity contours. The figure is adapted from [10].

Results showed that, compared to Edge and Back-Edge bleed wings, the Back bleed wing was able to exhibit a recovery in surface pressure distribution near the stall region, accompanied by an increase in cross-flow axial velocity and vorticity magnitudes. In addition, flow visualization showed the promotion of flow reattachment around that regime. Zhang et al. [73] applied the bleeding technique to a $\Lambda = 70°/50°$ double delta wing in comparison to the active blowing technique. The reported outcomes, based on particle image velocimetry measurements, included an increase in vortex strength, the formation of a counter-rotating secondary vortex, and an inboard shift of the axial core.

Yıldırım [74] numerically investigated various new bleeding configurations. The tested geometries included a back bleed wing with incrementally changing back orientation angles (θ), fully opened bleeding holes, and yawed bleeding holes, as detailed in Figure 2.27. Consistent with previous observations of the substantial benefits of bleeding at an angle of attack (α) of 16°, the numerical investigation confirmed these benefits for all newly proposed bleeding geometries. However, at higher angles

of attack, the effectiveness of the bleeding was reduced for the 5-hole designs. In contrast, the fully opened designs demonstrated greater resistance to the effects of increasing angles of attack, successfully inducing stronger vortical structures.

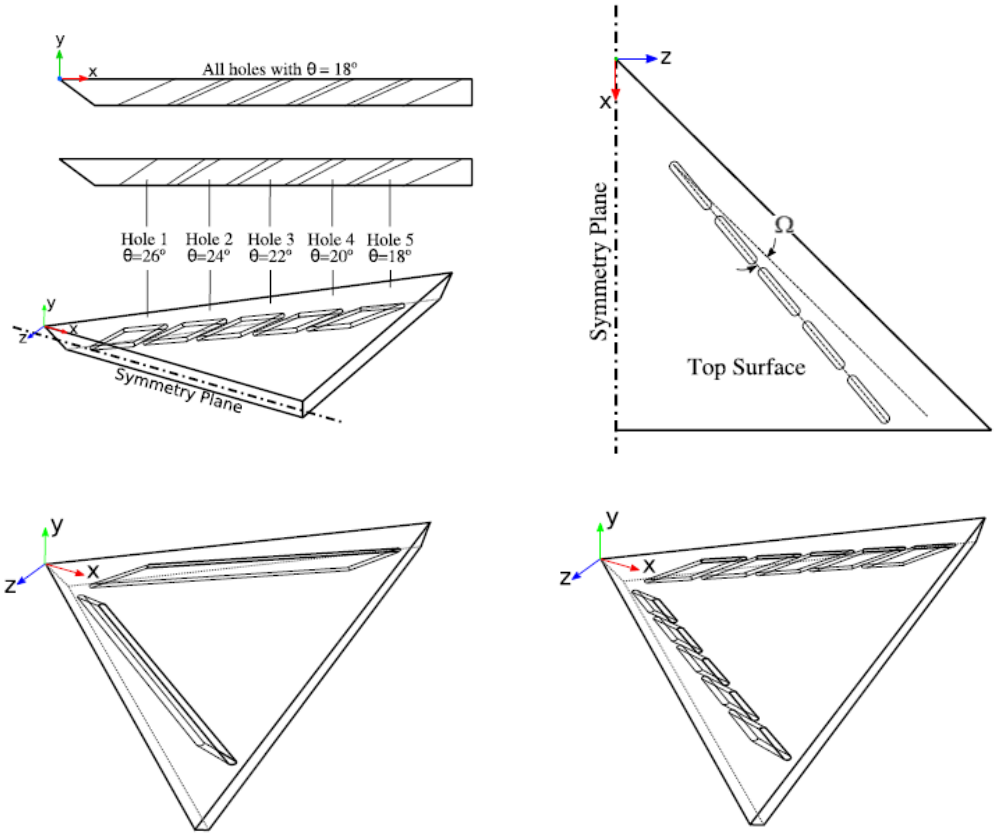

	Hole type [5 hole, fully opened]	θ [deg]	Ω [deg]
RBW	5 holes	18	0
Design 1	5 holes	18	5.5
Design 2	5 holes	26 –18	5.5
Design 3	Fully Opened	-	0
Design 4	Fully Opened	-	5.5

Figure 2.27: The geometric details of the passive bleeding configurations over a non-slender delta wing with $\Lambda = 45°$ [74].

Recently, Kestel et al. [53] addressed the effects of bleed slot geometry parameters, including the back orientation angle (θ) and the bleed opening ratio (bor), which is defined as the ratio of the total bleed surface area to the maximum possible continuous bleed slot area (bor $= 1$). Based on surface pressure measurements and cross

and near-surface particle image velocimetry measurements, they demonstrated that the capability to promote flow reattachment and eliminate three-dimensional surface separation was enhanced with an increase in these parameters. Particularly at high angles of attack, the bor $= 1$ bleed configuration exhibited optimal performance, such that axial flow reversal and surface separation could be favorably manipulated. Figure 2.28 (a) schematically represents the layout of the tested bleed geometries on the suction surface for different bleed opening ratios, while Figure 2.28 (b) illustrates the effect of the bleed opening ratio (bor) on the surface flow field. As the bor increases, the focus of the three-dimensional surface separation is shifted towards the apex, preventing flow reversals and resulting in increased vorticity levels.

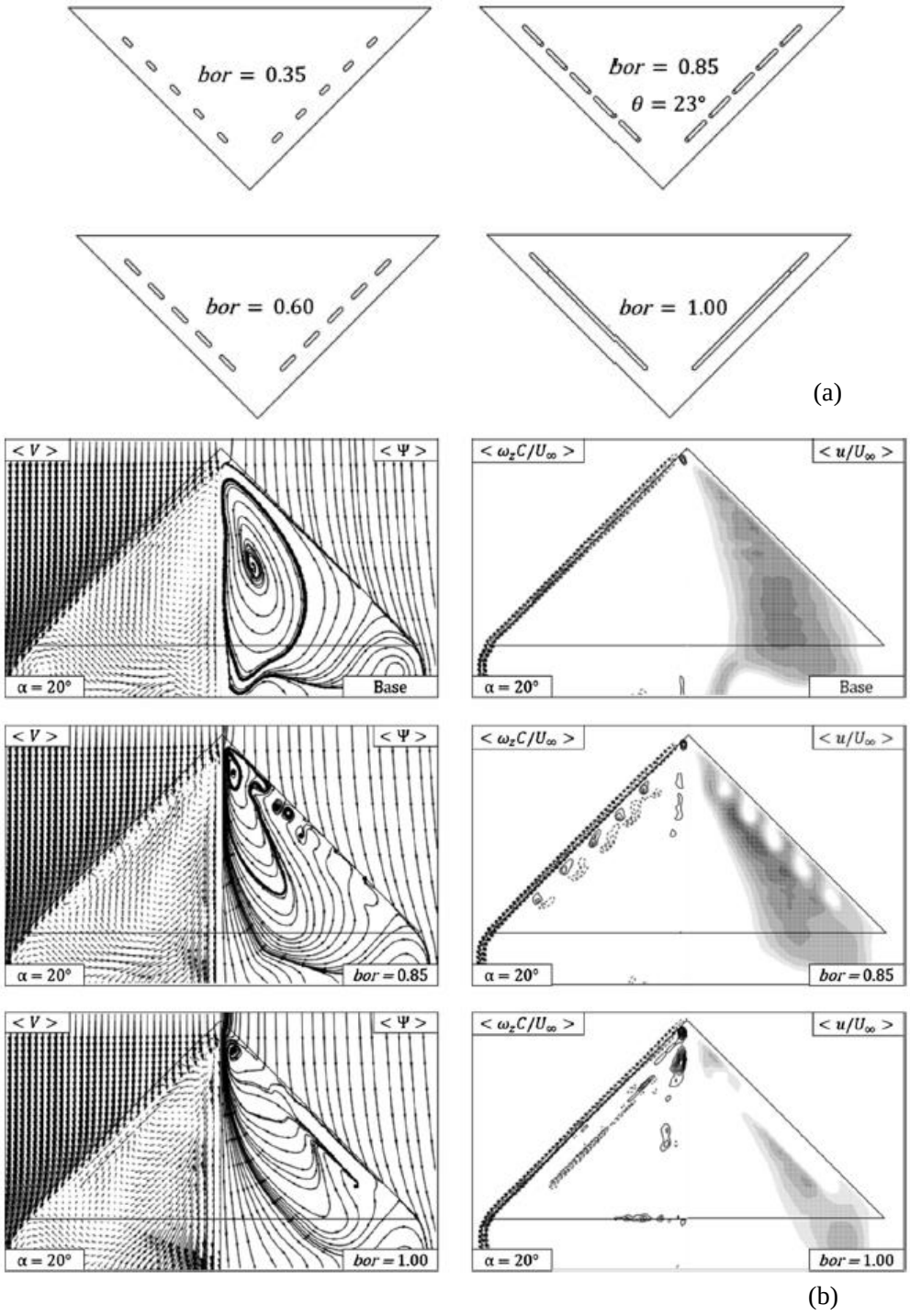

Figure 2.28: (a) Schematic representation of bleeding wings with different bleed opening ratios. (b) Time-averaged surface PIV comparisons at $Re = 5 \times 10^4$ and $\alpha = 20°$ [53].

2.2.2 Active Flow Control Techniques

2.2.2.1 Steady Blowing / Suction

Manipulation of delta wing leading-edge vortices using steady blowing and suction has been extensively studied in the literature, with major attention paid to slender wings, whereas relatively few attempts have been performed for non-slender delta wings. Gürsül et al. [25] classified steady blowing and suction techniques according to injection location as follows: along the core blowing, leading-edge suction/blowing, and trailing-edge blowing. They compared the effectiveness of these techniques in terms of their ability to delay the vortex breakdown location, which is represented in the following Figure 2.29 along with the adapted representations of the sample blowing schemes. As previously mentioned in the vortex breakdown discussion, the majority of the pneumatic techniques over slender wings focused on the delay or the elimination of the phenomena.

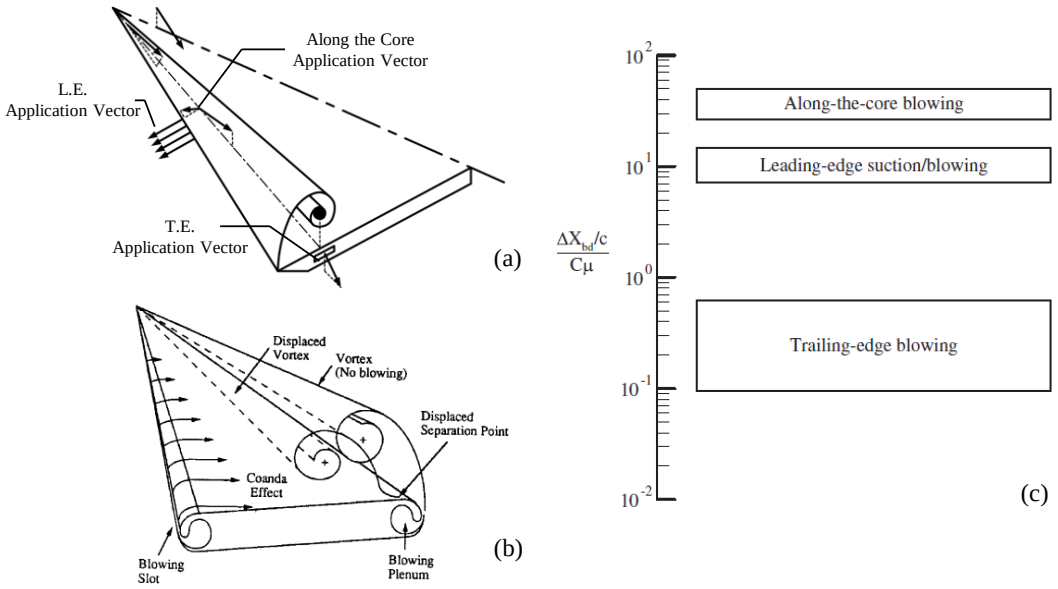

Figure 2.29: (a) Schematic of the blowing configurations (adapted from [3]), (b) schematic of the Coanda jet configuration [25], (c) effectiveness of blowing techniques [3].

Mitchell et al. [54] managed to postpone the vortex breakdown location by approx-

imately 20% of the root chord by performing along-the-core blowing over a slender wing with $\Lambda = 70°$. This benefit is attributed to the acceleration of the axial velocity and favorable modification of the pressure gradient, as also evident in other reference studies [55]. Leading-edge blowing and suction techniques take advantage of manipulating the primary vorticity resulting from leading-edge separation, thus controlling the strength and location of formation. As reviewed by Gürsül et al. [25], the direction of the blowing influences the effectiveness of the leading-edge control, including outward (lateral) direction, upward direction, and upward through a Coanda surface (see Figure 2.29 (b)). Hong et al. [56] showed that outward blowing is quite effective in altering the strength of the leading-edge vortices and can be effectively used to generate rolling moments in asymmetrical configurations over a $\Lambda = 60°$ slender delta wing. In addition, they reported that higher blowing rates resulted in higher magnitudes of forces and moments over the wing model. Zharfa et al. [57] performed leading-edge blowing oriented parallel to the bevel surface over a $\Lambda = 35°$ non-slender delta wing. They concluded that leading-edge blowing over a non-slender wing is quite effective in eradicating three-dimensional surface separation at low attack angles, as evident in Figure 2.30, with the reformation of the LEV close to the apex.

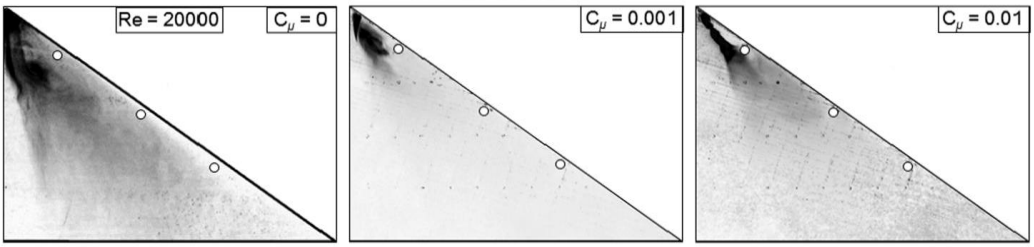

Figure 2.30: Surface flow visualization over a non-slender delta wing with $\Lambda = 35°$, at $Re = 2 \times 10^4$, $\alpha = 20°$ [57].

Günacar [75] conducted an experimental study on a $\Lambda = 45°$ non-slender delta wing, demonstrating that the extent of three-dimensional surface separation can be controlled and reduced with leading-edge blowing. They found that the momentum coefficient significantly affects the control's effectiveness. Additionally, they explored the impact of different blowing patterns—uniform, descending, and ascending—along the leading edge. Their results indicated that the descending blowing pattern was

more efficient, suggesting that control near the apex is particularly effective.

McCormick and Gürsül [58] performed leading-edge suction on a $\Lambda = 70^\circ$ slender delta wing, showing that both the swirl angle and circulation strength decreased with increasing suction momentum. This reduction may contribute to delaying vortex breakdown. Wood and Roberts [76] demonstrated that utilizing a Coandă surface could eliminate leading-edge vortices, achieving fully attached flow at low angles of attack on a $\Lambda = 60^\circ$ slender delta wing. Although a distinct advantage was not observed at low to moderate incidences, tangential blowing substantially controlled the post-stall regime.

Helin and Watry [59] conducted experiments to investigate the effect of trailing-edge blowing oriented towards the vortex burst location on a $\Lambda = 60^\circ$ slender delta wing. They concluded that trailing-edge blowing effectively delays the vortex breakdown location. Philipps et al. [77] conducted similar work on delta wing models with sweep angles ranging from $\Lambda = 65^\circ$ to 75° in the presence of a vertical tail, aiming to control fin buffeting. They reported that the effectiveness of trailing-edge blowing is quite sensitive to the sweep angle, with a preference for less slender delta wings. Yavuz and Rockwell [60] investigated the effects of dual and single trailing-edge blowing patterns on a $\Lambda = 35^\circ$ non-slender delta wing. They concluded that trailing-edge blowing has a remarkable global effect, capable of manipulating large-scale three-dimensional surface separation, as illustrated in the following Figure 2.31.

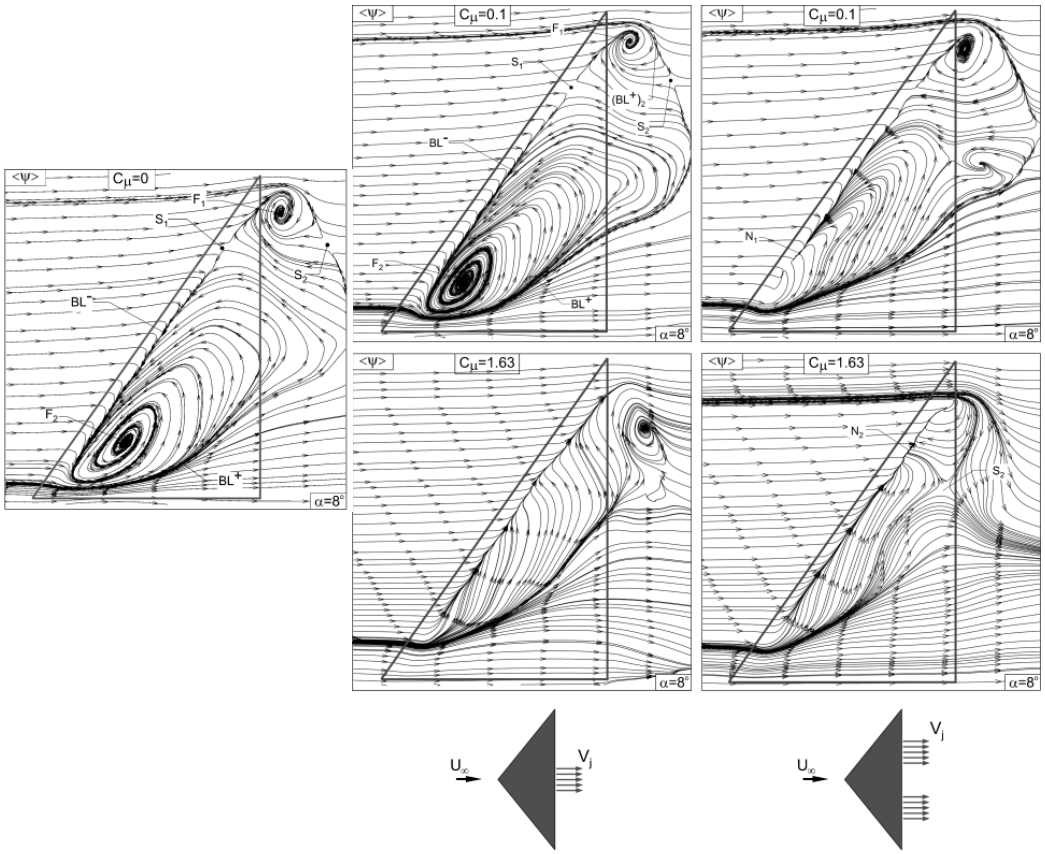

Figure 2.31: Effect of the trailing edge blowing configurations; near-surface vorticity contours of a $\Lambda = 35°$ non-slender delta wing at $Re = 10^4$, $\alpha = 8°$ [60].

2.2.2.2 Unsteady Excitation

Being one of the two focal points of the current work, unsteady excitation techniques of various approaches can be closely related to the research presented herein. In the literature, "unsteady" is not the only corresponding designation; terms such as "periodic," "transitional," and "oscillatory" excitation are also widely used. Unsteady flow control methods generally aim to manipulate the inherent instabilities present in the flow physics. The order of the unsteady actuation can be characterized by a dimensionless quantity known as the Strouhal number, defined in Eqn. 2.1,

$$St = \frac{f \cdot C}{U_\infty} \tag{2.1}$$

where f is the excitation frequency, c is the characteristic length (typically the chord dimension in our case), and U_∞ is the free stream velocity. The notation F^+ is also commonly used, which is essentially synonymous with the definition of the Strouhal number. Gürsül [25] distinguishes unsteady excitation techniques into low-frequency $St = O(0.1)$ and high-frequency $St = O(1)$ categories, relating them to the unsteady characteristics of the flow field, as previously represented in Figure 2.1 (c). The most employed techniques include periodic blowing and suction, plasma actuation, oscillating wings, and oscillating flaps. In this section, unsteady techniques other than pneumatic-based methods are briefly reviewed, followed by a detailed discussion of blowing applications.

Deng and Gürsül [78] demonstrated that oscillating leading edge flaps in a sinusoidal manner modify the strength of the vortices forming over a $\Lambda = 70^\circ$ slender delta wing, along with observations indicating a delay in the vortex breakdown location. Yang and Gürsül [79] applied the variable sweep angle concept, ranging from 60° to 70°, to a pitching delta planform, reporting that such excitation results in less phase shift in the swirl angle compared to the vortex breakdown location. Vardaki et al. [80] studied small amplitude roll oscillations applied to non-slender delta wings with sweep angles ranging from $\Lambda = 20^\circ$ to 50° for varying frequency, mode, and amplitude values. They were able to significantly promote flow reattachment in post-stall conditions, where the vortex core began to reform from the wing tip, leading to subsequent breakdown. A Strouhal number $St = 1 - 2$ was found to be generic for all sweep angles. The following Figure 2.32 illustrates the effect of roll oscillation at $St = 1$ on the time-averaged superposed cross-flow visualization for a $\Lambda = 50^\circ$ delta wing at $\alpha = 25^\circ$.

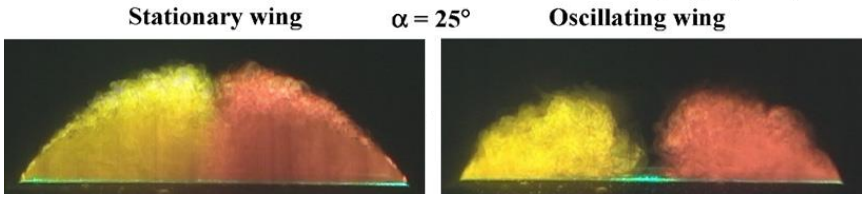

Figure 2.32: Effect of the roll oscillations; time-averaged cross-flow visualization of a $\Lambda = 50^\circ$ delta wing [80].

Yanıktepe and Rockwell [13] investigated the effect of small amplitude perturbations about the pitch axis for a non-slender delta wing with $\Lambda = 38.7°$, showing that significant improvements in topological characteristics are achieved at considerably high angles of attack, as evident in the sample time-averaged streamline patterns presented in Figure 2.33.

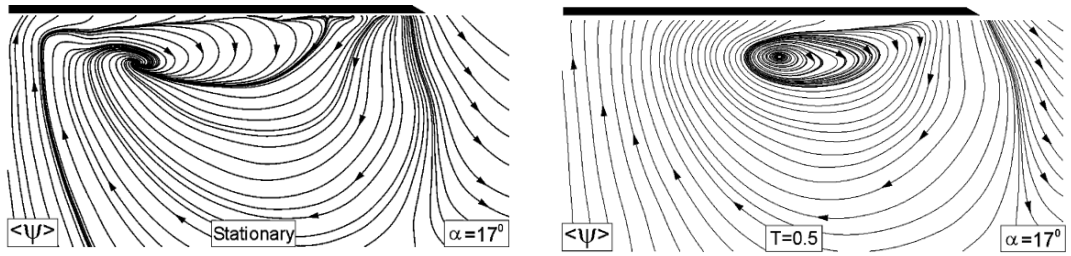

Figure 2.33: Effect of the pitch oscillations; time-averaged streamline patterns of a $\Lambda = 38.7°$ delta wing [13]

Greenblatt et al. [69] investigated the effects of leading edge plasma actuation on a $\Lambda = 60°$ delta wing, examining various Reynolds numbers, actuation frequencies, and duty cycles. They demonstrated that the effectiveness of this technique is sensitive to the Reynolds number, particularly in the post-stall regime. Furthermore, a duty cycle of 10% at a Strouhal number of $St = 1$ was identified as the optimal condition. Nelson et al. [70] successfully generated significant rolling control moments using plasma actuators positioned near the leading edge of a $\Lambda = 47°$ UAV configuration.

In the context of slender delta wings, pioneering examples of unsteady blowing and suction applications—either through the edges or along the core of the vortex—have resulted in a significant delay in the onset of vortex breakdown, an increase in the stall angle, and an enhancement in lift force [27], [64]–[66]. In the past decade, there has been a renewed interest in leading edge unsteady blowing control over slender wing models, including comparisons with numerical approaches [63], [67], [68]. Kölzsch and Breitsamter [67], performed periodic blowing through the leading edge of a VFE-2 $\Lambda = 65°$ delta wing model in relation to the existing dominant frequencies. Their findings indicated that this approach achieves maximum effectiveness in terms of aerodynamic characteristics, with the optimal blowing configurations iden-

tified at $St = 2.7$ and $St = 1.0 - 1.5$ at angles of attack $\alpha = 35°$ and $45°$, respectively. The following Figure 2.34 illustrates the VFE-2 geometry, the measured dominant frequency in axial velocity, waveforms of the applied leading edge blowing, and changes in the axial velocity distribution.

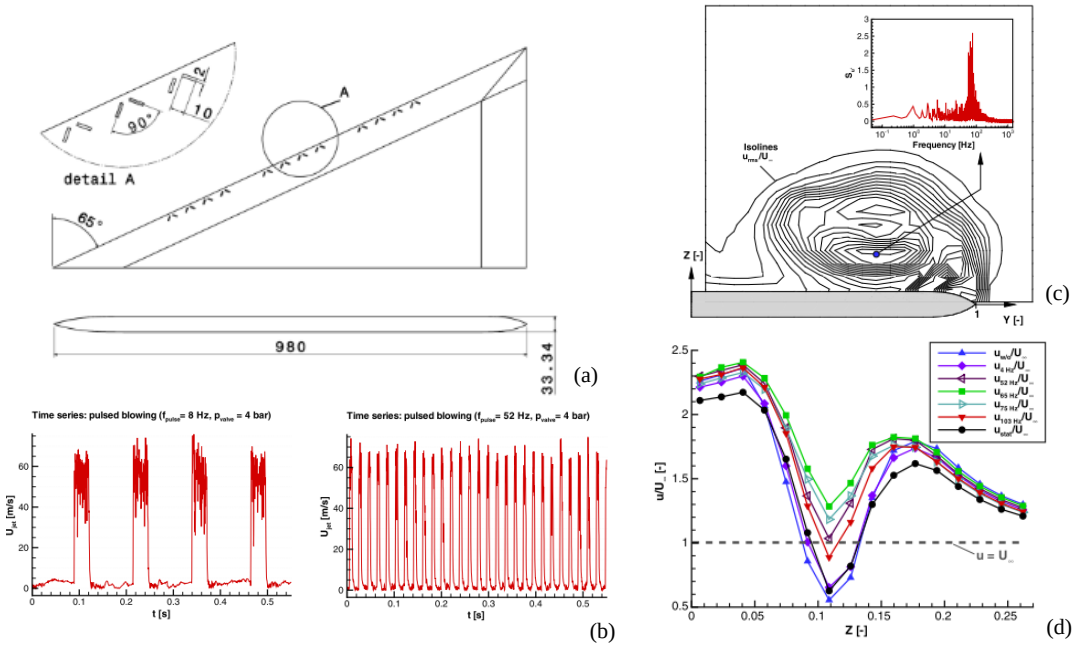

Figure 2.34: (a) VFE-2 $\Lambda = 65°$ delta wing model with blowing hole orientations, (b) Sample hot-wire measurements for pulsed blowing at 8 and 52 Hz, (c) Sample axial velocity RMS distribution with spectral estimations at $x/c_r = 0.8$ and $\alpha = 23°$, (d) Comparisons of axial velocity distribution in the normal direction at $x/c_r = 0.4$ and $\alpha = 23°$ [67].

Buzica et al. [63] conducted an experimental investigation to validate the results presented in the aforementioned reference [67] across representative pre-stall, stall, and post-stall regions. They introduced novel actuation strategies, including unison blowing (where all slots are synchronous and uniformly add momentum), frequency-modulated blowing, and phase-modulated blowing. Their findings indicated that synchronized blowing, referred to as unison, exhibited superior performance among the various strategies, achieving maximum momentum transport. Figure 2.35 (a) illustrates a comparison of aerodynamic characteristics, highlighting that the abrupt lift loss in the post-stall regime can be mitigated through the implementation of unsteady

blowing. Part (b) of Figure 2.35 presents time-averaged phase-locked cross-flow vorticity contours at $\alpha = 35°$. The blowing phases coincide with the 45-degree and 90-degree phase statuses, while the remaining phases correspond to the blowing-off periods. This aspect of the figure is crucial for understanding how periodic blowing interacts with the inherent unsteady nature of the flow. Key observations from the study include that regions close to the apex exhibited a more uniform vorticity distribution. Induced blowing initially appeared with a negative orientation, with magnitudes comparable to that of the high-strength vortex core. Blowing restructured the vortex shedding at the leading edge, transitioning through phases from 135 to 360 degrees, leading to a dissipation of negative direction and resulting in overall momentum transport in a downstream direction. This cyclical process demonstrated a superior performance compared to the baseline case in terms of both breakdown location and aerodynamic coefficients. In complementary works, Buzica and Breitsamter [68] conducted Detached Eddy Simulations (DES) to quantify the response of the previously mentioned configurations to periodic blowing. They demonstrated that the increase in axial velocity at the leading edge, associated with periodic blowing, exhibits a phase delay as it moves downstream.

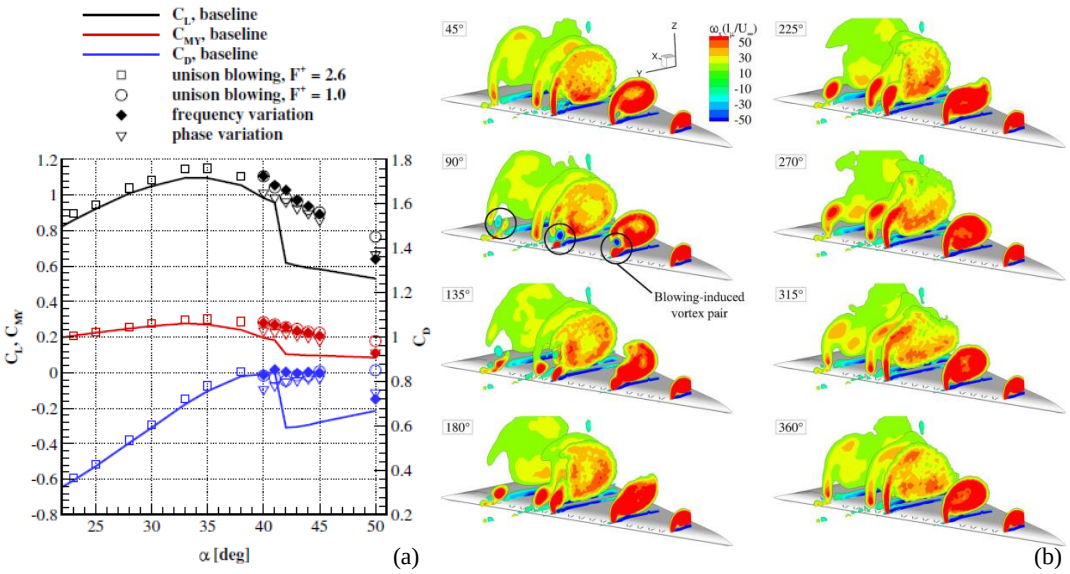

Figure 2.35: (a) VFE-2 $\Lambda = 65°$, effect of unsteady blowing on aerodynamic characteristics; (b) Time-averaged phase-locked cross-flow PIV results at $\alpha = 35°$ with $St = 2.7$ and 25% duty cycle [63].

In contrast to the numerous studies conducted on slender delta wings, there is a limited body of work addressing the effects of periodic momentum addition on non-slender delta wings. Williams et al. [26] demonstrated that unsteady leading edge blowing enhances flow reattachment, noting that higher momentum coefficient values are necessary to improve flow structure as the angle of attack increases for a non-slender wing with a sweep angle of $\Lambda = 50°$. Figure 2.36 illustrates how reattachment, along with vortex formation, is achieved at high angles of attack. This advantage is also reflected in the distribution of the suction force coefficient. Recently, Çetin et al. [62] investigated the effects of unsteady leading edge blowing on a non-slender delta wing with a sweep angle of $\Lambda = 45°$. The study employed periodic blowing in the form of a square wave at a fixed duty cycle across varying frequencies.

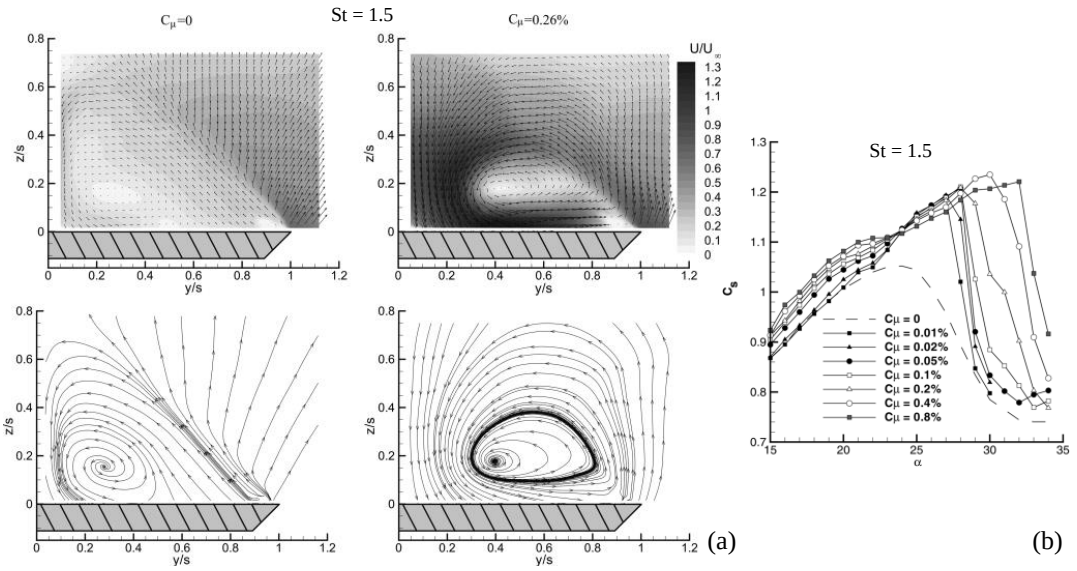

Figure 2.36: $\Lambda = 50°$ delta wing, (a) Time-averaged crossflow velocity field and streamlines at $\alpha = 30°$ and $x/C = 0.28$; (b) Comparison of suction force measurements [26].

2.2.2.3 Usage of Fast Switching Actuators

Being among the active flow control schemes, fluidic periodic actuation techniques have gained popularity due to their successful applications on various aerodynamic surfaces, not limited to delta wing applications. The intermittent activation of such

techniques is also considered a more efficient approach as the momentum, and thus the energy induced to the flow field, can be significantly reduced. Thus, to accurately assess the aerodynamic benefits of such applications, typically including increased lift, reduced drag, delayed flow separation and vortex breakdown, and improved stall angle relative to the induced energy, the actual momentum injected into the flow field must be quantified accurately. Compared to steady blowing actuation strategies, such quantification requires more intensive effort, which must be well organized from the design of experimental flow control setups to sophisticated measurement approaches.

Among the various actuation systems and devices, commercial fast-switching electromagnetic pneumatic solenoid valves, such as the FESTO MHJ series, have been widely utilized in numerous studies due to advantages in operating principle with high repetition rates. These applications represent a broadband spectrum including boundary layer separation control on airfoils [81]–[83], load alleviation by circulation control [84], wake manipulation behind a cylinder [85], circulation control by vortex generation on airfoils [86], [87], slender delta wing vortex control [63], [67], and non-slender delta wing three-dimensional surface separation control [62]. Considering the scopes of such flow control studies, they vary in purpose and application architecture, some of which represent a closed-loop control algorithm based on sensor feedback, typically the pressure measurements, whereas the majority of the studies rely on feedforward control schemes for parametric investigations.

All the aforementioned studies from the literature that utilize the fast-switching valves present the velocity response of the valve actuation with different measurement techniques, including total mass flux measurements, hot wire measurements, and PIV measurements. However, very few studies address the comprehensive characterization of the fast-switching solenoid valves. Kölzch and Breitsamter [67], Buzica et al. [63], Çetin et al. [62], and Abdolahipour et al. [87] presented sample velocity responses of the MHJ9 series valves to square wave type control signals, along with only the spectral content via hot wire measurements. As an accompanying study, Abdolahipour et al. [88] studied the pulsed jet characteristics limited to velocity fluctuations for different jet downstream locations with hot wire measurements and flow visualization. Düssler et al. [84] provided a more detailed characterization for a load alleviation circulation control study. They presented the delay characteristics

of the blowing response along with the oscillating jet velocity distribution across the blowing slot with pitot tube measurements. Despite not explicitly mentioning the utilization of the MHJ series valves, Steinfurth and Weiss [89] studied the diffuser geometry for active separation control on a diffuser ramp, where they investigated the forcing signals in relation to blowing responses with novel measurement techniques, including particle image velocimetry and wall shear measurements. They reported the effect of pulse duration, thus the duty cycle, and time delay on blowing response. Apart from flow control applications, Pipan and Herakovic [90] studied the volume flow characterization of MHJ series valves controlled with pulse width modulations. They studied the effect of the pulse width duration, thus the duty cycle, for different supply pressure values. They presented the minimum pulse width time to achieve the desired valve opening, yielding a converged flow at valve on state, particularly at high excitation frequencies $f_c = 200 \breve{} \, 300\,\text{Hz}$ which were about 3 to 5 microseconds.

Ternoy et al. [91] presented an overview of active flow control devices in which they summarized the characterization techniques for pulsed flow jets, particularly with the aid of hot wire anemometry systems. They suggested a procedure that, when the jet blowing hole dimensions are of comparable size to the hot wire dimension, calibration of the sensor at the location with respect to well-known supply conditions, where the blowing is to be employed, offers an efficient and useful approach. Recently, Çetin et al. [62] suggested an effective momentum coefficient term $C_{\mu,\text{eff}}$ for periodic blowing excitations that is found by multiplying the maximum momentum $C_{\mu,\text{max}}$ coefficient with the duty cycle DC, where the maximum momentum coefficient represents the momentum added to the flow field as if the valve operates always at open state with $DC = 100\%$. Thus, in order to report the momentum coefficient for such flow control studies in a more accurate way, in addition to the mean pulse rate, quantification of the actual duty cycle also holds significant importance.

CHAPTER 3

EXPERIMENTAL SYSTEMS AND MEASUREMENT TECHNIQUES

This chapter provides a comprehensive overview of the experimental methodologies employed, encompassing the wind tunnel facility, wing models, measurement techniques, flow control systems, and experimental matrix. Additionally, the approach to uncertainty estimation is discussed. The chapter also outlines the methodological framework applied in each of the subsequent results chapters.

3.1 Wind Tunnel

This experimental work was performed in a low-speed, open circuit, suction type wind tunnel facility located in the Fluid Mechanics Laboratory of the Mechanical Engineering Department at Middle East Technical University. The wind tunnel is constructed of five main sections, namely, the settling chamber, contraction cone, test section, diffuser, and the fan. A perspective view of the tunnel facility is illustrated in Figure 3.1

The test section, which is fully transparent, measures 750 mm in width, 510 mm in height, and 2000 mm in length. The maximum achievable free stream velocity within this section is 30 m/s. A closer look to the wind tunnel test section is given in Figure 3.2.

Air enters the tunnel through two symmetrical inlet sections situated on either side. To prevent the ingress of foreign objects and enhance airflow uniformity, fine-mesh screens are installed at both inlets. The length of the settling chamber, also referred to as the entrance section, is 2700 mm. This section is equipped with a honeycomb

structure and three additional fine-mesh screens to minimize turbulence intensity and improve airflow uniformity in the test section. The contraction cone has a length of 2000 mm and a contraction ratio of 8:1.

The diffuser serves to slow down the high-speed flow exiting the test section, thereby enabling static pressure recovery and reducing the operational load required to drive the system. Spanning a length of 7300 mm, the diffuser's cross-sectional area progressively decreases along its axis, maintaining a 3° divergence angle to prevent flow separation. An axial fan coupled with a 10kW AC motor is installed at the tunnel's exit, equipped with a remote frequency control unit to regulate the tunnel velocities.

The experiments were conducted at various Reynolds numbers ranging from $3.5 \times 10^4 \leq Re \leq 1 \times 10^5$, calculated based on the chord length c of the wing models using the equation 3.1. Throughout the entire test matrix, the maximum blockage ratio remained below 2.4% at the highest tested angle of attack $\alpha = 30°$.

$$Re = \frac{U_\infty \cdot C}{\nu} \tag{3.1}$$

The characterization of the wind tunnel was previously performed [92] directly via Laser Doppler Anemometry (LDA) meausrements and validated against with a Pitot-static probe connected to a pressure scanner. When calculating the velocity from the Pitot-static probe's dynamic pressure measurements, factors such as the air temperature, humidity, and altitude conditions of the laboratory were considered. The average velocity was plotted against tunnel power, as shown in Figure 3.3, which also presents turbulence intensity values. A nearly linear relationship was observed for fan power levels exceeding 4%, with the maximum turbulence intensity recorded in the test section at 0.9%.

Figure 3.1: METU ME Fluid Mechanics Laboratory wind tunnel facility

Figure 3.2: Wind tunnel test section

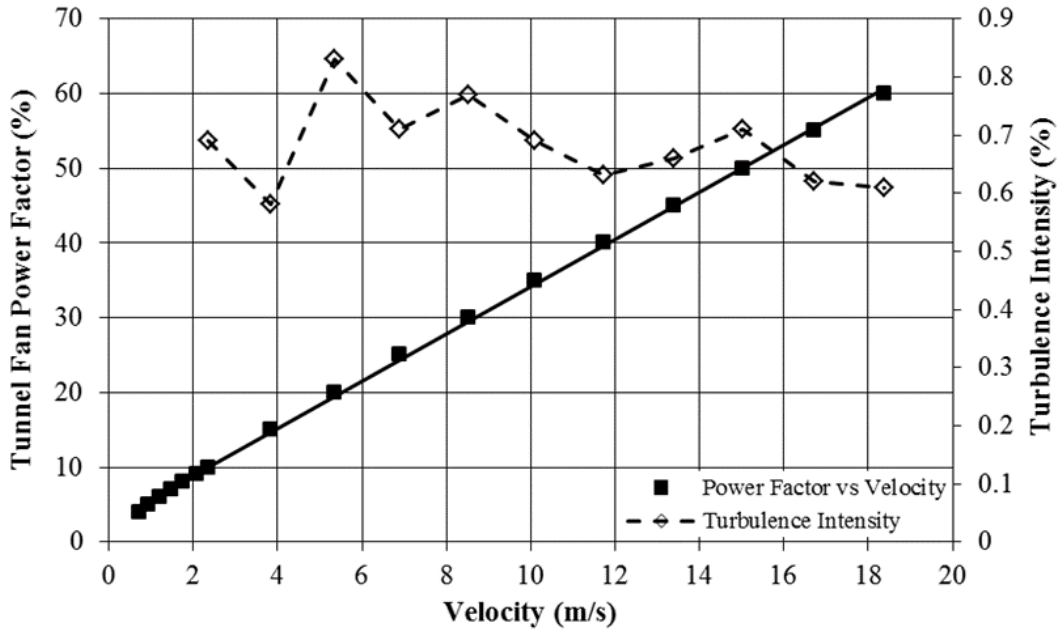

Figure 3.3: Wind tunnel test section calibration curve [92].

3.1.1 Wind Tunnel Axis Frames

In the present study, two distinct model positioning systems were utilized to align the wing model for wind tunnel aerodynamic measurements. Surface pressure measurements and particle image velocimetry (PIV) measurements were conducted using an in-house upper mounting strut, whereas force measurements were performed using a side-mounted model positioning system [93]. Due to the sophisticated mounting approach required for force measurements, detailed in subsequent sections, its axis definition differs from that used in the upper mounting strut. Figure 3.4 illustrates the details of the mounting systems along with the axis definitions employed on sample mounts. Additionally, Table 3.1 summarizes the axis definition details, angle of attack alignment, and wing surface positioning. For both definitions, the right-hand rule was employed, with the x-axis oriented in the freestream direction. The suction side of the wing models was positioned facing the down walls of the wind tunnel in the upper mounting strut experiments, while the opposite arrangement was utilized in the side-mounted strut experiments. During upper mounting strut experiments, the y-axis was oriented towards the port side of the wing model (leftwards direction when viewed

from the aft of the wing model), with the z-axis directed downwards as per the right-hand rule. Conversely, in the side-mounted strut experiments, the y-axis was directed towards the starboard side of the wing model (rightwards direction when viewed from the aft of the wing model), resulting in the z-axis pointing upwards. Due to these differences in axis definitions and the orientation of the suction surface, a positive angle of attack was achieved by rotating the model nose-down in the upper mounting strut setup, whereas a nose-up movement was used in the side-mounted strut experiments.

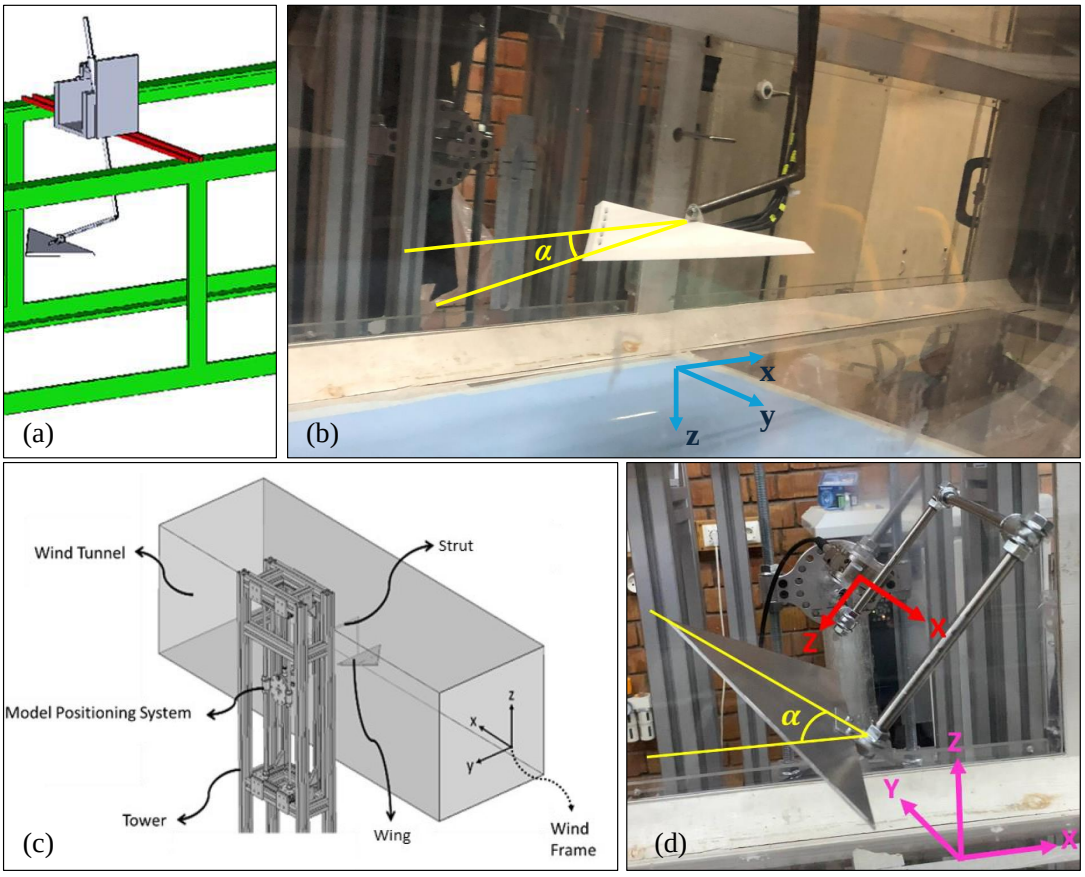

Figure 3.4: Wind tunnel model mount systems: (a) Upper mounting strut, (b) Sample mounted wing model via upper mounting strut and wind axis definitions, (c) Side mounting strut, (d) Sample mounted wing model via side mounting strut and wind axis definitions [93].

Table 3.1: Axis definitions utilized in different measurement techniques

Technique	x-Axis	y-Axis	z-Axis	Suction Side Positioning	Angle of Attack Direction
Surface Pressure Measurements	In Freestream Direction	Pointed Towards Port Side Of the Wing Model (Left Direction Looking From Aft View of the Wing)	Pointed Downwards (Looking From Top Side of the Wing)	Facing the Down Wall of the Wind Tunnel	Nose Down = (+) α
Particle Image Velocimetry Masurements	In Freestream Direction	Pointed Towards Port Side Of the Wing Model (Left Direction Looking From Aft View of the Wing)	Pointed Downwards (Looking From Top Side of the Wing)	Facing the Down Wall of the Wind Tunnel	Nose Down = (+) α
Force Masurements	In Freestream Direction	Pointed Towards Starboard Side Of the Wing Model (Right Direction Looking From Aft View of the Wing)	Pointed Upwards (Looking From Top Side of the Wing)	Facing the Upper Wall of the Wind Tunnel	Nose Up = (+) α

3.2 Wing Models

The present experimental study is based on a baseline nonslender delta wing planform featuring a sweep angle of $\Lambda = 45°$. The baseline wing design has a chord length of 135 mm, a span of 270 mm, and a thickness of 8 mm. The leading edges of the wing model are beveled at 45° on the windward side. All flow control wings were developed based on this baseline model and were fabricated separately from fine polyamide PA2200 using Selective Laser Sintering (SLS) rapid prototyping techniques.

For the passive bleeding control experiments, four different wing configurations were designed to investigate the effects of the nozzle bleed approach. Additionally, the Back Bleed 18 wing model from Çelik et al. [10] was employed in this study for force measurements, contributing to a comprehensive comparison alongside previously documented surface pressure and particle image velocity measurements. The Back Bleed 18 model was re-engineered to incorporate pressure measurement taps for the development of the proposed passive bleed momentum quantification method.

In the active flow control campaign, a model featuring circular blowing holes was designed and examined. The pressure taps were located on the suction side at a nondimensional chordwise distance of $x/C = 0.5$, extending across the spanwise direction from the symmetry plane towards the leading edges of all flow control wing

models.

The following Table 3.2 presents a list of the tested wing models along with their designations. Detailed explanations are provided in the subsequent subchapters, which describe the methodological approaches for each topic in depth. In addition the images of the tested wing models are shown in Appendix A.

Table 3.2: Wing model designations

Method	**Wing Designation**
Base Planform	Baseline Wing
Passive Flow Control Wings	Nozzle Bleed Wing Wide CR050
	Nozzle Bleed Wing Wide CR075
	Nozzle Bleed Wing Narrow CR050 Forward
	Nozzle Bleed Wing Narrow CR050 Rear
	Back Bleed B18
	Back Bleed B18 (for Bleed Momentum Estimation)
Active Flow Control Wing	Blowing Wing

3.3 Measurement Techniques

In this subsection, the technical methodologies associated with the various measurement techniques utilized in this study are presented. Specifically, the details of surface pressure measurements, force measurements, constant temperature anemometry (CTA) measurements, and particle image velocimetry (PIV) measurements are provided.

3.3.1 Surface Pressure Measurement

Pressure measurements were conducted using a Netscanner 9116 Intelligent Pressure Scanner, which incorporates 16 silicon piezoresistive pressure transducers. These sensors are capable of measuring pressures within the range of 0 to 2.5 kPa. The device was pre-calibrated by the supplier over specified pressure and temperature spans. Calibration settings for each transducer were stored in the EEPROM (Electri-

cally Erasable Programmable Read-Only Memory). The integrated microprocessor and temperature sensors enable the device to compensate for offset, nonlinearity, sensitivity, and thermal effects in the transducer outputs before data is transferred to the computer. The system ensures a measurement resolution of ±0.003% FS (full scale) and an uncertainty of ±0.05% FS (full scale).

Surface pressure data were recorded at a sampling rate of 500 Hz for a duration of 10 seconds at each test condition. The pressure scanner was connected to the pressure taps on the wing via pneumatic tubing. Noise values were acquired prior to each experiment and subtracted from the actual measurements to obtain noise reduced results. Preliminary tests were conducted to ensure symmetry along the spanwise pressure distribution, hence measurements were performed only for one half of the wing. These tests were also conducted under different ambient conditions to ensure the repeatability of the results. The non-dimensional pressure coefficient C_P was calculated using Eqn. 3.2.

$$C_p = \frac{\overline{p} - p_\infty}{\frac{1}{2}\rho U_\infty^2} = \frac{\overline{p} - p_\infty}{p_{\text{dyn}}} \tag{3.2}$$

3.3.2 Particle Image Velocimetry Measurement

Particle Image Velocimetry (PIV) is an advanced, optical, non-invasive technique used to visualize and measure fluid flow velocities. The method involves seeding the fluid with tracer particles that follow the flow dynamics. These particles are illuminated by a laser sheet, and their motion is captured using high-resolution cameras synchronously. By analyzing the captured images, the displacement of the particles over known time intervals is determined, allowing for the calculation of the flow velocity field. In a typical PIV setup, a laser generates a thin light sheet that illuminates the tracer particles within the fluid. A high-speed camera captures successive images of these illuminated particles at very short time intervals. The images are divided into smaller interrogation windows, and cross-correlation techniques are applied to pairs of images to determine the displacement of particle groups within each window. This displacement, combined with the known time interval between images, provides the local velocity vector of the fluid at numerous points. A representative

experimental setup for planar 2C-2D Particle Image Velocimetry (PIV) in a wind tunnel is illustrated in Figure 3.5 [94]. In the current study, a TSI PIV system was employed to conduct surface flow PIV experiments for obtaining quantitative flow patterns during passive flow control. The PIV system comprises seeding particles, a double-pulsed laser, a digital CMOS camera, a frame grabber, a synchronizer, and a computer equipped with software. The schematic and flow chart of the experimental process utilized in this study are presented in Figure 3.6.

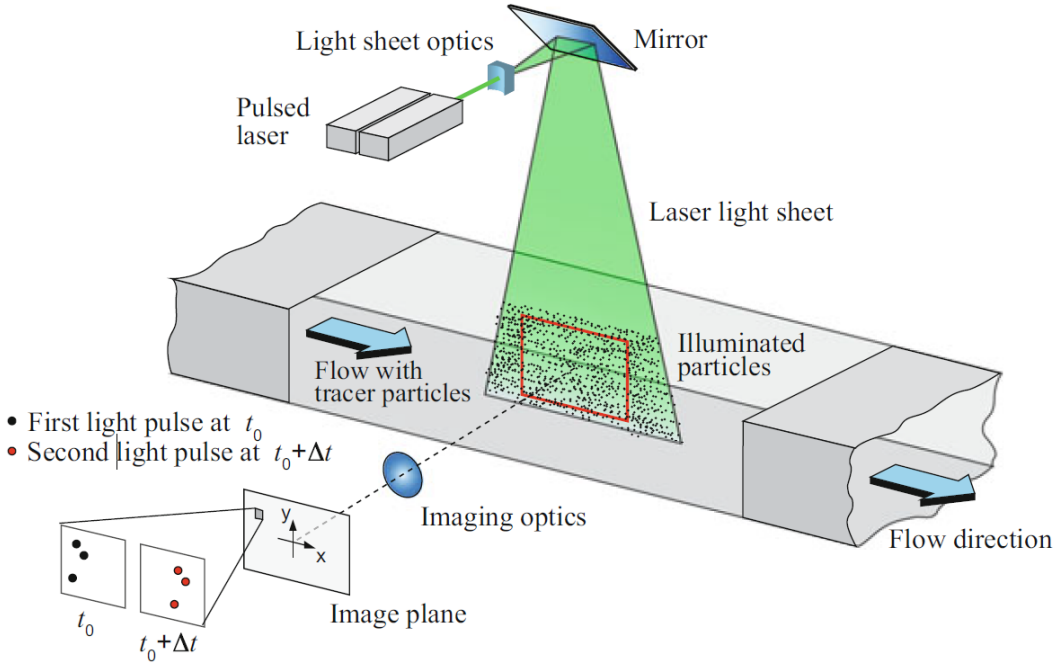

Figure 3.5: Sample experimental arrangement for a planar 2C-2D PIV setup in a wind tunnel [94].

Data acquisition begins with the generation of the flow and the introduction of tracer particles into the flow field. In this study, glycol-based smoke was used as the seeding material, producing particles with diameters ranging from 1 to 3 μm, generated by a commercial smoke generator. Once the seeding achieved homogeneity within the flow field, the camera and laser were triggered via software to capture image pairs. A double-frame double-exposure imaging technique was employed, capturing image pairs at time instances t and $t + \Delta t$, where Δt defines the pulse separation time.

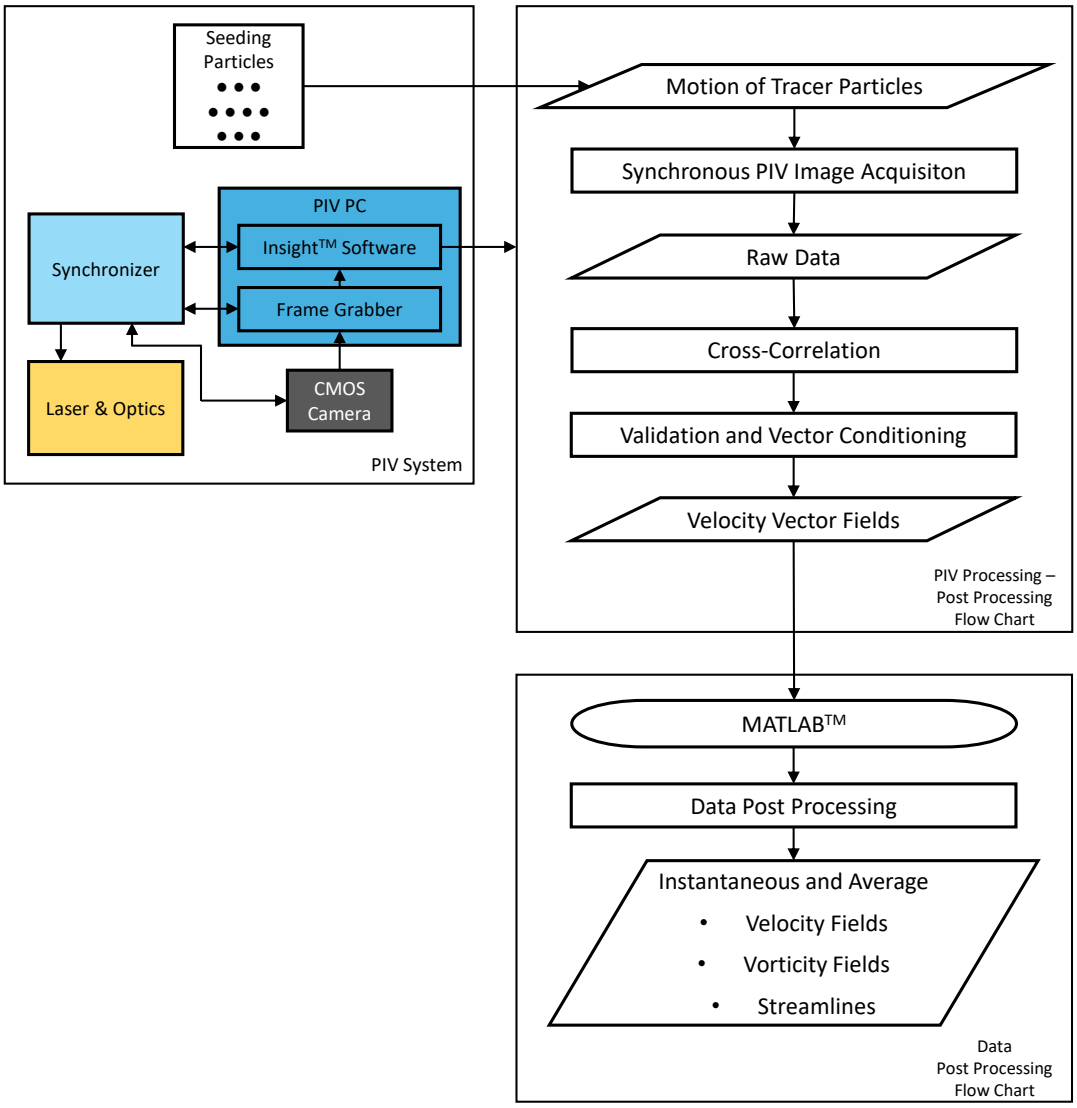

Figure 3.6: Flowchart of the PIV processing and post processing and interface with the setup.

A high image density PIV experiment necessitates specific principles for tracer particle seeding and the adjustment of the pulse separation time Δt:

- Seeding particles should be homogeneous for reliable statistical analysis.
- Interrogation areas must be large enough to represent the field and small enough to ensure the absence of velocity gradients.

- Each interrogation area should contain 15-20 particles. Fewer particles will result in a Particle Tracking Velocimetry system, while higher densities will lead to a Particle Speckle technique, reducing the signal-to-noise ratio (S/N).
- The separation time Δt should be sufficiently large to accurately represent the flow but small enough to ensure particles remain within the interrogation area. Typically, particles should move less than one-fourth of the interrogation window. Additionally, to prevent out-of-plane motion, the laser sheet should be four times the maximum displacement thickness.

Illumination in the experiments was provided by a dual-pulsed Q-switched Litron Nano L200-15 200mJ Nd:YAG laser system. The laser sheet thickness, focal distance, and orientation were configured by transmitting the laser beam through a cylindrical lens of -15 mm and a spherical lens of 1000 mm. The laser sheet was positioned paralle to the wing suction surface at a dimensionless distance of z/C = 0.03. Image acquisition was performed using a high-speed 2K x 2K Powerview™ Plus 4-megapixel CMOS camera with a Nikon 50mm f/1.8D lens, capturing 15 double frames per second. The camera was located outside of the wind tunnel to capture the images facing the wing surface thus the laser sheet plane normal. The schematic illustration for the PIV arrangement used in the current study is provided in Figure 3.7. Synchronization of the laser and camera was managed using a TSI LaserPulse™ 610036 synchronizer. The images captured by the camera were digitally stored in RAM via a frame grabber.

Image processing was conducted using the commercial software TSI Insight 4G to extract velocity vectors, V. The patterns of instantaneous velocity vectors were evaluated using a frame-to-frame cross-correlation technique from raw images, with a 50% effective overlap to satisfy the Nyquist criterion. Acquired images were processed for 32 x 32 pixels interrogation areas, corresponding to an effective grid size of $\delta/C = 0.021$. An FFT-based cross-correlation algorithm was applied to process the data (raw images).

Following the processing of each pair of frames with the FFT cross-correlation algorithm, post-processing was necessary to remove erroneous vectors and interpolate vectors for interrogation windows where the initial FFT process failed to obtain velocity vectors. The post-processing procedure included vector validation and vector

conditioning, which could be performed either locally or globally. In this study, local vector validation and vector conditioning were applied. For an interrogation window, local vector validation gathered information from neighboring cells and calculated a reference vector. The difference between the reference vector and the vector in the interrogation area was calculated and checked against a predefined threshold. If the difference exceeded the preset value, validation failed. Local vector validation was performed using the TSI Insight 4G™ software with a median test in a neighboring size of 5 x 5. Following vector validation, vector conditioning was applied to fill gaps due to failed S/N or validation procedures. Vector conditioning was executed using the TSI Insight 4G™ software, employing a recursive filling method within a 5 x 5 neighborhood. Upon calculating the instantaneous velocity field V under the desired conditions, vorticity and streamline patterns could be derived from the velocity vector field for each image pair.

After completing the processing and post-processing routine for all 250 image pairs obtained in this study, the instantaneous and time-averaged velocity field $\langle V \rangle$ could be exported as vector files from the Insight software. Further post-processing was performed using MATLAB to calculate vorticity fields and streamlines.

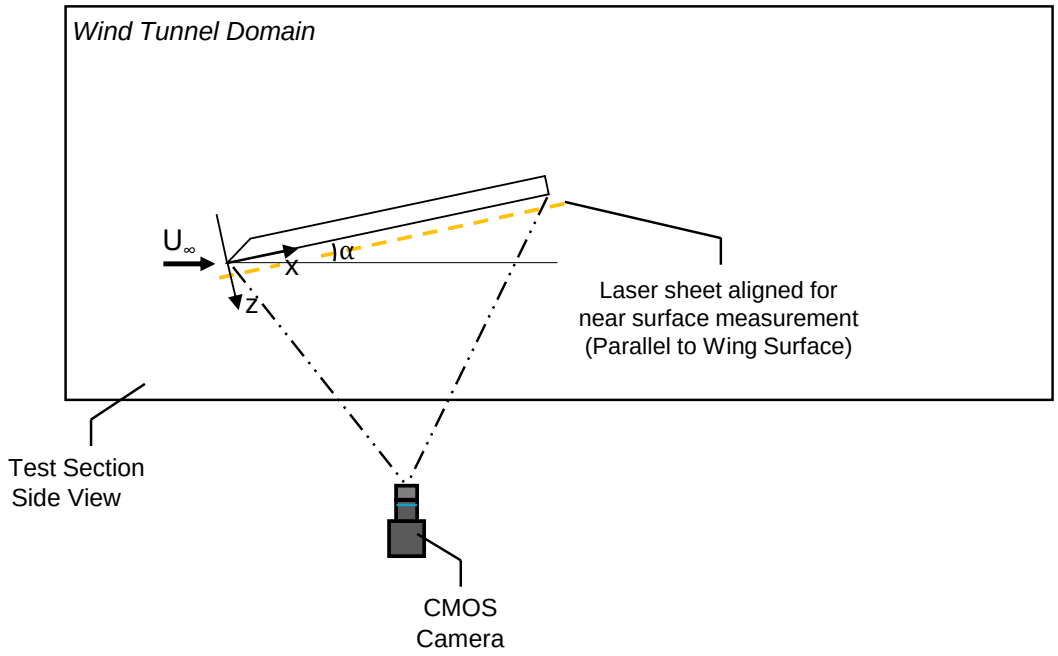

Figure 3.7: Schematic for near surface PIV arrangement.

3.3.3 Force Measurement

Aerodynamic forces and moments were measured using an external force balance system. An ATI Gamma Series 6-Axis Force and Torque sensor, calibrated according to the SI-32-2.5 scheme, was installed outside the wind tunnel near the sidewall and attached to the wing with a strut to obtain drag, lift, and pitch moment measurements. The aerodynamic and inertial forces and moments acting on the bare strut were also measured for each angle of attack. These loads were subtracted from the measurements of the wings to exclude the effect of the strut on the force and moment measurements. The pitch axis was located at the trailing-edge or trailing-apex of the wing. Force and moment data were collected for angles of attack $0° \leq \alpha \leq 30°$. The aerodynamic forces are presented as C_D versus α, C_D versus α, C_L/C_D versus α, and C_M versus α. The C_M data are expressed at the trailing edge. Coefficient calculations are detailed in following paragraphs. A National Instrument NI-PCIe-6321 16-bit data acquisition (DAQ) card was used, coupled with LabVIEW software for digitization of the raw voltage data, which were collected at 10 kHz for 10 seconds for each data point. Sensor specifications, including the measurement range, resolution, and accuracy obtained with the data acquisition system, are provided in Table 3.3 for each measurement axis.

Table 3.3: Force measurement system range, resolution, and accuracy values.

	Fx (N)	**Fy (N)**	**Fz (N)**	**Tx (N-m)**	**Ty (N-m)**	**Tz (N-m)**
Range	±32	±32	±100	±2.5	±2.5	±2.5
Resolution	0.0063	0.0063	0.0125	0.0005	0.0005	0.0005
Uncertainty	0.2400	0.2400	0.7500	0.0250	0.0310	0.0370

Considering the measured resultant loads by the force transducer when the tunnel is operating at the desired speed, the measurements include both the inertial and aerodynamic loads from the mounting strut and wing model. To isolate the pure aerodynamic loads generated by the wing model, sophisticated approaches were followed for both passive and active flow control experiments, based on the principles presented by

Koçak [93]. For all tested cases, four different principal force measurements at each angle of attack were performed. These tests are classified according to the measured loads, as shown in Tables 3.4 and 3.5 for passive and active flow control cases, respectively, based on the mount condition and wind tunnel operation status. The occupancy of the pneumatic tubes connected to the blowing wing model required additional attention during force measurements, which is detailed in the following paragraphs.

For passive flow control experiments, the procedure followed was identical to that implemented by Koçak [93]. The first two test conditions involved measuring the inertial and combined inertial and aerodynamic forces and moments when both the wing and strut were mounted, with the tunnel off and on, respectively. The latter two conditions involved measuring the inertial and combined inertial and aerodynamic forces and moments when only the strut was mounted, with the tunnel off and on, respectively. By subtracting these four different tests from each other, the necessary taring was performed, resulting in the aerodynamic forces and moments generated by the wing only. The test conditions are summarized in Table 3.4.

Table 3.4: Force measurement experiment sequence for passive flow control experiments

TEST ID #	**Model Configuration**	**Tunnel Status**	**Measurement**
1	Wing + Strut	Off	Wing (Inertial) Strut (Inertial)
2	Wing + Strut	On	Wing (Inertial + Aero) Strut (Inertial + Aero)
3	Strut	Off	Strut (Inertial)
4	Strut	On	Strut (Inertial + Aero)

The subtraction operations of different tests and measured loads after these operations are given below. Since the exact weight of the wing is known, the results in B can also be generated without actually conducting Test ID 1 and Test ID 3.

$$\text{(Wing Inertial + Aerodynamics)} = A = \#2 - \#4$$

$$\text{(Wing Inertial)} = B = \#1 - \#3$$

$$\text{(Wing Aerodynamics)} = C = A - B$$

For active flow control experiments, in addition to the procedure mentioned above, the effect of the tubing on the inertial and aerodynamic forces was also considered. Both at tunnel on and off conditions, the tube contribution was measured for the first two tests. In addition, in Test ID 1, the desired flow control actuation, whose details are provided in the following sections, was employed, allowing us to subtract the flow control effect on the inertial condition (tunnel off) in calculations to refine the pure aerodynamic effect. The test conditions are summarized in Table 3.5.

Table 3.5: Force measurement experiment sequence for active flow control experiments.

TEST ID #	**Model Configuration**	**Flow Control Configuration**	**Tunnel Status**	**Measurement**
1	Wing + Strut + Tubes	No Control (Base) Steady Blowing Periodic Blowing	Off	Wing (Inertial) Strut (Inertial) Tubes (Inertial)
2	Wing + Strut + Tubes	No Control (Base) Steady Blowing Periodic Blowing	On	Wing (Inertial + Aero) Strut (Inertial + Aero) Tubes (Inertial + Aero)
3	Strut	N/A	Off	Strut (Inertial)
4	Strut	N/A	On	Strut (Inertial + Aero)

$$\text{(Wing \& Tube Inertial + Aerodynamics)} = A = \#2 - \#4$$

$$\text{(Wing \& Tube Inertial)} = B = \#1 - \#3$$

$$\text{(Wing \& Tube Aerodynamics)} = C = A - B$$

Before starting force measurements for the active flow control campaign, the bare effect of the tube for the baseline condition with no flow control effector was studied, as shown schematically in Figure 3.8. The investigation of the tube effect on the baseline condition is presented in Chapter 8, prior to the results of the active flow control campaign force measurements.

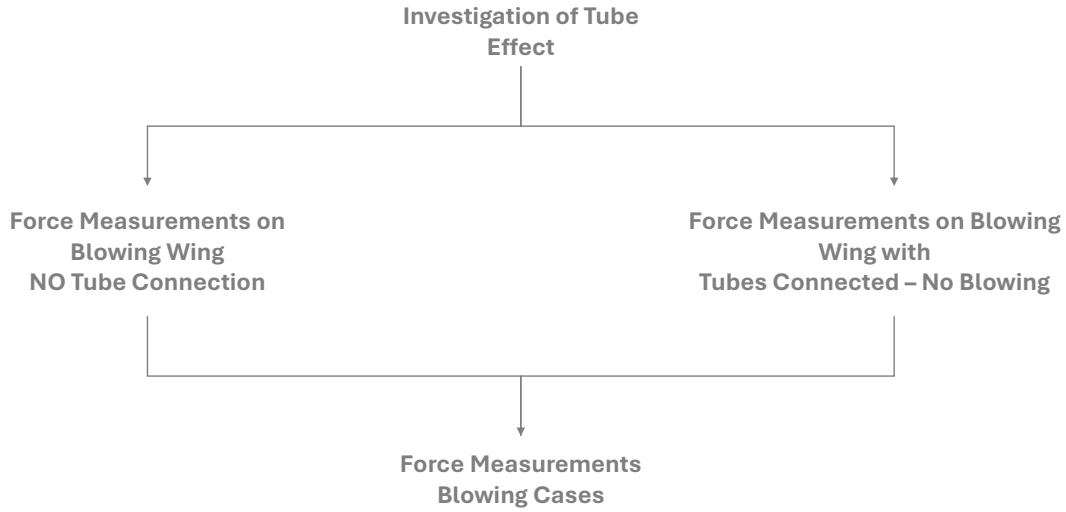

Figure 3.8: Approach to investigate the effect of blowing tubing on force measurements.

During force measurements, wind and body frame definitions, along with respective transformations, were utilized. The wind frame, previously shown in Figure 3.4 (d), is stationary and does not vary with angle of attack changes, whereas the body frame is positioned on the sensor and rotates with the sensor when the angle of attack is altered. The loads on all six channels are measured on the sensor in the body frame. The body (red) and wind frame (magenta) axes are also shown in Figure 3.4 (d) at a certain angle of attack value. Both frames follow the right-hand rule. Therefore, the y-axis for the body frame is not shown for the sake of visualization. The respective angle of attack (α) between these axis frames is the angle between the yellow lines. Additionally, the nature of the model positioning system (MPS) and sensor rotation around the wind frame y-axis yield that the resolution of the force measurement in the wind frame z-axis improves as the angle of attack increases. This is because the sensor resolution of the measured forces in the x and y axes of the body frame is twice as good as the z-axis, as provided in Table 3.3.

Measured loads can be transformed into the wind frame and translated to any point inside the wind tunnel. Since the measured forces do not carry any location information, the appropriate translation of the forces in the wind frame enables the determination of the moment coefficients on the wing surface. By doing so, the pressure center and the aerodynamic centers in pitch and height can be found, allowing for stability assessment in the longitudinal axis.

The necessary transformation from the body frame to the wind frame is conducted using the following formulas, where subscripts b and w denote the body and wind frames, respectively:

$$\begin{aligned} F_{x,w} &= F_{x,b} \cdot \cos(\alpha) - F_{z,b} \cdot \sin(\alpha) \\ F_{y,w} &= -F_{y,b} \\ F_{z,w} &= -(F_{x,b} \cdot \sin(\alpha) + F_{z,b} \cdot \cos(\alpha)) \\ M_{x,w} &= M_{x,b} \cdot \cos(\alpha) - M_{z,b} \cdot \sin(\alpha) \\ M_{y,w} &= -M_{y,b} \\ M_{z,w} &= -(M_{x,b} \cdot \sin(\alpha) + M_{z,b} \cdot \cos(\alpha)) \end{aligned} \tag{3.3}$$

In the above formulas, $F_{x,w} = F_D$, $F_{y,w}$, and $F_{z,w} = F_L$ are the wind frame drag, side, and lift forces, respectively, whereas $M_{x,w}$, $M_{y,w} = M_y$, and $M_{z,w}$ are the wind frame roll, pitch, and yaw moments, respectively. The aerodynamic coefficients are determined using the measured aerodynamic forces (drag and lift) and moments (pitch) with the following Eqn.s 3.6 and 3.5, where ρ is the air density, U_∞ is the free-stream velocity, A is the characteristic area, L is the characteristic length, S is the wingspan, and C is the chord length. The characteristic area A and characteristic length L were the surface area and the chord length of the delta wing models, which were 0.0182 m^2 and 0.135 m, respectively.

$$C_D, C_L = \frac{(F_D, F_L)}{\frac{1}{2}\rho U_\infty^2 A} \tag{3.4}$$

$$C_M = \frac{M_Y}{\frac{1}{2}\rho U_\infty^2 A L} \tag{3.5}$$

$$
\begin{aligned}
A &= \frac{1}{2}SC \\
L &= C \\
p_{\text{dyn}} &= \frac{1}{2}\rho U_{\infty}^{2}
\end{aligned}
\tag{3.6}
$$

3.3.4 Hot Wire Anemometry Measurement

Hot-wire anemometry is a highly adaptable technique utilized for measuring velocity and temperature fluctuations in the time domain, making it particularly valuable for studies of turbulent and oscillating flows. With suitable design configurations, hot-wire anemometry is effective across a broad range of speeds, from low subsonic to high supersonic flows. This method is quite succesful detecting turbulent disturbances as well as the periodic flow features due to its minimal thermal inertia and effective corrections implemented within the anemometer.

The hot-wire can operate in three widely used modes: constant current, constant temperature, and the newer constant voltage method. The fundamental operational principle of hot-wire anemometry systems rely on detecting changes in heat transfer from a small, electrically heated wire exposed to fluid motion. The heat transfer occurs primarily through convection, which depends on the fluid velocity, with radiative heat transfer considered negligible. Consequently, a relationship can be established between the fluid velocity and the electrical output of the system. In the current study, a constant temperature anemometry system was employed for two distinct purposes: first, to estimate the bleeding momentum coefficient in the passive flow control campaign, and second, to measure the blowing velocity profiles in the active flow control campaign.

A Dantec 54T052 Mini CTA constant temperature anemometry device was utilized in the current study. The general technical specifications are provided in Figure 3.9. Measurements were conducted using a 55P16 single wire straight probe with an embedded wire support. The CTA system features an integrated Wheatstone bridge circuit, with the hot wire probe connected to one arm of the bridge. It requires a power input of 11–14 V, and the overall operating resistance range is between 4 and 36

ohms. The signal output range of the CTA system is from 0 to 5 V, and the output is acquired and digitized using an NI SCB 68 Chassis connected to a 12-bit PCI-6024E DAQ card. The 55P16 hot wire probe has a wire diameter of 5 microns and an active sensor length of 1.25 mm, which can be connected to the CTA system using a 4 m BNC cable.

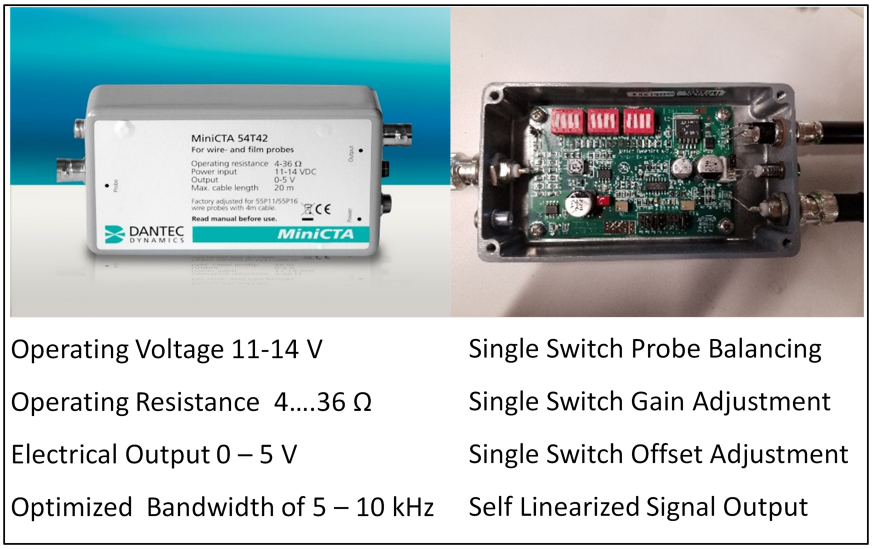

Figure 3.9: General overview of the DANTEC Mini CTA 54T042.

The system is based on a compact electronic structure that includes:

- Dip switches for adjusting the probe overheat setting based on the probe's factory data sheet,
- Gain switches,
- Zero offset switches, and
- Filter switches.

The most critical step is adjusting the overheat setting, also referred to as decade resistance, to establish the desired wire operating temperature. To facilitate this, the manufacturer provided a spreadsheet that generates the binary arrangements for the dip switches specific to each probe. The spreadsheet requires the following properties of the probe: sensor wire resistance, sensor lead resistance, sensor support resistance,

cable resistance, temperature coefficient of resistance, desired mean sensor temperature, and the temperature of the working medium.

Ternoy et al. [91] presented an overview of the actuation capabilities of ONERA for various aerodynamic surfaces across different flow regimes. In the third part of their summary, they outlined approaches for characterizing fluidic actuators, with an emphasis on periodic actuation. When the blowing dimension exceeds the wire length, the blowing velocity pattern can be effectively captured by traversing the probe along the hole. In this scenario, assuming uniform cooling of the wire due to the negligible velocity gradient at each increment yields accurate results. Conversely, when the hole dimension is comparable to the typical straight hot wire length of 1.25 mm, traversing becomes impractical, leading to non-uniform cooling of the wire due to a moderate gradient. Nevertheless, the wire still represents a bulk characteristic and remains responsive at significantly high sampling rates, aided by the servo loop control system integrated within the anemometry system. Considering the steady actuation or bulk characteristics estimation in-situ calibration still can be used for slots having characteristic length slightly greater than wire length. For both passive and active flow control campaign hot wire measurements, in-situ calibration approach was utilized based on the procedures suggested by Ternoy et al. [91].

The existing data acquisition systems, combined with the LabVIEW environment, allowed us to develop an in-house acquisition scheme, which is considered more flexible for integration with flow control systems while performing an in-situ calibration approach. The details of the hot wire calibration scheme are elaborated for both passive bleeding characterization and active blowing measurements in the following sections.

3.4 Active Flow Control System

In order to supply control flow, a comprehensive experimental setup has been designed, built, and integrated, as illustrated schematically in Figure 3.10. The system comprises three domains: the Pneumatic Plant, the Control-Measurement and DAQ Plant, and the Wind Tunnel Domain, enabling the control of each blowing station

either individually or synchronously.

Blowing air, supplied from a pressurized line, is conditioned using FESTO MS4-LFR series filter regulators and delivered to the wing model in an actuated manner using FESTO MHJ9 series fast-switching solenoid valves across the pneumatic plant. A FESTO SFAH series digital flow meter is positioned between the regulator and valve for both in-situ calibration and monitoring the steady supply rate prior to periodic blowing experiments. The filter regulators have a pressure regulating range of 0.5 to 12 bar with a 40-micron grade of filtration. Initial flow rate adjustments are performed using the regulator's rotary knob, allowing constant output pressure. The solenoid valves, of type 2/2 way, have a working pressure range of 0.5 to 6 bar. The valve on and off times, specified as 0.9 and 0.4 milliseconds by the manufacturer, allow the use of periodic signals in square waveforms with high repeatability.

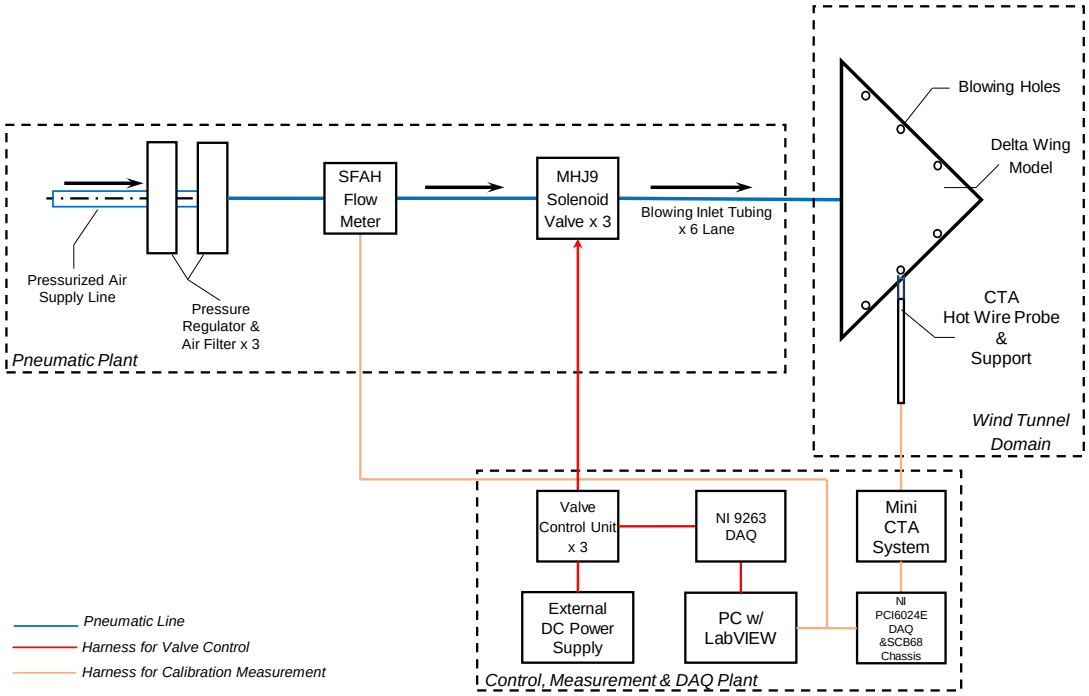

Figure 3.10: Schematic representation of the active flow control setup.

The flow control system includes three regulator and valve pairs, one for each blowing station. The digital flow meter, with a measurement range of 0–50 l/min, is equipped with a digital readout unit and a 0–10 V output signal. Each station has a dedicated valve, with the outlet of each valve divided for each half of the respective station using

a doubler junction. All pneumatic tubing is of equal length up to the valve connection. Since the forward, middle, and aft blowing stations have different lengths from the trailing edge input to the blowing hole exits, tubing lengths after the valve output port are adjusted to ensure that the total length from the valves to the blowing hole stations is the same. To ensure symmetrical and identical flow rate patterns after the valve and doubler through the station halves, pneumatic mechanical rotameters were used to confirm the behavior of each hole half. Figure 3.11 shows views of the pneumatic plant and wind tunnel domain.

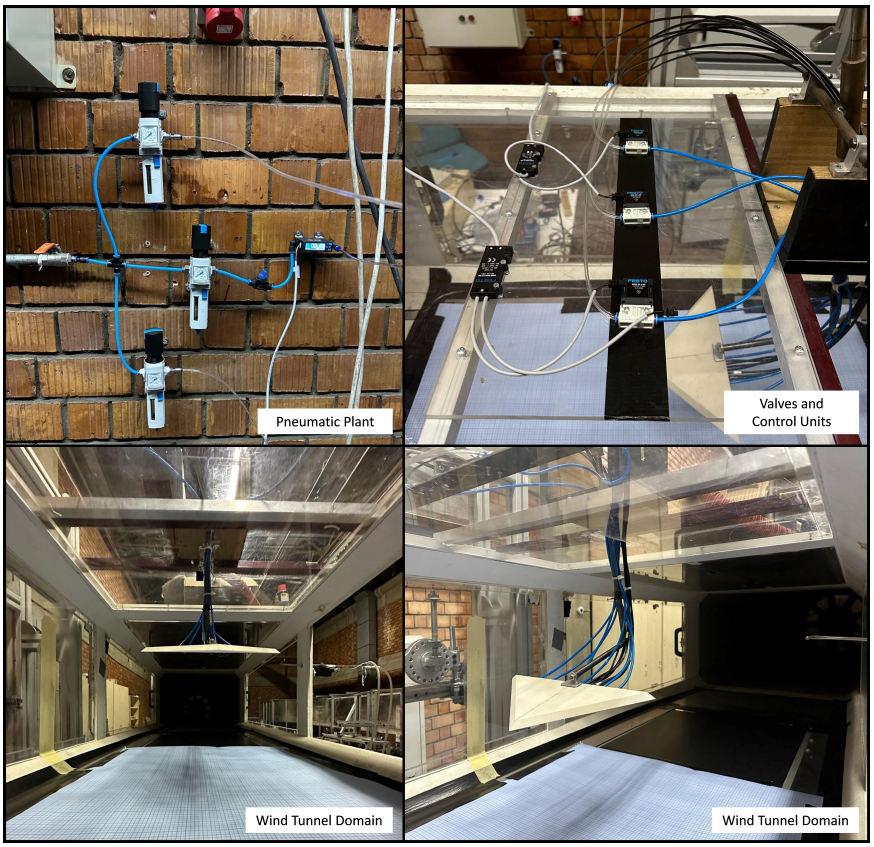

Figure 3.11: Flow control setup: pneumatic plant and wind tunnel domain.

The control, measurement, and DAQ plant has two main functions: generating control signals to drive the solenoid valves at the desired waveform, frequency, and duty cycle values, and performing in-situ calibration and quantification of control flow from each blowing hole using a constant temperature anemometry system and a digital flow meter. To achieve these purposes, comprehensive software with a visual interface was developed in the LabVIEW environment. The software's front panel and block

diagram are shown in Figure 3.12 and Figure 3.13, respectively. The software has the following features:

- Selection of the experiment phase:
  - Calibration state,
  - Flow control state,
- Selection of the valve control state:
  - Regular periodic signal generation,
  - Burst modulated signal generation,
  - Steady signal generation,

The software allows the user to implement different periodic and steady flow control scenarios both systematically and parametrically. Additionally, the selection of the in-situ calibration phase is made practical. The control signal output of the software is transmitted to the valve control module via a National Instruments NI-9263 analog data acquisition card, which has a 16-bit resolution and an output control signal range of ±10 V with 4 analog output channels. The operating voltage for the valve control system is supplied using an external DC power source. Calibration and blowing characterization measurements were conducted in the calibration state mode of the developed program. CTA signals were digitized using an NI SCB-68 Chassis connected to a 12-bit PCI-6024E DAQ card.

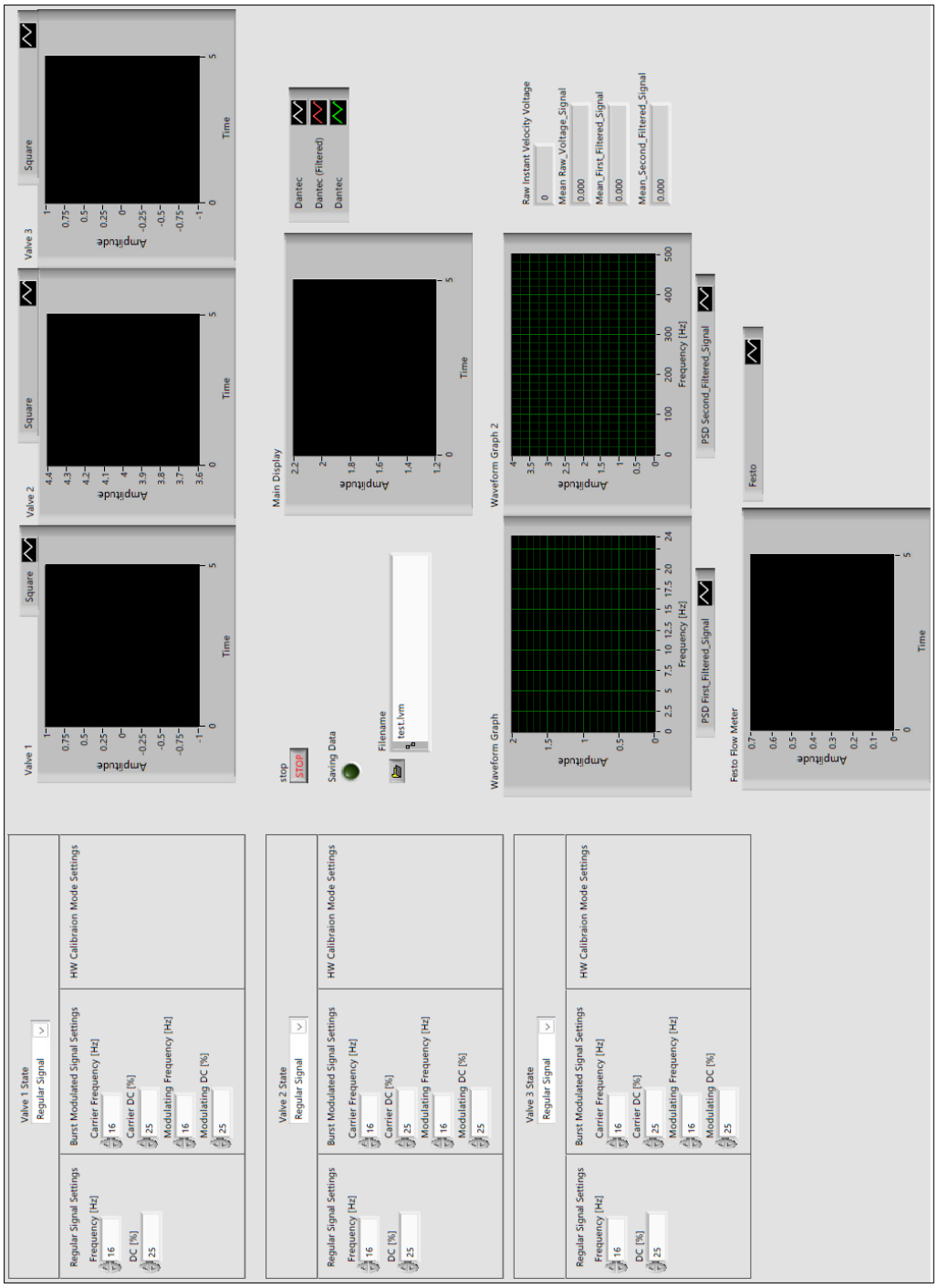

Figure 3.12: Developed LabVIEW front panel for active blowing system control.

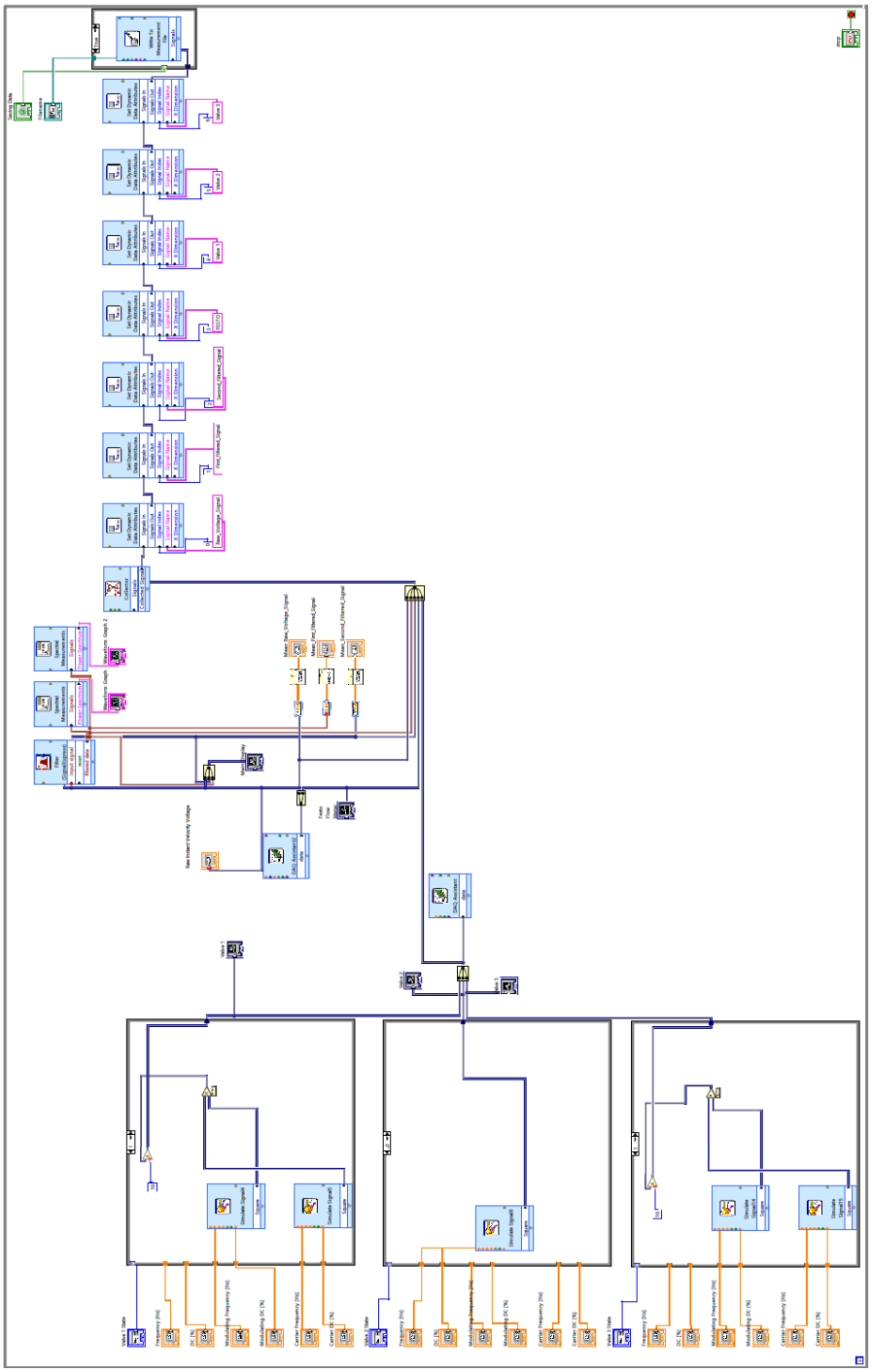

Figure 3.13: Developed LabVIEW block diagram for active blowing system control.

3.5 Experimental Matrix

The present study investigates the effects of passive and active flow control techniques, namely passive bleeding with nozzle-type slots and periodic blowing, on flow structures over a $\Lambda = 45^{\circ}$ swept nonslender delta wing. Wind tunnel experiments were conducted using surface pressure measurements, force measurements, and particle image velocimetry (PIV) for various angles of attack and Reynolds numbers. In the passive bleeding campaign, four different wing models with various nozzle bleed slots were tested and compared to a baseline model and a back-bleed wing. For the active flow control campaign, the effects of periodic blowing patterns generated with regular and burst-modulated square waves were examined for various excitation frequencies and duty cycle settings. In addition to the wind tunnel measurements, comprehensive characterization of bare flow control approaches was performed. For passive bleeding control, a methodology was proposed to estimate the bleeding momentum coefficient based on bleed pressure measurements calibrated with in-situ hot wire measurements. This proposed scheme was applied to actual representative wind tunnel measurements. For active blowing flow control, the system's response was thoroughly investigated prior to wind tunnel measurements using in-situ calibrated hot wire measurements. The overall performance of the blowing system was assessed for varying excitation frequencies, blowing velocities, momentum coefficients, and duty cycle values. The overall experimental campaign is parametrically presented in Figure 3.14.

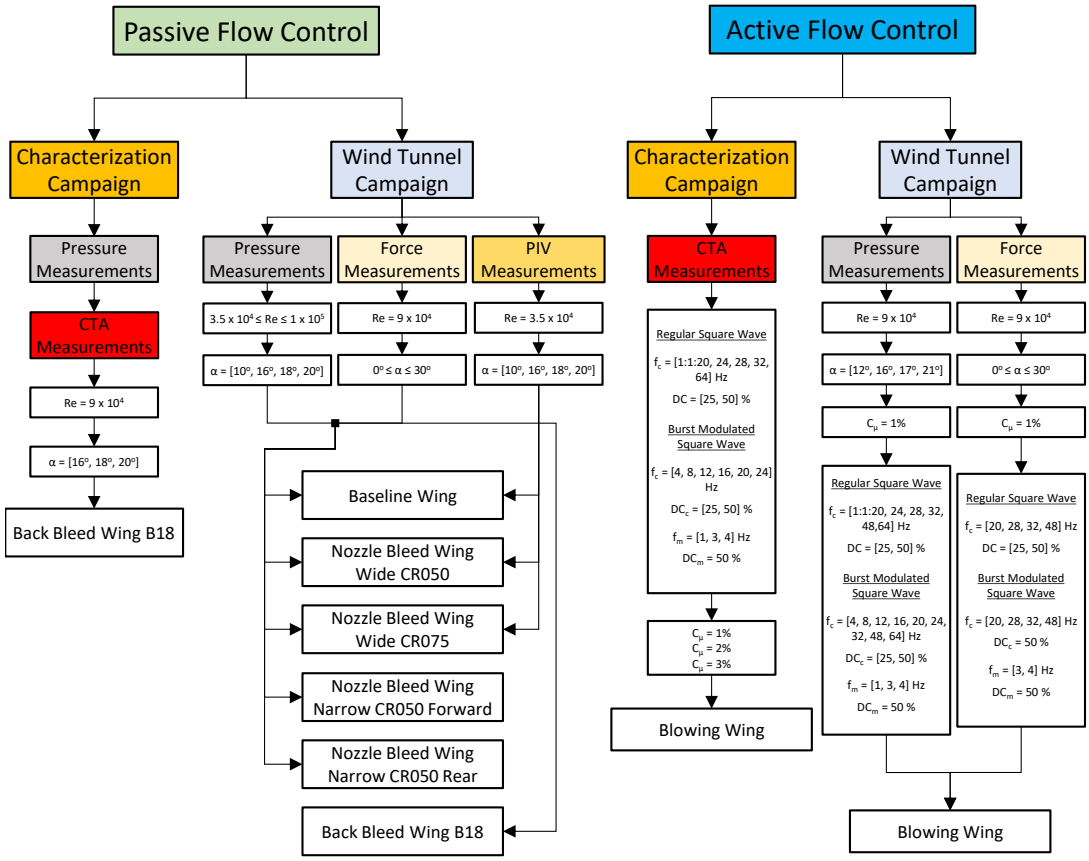

Figure 3.14: Experimental matrix.

3.6 Measurement Uncertainty

Experimental measurements invariably contain some degree of uncertainty, which can arise from the inherent inaccuracies of measuring instruments and random variations in the quantities being measured. It is crucial to conduct an uncertainty analysis to validate results before presenting any experimental reports.

This section aims to identify and document the potential sources of uncertainty involved in the calculations of the pressure coefficient, force coefficients and moment coefficient as well as the derived respective uncertainty equations. The calculated uncertainty estimates are expressed in each methodology chapter respectively.

To calculate the best estimate uncertainty of a result R, which is a function of n

measured variables the following Eqn 3.7 was used as suggested by Wheeler and Ganji [95]:

$$\omega_R = \left[\left(\omega_{x_1} \frac{\partial R}{\partial x_1} \right)^2 + \left(\omega_{x_2} \frac{\partial R}{\partial x_2} \right)^2 + \cdots + \left(\omega_{x_n} \frac{\partial R}{\partial x_n} \right)^2 \right]^{1/2} \tag{3.7}$$

Here, ω_{x_i} represents the uncertainty estimate for each measured variable. Additionally, the fractional or relative uncertainty for each result or measured variable can be expressed as follows in Eqn. 3.8:

$$\frac{\omega_R}{R} = u_R \tag{3.8}$$

The absolute uncertainty values of the measured quantities are provided in Table 3.6.

Table 3.6: Uncertainty of each measured variable

Parameter	**Value**
$\omega_{F_{x,b}}$ [N]	0.064
$\omega_{F_{y,b}}$ [N]	0.064
$\omega_{F_{z,b}}$ [N]	0.2
$\omega_{M_{x,b}}$ [Nm]	0.005
$\omega_{M_{y,b}}$ [Nm]	0.005
$\omega_{M_{z,b}}$ [Nm]	0.005
ω_P [Pa]	1.25
ω_{P_∞} [Pa]	1.25
$\omega_{P_{dyn}}$ [Pa]	1.7678
ω_α [deg]	0.1
ω_A [m²]	1.51E-04
ω_L [m]	0.001
ω_Q [lit/min]	0.53 – 1.5
ω_E [V]	0.67% omv

3.6.1 Uncertainty Estimate for C_p

As per the definitions given for pressure coefficient in section 3.3.1, the equation can be written as a function of measured static pressure, static pressure of the freestream, and dynamic pressure as follows:

$$C_p = \frac{\bar{p} - p_\infty}{p_{\text{dyn}}} \tag{3.8}$$

The uncertainty ω_{C_p} can be estimated by utilizing the Eqn. 3.7:

$$\omega_{C_p} = \left[\left(\omega_{\bar{p}} \frac{\partial C_p}{\partial \bar{p}} \right)^2 + \left(\omega_{p_\infty} \frac{\partial C_p}{\partial p_\infty} \right)^2 + \left(\omega_{p_{\text{dyn}}} \frac{\partial C_p}{\partial p_{\text{dyn}}} \right)^2 \right]^{1/2} \tag{3.9}$$

Performing the partial fraction operations in above equation, the uncertainty ω_{C_p} could be obtained using the resultant form:

$$\omega_{C_p} = \left[\left(\frac{\omega_{\bar{p}}}{p_{dyn}} \right)^2 + \left(\frac{\omega_{p_\infty}}{p_{dyn}} \right)^2 + \left(\omega_{p_{dyn}} \left(-\frac{\bar{p} - p_\infty}{p_{dyn}^2} \right) \right)^2 \right]^{1/2} \tag{3.10}$$

3.6.2 Uncertainty Estimate for C_D

As per the definitions given for drag coefficient in section 3.3.3, the equation can be written as a function of measured body forces, angle of attack, dynamic pressure and reference area as follows:

$$C_D = \frac{F_D}{\frac{1}{2}\rho U_\infty^2 A} = \frac{F_D}{p_{\text{dyn}} A} \tag{3.11}$$

$$C_D = \frac{F_{x,b}\cos(\alpha) - F_{z,b}\sin(\alpha)}{p_{\text{dyn}} A} \tag{3.12}$$

$$C_D = f(F_{x,b}, F_{z,b}, \alpha, p_{\text{dyn}}, A) \tag{3.13}$$

The uncertainty ω_{C_D} can be estimated by utilizing the Eqn. 3.7:

$$\begin{aligned}\omega_{C_D} = \Bigg[&\left(\omega_{F_{x,b}} \frac{\partial C_D}{\partial F_{x,b}}\right)^2 + \left(\omega_{F_{z,b}} \frac{\partial C_D}{\partial F_{z,b}}\right)^2 + \left(\omega_{\alpha} \frac{\partial C_D}{\partial \alpha}\right)^2 \\ &+ \left(\omega_{p_{\text{dyn}}} \frac{\partial C_D}{\partial p_{\text{dyn}}}\right)^2 + \left(\omega_{A} \frac{\partial C_D}{\partial A}\right)^2 \Bigg]^{1/2}\end{aligned} \tag{3.14}$$

Performing the partial fraction operations in above equation, the uncertainty ω_{C_D} could be obtained using the resultant form:

$$\begin{aligned}\omega_{C_D} = \Bigg[&\left(\omega_{F_{x,b}} \frac{\cos(\alpha)}{p_{\text{dyn}} A}\right)^2 + \left(\omega_{F_{z,b}} \frac{-\sin(\alpha)}{p_{\text{dyn}} A}\right)^2 \\ &+ \left(\omega_{\alpha} \frac{-F_{x,b}\sin(\alpha) - F_{z,b}\cos(\alpha)}{p_{\text{dyn}} A}\right)^2 \\ &+ \left(\omega_{p_{\text{dyn}}} \frac{-(F_{x,b}\cos(\alpha) - F_{z,b}\sin(\alpha))}{p_{\text{dyn}}^2 A}\right)^2 \\ &+ \left(\omega_{A} \frac{-(F_{x,b}\cos(\alpha) - F_{z,b}\sin(\alpha))}{p_{\text{dyn}} A^2}\right)^2 \Bigg]^{1/2}\end{aligned} \tag{3.15}$$

3.6.3 Uncertainty Estimate for C_L

As per the definitions given for lift coefficient in section 3.3.3, the equation can be written as a function of measured body forces, angle of attack, dynamic pressure and reference area as follows:

$$C_D = \frac{F_L}{\frac{1}{2}\rho U_\infty^2 A} = \frac{F_L}{p_{\text{dyn}} A} \tag{3.16}$$

$$C_L = \frac{-(F_{x,b}\sin(\alpha) + F_{z,b}\cos(\alpha))}{p_{\text{dyn}} A} \tag{3.17}$$

$$C_L = f(F_{x,b}, F_{z,b}, \alpha, p_{\text{dyn}}, A) \tag{3.18}$$

The uncertainty ω_{C_L} can be estimated by utilizing the Eqn. 3.7:

$$\omega_{C_L} = \left[\left(\omega_{F_{x,b}} \frac{\partial C_L}{\partial F_{x,b}} \right)^2 + \left(\omega_{F_{z,b}} \frac{\partial C_L}{\partial F_{z,b}} \right)^2 + \left(\omega_{\alpha} \frac{\partial C_L}{\partial \alpha} \right)^2 + \left(\omega_{p_{\text{dyn}}} \frac{\partial C_L}{\partial p_{\text{dyn}}} \right)^2 + \left(\omega_A \frac{\partial C_L}{\partial A} \right)^2 \right]^{1/2} \tag{3.19}$$

Performing the partial fraction operations in above equation, the uncertainty ω_{C_L} could be obtained using the resultant form:

$$\begin{aligned} \omega_{C_L} = \Bigg[& \left(\omega_{F_{x,b}} \frac{-\sin(\alpha)}{p_{\text{dyn}} A} \right)^2 + \left(\omega_{F_{z,b}} \frac{-\cos(\alpha)}{p_{\text{dyn}} A} \right)^2 \\ & + \left(\omega_{\alpha} \frac{-(F_{x,b}\cos(\alpha) - F_{z,b}\sin(\alpha))}{p_{\text{dyn}} A} \right)^2 \\ & + \left(\omega_{p_{\text{dyn}}} \frac{(F_{x,b}\sin(\alpha) + F_{z,b}\cos(\alpha))}{(p_{\text{dyn}})^2 A} \right)^2 \\ & + \left(\omega_A \frac{-(F_{x,b}\sin(\alpha) + F_{z,b}\cos(\alpha))}{p_{\text{dyn}} A^2} \right)^2 \Bigg]^{1/2} \end{aligned} \tag{3.20}$$

3.6.4 Uncertainty Estimate for C_M

As per the definitions given for lift coefficient in section 3.3.3, the equation can be written as a function of measured body forces, angle of attack, dynamic pressure and reference area as follows:

$$C_M = \frac{M_y}{\frac{1}{2}\rho U_\infty^2 A L} = \frac{M_y}{p_{\text{dyn}} A L} \tag{3.21}$$

$$C_M = \frac{-M_{y,b}}{p_{\text{dyn}} A L} \tag{3.22}$$

$$C_M = f(M_{y,b}, \alpha, p_{\text{dyn}}, A) \tag{3.23}$$

The uncertainty ω_{C_M} can be estimated by utilizing the Eqn. 3.7:

$$\omega_{C_M} = \left[\left(\omega_{M_{y,b}} \frac{\partial C_M}{\partial M_{y,b}} \right)^2 + \left(\omega_{p_{\text{dyn}}} \frac{\partial C_M}{\partial p_{\text{dyn}}} \right)^2 + \left(\omega_A \frac{\partial C_M}{\partial A} \right)^2 + \left(\omega_L \frac{\partial C_M}{\partial L} \right)^2 \right]^{1/2} \tag{3.24}$$

Performing the partial fraction operations in above equation, the uncertainty ω_{C_L} could be obtained using the resultant form:

$$\omega_{C_M} = \left[\left(\omega_{M_{y,b}} \frac{-1}{p_{\text{dyn}} AL} \right)^2 + \left(\omega_{p_{\text{dyn}}} \frac{M_{y,b}}{(p_{\text{dyn}})^2 AL} \right)^2 + \left(\omega_A \frac{-M_{y,b}}{p_{\text{dyn}} A^2 L} \right)^2 + \left(\omega_L \frac{-M_{y,b}}{p_{\text{dyn}} AL^2} \right)^2 \right]^{1/2} \tag{3.25}$$

3.7 Measurement Approaches and Geometry Details

In this section, the methodologies followed for each experimental campaign are presented. The campaigns include the Bleed Momentum Estimation Study, the Nozzle Bleed Flow Control Study, the Comprehensive Characterization of the Active Flow Control System Study, and the Periodic Blowing Active Flow Control Study.

For each study, detailed accounts of the experimental conditions, the arrangements of the measurement systems, and the specifications of the wing models are provided. The results of each study are discussed in the subsequent main chapters.

3.7.1 Bleed Momentum Estimation Study

This part of the current study was organized in two main steps, namely the calibration phase and the implementation of calibration to representative wind tunnel tests. Calibration experiments were performed in two stages, namely Stage 1 and Stage 2. During Stage 1, bleed supply velocity in the range of $1\,\text{m/s} \leq V_{\text{bleed,supply}} \leq 13.64\,\text{m/s}$ was supplied actively for in situ supply measurements at tunnel off setting. Reynolds numbers corresponding to the bleed supply velocity range were calculated based on the bleed slot length l as $1.4 \times 10^3 \leq Re_b \leq 1.89 \times 10^4$. In Stage 2, wind

tunnel operating calibration measurements were conducted at a freestream range of $2.4\,\text{m/s} \leq U_\infty \leq 12.1\,\text{m/s}$ corresponding to the freestream Reynolds number range of $1.9 \times 10^4 \leq Re \leq 9.6 \times 10^4$. Wind tunnel tests were performed for representative angles of attack in the range of $16^\circ \leq \alpha \leq 20^\circ$ at a Reynolds number of $Re = 1 \times 10^5$.

Details of the passive bleeding technique employed on delta wing planforms were extensively discussed in the aforementioned literature. In the current work, a surface pressure measurement-based bleed momentum estimation scheme is proposed. For that purpose, the candidate wing model was selected as the Back Bleed Wing from the study presented by Çelik et al. due to its superior performance compared to other suggested design alternatives [10]. The wing model had a sweep angle of $\Lambda = 45$ degrees and sharp edges beveled on the windward side with a bevel angle of 45 degrees. The wing was reproduced by maintaining the principal as same as baseline wing model and reference work as well.

Figure 3.15 was constructed to demonstrate and designate the details of the wing geometry such that: part (a) represents the isometric view of the wing model with bleed slot geometry and axis designation, part (b) represents the integration of the bleed pressure measurement tap to the wing model, and part (c) represents details of the bleed slot on pressure and suction sides along with the cross-sectional view. Axes for bleed slot orientation are designated such that the x' axis is normal to the leading edge on the wing surface, the y' axis is parallel to the leading edge, and the z' is normal to the wing surface. Bleed slots are located parallel to the leading edges, five on each half and oriented with a back angle of $\theta = 18$ degrees with respect to the y' axis aiming to direct the control flow from the pressure to the suction side. Slots have a length of $l = l_p = l_s = 21$ mm on both sides with an equal spacing of $s_p = s_s = 4$ mm and an end diameter of $d = 3$ mm. The corresponding bleed slot area is $A_b = 61.07$ mm^2. The local surface pressure in the vicinity of the bleed slots on the pressure and suction sides was measured with pressure taps of 0.5 mm diameter positioned 2 mm from the midpoint of the downstream edge of each slot. Considering the wing thickness and manufacturing tolerances, inlet and exit taps were separately placed on each half benefiting from the symmetric design of the wing. In order to supply controlled bleed actuation, a calibration adapter was designed and made of PLA using a 3D printer. The geometric details of the adapter along with the assembly

view to the wing model are provided in Figure 3.16. The model had an air inlet port where a pneumatic fitting was integrated in order to connect the supply air and an air outlet of the bleed geometry with a wall thickness of 0.2 mm that could fit directly to the wing bleed slots. In order to compare and present the positioning of the wing model both at calibration measurements and wind tunnel tests, respective wind tunnel orientations are presented in Figure 3.17.

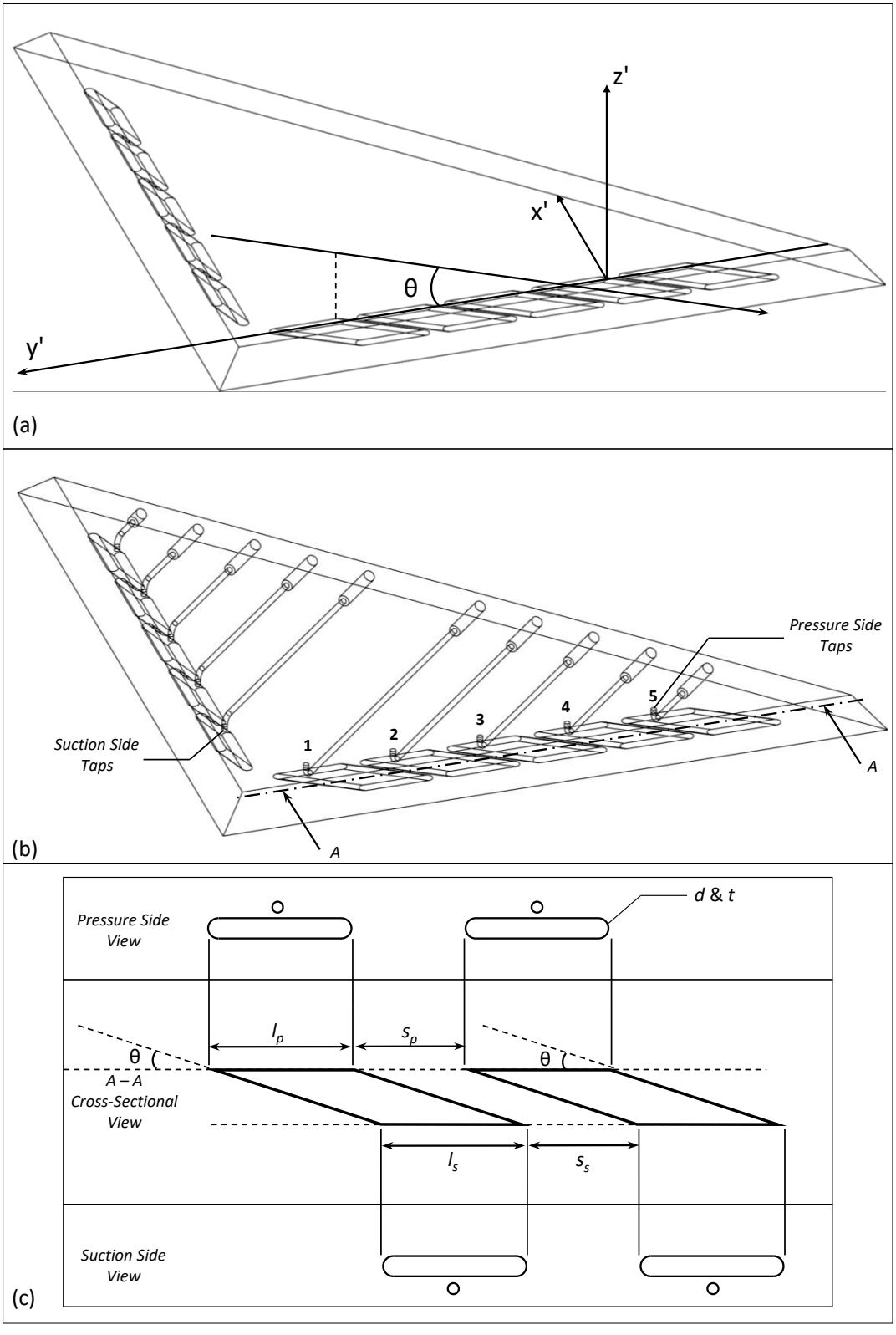

Figure 3.15: Schematic representation of the bleed geometry design and pressure taps for momentum coefficient estimation: (a) Back angle bleed wing geometry [10], (b) Wing with bleed pressure taps, (c) Dimension designation.

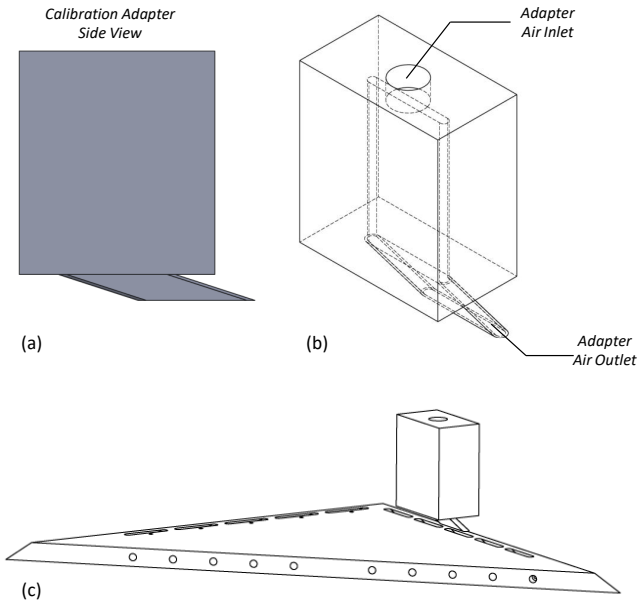

Figure 3.16: Bleed calibration adapter CAD model: (a) Side view, (b) Iso-view with details, (c) Adapter – wing assembly.

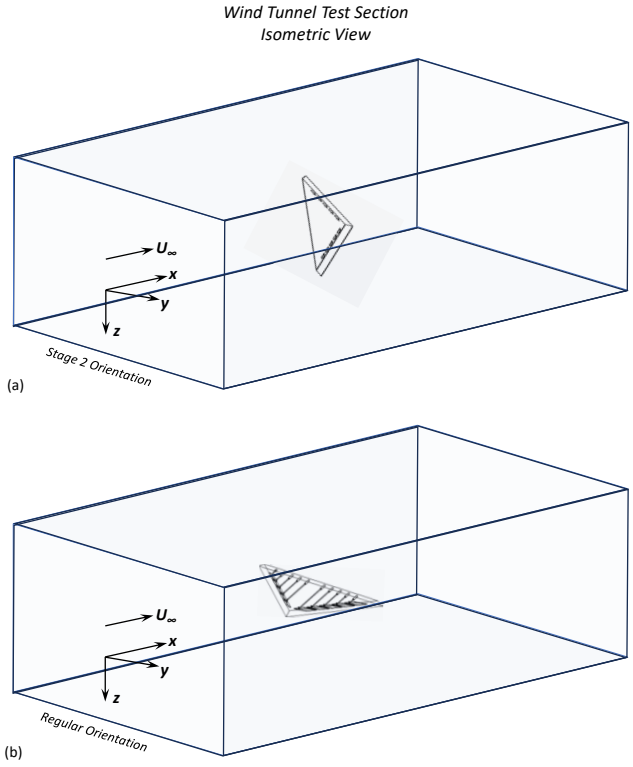

Figure 3.17: Illustration of the wing model orientation in the wind tunnel (a) Stage 2 setting, (b) Regular wind tunnel testing setting (not to scale).

The pressure coefficient at either the inlet and outlet of the bleeding slots was calculated using Eqn. (3.2) where $\overline{p}$ is the mean pressure of the surface pressure of interest, p_∞ and p_{dyn} are the mean static and dynamic pressure values of the freestream. The maximum uncertainty value for the presented pressure coefficient difference is ± 0.056.

Bleed velocity based on surface pressure measurement for the ith bleeding slot with no correction can be obtained using Eqn. (3.26) based on the Bernoulli principle, where $\Delta p_i = p_{p,i} - p_{s,i}$ represents the pressure difference across the ith slot, ρ is the air density and V_{ent} is the bleed slot entrance velocity assumed equal to the freestream velocity U_∞. For the characterization of the passive bleeding actuation across the ith slot, a nondimensional momentum coefficient $C_{\mu,i}$ defined in Eqn. (3.27) was used where A_{bleed} is the bleed slot cross-sectional area and A is the surface area of the planform.

$$V_{\text{bleed},i} = \sqrt{\frac{\Delta p_i}{0.5\rho} + V_{\text{ent},i}^2} \tag{3.26}$$

$$C_{\mu,i} = \frac{V_{\text{bleed},i}^2 \cdot A_{\text{bleed}}}{U_\infty^2 \cdot A} \tag{3.27}$$

In order to suggest a correction and propose an improved accuracy, a two stage in-situ calibration scheme is suggested, whose sequence is presented in Figure 3.18 as a complement to the schematic representation of the experimental approach given in Figure 3.19. The presented calibration approach is in-line with the techniques used to characterize active flow control devices for which a detailed explanation and sample work models are demonstrated by Ternoy et al. [91]. For the Stage 1 processes, the calibration adapter was assembled to one of the bleeding slots in the wing model ensuring leakage free integration while the remaining slots were kept blind using removable surface tape. The wing model was placed normal to the tunnel cross-section for the sake of positioning and uniform calibration supplies. The bleed air through the adapter was supplied from the compressor which was first connected to a high precision pressure regulator and filter assembly to control the supply rate. To construct the in-situ calibration charts, the FESTO SFAH-50U-Q6AR flow meter was connected

to the supply line. The bleed velocity at the exit of a representative blowing slot was measured using a Dantec 55P16 hot-wire probe and a 54T42 mini-CTA device anemometer. Both flow meter and anemometer raw voltage data were digitized using the National Instrument NI-PCI 6024E data acquisition (DAQ) card and the generated visual interface on the LabVIEW environment. Flow meter and hot wire measurements in Stage 1 were simultaneously collected at 200 and 1000 Hz sampling rates respectively for a period of 10 seconds. The supply rate varied from $Q = 1.5$ l/min to 50 l/min corresponding to the aforementioned bleed slot exit velocities $V_{\text{bleed,supply}}$ that is obtained by dividing the flow rate with the bleed slot area A_b. The maximum uncertainty levels for bleed supply velocities were estimated as ± 0.14 m/s to ± 0.4 m/s for the investigated range. For the Stage 2 processes, the calibration adapter was removed from the set-up while keeping the wing model and hot wire probe as they were in Stage 1 for the in-situ principle. In order to establish a relation between hot wire measurements and bleed surface pressure measurements simultaneously, wind tunnel experiments were performed for varying free stream velocities U_∞. During that process, all bleeding slots other than the slot where the inspection was performed were covered, in order to minimize the interaction with neighbor slots and represent a single slot's characteristics during characterization. Implementation of the TF1 to Stage 2 hot wire acquisition might lead to actual bleed slot exit response whereas the application of Eqn. (3.26) to Stage 2 pressure measurements gave the bleed exit velocity estimation simultaneously. Considering uncertainty assessments of the hot wire system and flow meter in a combined manner, the total relative uncertainty estimate of the bleed velocities obtained using TF1 ranged from 13% to 3.7% with increasing velocity.

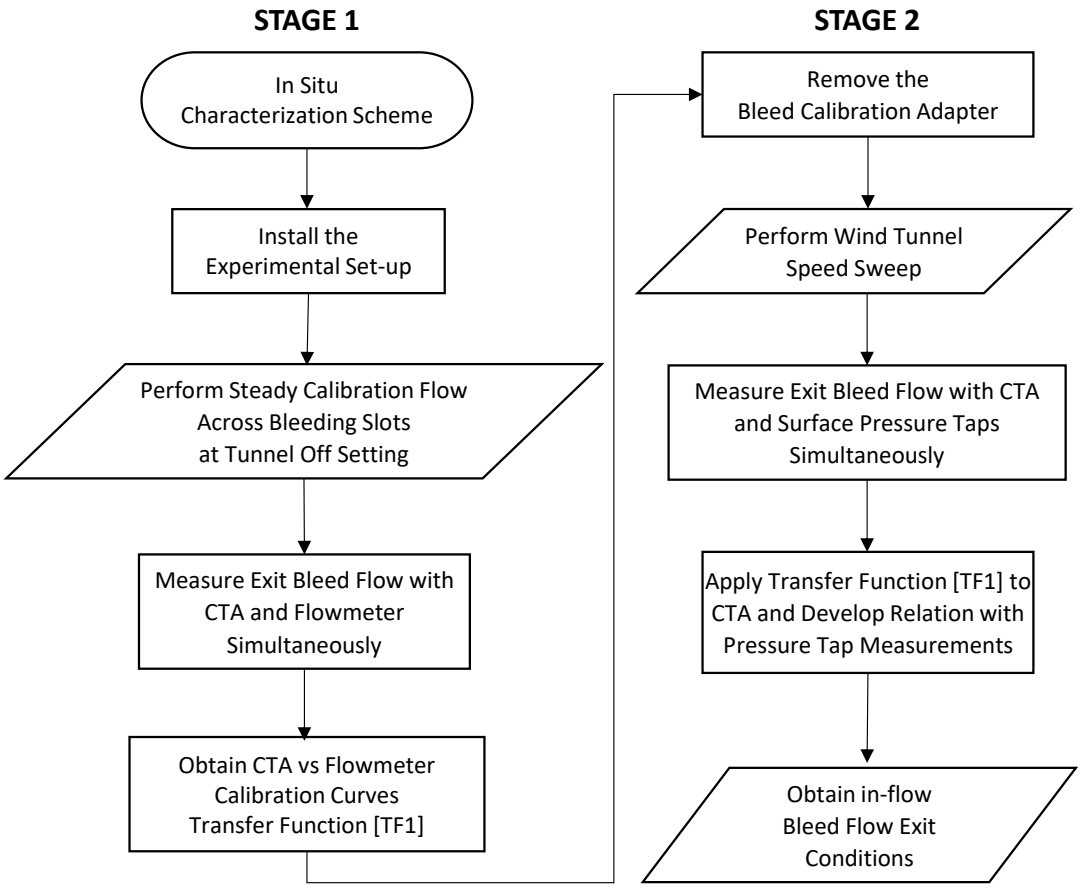

Figure 3.18: Bleed flow calibration process flow chart.

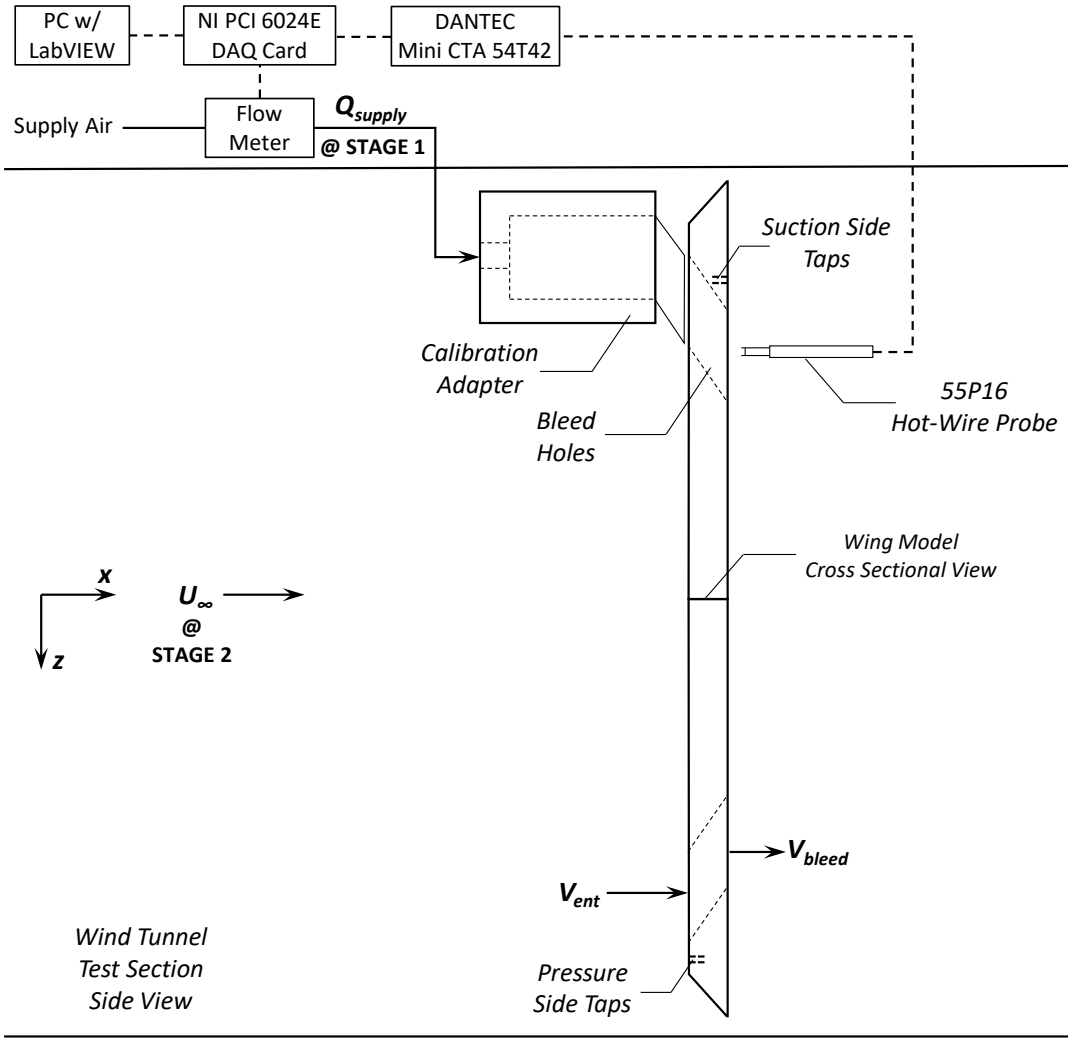

Figure 3.19: Schematic of the bleed flow estimation experimental setup (not to scale).

3.7.2 Passive Bleeding Flow Control with Nozzle Type Slots

The experiments for passive bleeding flow control were performed at a Reynolds number range of $3.5 \times 10^4 \leq Re \leq 1 \times 10^5$, calculated based on the chord length c of the wing models with a corresponding freestream velocity range of $4.4\,\text{m/s} \leq U_\infty \leq 12.5\,\text{m/s}$. In addition to the base wing design with no passive flow control applied, four different delta wing models with a $\Lambda = 45^\circ$ sweep angle and sharp edges beveled on the windward side with a bevel angle of 45° were tested. All wing models had the same principal dimensions as the baseline wing model. For the proposed

nozzle bleed slot concept, four different wings were designed and manufactured. Figure 3.20 demonstrates the details of the nozzle bleed wing geometry such that part (a) illustrates the isometric view of the entire wing including the bleed slot and axis definition on a plane A-A positioned parallel to the leading edge, and part (b) illustrates the details of the bleed slot geometry from pressure and suction side views along with the A-A cross-sectional view. The dimension designation defines the slot length on the pressure side l_p, slot length on the suction side l_s, slot end diameter and thickness d and w, hole spacing on the pressure side s_p, contraction ratio CR, forward back angle θ and rear back angle θ'. Axes for bleed slot orientations are designated such that the y' axis is parallel to the leading edge and the z' axis is normal to the wing surface. Bleed slots are positioned parallel to the leading edges, with five on each half. As discussed in the introduction, Çelik et al. [10] introduced possible leading edge bleed slot geometry orientations. In the current work, the back bleed concept is utilized for the bleed flow direction orientation, and the slot contraction is achieved by defining forward and rear back angles θ and θ' respectively.

Nozzle bleed wings were designated according to their slot dimensions and contraction ratios. For comparison purposes, the back bleed wing B18 from Çelik et al. [10] was also studied. Considering the dimension designation, nozzle bleed wings were divided into two types, namely narrow nozzle bleed wings and wide nozzle bleed wings, based on their thickness values. For narrow nozzle bleed wings, two models were designed and tested: "Nozzle Bleed Wing Narrow CR050 Fwd" and "Nozzle Bleed Wing Narrow CR050 Rear," both with a thickness value of $t = 3\,\text{mm}$. For both narrow wings, the contraction ratio was kept the same at CR = 1:0.5, achieved by varying the rear and forward back angles, respectively. Additionally, the bleeding dimensions on the pressure side were kept the same as those of the back bleed wing B18. The forward designation indicates that the forward back angle of the bleeding slot was kept the same as the back bleed B18 at $\theta = 18^\circ$, while the rear designation indicates that the rear back angle of the bleeding slot was kept the same as the back bleed B18 at $\theta' = 18^\circ$. For wide nozzle bleed wings, the thickness value was selected as $t = 4\,\text{mm}$, and two different contraction ratios were tested: CR = 1:0.5 and CR = 1:0.75, named "Nozzle Bleed Wing Wide CR050" and "Nozzle Bleed Wing Wide CR075," respectively. The contraction ratio was varied by changing the rear back

angle θ'.

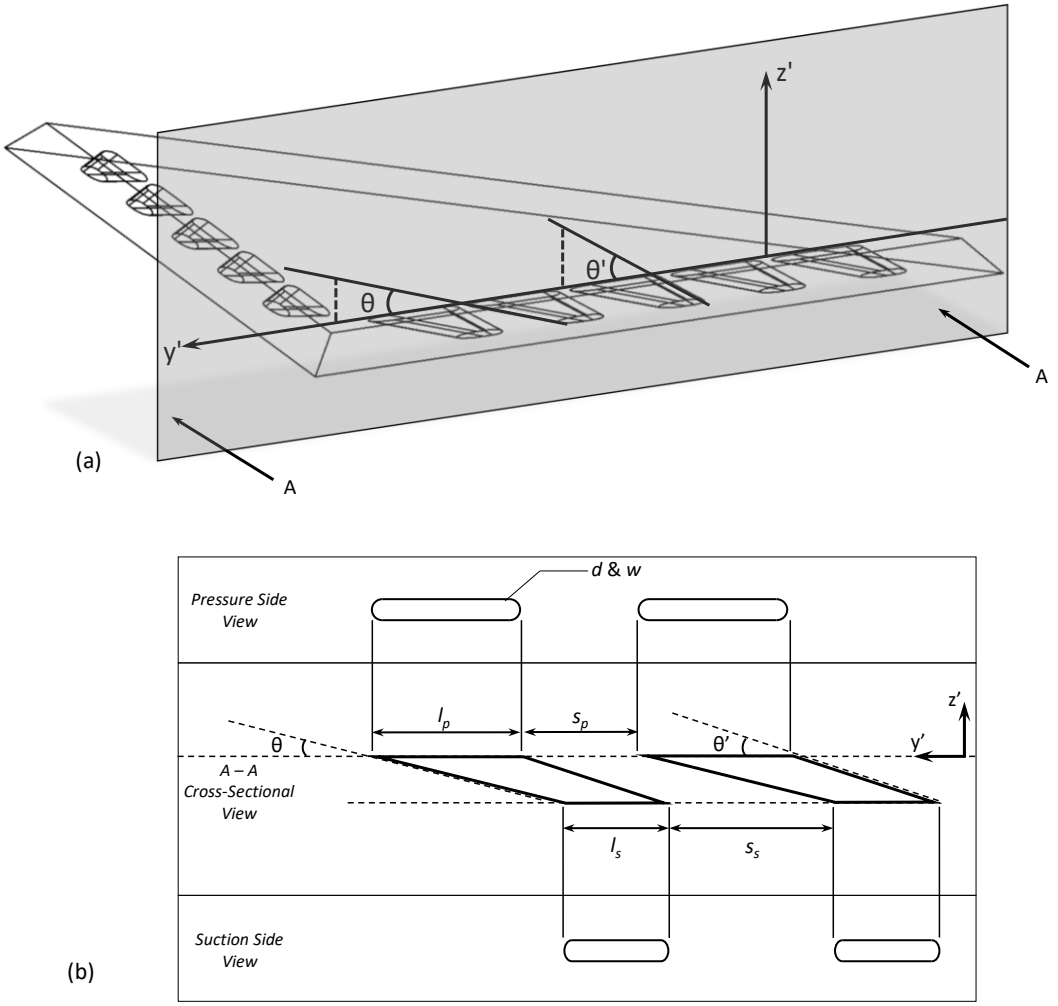

Figure 3.20: Schematic representation of the nozzle bleed geometry design: (a) wing geometry and bleed slot plane definition, (b) nozzle bleed slots dimension designation.

Table 3.7 summarizes the values for the bleed slot dimensions on the pressure side, along with their corresponding values on the suction side as designated in Figure 3.20 (b) for all wing models. The Back Bleed 18 wing from Çelik et al. [10] was also used in the current study for force measurements to build a comprehensive comparison domain, in addition to the surface pressure and particle image velocimetry measurements previously documented. The bleed slot dimensions for the Back Bleed 18 wing are also given in Table 3.7. The surface and pressure side views, along with the isometric perspective, are demonstrated in Figure 3.21 for all five bleeding wings.

The schematic representations of the utilized measurement techniques, along with the measurement axes and planes, are illustrated in Figure 3.22, including (a) near-surface particle image velocimetry, (b) surface pressure measurements, and (c) force measurements.

Table 3.7: Nozzle bleed slot dimensions

	Nozzle Bleed Wing Narrow CR050 Forward	Nozzle Bleed Wing Narrow CR050 Rear	Nozzle Bleed Wing Wide CR050	Nozzle Bleed Wing Wide CR075	Back Bleed Wing B18 [33]
Hole Length Pressure Side l_p [mm]	21	21	25	25	21
Hole Length Suction Side l_s [mm]	10	10	12.5	18.7	21
Hole End Dia. & Thickness d & w [mm]	3	3	4	4	3
Hole Spacing s_p [mm]	4	4	3	3	4
Contraction Ratio	1 : 0.5	1 : 0.5	1 : 0.5	1 : 0.75	1 : 1
Forward Back Angle θ [deg]	18	12.8	18	18	18
Rear Back Angle θ' [deg]	29.5	18	33.4	21.5	18

The pressure tabs were located on the suction sides at a non-dimensional chordwise distance of $x/C = 0.5$ across the spanwise direction from the symmetry plane towards the leading edges on all wing models. The baseline wing and bleeding wing models had 10 and 7 pressure taps on the half span, respectively. Maximum relative uncertainty values were estimated as 30%, 5.5%, and 2.5% for Reynolds numbers of Re $= 3.5 \times 10^4$, Re $= 7.5 \times 10^4$, and Re $= 1 \times 10^5$, respectively.

PIV experiments were performed for wide nozzle bleeding wings along with the baseline wing at a Reynolds number of Re $= 3.5 \times 10^4$. The angles of attack values α tested were $10°$, $16°$, $18°$, and $20°$. A sequence of 250 image pairs sampled at 15 Hz was used to obtain time-averaged contours of constant non-dimensional streamwise velocity $\langle u/U_\infty \rangle$, streamlines $\langle \Psi \rangle$, and contours of constant non-dimensional vorticity $\langle \omega_z C/U_\infty \rangle$, respectively. The maximum relative uncertainty estimated by the TSI Insight 4G software is below 10% for the performed measurements.

Aerodynamic force and moment measurements were performed for the angle of attack range $0° \leq \alpha \leq 30°$. The aerodynamic lift and drag forces and pitching moments were calculated using Eq. (2) and Eq. (3), for which the reference area A and reference length L were taken as the planform area of $0.0182\,\mathrm{m}^2$ and chord length $0.135\,\mathrm{m}$,

respectively. Measurements were sampled at 10 kHz for 15 seconds. The maximum uncertainties for aerodynamic coefficients C_D, C_L, and C_M are estimated as ± 0.05, ± 0.05, and ± 0.06, respectively.

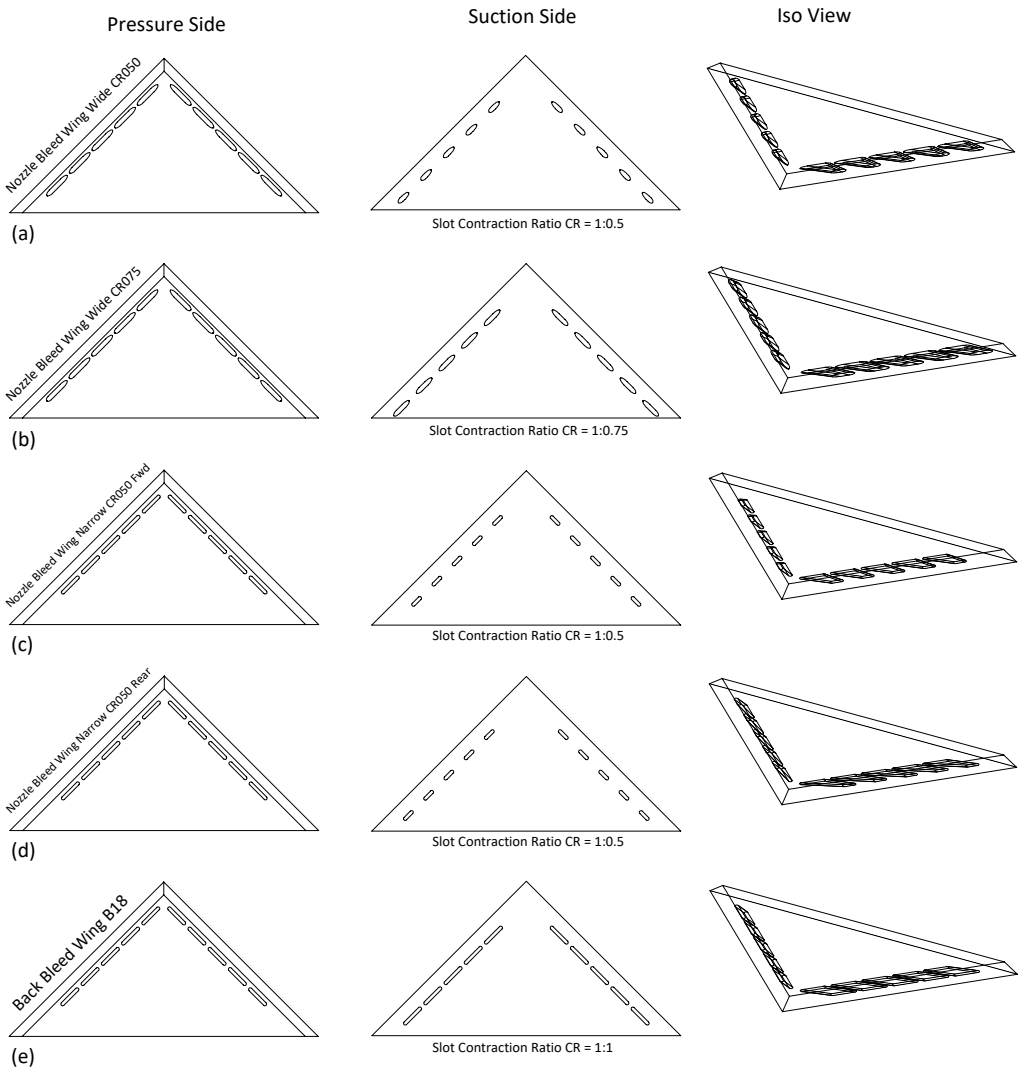

Figure 3.21: Design overview of the tested bleeding wing models, pressure side view, suction side view, and isometric view: (a) Nozzle bleed wing wide CR050, (b) Nozzle bleed wing wide CR075, (c) Nozzle bleed wing wide narrow CR050 Fwd, (d) Nozzle bleed wing narrow CR050 Rear, and (e) Back bleed 18 wing [10].

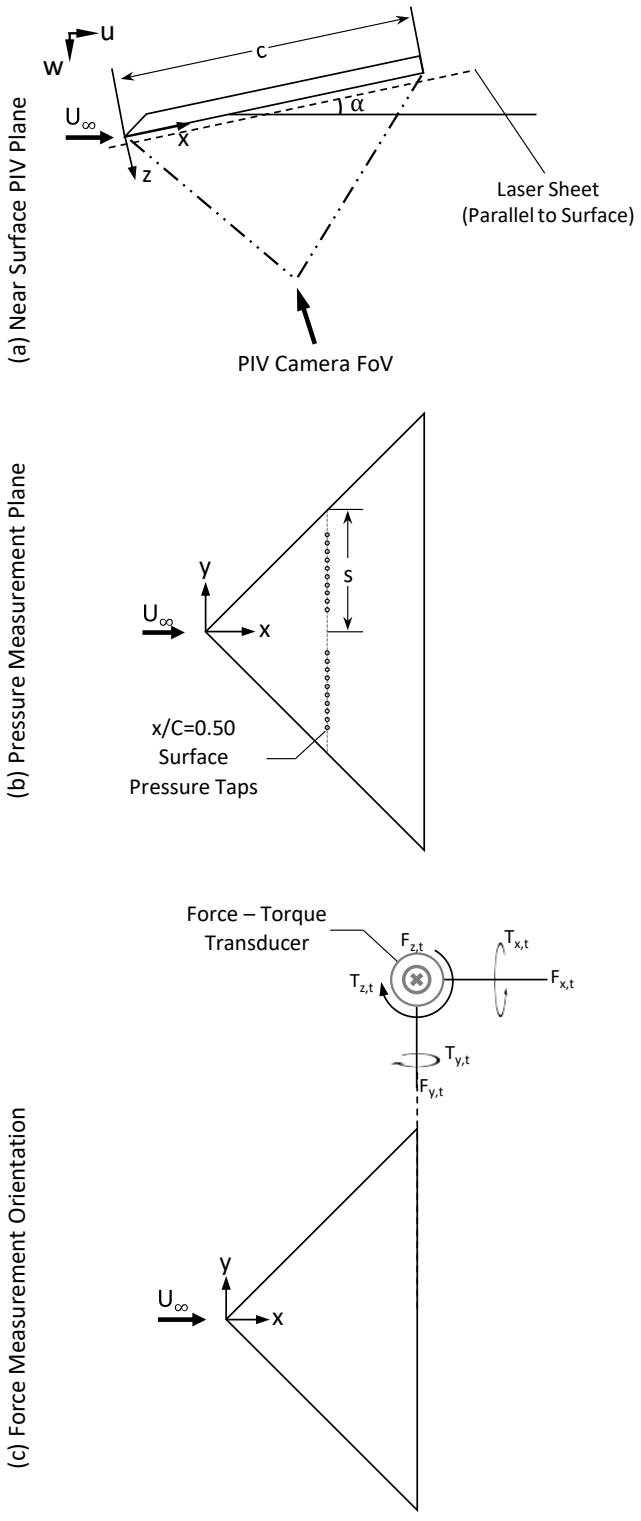

Figure 3.22: Schematic representation of the utilized measurement techniques: (a) Near surface PIV plane, (b) Pressure measurement plane, and (c) Force measurement orientation.

3.7.3 Comprehensive Characterization Approach for the Active Flow Control System

The performance assessment of the flow control system was conducted after a two-stage in-situ calibration scheme was completed. Figure 3.23 schematically represents the integration of the flow control system and in-situ calibration approach to the wind tunnel domain and the aerodynamic surface. During Stage 1, calibration curves were obtained by supplying pressurized air with the flow rate range of $0\,\text{l/min} \leq Q_{\text{supply}} \leq 18\,\text{l/min}$. In Stage 2, the response of all blowing holes to periodic blowing actuation was acquired individually for a square wave form excitation with control parameter settings including excitation frequency range of $f_c = 1\,\text{Hz} - 32\,\text{Hz}$, duty cycle values of $DC = 25\%$ and 50%, and momentum coefficients of $C_\mu = 1\% - 3\%$. All experiments were performed at the tunnel off setting.

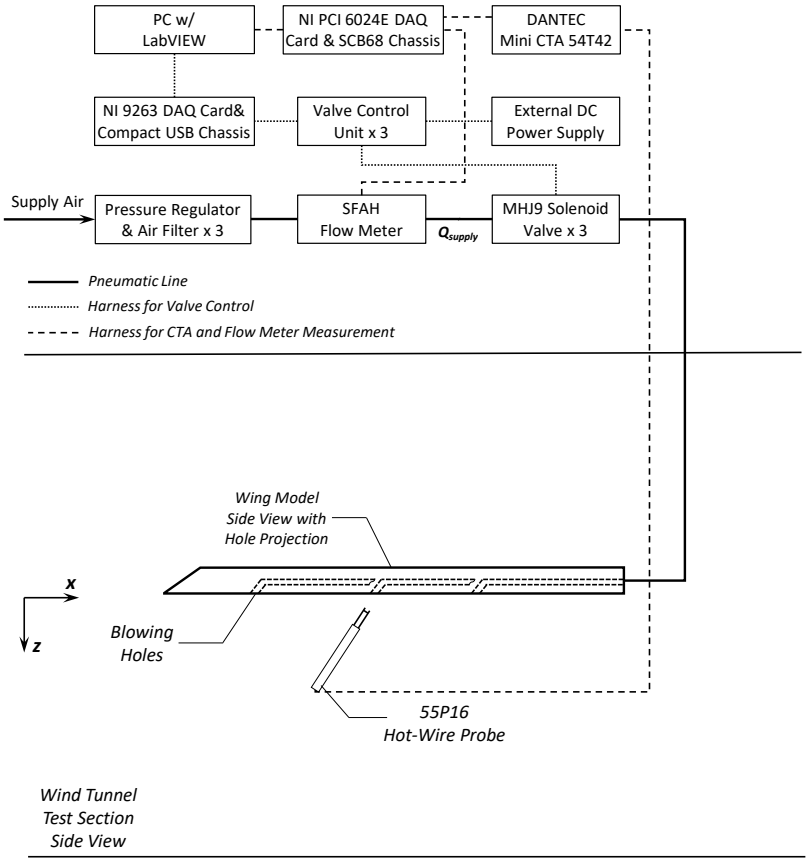

Figure 3.23: Schematic of the active flow control experimental setup: Pneumatic line, control and measurement systems, and aerodynamic surface (not to scale).

The in-house built flow control system consisted of three major branches, including pneumatic line for air supply, control and measurement systems, and aerodynamic surface domain that allows for the control of multiple blowing stations either individually or synchronously whose details were previously given in upper section 3.4. The approach is applied for the blowing model for which the aerodynamic investigation was performed afterwards. The isometric and side views of the wing model are given in Figure 3.24. A total of six blowing holes of 2 mm in diameter, three in each half of the wing model, were located 1 mm inboard of the leading edges at chordwise distances of $x/C = 0.2, 0.47,$ and 0.67 respectively. Blowing stations were also named forward, middle, and aft stations. The centerline axes of the blowing holes were parallel to the beveled leading-edge surfaces, leading to a jet angle of 45° from the wing surface. The pneumatic connection inlets of the blowing holes were located across the trailing edge of the wing model. The outlet port of each valve was manifolded for each station, aiming at a symmetrical supply on each side of the blowing stations.Such that, blowing holes #1 and #2, located at $x/C = 0.2$, are paired and connected to the first valve; blowing holes #3 and #4, located at $x/C = 0.47$, are paired and connected to the second valve; and blowing holes #5 and #6 are paired and connected to the third valve. All pneumatic tubing was kept the same in length up to the valve connection. Since the forward, middle, and aft blowing stations had different lengths from trailing edge input to blowing hole exits as can be inferred from the isometric drawing given in Figure 3.24, the tubing lengths after the valve output port were adjusted such that the total length from valves to blowing hole stations was similar.The breakdown of the piping sections are given in the following Table 3.8 and the blowing hole section division are shown in Figure 3.24. The inlet and outlet ports of the FESTO MHJ9 valves are equipped with 4 mm diameter pneumatic couplings. Tubing from the valve's outlet port to the pneumatic doubler junction was kept equal for each station, measuring 25 cm. From the junction to the wing connections, tubing lengths of 37 cm, 41 cm, and 44 cm were used to ensure the minimum required distance from the active flow control system for the forward, middle, and aft stations, respectively. Each pneumatic tube had a consistent cross-section with an outer diameter of 4 mm and an inner diameter of 2.7 mm. The tubing was connected to the wing model at the trailing edge via 4 mm diameter slots with a length of 15 mm, using a shrink-fit technique. At this connection point, the tubing cross-section reduces to 2 mm, a dimension that remains

consistent in the interior wing tubing, except at the bend sections. The distances from the trailing edge blowing hole connection inlet to the blowing hole exits were 10.3 cm, 6.5 cm, and 3.6 cm for the forward, middle, and aft holes, respectively. This arrangement results in a total distance of approximately ~72.5 cm from the valve outlet to the blowing exit surface for each station. Potential minor loss sources in the tubing for this setup may arise from several factors, including the valve-to-tubing connection, the pneumatic doubler junction (Y-type quick coupling), the diameter reduction from tubing to blowing hole (2.7 mm to 2 mm), and the bend towards the beveled surface.

The process flow chart is presented in Figure 3.25 as a complement to the schematic representation of the experimental approach given in Figure 3.23. The presented calibration scheme is in line with approaches used by Ternoy et al. [91] for the calibration of active blowing and suction flow control systems. In the current work, the whole process is performed for each blowing hole, such that their individual in-situ characteristics were used to derive the steady and unsteady blowing profiles.

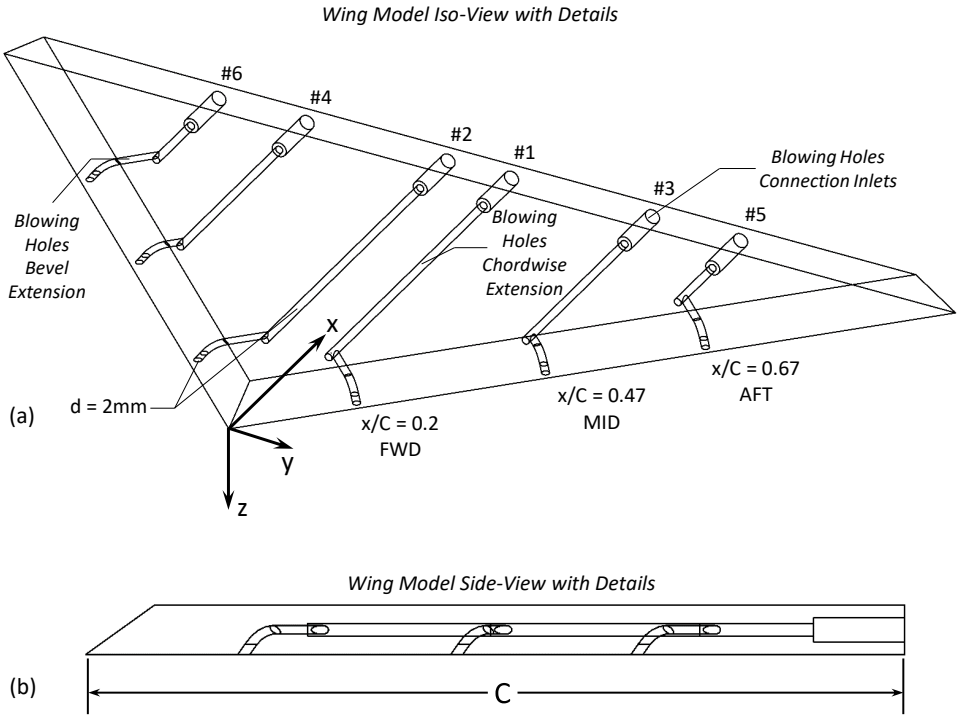

Figure 3.24: Schematic representation of the blowing wing geometry design: (a) Iso-view, (b) Side-view.

Table 3.8: Detailed dimensions of the blowing hole and tubing sections

STA	Hole #	Valve to Tubing Doubler [cm]	Tubing Doubler to Wing Connection [cm]	Blowing Hole Connection Inlet [cm]	Blowing Hole Chordwise Extension [cm]	Blowing Hole Bevel Extension [cm]	Total Blowing Piping Length [cm]
FWD	#1	25	37	1.5	8.2	2.1	72.3
	#2		37	1.5	8.2	2.1	72.3
MID	#3	25	41	1.5	5.1	1.4	72.5
	#4		41	1.5	5.1	1.4	72.5
AFT	#5	25	44	1.5	1.6	2	72.6
	#6		44	1.5	1.6	2	72.6

For the Stage 1 processes, supply air was directed towards the solenoid valves through the SFAH digital flow meter. Before integrating the digital flow meter, its calibration was confirmed using a mechanical rotameter type air flow meter. The flow rate data were acquired at a 200 Hz sampling rate for 10 seconds with an accuracy of 2% of the measured value and 1% FS (full scale = 0 l/min to 50 l/min). The steady calibration blowing velocity at the exit of the holes was measured using a Dantec 55P16 hot-wire probe and a 54T42 mini-CTA device anemometer. The periodic blowing leaves the leading edge of the wing model being parallel to the bevel surface. The hot-wire probe was positioned facing the center of the blowing jet in perpendicular orientation (in the jet direction) using a custom designed alignment stand at a 3 mm distance apart. The maximum combined uncertainty level estimated for the CTA voltage reading is around 0.67%, considering the experimental conditions, including linearization, A/D resolution, temperature variation, and ambient pressure variation. Flow meter and hot wire measurements in Stage 1 were simultaneously collected at 200 and 1000 Hz sampling rates, respectively, for a period of 10 seconds to construct the in-situ CTA vs Flowmeter calibration curves transfer functions, named TF1. The supply rate varied from $Q = 0$ l/min to 19 l/min corresponding to the blowing hole exit velocities 0 m/s $\leq U_{\text{blow,supply}} \leq 95$ m/s that was obtained by dividing the flow rate with the hole exit area A_h. The maximum Reynolds number for the blowing calibration supply based on the blowing exit diameter was around $Re_b = 4080$. The maximum uncertainty levels for blowing calibration supply velocities were estimated as ± 2 m/s to ± 4 m/s for the investigated calibration range.

For the Stage 2 processes, first, the desired momentum coefficient is adjusted at steady blowing conditions by using the digital flow meter while keeping the wing model and hot wire probe as they were in Stage 1 for the in-situ principle. In the current work, the sensitivity of the blowing velocity response to frequency and duty cycle parameters at a fixed regulator condition was investigated at a momentum coefficient value of $C_{\mu,\text{max}} = 1\%$ calculated based on Eqn. 3.28 where $\overline{U}_{\text{blow}}$ was the mean blowing velocity, A_h was the hole exit area, U_∞ was the freestream velocity, and A was the planform area.

$$C_{\mu,\text{max}} = \frac{\overline{U}_{\text{blow}}^2 A_h}{U_\infty^2 A} \tag{3.28}$$

This value was selected since it was planned to be used in actual wind tunnel aerodynamic measurements with Reynolds number of $Re = 9 \times 10^5$ and corresponding freestream velocity of $U_\infty = 11.8\,\text{m/s}$. In addition, sample spot check experiments were also conducted for three different momentum coefficients of $C_{\mu,\text{max}} = 1, 2,$ and 3% at a sample blowing hole #3. Second, the CTA response was recorded for the varying control frequency and duty cycle values, respectively. Both for the steady and periodic control signal, the output of the software was transmitted to the valve control module via the National Instrument NI-9263 analogue data acquisition card. A sample square wave control signal along with the CTA response obtained with the application of TF1 is illustrated in Figure 3.26. The control signal designation represents the parameters including signal amplitude A, signal period T, pulse width time T_w, and duty cycle obtained by dividing the pulse width time with the period $DC = T_w/T$. Sample CTA response, obtained as a result of the sample square signal actuation, represents the velocity distribution by time. The CTA response was analyzed using the pulsewidth function from MATLAB's Signal Processing Toolbox, specifically designed for bilevel waveforms. This function enables interpretation of the signal's upper and lower states, as well as identification of the mid-reference level. The mid-reference level serves as a threshold for determining transitions from low to high (or high to low), marking the start and end points of each pulse. By default, this threshold is set to 50% of the waveform's peak-to-peak amplitude. For a single pulse, the first mid-level crossing is designated as the "initial cross," while the second crossing is designated as the "final cross." In each subsequent pulse, the first mid-level

crossing is also referred to as the "next cross". The valve on state was investigated in three levels, namely mean blowing velocity $\overline{U}_{\text{blow}}$, and its lower and upper bounds determined based on the root mean square level of the valve active state distribution. The time series distribution obtained by the aforementioned process has been found quite in line with similar studies performed with similar valves in the aforementioned literature. Considering the combined uncertainty assessments of the hot wire system and flow meter, the total relative uncertainty of the bleed velocities obtained using TF1 ranged from 14% to 3.4% as the velocity increased.

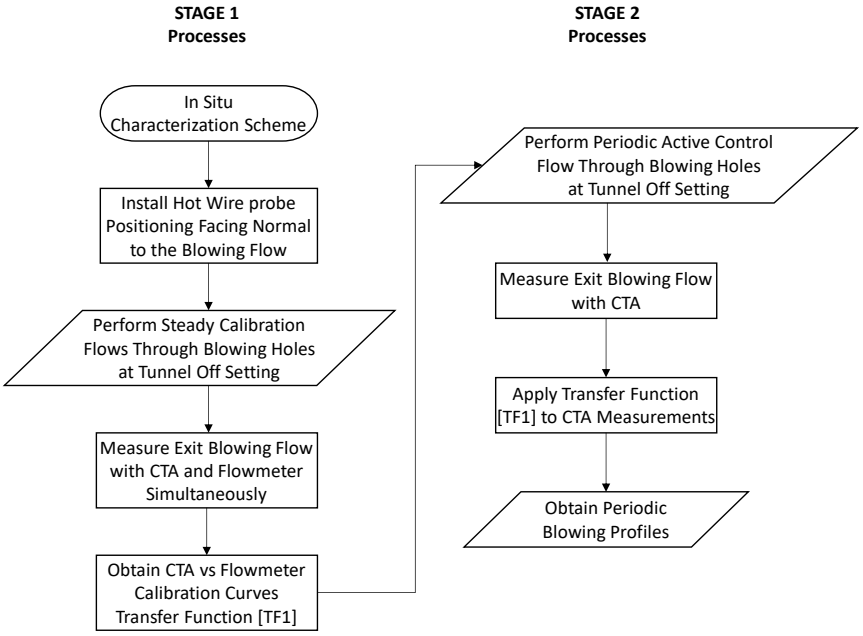

Figure 3.25: Active flow control in situ calibration process flow chart.

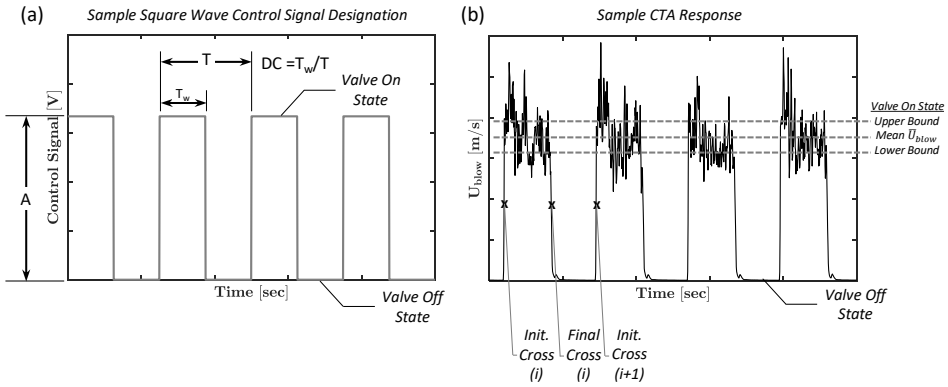

Figure 3.26: Sample square wave control signal and CTA response designation.

3.7.3.1 Burst Modulated Square Wave Generation and Response Measurement

Burst-modulated actuation offers the advantage of implementing distinct excitation frequencies in the actuation spectral content. A representative burst-modulated square wave signal is demonstrated in Figure 2.3. The resultant signal can be obtained by the multiplication of a carrier signal, which is a regular square wave signal, with another regular square wave signal named the modulating signal. Both the carrier and modulating signals are designated with individual frequency and duty cycle values, where T, f, and DC are distinguished with subscripts c and m, respectively. Modulating signals are typically used to burst the carrier signal by multiplying active and passive state implementations.

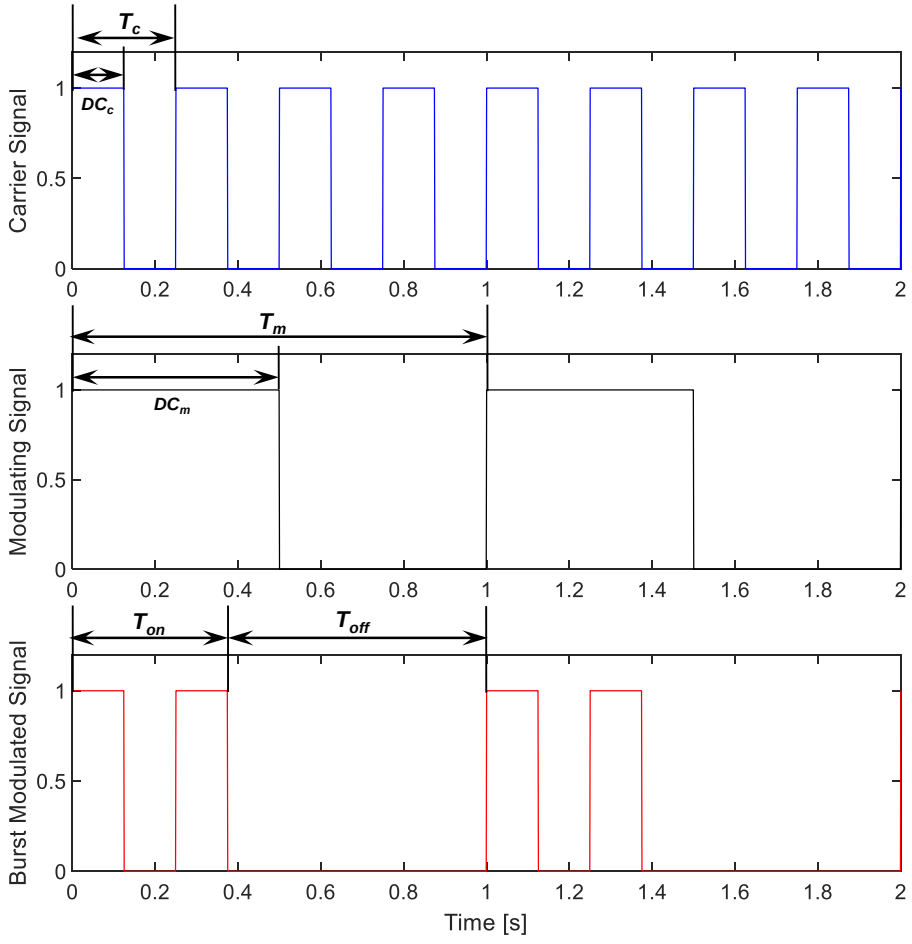

Figure 3.27: Representative burst modulated square wave signal generation as a function of time.

In the current study, the effect of burst-modulated blowing actuation on the flow structure over a non-slender delta wing was investigated in addition to regular square wave periodic signals. Prior to starting the aerodynamic measurements, sample burst-modulated blowing actuations were measured for each hole, following the same procedures described for regular square waves in Section 3.7.3. The carrier signal was tested with excitation frequencies of $f_c = [4, 8, 12, 16, 20, 24]$ Hz and commanded carrier duty cycle values of $DC_c = [25, 50]\%$, whereas the modulating signal was tested with frequencies of $f_m = [1, 3, 4]$ Hz and a commanded modulating duty cycle value of $DC_m = 50\%$.

Considering the size of the experimental matrix for burst-modulated signal hot-wire measurements, sample hot-wire measurement responses for two different blowing scenarios obtained from Hole #1 are represented in Figure 3.28. It is observed that burst-modulated signals can be effectively generated with the in-house active flow control system, and their responses can be measured using the same calibration procedure. A further system performance assessment has not been conducted since the characterization of the regular square wave signal was found to be quite satisfactory, and the calibration charts can be used to compute effective momentum coefficients for carrier frequency settings.

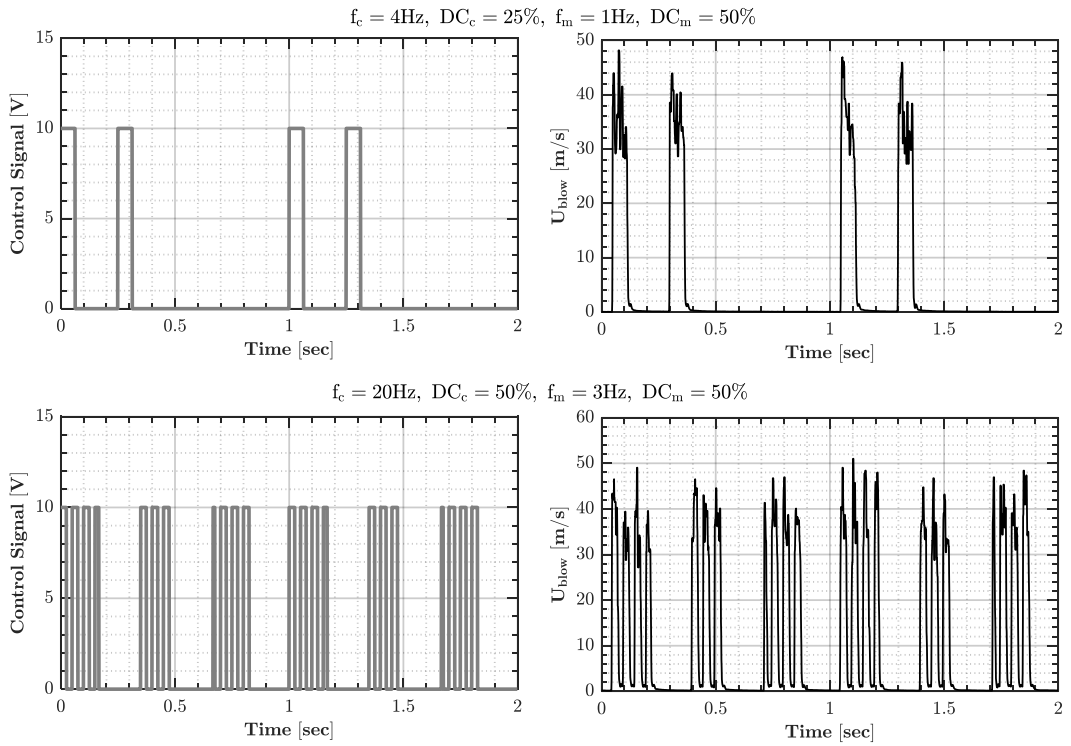

Figure 3.28: Sample burst modulated square wave control signal and CTA response measurements for #1 Blowing Hole: (a) $f_c = 4$ Hz, $DC_c = 25\%$ and $f_m = 1$ Hz, $DC_c = 50\%$, (b) $f_c = 20$ Hz, $DC_c = 50\%$ and $f_m = 3$ Hz, $DC_c = 50\%$.

3.7.4 Periodic Blowing Active Flow Control

The experiments for periodic blowing active flow control were performed at a Reynolds number range of $3.5 \times 10^4 \leq Re \leq 9 \times 10^4$, calculated based on the chord length c of the wing models with a corresponding freestream velocity range of 4.4 m/s $\leq U_\infty \leq$ 11 m/s. To investigate the effect of periodic blowing both surface pressure and aerodynamic force measurements were performed. The schematic representations of the utilized measurement techniques, along with the measurement axes and planes, are illustrated in Figure 3.29, including (a) surface pressure measurements, and (b) force measurements. A total 14 pressure tabs 7 in each half span were located on the suction sides at a non-dimensional chordwise distance of $x/C = 0.5$ across the spanwise direction from the symmetry plane towards the leading edges on the blowing wing.

In the sections 3.7.3 and Chapter 6, the active flow control system and its characterization were detailed, highlighting the individual system response of each blowing hole.

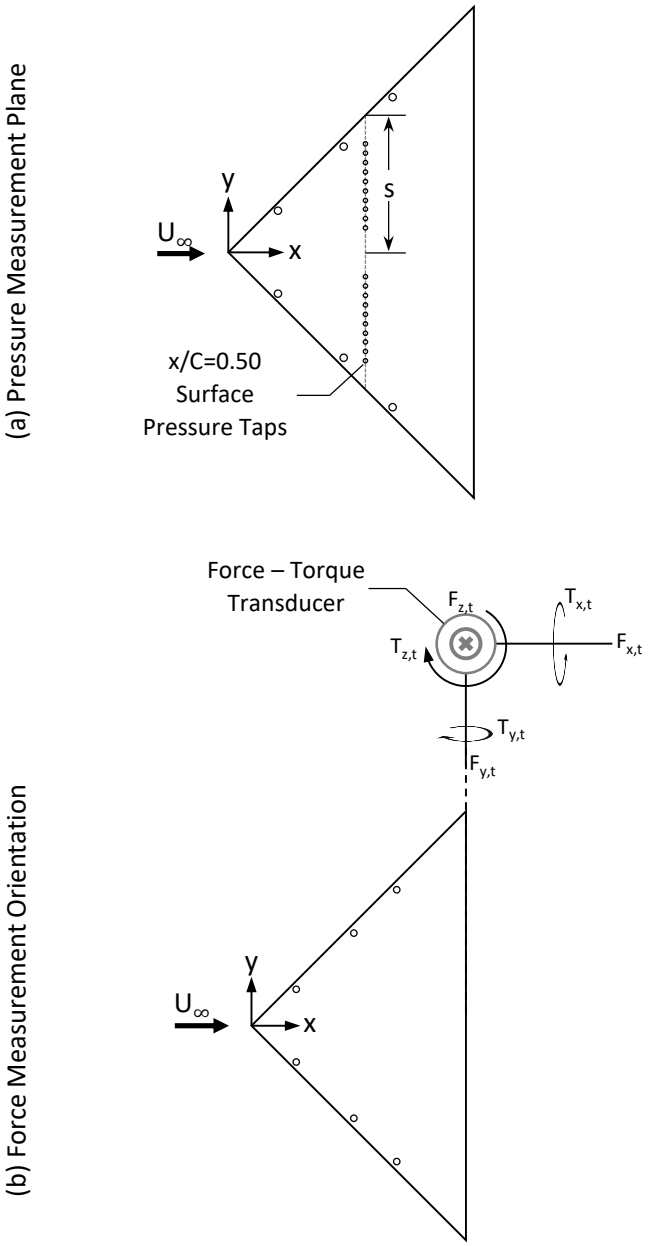

Figure 3.29: Schematic representation of the utilized measurement techniques: (a) Pressure measurement plane, and (b) Force measurement orientation.

Surface pressure measurements are performed for both wave forms at a Reynolds number range of $3.5 \times 10^4 \leq Re \leq 9 \times 10^4$ and $\alpha = 12°$, $\alpha = 16°$, $\alpha = 17°$,

and $\alpha = 21°$. For the regular square wave form, $f_c = [1:1:20, 24, 28, 32, 48, 64]$ Hz excitation frequencies are investigated at commanded duty cycle values of $DC = [25, 50]\%$. For the burst modulated square wave form, the carrier signal is tested with $f_c = [4, 8, 12, 16, 20, 24, 32, 48, 64]$ Hz excitation frequencies with commanded carrier duty cycle values of $DC_c = [25, 50]\%$, whereas the modulating signal is tested with $f_m = [1, 3, 4]$ Hz frequency with a commanded modulating duty cycle value of $DC_m = 50\%$. For both regular and burst modulated signal types, a maximum momentum coefficient setting of $C_{\mu,\text{max}} = 1\%$ is used. Maximum relative uncertainty values were estimated as 2.7% at Reynolds numbers of Re $= 9 \times 10^4$, respectively.

Considering the context of the experimental matrix, aerodynamic force measurements are performed for the selected configurations with the same commanded momentum coefficient setting, for which ultimate benefit was expected based on surface pressure measurements. For the regular square wave form, $f_c = [20, 28, 32, 48]$ Hz excitation frequencies are investigated at commanded duty cycle values of $DC = [25, 50]\%$. For the burst modulated square wave form, the carrier signal is tested with $f_c = [20, 32, 48]$ Hz excitation frequencies with commanded carrier duty cycle values of $DC_c = 50\%$, whereas the modulating signal is tested with $f_m = [3, 4]$ Hz frequencies with a commanded modulating duty cycle value of $DC_m = 50\%$. The maximum uncertainties for aerodynamic coefficients C_D, C_L, and C_M are estimated as ± 0.05, ± 0.05, and ± 0.06, respectively.

CHAPTER 4

METHOD DEVELOPMENT FOR ESTIMATION OF BLEED MOMENTUM COEFFICIENT USING SURFACE PRESSURE MEASUREMENTS AND IN SITU HOT WIRE CALIBRATION

Recently, as a passive flow control method, the bleeding technique, which allows flow from upstream towards the suction side via interior passages, has been utilized on non-slender delta wing planforms. Effective geometries can enhance the flow field characteristics. To quantify the effect of this flow control, estimating the momentum induced by the technique is crucial, in addition to quantifying aerodynamic benefits. In the current part of the thesis, a passive bleeding momentum coefficient estimation method is developed and presented based on surface pressure measurements, utilizing the Bernoulli equation and loss coefficient for a 45° swept non-slender delta wing. To characterize the presented technique, in-situ hot wire measurements were performed to extract the pressure loss coefficient across the bleed slot. Results indicate that the proposed approach can be used to compute the bleeding momentum, with potential advancements leading to an important control parameter for active bleeding systems in various flow regimes.

4.1 Results and Discussions

4.1.1 Stage 1: In-Situ Calibration Results

In situ flow calibration across a sample bleed slot is conducted for a supply flow rate ranging from 1.5 l/min to 50 l/min when the tunnel is off. Figure 4.1 shows the hot wire probe response with respect to the supply, thus the bleed slot average exit veloc-

ity. The vertical axis represents the CTA voltage value E and the bottom horizontal axis represents the supply rate Q. The corresponding bleed slot exit average velocity obtained by dividing the supply flow rate Q with the bleed slot area A_b is given at the top horizontal axis. Considering typical hot wire responses to linear velocity variations, the supply rate was kept frequent at lower supply rates and then extended for increasing values. Square markers represent average values of each increment where a fifth order fit can be employed over the entire span, which is a well-known typical polynomial CTA response and demonstrated as the hot wire response transfer function TF1 in Eqn. (4.1). Polynomial fit usually offers more accurate estimation than power-law curves with linearization errors often less than 1% as suggested by the manufacturer [96]. However, such curves may oscillate if the velocity is outside the calibration velocity range. Thus in the current Stage 1 measurements two issues are aimed: first verifying the response of the hot wire probe for in-situ positioning, and then assuring an adequate calibration curve range.

$$\begin{aligned} \text{TF1} \rightarrow V_{\text{bleed,supply}} = &-2760 \cdot E^5 + 2.09 \times 10^4 \cdot E^4 - 6.297 \times 10^4 \cdot E^3 \\ &+ 9.447 \times 10^4 \cdot E^2 - 7.06 \times 10^4 \cdot E + 2.103 \times 10^4 \end{aligned} \tag{4.1}$$

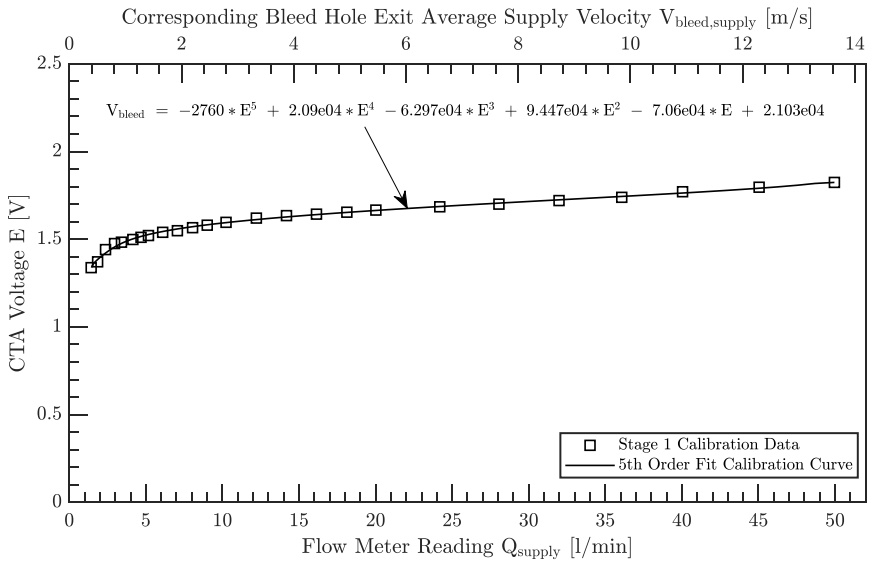

Figure 4.1: Stage 1, steady bleed supply vs. CTA voltage calibration curve: Flow meter reading (bottom X-axis), corresponding bleed slot exit average supply velocity (top X-axis).

4.1.2 Stage 2: Comparison of Synchronous Surface-Pressure and CTA Measurements

In the second stage of the bleed slot flow characterization scheme, the bleed adapter is removed, and the wind tunnel is operated for a freestream range of $2.4 \leq U_\infty \leq 12.1$ m/s. Considering the layout of the bleeding slots, which are in the vicinity of the leading edges, it was expected that CTA measurements might be prone to flow passing and separating through the leading edges. To minimize such interference during this calibration phase with the freestream, the wing model was positioned perpendicular to the freestream during Stage 2 measurements as detailed in the methodology part. The expected drawback of such an orientation might be the overestimation of the bleed velocity due to stagnation of the freestream. Before starting Stage 2 experiments, the CTA response to the freestream with all bleeding slots covered was investigated when the wind tunnel was operating at $U_\infty = 8.9$ m/s. The average voltage acquired during the slot covered case was around $E_{\text{covered}} = 1.565$ V, while the slot open case was around $E_{\text{open}} = 1.655$ V. When TF1 is applied to acquired voltages, the velocity measured during slot covered and open cases are found as 2.06 and 5.04 m/s respectively, yielding a 2.5 times difference.

The results of the surface pressure measurements along with the CTA response in relation to the bleed slot entrance velocity are given in Figure 4.2. In the upper part (a), the pressure difference between the bleed slot inlet and outlet is shown. In the bottom part, the estimated bleed slot exit velocity and the momentum coefficient distributions based on both measurements are presented in subplots (b) and (c) with associated uncertainty error bars respectively. After implementing the pressure difference into Eqn. (3.26) and (3.27), the trend of the estimated bleed exit velocity V_{bleed} exhibits a linear variation ranging from 3.4 m/s to 17 m/s, representing a strong acceleration across the slot. Whereas the accompanying momentum coefficient shows a constant trend at the order of 0.66% as a result of the observed linear response. As discussed in the methodology part, bleed velocity uncertainty estimate does not interfere significantly with the distribution, whereas its impact on momentum coefficient estimation appears to be considerable. Since the momentum coefficient equation is in the non-dimensional form utilizing the square of the velocities, uncertainty estimates

were propagated at lower entrance velocities and decreased with increasing velocity. When the CTA response with TF1 is investigated, which can be considered as the actual local velocity measurement, estimated bleed velocity is ranging between 0.8 m/s to 6 m/s, and the corresponding momentum coefficient is between 0.032 to 0.082%. Considering the magnitude of the presented bleed velocity and respective momentum coefficient estimated by TF1, error bars do not occupy an observable portion; however, relative uncertainty values are similar to those obtained with pressure difference as discussed in the methodology part. Observed differences between the two approaches suggested discussing momentum losses across bleeding slots due to possible phenomena including frictional loss, direction change as per the bleed slot geometry orientation, interaction of bleed flow with separated leading-edge flow, and possible flow reversal across the bleeding slots. To further evaluate the results, estimated bleed velocities are replotted with associated uncertainty error bars in a cross plot given in the upper part (a) of Figure 4.3, where the vertical axis shows the hot wire measurement, and the horizontal axis shows the pressure measurement based estimation. A parabolic fit can be embedded into the distribution, suggesting fitting a possible total loss coefficient k_{across} that can be originated from the extended form of the Bernoulli principle as demonstrated in Eqn. (4.2). Here, surface pressure measurements at the inlet and outlet of the bleeding slots are used to model the across pressure loss, and bleed exit velocity is taken as actual results obtained by hot wire measurements. The only unknown presented here, k_{across}, can be found via the reordered form given in Eqn. (4.3). Estimated total loss coefficient as a function of the entrance velocity is given with associated uncertainty estimate error bars in the bottom part (b) of Figure 4.3. The observed trend represents consistent behavior with increasing entrance velocity and shows a very slight decrease from 1.9 to 1.7. Similarly, pressure loss coefficient k_{across} in Eqn. (4.3) is in the non-dimensional form utilizing the square of the velocities as well as the pressure difference, relative uncertainty estimates were propagated at lower entrance velocities and decreased with increasing velocity corresponding to a range of 28% to 2%.

$$\frac{p_p}{\rho g} + \frac{V_{\text{ent}}^2}{2g} = \frac{p_s}{\rho g} + \frac{V_{\text{bleed}}^2}{2g} + k_{\text{across}} \frac{V_{\text{ent}}^2}{2g} \tag{4.2}$$

$$k_{\text{across}} = \left(\frac{\Delta p}{\rho g} + \frac{V_{\text{ent}}^2 - V_{\text{bleed,hw}}^2}{2g} \right) \cdot \frac{2g}{V_{\text{ent}}^2} \tag{4.3}$$

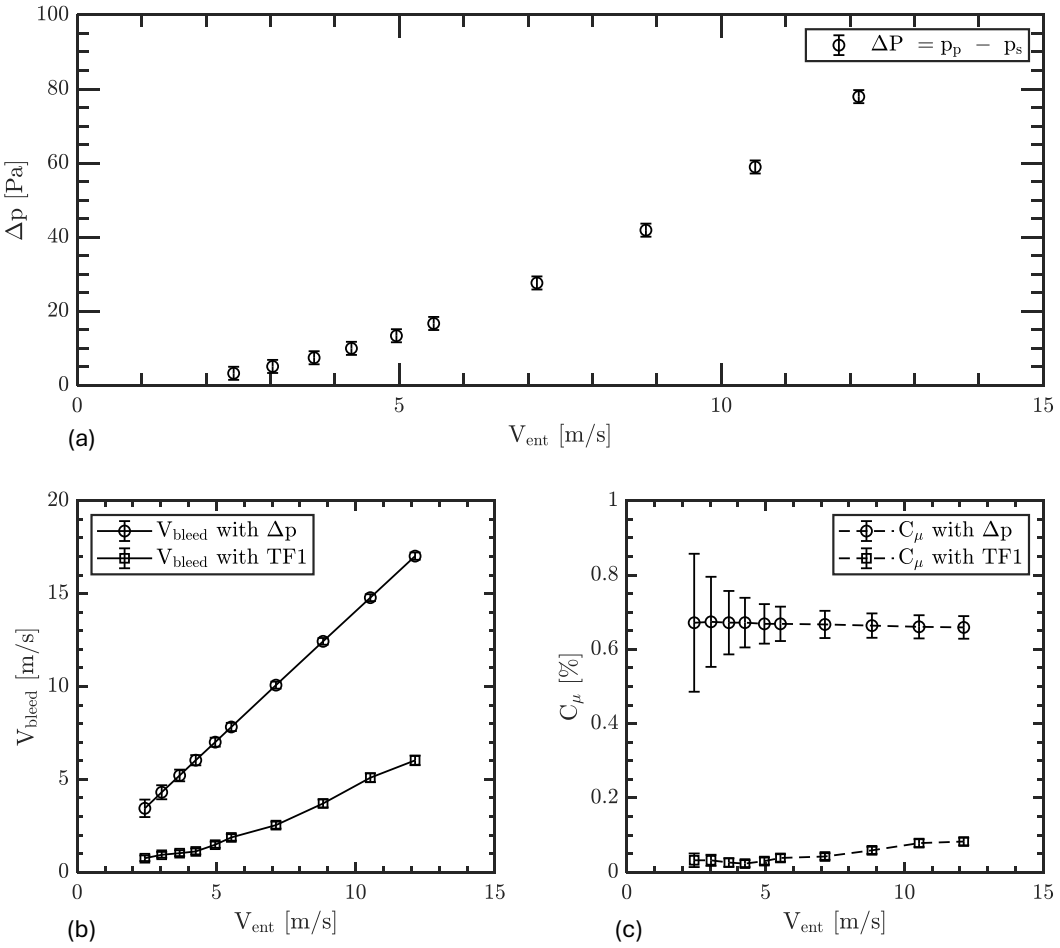

Figure 4.2: Stage 2, tunnel on measurements: (a) Pressure difference across the bleed hole with respect to bleed entrance velocity $V_{ent} = U_\infty$, $(0.9 \times 10^4 \leq \text{Re} \leq 1.1 \times 10^5)$, (b) Bleed velocity V_{bleed}, and (c) Momentum coefficient estimation C_μ, pressure difference Δp (circle markers), and hot wire TF1 (square markers).

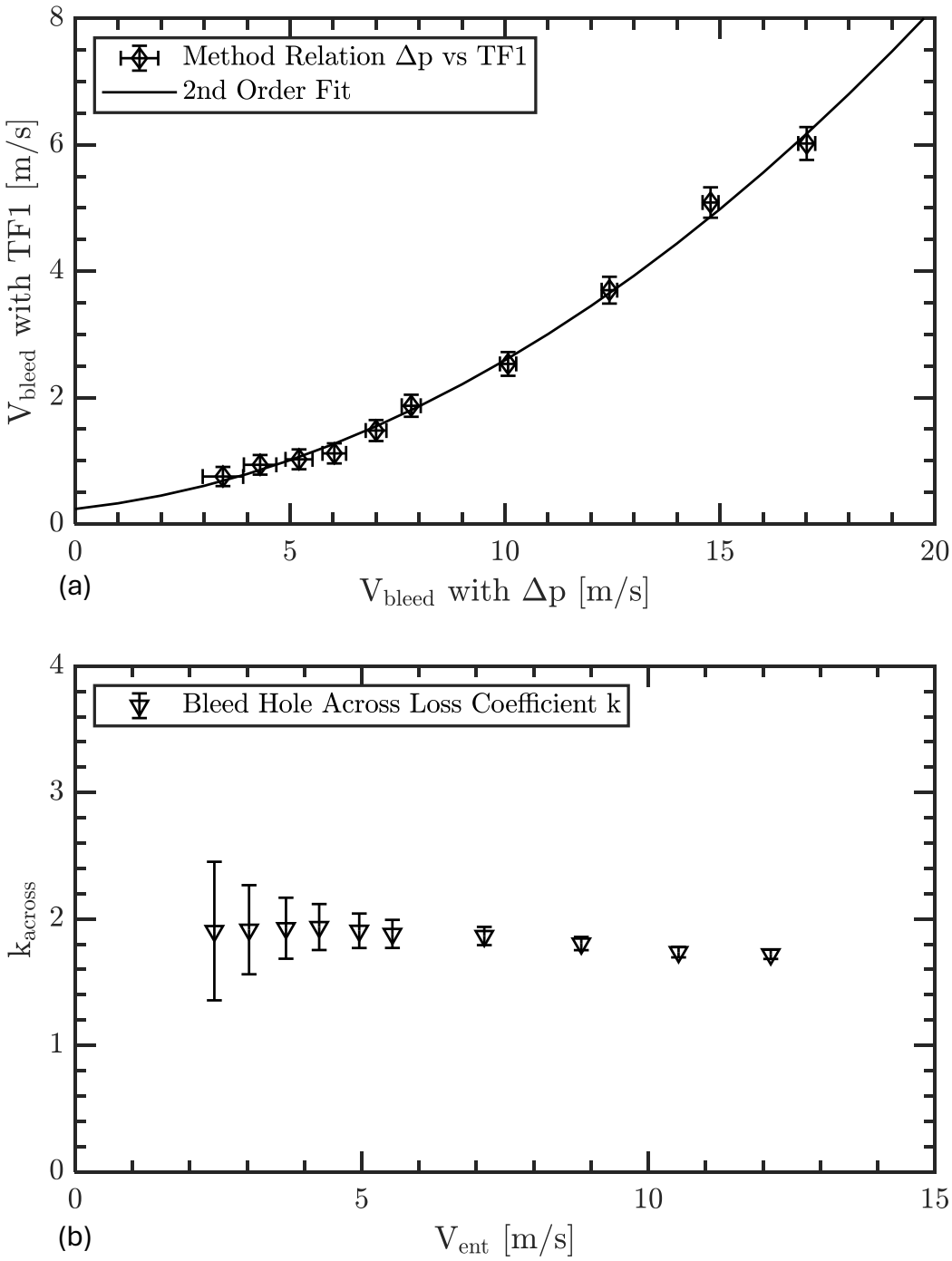

Figure 4.3: (a) Bleed velocity estimation method comparison and relation, (b) Adapted bleed slot across loss coefficient k_{across} based on the extended Bernoulli equation with respect to bleed entrance velocity $V_{\text{ent}} = U_\infty$ ($0.9 \times 10^4 \leq \text{Re} \leq 1.1 \times 10^5$)

4.1.3 Implementation of the Characterization Scheme Results to Wind Tunnel Measurements

To characterize the response of the bleed surface pressure measurement taps for actual wind tunnel measurements, a representative experiment set is performed at Reynolds number of $Re = 1 \times 10^5$ for three different angles of attack $\alpha = 16°$, $\alpha = 18°$, and $\alpha = 20°$, where the wing offers the ultimate lift performance around that region, namely linear maximum, pre-stall, and stall regimes, which is known based on previous studies [10], [53] and ongoing research. Surface pressure measurements are conducted for all five bleeding slots simultaneously. Results of the bleed momentum estimation implementing the presented characterization scheme are presented in comparison to the baseline model given in Eqn. 3.26. Characterization model estimations were obtained using Eqn. 4.2 with an average k_{across} value of 1.8 as per the aforementioned results. For both models, entrance velocity V_{ent} was obtained by performing axis transformation as per the orientation of bleeding slots to the freestream with sweep angle $\Lambda = 45°$ such that

$$V_{\text{ent}} = U_\infty(\cos\Lambda) \tag{4.4}$$

Figure 4.4 is constructed using three subplots where horizontal axes represent bleed slot stations 1 – 5 from the apex through the trailing edge. The upper part (a) represents the across slot pressure difference coefficient ΔC_p obtained using Eqn. (3.2) along with the associated uncertainty error bars. The bottom left part (b) represents the bleed velocity estimations, and the bottom right part (c) represents the corresponding momentum coefficient obtained using bleed velocity from part (b) and Eqn. (**??**). Angles of attack $\alpha = 16°$, $\alpha = 18°$, and $\alpha = 20°$ are represented with plus "+", circle "o", and square "□" markers respectively, whereas the baseline model and modified models are given with solid and centerlines respectively.

Considering the pressure difference coefficient distribution for $16°$ angle of attack, where the wing is known to be in the linear regime of the lift and angle of attack distribution, there exists an increasing trend towards the last bleed station, demonstrating that the bleed slot region momentum transfer capability might be increased from the

apex to the trailing edge with a similar geometry. When the angle of attack is further increased to 18° and 20°, the pressure difference increases for the first four bleeding stations, beyond which no increase is observed.

When the results of bleed velocity thus the momentum estimations are investigated, the effect of the characterization model with the loss coefficient is quite evident and significantly alters the estimation. In the baseline model, the rate of the change of bleeding velocity from the wing apex to the trailing edge is slightly limited compared to the modified characterization model. When momentum coefficient change behavior is considered, both models represent similar trend-wise behavior. As per the distribution of the pressure coefficient results at $\alpha = 16^\circ$, the bleeding momentum increases towards the last bleeding station where the bleeding velocity estimated by the modified characterization model is $V_{\text{bleed},5} = 12.7$ m/s. The estimated momentum coefficient is $C_{\mu,5} = 0.37\%$, which is approximately 55% of the value estimated by the baseline model. Considering the results for angles of attack $\alpha = 18^\circ$ and $\alpha = 20^\circ$, a slight saturation of the bleeding momentum is observed beyond the fourth bleeding station, where discussions were made for pressure coefficients. This trend is believed to be observed since the wing is almost at the pre-stall and stall onset. The aforementioned angles of attack region is selected to evaluate the performance and response of the surface pressure measurements. Uncertainty estimates for bleed velocity calculations ranged from ± 0.25 to 0.20 m/s and ± 0.47 to 0.25 m/s for baseline and modified methods respectively, which does not yield an interference between both methods. Similarly, for momentum coefficient uncertainty estimates are ranging from 0.047% to 0.06% and 0.03% to 0.04% respectively. As the above discussions evidence, surface pressure taps can capture the bleed slot behavior at transitional aerodynamic regimes.

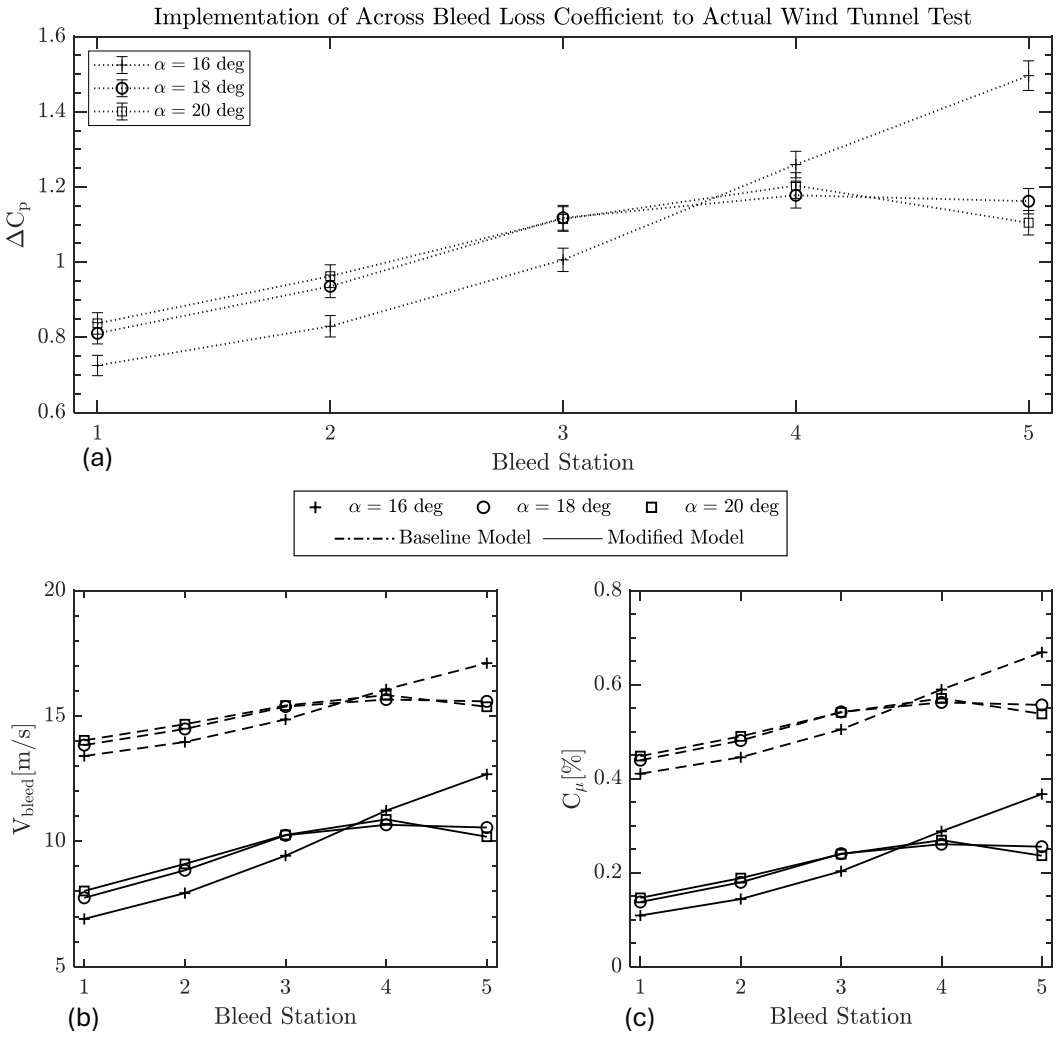

Figure 4.4: Implementation of the presented method to actual wind tunnel tests at Re $= 1.1 \times 10^5$ and $\alpha = 16°$, $\alpha = 18°$, $\alpha = 20°$: (a) Pressure difference across the bleed slots 1–5, (b) Estimated bleed velocity V_{bleed}, baseline model, and modified model using the extended Bernoulli equation with $k_{\text{across}} \sim 1.8$, (c) Corresponding bleed momentum coefficients.

4.2 Conclusions

The current chapter presents a method development scheme for the estimation of the bleed momentum coefficient with the aid of surface pressure measurements calibrated

using in-situ hot wire measurements. First, a two-stage characterization scheme experiment is performed, namely, Stage 1: tunnel off bleed slot exit velocity calibrations and Stage 2: wind tunnel operating pressure tap calibration measurements. Once the relation is developed between the surface pressure tap responses and hot wire measurements, a total loss coefficient is estimated, and a systematic behavior is observed. Then, to facilitate the performance of the surface pressure measurements with the proposed calibration scheme, a set of representative low-speed wind tunnel measurements is performed at $Re = 1 \times 10^5$ for three different angles of attack $\alpha = 16°$, $\alpha = 18°$, and $\alpha = 20°$. Considering the combined assessments of the calibration effort and wind tunnel measurements, the principal findings are as follows:

- As the first step, a typical hot wire response is obtained for the well-known bleed slot exit via supply flow in-still air environment, which is named as the first transfer function TF1 to be used in simultaneous pressure tap and hot wire comparison and characterization steps.

- The bleed exit velocity obtained with surface pressure measurement and Eqn. (3.26) during Stage 2 of the characterization scheme exhibits a linear behavior with increasing upstream velocity and is seen to be overestimating the exit conditions compared to the hot wire response, which can be considered as the local actual measurements. The systematic parabolic relation between the two estimation schemes of the bleed exit velocity suggests computing a correction loss coefficient where a consistent across loss behavior is observed for the tested calibration range.

- When the average of the across slot loss coefficient is used in actual wind tunnel tests, it is seen that surface pressure taps can estimate the bleed slot flow responses at different aerodynamic regimes in terms of the attack angle including the linear maximum lift and stall onset regions.

To conclude, the results suggest that surface pressure taps located in proximity to the bleeding slot inlets and outlets on a non-slender delta wing can be effectively used to estimate the across slot momentum coefficients once a controlled calibration scheme is applied. The systematic approach and observed behavior mentioned above

are believed to be helpful in characterizing the effectiveness of passive bleeding flow control in relation to the measured aerodynamic favor. In addition, all the procedures presented above can be useful in designing closed-loop flow control schemes based on passive bleeding technique effectiveness charts and on-off valve action with proper pressure sensor relations at different flow regimes.

CHAPTER 5

CONTROL OF FLOW STRUCTURES ON A NONSLENDER DELTA WING UTILIZING NOZZLE TYPE BLEEDING SLOTS

In the current chapter, results for the effect of an innovative nozzle-type bleeding geometry design, aimed at increasing the bleeding momentum on the flow structure over a 45° swept delta wing, are presented. The experiments are conducted in a low-speed wind tunnel performing surface pressure measurements, Particle Image Velocimetry (PIV) measurements, and aerodynamic force measurements. The suggested bleed geometry is defined by the contraction ratio of the bleed inlet and outlet areas as well as their slot thickness values. Two different main types namely narrow nozzle bleed wings and wide nozzle bleed wings, have been tested in comparison to the baseline planform for the angle of attack range of $0^\circ \leq \alpha \leq 30^\circ$ at Reynolds numbers $3.5 \times 10^4 \leq Re \leq 1 \times 10^5$. To expand the scope of comparison, force measurements were also conducted for the back bleed wing configuration previously studied by Çelik et al. [10]. The results suggest that nozzle-type bleeding geometry with wide slots is quite effective in altering the flow structure and aerodynamic characteristics. Lift stall characteristics can be delayed with accompanying improved pitching moment beyond stall. This behavior is associated with the elimination or modification of three-dimensional surface separation, indicated by large swirl and focal point in the streamline patterns and recovery in $-C_p$ distributions on the base planform around the stall regime. These findings indicate that nozzle-type bleeding slots might be effectively used to control the flow structures and enhance aerodynamic behavior over non-slender delta wing planforms.

5.1 Results and Discussions

5.1.1 Surface Pressure Measurements

The effect of the nozzle bleed slots on the flow structure is characterized with surface pressure measurements at a Reynolds number of $Re = 1 \times 10^5$. Figure 5.1 shows the negative pressure coefficient $-C_p$ distributions of wide nozzle bleeding wings (Nozzle Bleed Wing CR050: dash dot square "-.□", Nozzle Bleed Wing CR075: dash dot diamond "-.◇") in comparison to the baseline wing model (solid circle "o-") at a chordwise distance of $x/C = 0.50$ for four different angles of attack $\alpha = 10°$, $16°$, $18°$, and $20°$. For narrow nozzle bleeding wings (Nozzle Bleed Wing Narrow CR050 Fwd: dash dot upper triange "-.△", Nozzle Bleed Wing Narrow CR050 Rear: dash dot lower triangle "-.▽"), results are presented in Figure 5.2 using the same graphing approach as in wide nozzle bleed wings. In addition, considering the sake of discussion, results for Reynolds numbers of $Re = 3.5 \times 10^4$ and $Re = 7.5 \times 10^4$ are given in Appendix B. The vertical axes of each plot represent the $-C_p$ values and the horizontal axes represent the dimensionless spanwise distance y/s from the wing symmetry plane, where s is the half span at $x/C = 0.50$. In the charts, higher $-C_p$ values indicate suction zones and possibly correspond to the projection of the vortex core onto the wing surface, whereas the lowest $-C_p$ values indicate where the flow reattaches to the wing surface.

Considering the results of the wide nozzle bleeding wings, for the angle of attack $\alpha = 10°$, all wing models represent a hump-like pattern, which is known as the typical footprint of vortical flow structure on the wing surface. The baseline wing model shows a higher $-C_p$ peak value of 1.37 at $y/s = 0.65$ with a possible reattachment zone around $y/s \approx 0.40$. Wide nozzle bleeding wings CR075 and CR050 indicate slightly reduced suction peak $-C_p$ at spanwise location of $y/s = 0.55$ with 12% and 20% reductions, respectively. The reattachment zone slightly moves inboard for both nozzle bleed wings to around $y/s \approx 0.27$.

For the angle of attack $\alpha = 16°$, the footprint of the vortical structure is still apparent for all wing models, with nozzle bleed wing models showing very similar distribution to the baseline model. There is a slight decrease in suction peak $-C_p$ by about 5%

and 8% for CR050 and CR075, respectively. Compared to $\alpha = 10°$, the suction peak location for all wing models moves inboard with a spanwise increment of $\Delta y/s = 0.07$. In addition, the decrease in suction peak is quite limited for nozzle bleed wings where the baseline model experiences a 12% reduction in $-C_p$.

For the angle of attack $\alpha = 18°$, the baseline wing model represents a flat-like pressure distribution which indicates localized surface separations and degradation in aerodynamic performance. Considering the results for the nozzle bleed wings, a hump-like pattern is apparent, with a suction peak observed around $y/s = 0.50$ at an order of $-C_p = 1.05$ and $-C_p = 0.95$ for CR050 and CR075, respectively. Wide nozzle bleeding wings are found to successfully maintain the footprint of the vortical structure up to $\alpha = 18°$, such that the differences in the suction peak pressure compared to lower angles of attack are found as $|\Delta C_p|_{10-16} = 0.02$ (increasing), $|\Delta C_p|_{16-18} = 0.1$ (decreasing) for CR050 and $|\Delta C_p|_{10-16} = 0.1$ (decreasing), $|\Delta C_p|_{16-18} = 0.12$ (decreasing) for CR075. The surface pressure measurement results of $\alpha = 18°$ are quite in line with results obtained by Kestel et al. [34], where nozzle bleed could represent a similar improvement with the maximum opening ratio case. Considering the results for angle of attack $\alpha = 20°$, baseline and nozzle bleeding wing models exhibit completely flat surface pressure coefficient distribution, clearly indicating localized three-dimensional surface separation from the wing surface.

Considering the results of the narrow nozzle bleeding wings for the angle of attack $\alpha = 10°$, both wings exhibit a hump-like pressure distribution pattern, similar to the wide nozzle bleeding wings. Both the narrow CR050 forward and narrow CR050 rear nozzle bleeding wings show a slight reduction in suction peak $-C_p$ at the spanwise location $y/s = 0.55$, with reductions of 13% and 20%, respectively. Additionally, both models exhibit a similar movement of the reattachment zone inboard, around $y/s \approx 0.27$. In the spanwise region corresponding to $0.35 \leq y/s \leq 0.50$, the narrow CR050 forward wing displays higher $-C_p$ values compared to the narrow CR050 rear wing. However, beyond the suction region, this trend is reversed.

For the angle of attack $\alpha = 16°$, the footprint of the vortical structure remains apparent for all wing models, maintaining a distribution similar to that of the baseline

model. The decrease in suction peak $-C_p$ for the narrow nozzle bleeding wings is slightly greater than for the wide nozzle bleeding wings, with reductions of approximately 19% and 12% for the narrow CR050 forward and narrow CR050 rear wings, respectively.

At $\alpha = 18°$, the narrow nozzle bleeding wings do not show an improvement over the baseline model's flat-like pressure distribution, unlike the wide nozzle bleeding wings. At $\alpha = 20°$, all bleeding wing models, including the narrow nozzle variants, exhibit a completely flat surface pressure coefficient distribution.

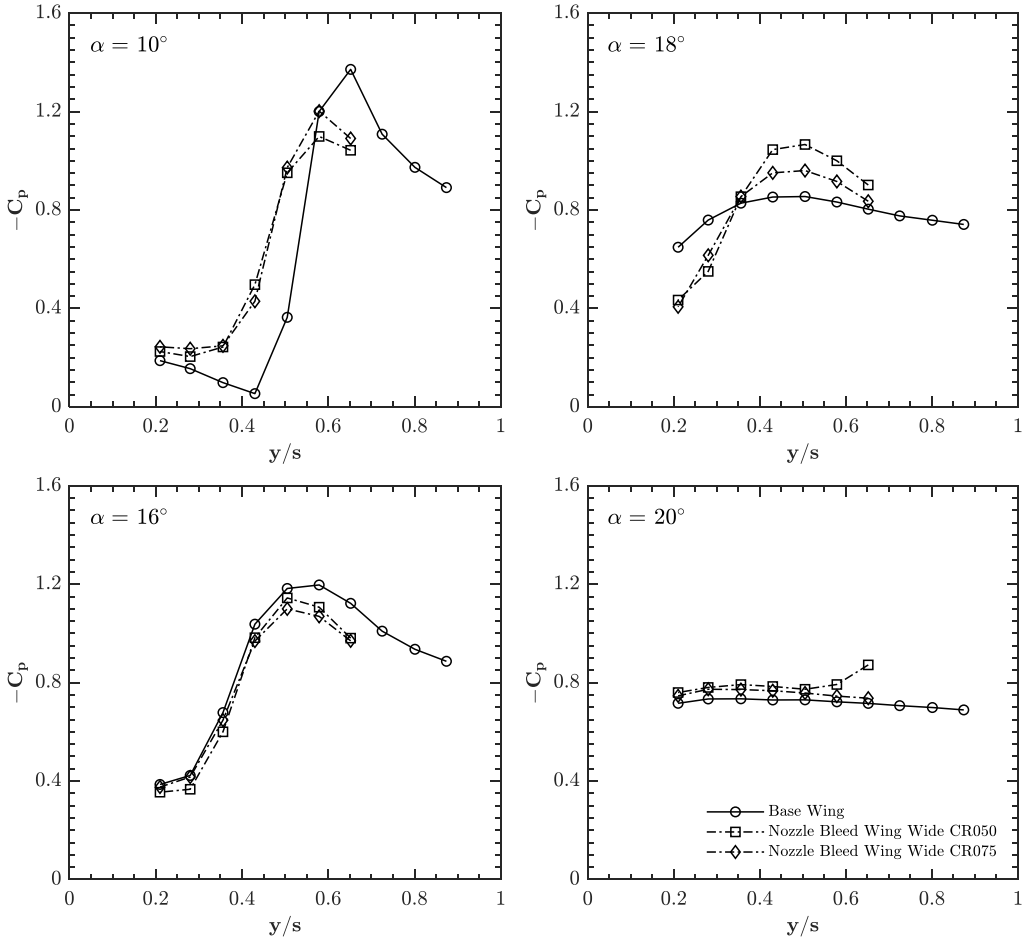

Figure 5.1: $-C_p$ distribution at half span for base wing, nozzle bleed wing wide CR050, and nozzle bleed wing wide CR075 at angles of attack $\alpha = 10°$, $\alpha = 16°$, $\alpha = 18°$, and $\alpha = 20°$ at Re $= 1 \times 10^5$

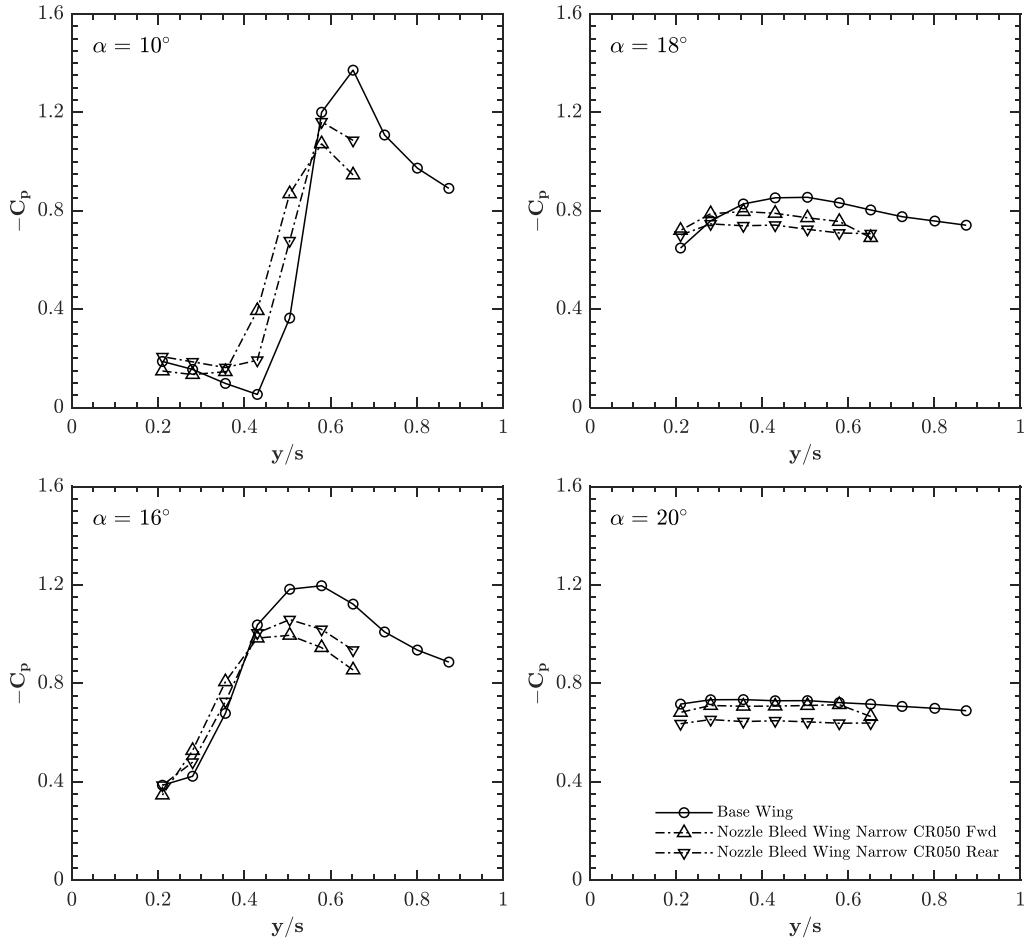

Figure 5.2: $-C_p$ distribution at half span for base wing, nozzle bleed wing narrow CR050 Fwd, and nozzle bleed wing narrow CR050 Rear at angles of attack $\alpha = 10°$, $\alpha = 16°$, $\alpha = 18°$, and $\alpha = 20°$ at Re $= 1 \times 10^5$

5.1.2 Aerodynamic Force and Moment Measurements

In Figure 5.3 and **??**, distributions of drag coefficient C_D, lift coefficient C_L, lift to drag ratio C_L/C_D and pitching moment coefficient C_M at the trailing edge are given as a function of angle of attack for wide (Nozzle Bleed Wing CR050: dash dot square "-.□", Nozzle Bleed Wing CR075: dash dot diamond "-.◇") and narrow nozzle bleeding wings (Nozzle Bleed Wing Narrow CR050 Fwd: dash dot upper triange "-.△", Nozzle Bleed Wing Narrow CR050 Rear: dash dot lower triangle "-.▽") respectively in comparison to baseline wing (Baseline wing: solid circle "-o").

In addition to the presented bleeding approach utilizing nozzle type of bleeding slots, experiments for the back bleed wing [10] were also performed in the current work, and results are included in the charts (Back Bleed Wing B18: solid left triangle "-◁") to compare the effectiveness of the nozzle bleeding technique.

Considering the results of the drag coefficient distribution shown in the top left chart of Figure 5.3, the wide nozzle bleed wings CR050 and CR075 demonstrate higher C_D values, respectively, compared to the baseline wing with a very similar rate of change in an angle of attack range $4° \leq \alpha \leq 18°$. Beyond $\alpha = 18°$, the baseline wing model indicates a settled C_D distribution up to $\alpha = 24°$, whereas further increase in angle of attack up to $\alpha = 28°$ results in linear increase in C_D. Nozzle bleeding wings maintain the preceding linear increasing trend up to $\alpha = 22°$, beyond which both CR050 and CR075 exhibit similar C_D values up to $\alpha = 30°$. When considering the distribution of Back Bleed Wing B18, a slight increase in C_D distribution compared to the baseline wing is observed up to $\alpha = 14°$. This behavior does not appear as a systematic shift as witnessed by nozzle bleeding wings. Beyond $\alpha = 14°$, back bleed wing B18 represent a linear increasing trend up to $\alpha = 24°$, then it settles. Overall, bleeding wings indicate higher C_D distributions in the entire range.

Considering the lift coefficient distribution shown in the top right chart of Figure 5.3, the baseline delta wing demonstrates typical stall characteristics around $\alpha = 18°$ with $C_{L,\text{max}} = 0.74$, beyond which a considerable loss is observed. The lift curve slope, the so-called linear regime, is modified with the presence of the bleeding slots which becomes apparent beyond $\alpha = 10°$ for the nozzle bleed wing CR050 and the back bleed wing B18. Such a change is not observed for the nozzle bleed wing CR075; instead, a remarkable increase in the stall angle is achieved by $\Delta\alpha = 6°$ which is observed around $\alpha \approx 22°$ to $24°$ with an accompanying improvement in maximum lift coefficient to $C_{L,\text{max}} = 0.79$. When considering the results of the nozzle bleed wing CR050, a similar delay of the stall angle is evident up to $\alpha = 22°$ with a decrease in maximum lift coefficient to $C_{L,\text{max}} = 0.72$. The back bleed wing B18 could delay the lift stall up to $\alpha = 20°$, representing no change in maximum lift coefficient. For all bleeding wings, the decay characteristic beyond the stall angle is considerably attenuated, such that they exhibit a flat-like lift distribution in the proximity of the stall angle.

To discuss the aerodynamic performance of the passive nozzle bleeding technique, the lift to drag ratio C_L/C_D are shown in bottom left chart of Figure 5.3. All wings indicate a peak in the overall distribution at low angles of attack, around $\alpha \approx 6^\circ$ to 8°, then exhibit a reduction systematically with increasing angle of attack. Due to the increase in the drag coefficient distributions with the presence of bleeding slots, the baseline wing model demonstrates a higher C_L/C_D distribution. At high angles of attack, the difference with the baseline wing is significantly reduced for the nozzle bleed wing CR075 and the back bleed wing B18, resulting from the improved lift performances of these planforms.

In the bottom right chart of Figure 5.3, the variation of the pitching moment coefficient C_M at the trailing edge (T.E.) as a function of angle of attack is shown. For the baseline wing model, the linear positive slope extends up to $\alpha = 16^\circ$ and becomes negative beyond that angle, which can be considered as the moment stall angle. When the nozzle bleeding wing CR075 is investigated, an increase in slope is evident with increase in C_M magnitudes beyond $\alpha = 12^\circ$. In addition, the stall behavior is not evident for CR075, and C_M distributions remain almost constant for angles of attack greater than $\alpha = 18^\circ$. For the nozzle bleeding wing CR050, the slope is very similar to the baseline wing model with a decrease at order of $\Delta C_M \approx 0.04$. CR050 also does not exhibit a reversal in C_M distribution and indicates constant behavior at high angles of attack, similar to CR075. This behavior can be considered as a significant improvement in longitudinal stability characteristic for this angle of attack regime. Considering the results of the back bleed wing B18, lower values of C_M are observed in the linear regime compared to all other wings. A stall angle of $\alpha = 18^\circ$ is evident with an instant recovery beyond $\alpha = 20^\circ$.

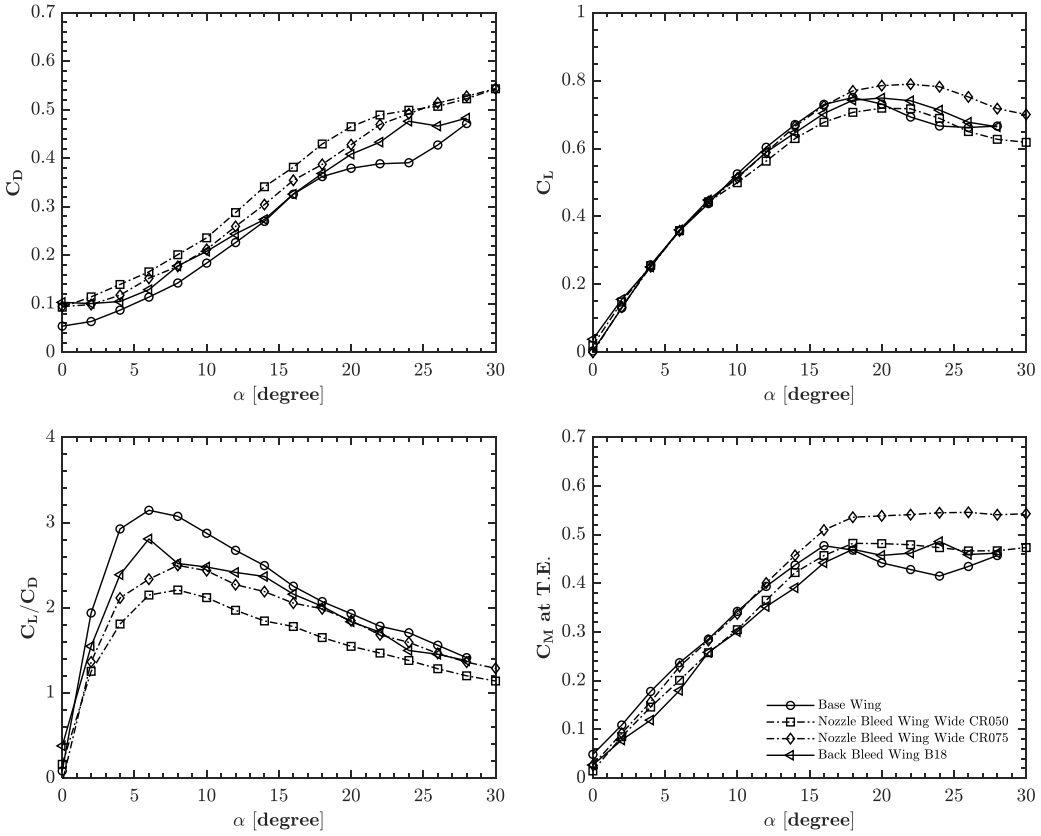

Figure 5.3: Distributions of drag coefficient C_D, lift to drag ratio C_L/C_D, lift coefficient C_L, and pitching moment coefficient at trailing edge C_M for base, nozzle bleed wide, and back bleed wings at Re $= 9 \times 10^4$.

Considering the results for the narrow bleeding wings shown in Figure **??**, the drag coefficient distribution in the top left chart indicates that both the forward and rear narrow nozzle bleed wings demonstrate higher C_D values compared to the baseline and back bleed B18 wings within an angle of attack range of $4^\circ \leq \alpha \leq 16^\circ$. Up to $\alpha = 16^\circ$, both narrow nozzle bleeding wings exhibit very similar magnitudes, beyond which the first narrow nozzle bleed wing exhibits slightly higher magnitudes than the rear model up to $\alpha = 24^\circ$, then this trend is reversed. Overall, the narrow nozzle bleeding wings indicate higher C_D distributions across the entire range.

Considering the lift coefficient distribution shown in the top right chart of Figure **??**,

no significant improvement is observed with the implementation of the narrow nozzle bleeding wings in the overall lift distribution in terms of the lift curve slope, stall angle, and magnitudes. In the linear regime, a slight positive shift is observed for the narrow nozzle bleed wing with the rear slot configuration.Similar to the results for the wide nozzle bleed wing, due to the increase in drag coefficient distributions with the presence of bleeding slots, the baseline wing model demonstrates a higher C_L/C_D distribution. Beyond $\alpha = 10^\circ$, both narrow nozzle bleeding wings exhibit very similar magnitudes.

In the bottom right chart of Figure 5.4, the variation of the pitching moment coefficient C_M at the trailing edge (T.E.) as a function of the angle of attack is presented. Similar to the baseline wing model, the linear positive slope extends up to $\alpha = 16^\circ$ for both narrow nozzle bleeding wings with a slight decrease in magnitudes. With increasing angle of attack, the reduction in pitching moment is very limited for the forward configuration slot. Considering the results of the back bleed wing B18, higher values of C_M are observed for the angle of attack values greater than $\alpha = 10^\circ$ compared to both narrow nozzle bleeding wings.

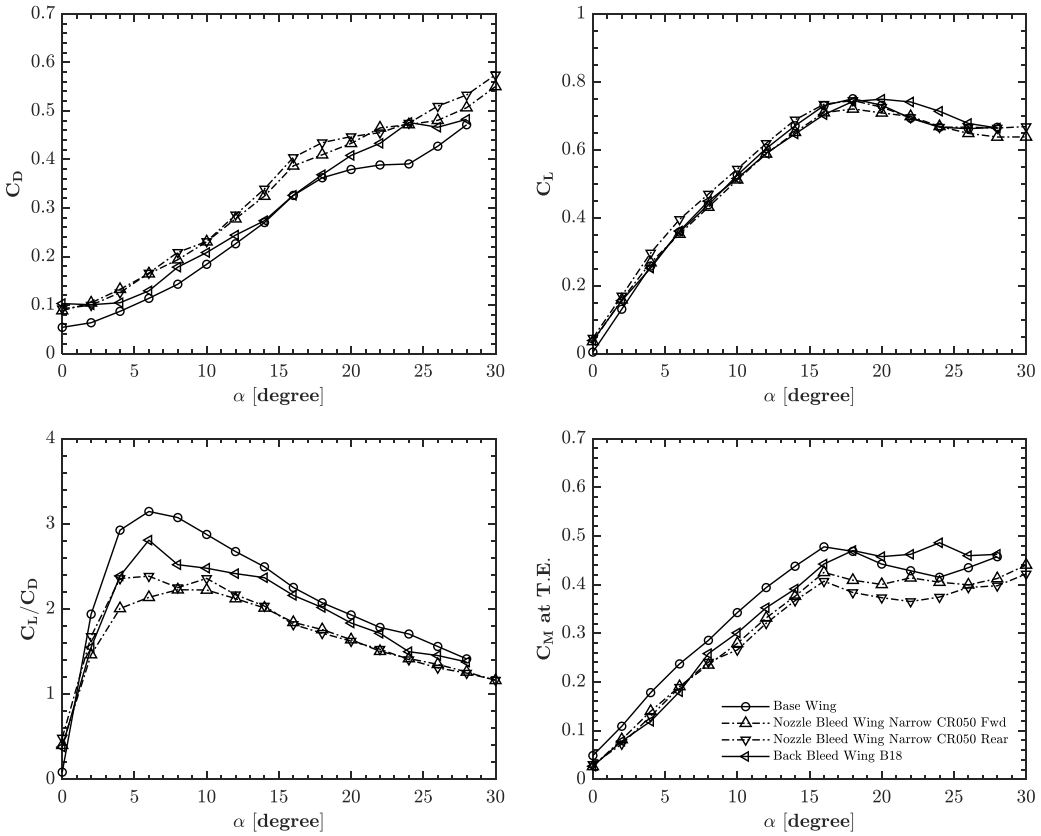

Figure 5.4: Distributions of drag coefficient C_D, lift to drag ratio C_L/C_D, lift coefficient C_L, and pitching moment coefficient at trailing edge C_M for base, nozzle bleed narrow, and back bleed wings at Re $= 9 \times 10^4$.

5.1.3 Near surface particle image velocity measurements

To investigate the effect of nozzle bleeding wings CR050 and CR075 on the global flow field, near surface particle image velocimetry measurements were performed at $Re = 3.5 \times 10^4$ in comparison to the baseline wing model. Figures 5.5, 5.6, 5.7, and 5.8 demonstrate the results for $\alpha = 10°$, $\alpha = 16°$, $\alpha = 18°$, and $\alpha = 20°$ respectively. Each row in the figures represents time-averaged streamline patterns $\langle \Psi \rangle$, time-averaged contours of constant non-dimensional streamwise velocity $\langle u/U_\infty \rangle$, and time-averaged contours of constant non-dimensional vorticity $\langle \omega_z C/U_\infty \rangle$ for the baseline wing, nozzle bleed CR050 wing, and nozzle bleed CR075 wing from top to

bottom, respectively. All figures utilize the same scaling approach for comparison. The contours of constant non-dimensional streamwise velocity $\langle u/U_\infty \rangle$ are presented with solid lines indicating the streamwise direction and dashed lines indicating the negative streamwise direction, with absolute minimum and absolute contour increment values set to 0.05 and 0.1 respectively ($[|u/U_\infty|]_{\text{min}} = 0.05$, $[|\Delta(u/U_\infty)|]_{\text{min}} = 0.1$). The contours of constant non-dimensional vorticity in the surface normal direction $\langle \omega_z C/U_\infty \rangle$ are presented with solid lines indicating positive contours and dashed lines indicating negative contours, where positive contours designate vorticity in the outward direction of the surface normal. Both absolute minimum and absolute contour increment values are set to 3 ($[|\omega_z C/U_\infty|]_{\text{min}} = 3$, $[|\Delta(\omega_z C/U_\infty)|] = 3$).

Figure 5.5 shows the results for $\alpha = 10°$. The patterns of time-averaged streamline topology for all wing models exhibit a clear representation of the positive bifurcation line BL^+, indicating flow attachment to the surface. The extent of the bifurcation line for all wings starts approximately at $x/C \approx 0.25$ in the axial direction, with a span of $y/s \approx 0.60$ and passes the trailing edge at a corresponding span of $y/s \approx 0.35$. Considering the outboard region of the positive bifurcation lines on the baseline wing, streamlines are directed towards the leading edge creating another positive bifurcation across the leading edge with a comparably shorter extent, indicating the onset of flow reversal. In this outboard region, both nozzle bleed wings CR050 and CR075 exhibit streams elongated parallel to the leading edge, which might indicate a flow reversal prevention mechanism. When the results of the streamwise velocity contours are investigated for all wing models, no negative streamwise velocity contours are observed. Instead, all wing models represent constant intense contours starting approximately at $x/C \approx 0.25$, similar to the streamline positive bifurcation line patterns. For the nozzle bleed wing CR050, streamwise velocity contours appear in a narrow spanwise extent with similar magnitudes as the baseline wing model, whereas nozzle bleed wing CR075 exhibits slightly scattered behavior. Considering the results for the time-averaged constant non-dimensional vorticity contours, all wing models indicate positive normal vorticity contours along the aforementioned bifurcation line extent, where both nozzle bleeding wings CR050 and CR075 represent apparently higher vorticity levels. For the baseline wing, well-defined clusters of negative contours appear along the leading edge, starting approximately at $x/C \approx 0.40$. Such

structures are known as the footprints of shear layer instabilities emanating from the windward side of the planform. For nozzle bleeding wing CR050, these clusters are elongated toward $x/C \approx 0.20$ whereas CR075 does not exhibit such a distribution, instead representing clusters of weaker negative contours beyond $x/C \approx 0.50$.

The results for $\alpha = 16^{\circ}$ are shown in Figure 5.6. For the baseline wing model, time-averaged streamline topology clearly represents a large swirl structure in the form of a stable focus. Such structures were previously shown in non-slender delta wing flow topology and flow control studies, which were reported as indications of three-dimensional surface separation [97]. Near surface flow visualization performed by Çelik et al. [10] on the same baseline wing model, represented very similar behavior, where the focal point was observed in the proximity of the apex. This behavior is also evident with negative streamwise velocity contours (dashed lines) observed in a region corresponding to the outboard half, whereas there exist broadly distributed positive axial velocity contours covering the inboard half. Considering the results for both nozzle bleed wings CR050 and CR075, no stable focus is observed in the streamline topology, suggesting the elimination of three-dimensional surface separation at this incidence. Instead, positive bifurcation lines representing the reattachment line are evident. Flow reversals tend to occur for both nozzle bleed wings at a region beyond $x/C \approx 0.70$ close to the leading and trailing edges where no significant negative streamwise velocity contour is observed. Compared to the baseline wing model, positive axial velocity contours appear in a comparatively concentrated region. Results of the time-averaged constant non-dimensional vorticity contours show that there are weak positive vorticity contours over the baseline model, along with strong negative vorticity contours up to the level of $[\omega_z C/U_\infty] = -18$, covering the entire leading edge. On the contrary, both nozzle bleed wings represent well-organized positive vorticity contours extending along the entire wing, starting from the apex in the inboard region. The maximum level may reach up to $[\omega_z C/U_\infty] = 21$ in these vorticity extensions, approximately at $x/C \approx 0.20$. In addition, negative vorticity elongated across the leading edges is significantly weakened down to the level of $[\omega_z C/U_\infty] = -9$ with the presence of nozzle bleed slots. These results are considerably in line with the surface flow visualization and cross flow measurements of the B18 wing performed previously [10], where bleeding could adjust the reattachment

line and improved crossflow vorticity contours.

Considering the results of $\alpha = 18^{\circ}$ shown in Figure 5.7, the baseline wing model exhibits large-scale swirling streamline patterns, clearly indicating three-dimensional surface separation, with the focal point moved downstream by $\Delta x/C \approx 0.20$ compared to an angle of attack $\alpha = 16^{\circ}$. For $\alpha = 18^{\circ}$, the non-dimensional negative streamwise velocity contours (dashed lines) over the baseline wing model dominate approximately two-thirds of the half wing, whereas the remaining portion exhibits positive streamwise velocity contours reduced compared to an angle of attack $\alpha = 16^{\circ}$. In addition, positive contours of non-dimensional normal vorticity significantly disappear on the baseline wing, representing only minimum levels in the proximity of the apex region. When the results of the nozzle bleed wing CR050 at an angle of attack $\alpha = 18^{\circ}$ are investigated, bleeding slots appear to significantly alter the time-averaged flow field such that the focus of the swirl appears in a squeezed form, the reattachment line starts to emerge, and reversing streamlines create saddle points across the exit of the bleeding slots. Flow reversals, indicated by negative streamwise velocity contours (dashed lines), are observed for CR050, the extent of which is narrower than that of the baseline wing. The positive streamwise velocity contours are highly concentrated near the centerline symmetry plane at this incidence for CR050, which still generates coherent positive vorticity structures extending from the apex to the trailing edge in that region. For the nozzle bleed wing CR075, the focus of the large swirl structure is moved towards the apex compared to both the baseline wing and the nozzle bleed wing CR050 at an angle of attack $\alpha = 18^{\circ}$. In addition, the promotion of the reattachment line is obvious. In the proximity of the nozzle bleed slots, small-scale swirls have started to appear, which are fed by flow reversals. The spatial extent of negative streamwise velocity occurs in a very narrow region towards the outboard region beyond $x/C \approx 0.55$ with reduced contour levels. Similar to CR050, positive streamwise velocity contours appear across the symmetry plane, creating elongated positive vorticity structures from the apex to the trailing edge for CR075.

Figure 5.8 shows the results for $\alpha = 20^{\circ}$. For the baseline wing model, flow structures are further reduced such that the scale of the large swirl is increased with downstream movement of the focal point. The spatial extent of the negative streamwise velocity

is increased further, occupying almost 80% of the planform whereas the remaining portion demonstrates very weak positive streamwise velocity contours up to 2 levels. This is a clear indication of the almost stagnant condition over the wing surface with the absence of either discrete or coherent vortical structures. When the results of the nozzle bleed wing CR050 are considered, the focus of the swirl appears in a squeezed form as in prior angles of attack. The occupancy of the negative streamwise velocity contours reduces below 50% of the planform area whereas there are still high positive

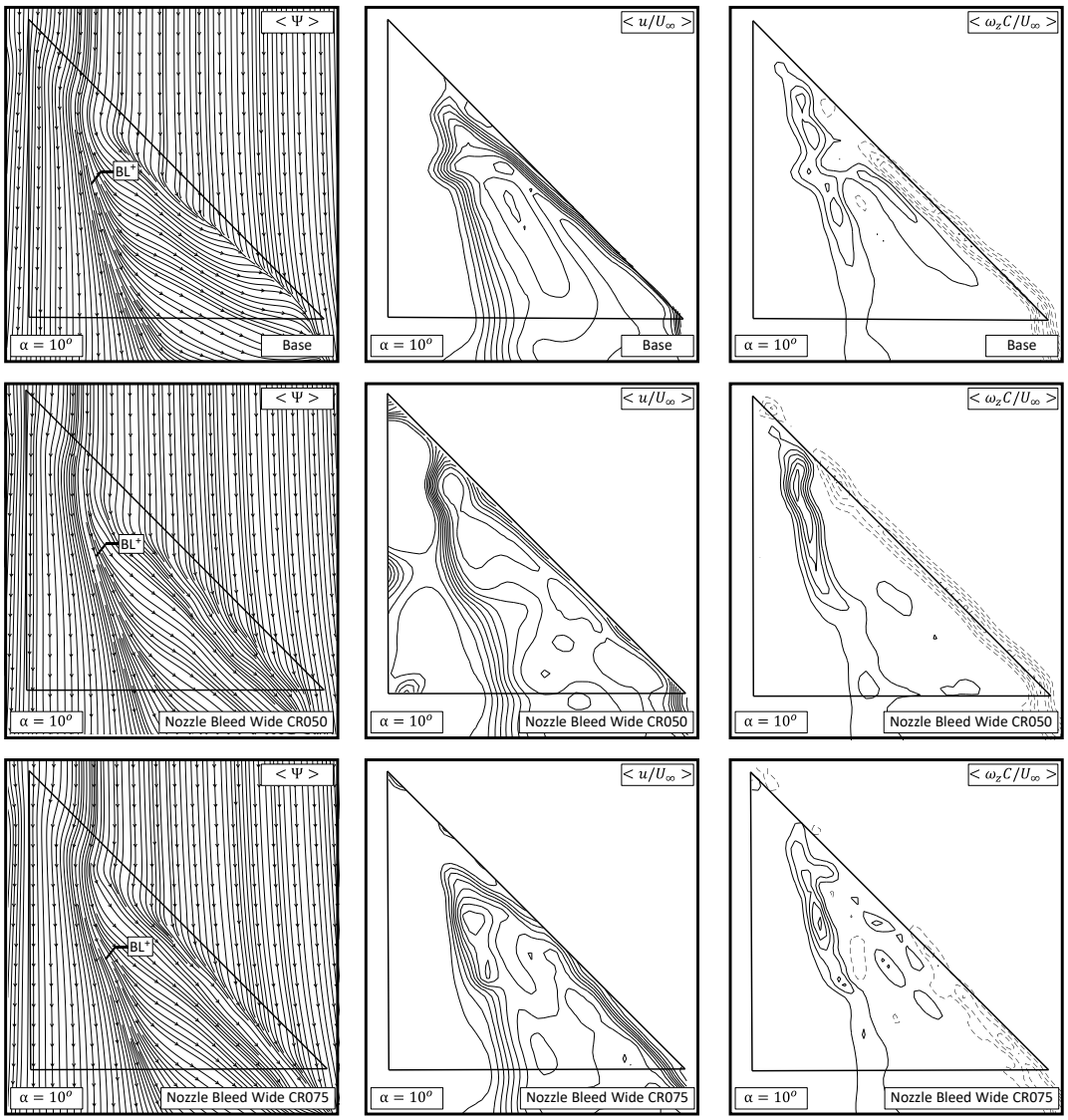

Figure 5.5: Near surface plane PIV results: time averaged contours of constant non-dimensional streamwise velocity $\langle u/U_\infty \rangle$, streamlines $\langle \Psi \rangle$, and contours of constant non-dimensional vorticity $\langle \omega_z C/U_\infty \rangle$ for angle of attack $\alpha = 10^\circ$ at Re $= 3.5 \times 10^4$; $[|u/U_\infty|]_{\min} = 0.05$, $[|\Delta(u/U_\infty)|] = 0.1$ and $[|\omega_z C/U_\infty|]_{\min} = 3$, $[|\Delta(\omega_z C/U_\infty)|] = 3$.

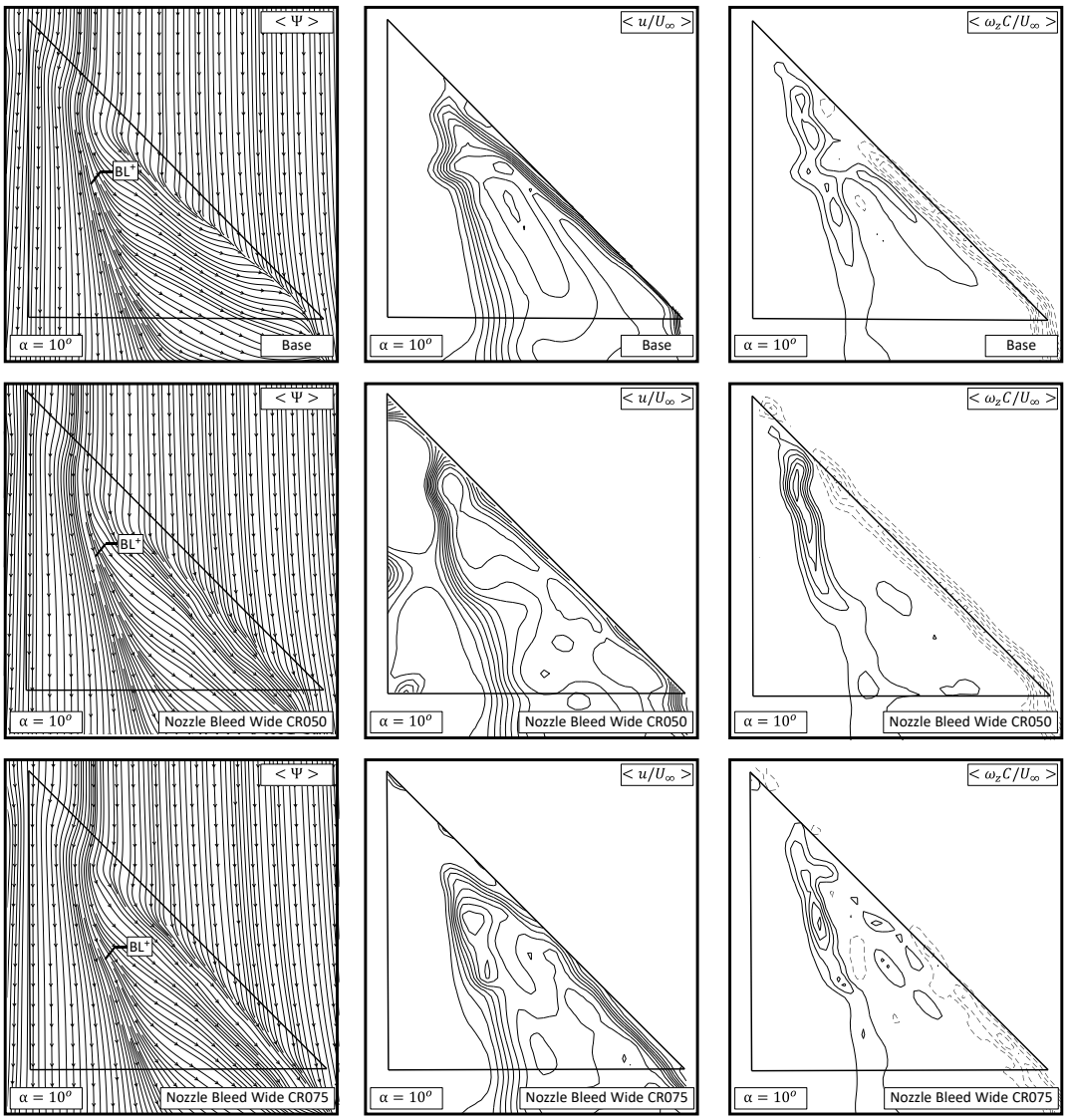

Figure 5.6: Near surface plane PIV results: time averaged contours of constant non-dimensional streamwise velocity $\langle u/U_\infty \rangle$, streamlines $\langle \Psi \rangle$, and contours of constant non-dimensional vorticity $\langle \omega_z C/U_\infty \rangle$ for angle of attack $\alpha = 16^\circ$ at Re $= 3.5 \times 10^4$; $[|u/U_\infty|]_{\min} = 0.05$, $[|\Delta(u/U_\infty)|] = 0.1$ and $[|\omega_z C/U_\infty|]_{\min} = 3$, $[|\Delta(\omega_z C/U_\infty)|] = 3$.

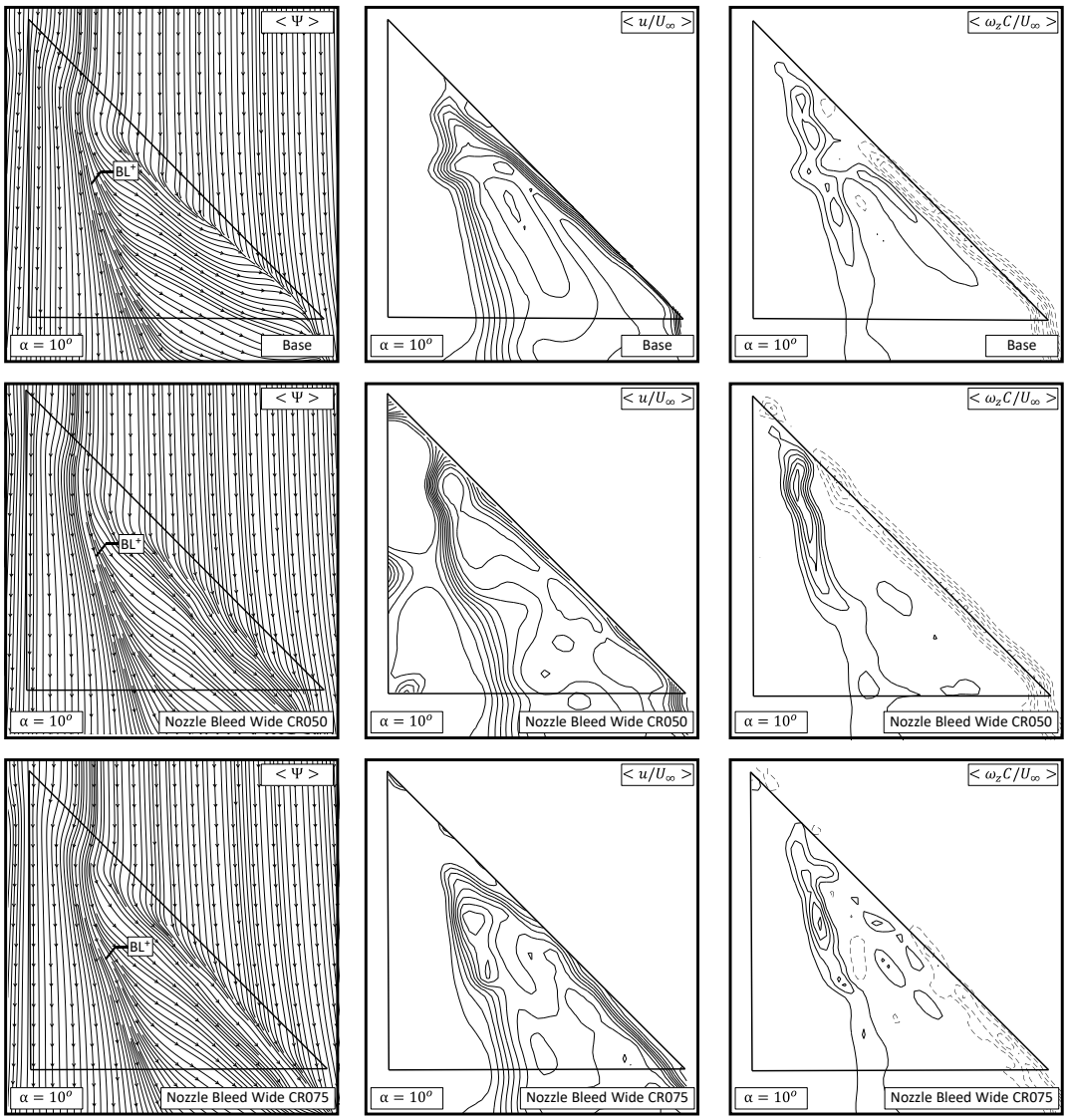

Figure 5.7: Near surface plane PIV results: time averaged contours of constant non-dimensional streamwise velocity $\langle u/U_\infty \rangle$, streamlines $\langle \Psi \rangle$, and contours of constant non-dimensional vorticity $\langle \omega_z C/U_\infty \rangle$ for angle of attack $\alpha = 18^\circ$ at Re $= 3.5 \times 10^4$; $[|u/U_\infty|]_{\min} = 0.05$, $[|\Delta(u/U_\infty)|] = 0.1$ and $[|\omega_z C/U_\infty|]_{\min} = 3$, $[|\Delta(\omega_z C/U_\infty)|] = 3$.

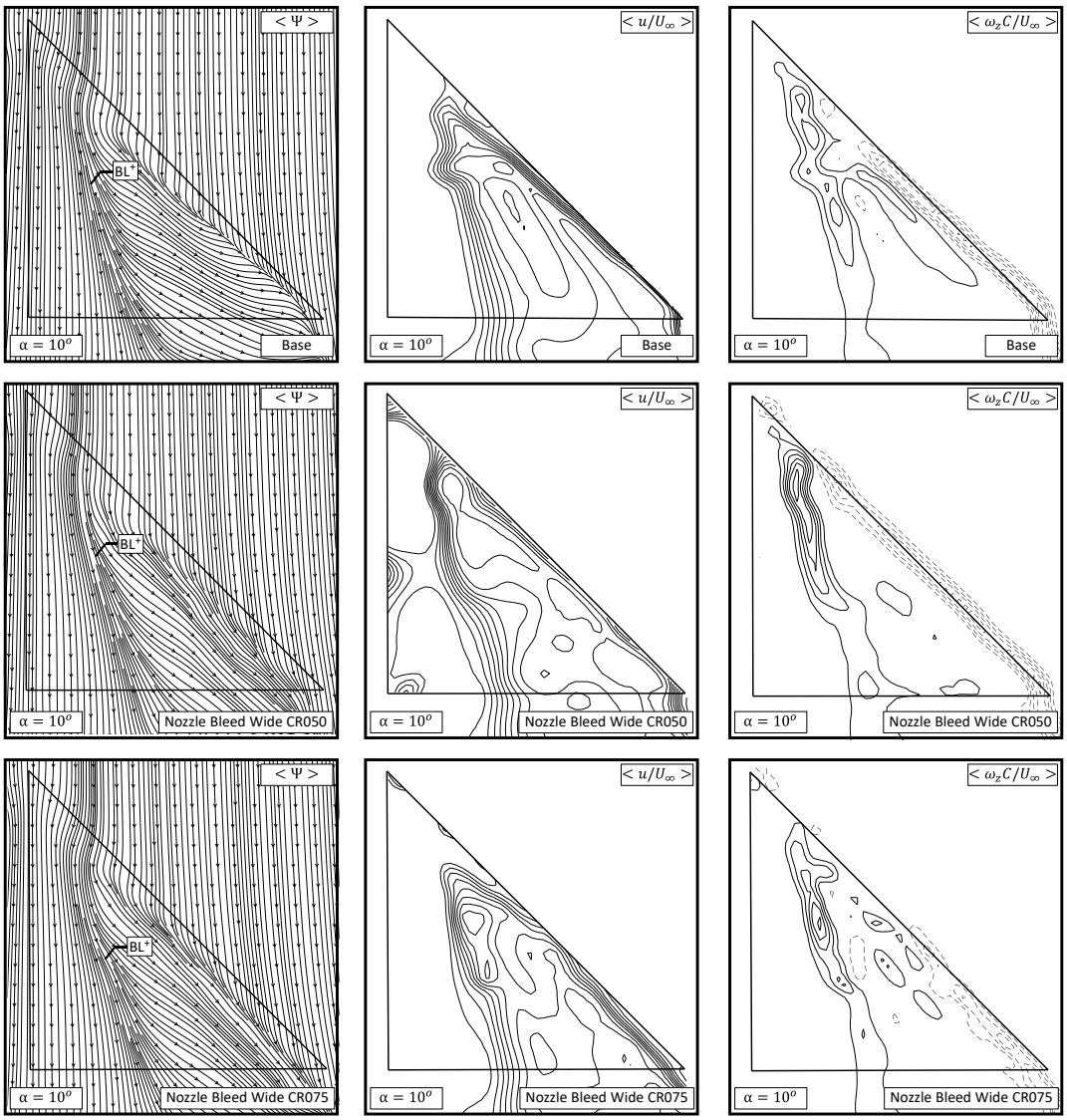

Figure 5.8: Near surface plane PIV results: time averaged contours of constant non-dimensional streamwise velocity $\langle u/U_\infty \rangle$, streamlines $\langle \Psi \rangle$, and contours of constant non-dimensional vorticity $\langle \omega_z C/U_\infty \rangle$ for angle of attack $\alpha = 20^\circ$ at Re $= 3.5 \times 10^4$; $[|u/U_\infty|]_{\min} = 0.05$, $[|\Delta(u/U_\infty)|] = 0.1$ and $[|\omega_z C/U_\infty|]_{\min} = 3$, $[|\Delta(\omega_z C/U_\infty)|] = 3$.

5.2 Conclusions

The current chapter presents the effect of a new passive bleeding concept on the flow structures of a non-slender delta wing with a sweep angle $\Lambda = 45^\circ$ using quantita-

tive measurement techniques including surface pressure measurement, particle image velocimetry, and aerodynamic force measurements. The new concept, namely the nozzle bleed, utilizes contracting slots aiming at the acceleration of the bleeding flow from the pressure side to the suction side. The delta wings with two different contraction ratios, $CR = 1 : 0.5$ and $CR = 1 : 0.75$, have been tested in comparison to the baseline wing model and the back bleed concept with a back angle of $18°$. The experiments were performed in a low-speed wind tunnel at Reynolds numbers $3.5 \times 10^4 \leq Re \leq 1 \times 10^5$ for the angle of attack range of $0° \leq \alpha \leq 30°$. Considering the collective evaluations of the surface pressure coefficient distributions, surface velocity fields, and aerodynamic force measurements, the principal findings are the following:

1. With the presence of the nozzle bleeding slots, the three-dimensional surface separation on the baseline wing model could be effectively eliminated or modified at angles of attack $\alpha = 16°$ and $\alpha = 18°$, and reattachment could be promoted. This is evident from the increases in the surface normal positive vorticity contours, axial positive streamwise velocity contours, and recoveries in $-C_p$ distribution. Even at higher angles of attack $\alpha = 20°$, velocity field results show that the dominancy of the flow reversal could be manipulated with nozzle slots. CR075, in particular, could deflect and move the focal point of the three-dimensional surface separation by representing a considerable increase in positive streamwise velocity.

2. Aerodynamic force measurements reveal that the nozzle bleeding slots significantly improve the lift stall and moment stability characteristics such that CR075 could delay the lift stall up to $\alpha \approx 24°$ with an accompanying increase in the maximum lift coefficient value. In addition, pitching moment characteristics are significantly altered such that the moment stall is prevented and replaced by a constant distribution at high angles of attack. Similar trends are valid for CR050 with a very slight reduction in the maximum lift coefficient compared to the baseline wing model. The back bleed wing 18 also indicated improvement in stall delay but to a limited extent compared to the nozzle bleed wings. The presence of the bleeding slots results in an increase in drag coefficient C_D and thus a degradation in C_L/C_D performance particularly in the

linear regime.

To conclude, the results suggest that the proposed passive nozzle bleeding slots are successful in manipulating the surface flow field by preventing or modifying the three-dimensional surface separation. In addition, lift and stability characteristics are improved. Despite an increase in the drag distribution, such a technique shows potential to be effectively used in designing an active bleeding system, particularly targeting the stall and stability characteristics of non-slender delta wing planforms.

CHAPTER 6

COMPREHENSIVE CHARACTERIZATION OF A PNEUMATIC ACTIVE FLOW CONTROL SYSTEM USING IN-SITU HOT WIRE CALIBRATION

Pneumatic active flow control systems have great potential to control aerodynamic phenomena including separation, circulation, and turbulence. To quantify the effectiveness of such flow control schemes, thorough characterization of developed systems is critical in addition to estimating aerodynamic and stability favor. In the current chapter, results for the experimental characterization of in-house active blowing system capable of steady and periodic excitations, based on fast switching solenoid valves, is presented via an in-situ calibration scheme. Characterization is presented for 45° swept delta wing aerodynamic surface. The performance of the developed system is comprehensively investigated for a square wave form excitation with control parameters including an excitation frequency range of 1 – 32 Hz, duty cycle values of 25 and 50%, and momentum coefficients of 1x, 2x, and 3x. The results indicate that the response of the flow control system to control signals is influenced by both the signal parameters and the aerodynamic surface design. Full characterization of such systems using in-situ approaches provides valuable calibration schemes for the mentioned parameters, which is crucial for assessing aerodynamic effectiveness and developing closed-loop flow control systems.

6.1 Results and Discussions

6.1.1 Stage 1: In-Situ Calibration Results

In situ flow calibration for all blowing holes at forward, middle, and aft stations is conducted at a supply flow rate up to 18 l/min when the tunnel is off. Figure 6.1

shows the hot wire probe response with respect to the supply, thus the blowing hole average exit velocity for each hole, respectively. The vertical axis of the plot represents the CTA voltage value E and the bottom horizontal axis represents the supply rate Q. The corresponding bleed slot exit average velocity blowing velocity U_{blow} obtained by dividing the supply flow rate Q with the bleed slot area A_h is given at the top horizontal axis. To capture the typical hot wire responses to velocity variations, the supply rate is kept frequent at lower values and then extended as the values increase. Square markers represent average values of each increment. A piecewise continuous function, as given in Eqn. 6.1, was used, consisting of a lower portion with a linear fit and an upper portion with a fifth-order polynomial fit. Considering the valve actuation principle described in the previous section, the response of the CTA system under no-flow conditions is also included in the curve covered by the lower portion to capture the valve's closed-state behavior. The upper portion for all blowing holes represents a well-known typical polynomial CTA response, which generally provides a more accurate estimation than power-law curves, with linearization errors often less than 1% as suggested by the manufacturer [96]. However, these curves may exhibit oscillations if the velocity falls outside the calibration range. Thus, for the current approach calibration curves were only used within the designated calibration range, after verifying the hot wire probe's response for in-situ positioning. The function coefficients for each blowing hole are tabulated in Table 6.1. It should be noted that the differences in coefficients are not of significant importance; instead, ensuring the accurate polynomial fit for an accurate calibration range principally guarantees an accurate velocity response within the in-situ approach.

$$U_{\text{blow}} = \begin{cases} aE + b, & 0 < E < E_{\text{low}} \\ p_5E^5 + p_4E^4 + p_3E^3 + p_2E^2 + p_1E + p_0, & E_{\text{low}} \leq E < E_{\text{high}} \end{cases} \tag{6.1}$$

Table 6.1: Steady air supply vs. CTA voltage calibration curves, lower portion linear fit and upper portion 5^{th} order fit constants.

STA	Hole #	a	b	p_1	p_2	p_3	p_4	p_5	p_6
FWD	#1	9.80	-13.10	-0.35	46.43	-305.18	766.92	-820.17	293.05
	#2	9.60	-12.75	-152.85	1500.20	-5688.88	10441.40	-9230.31	3106.58
MID	#3	8.66	-11.51	-292.37	3221.60	-13944.90	29753.93	-31336.10	13041.65
	#4	7.44	-9.88	-107.72	1254.76	-5718.05	12830.28	-14190.10	6189.00
AFT	#5	9.83	-13.08	-19.57	332.22	-1920.36	5162.56	-6613.76	3265.26
	#6	9.62	12.90	-64.38	763.68	-3502.36	7871.28	-8704.91	3796.11

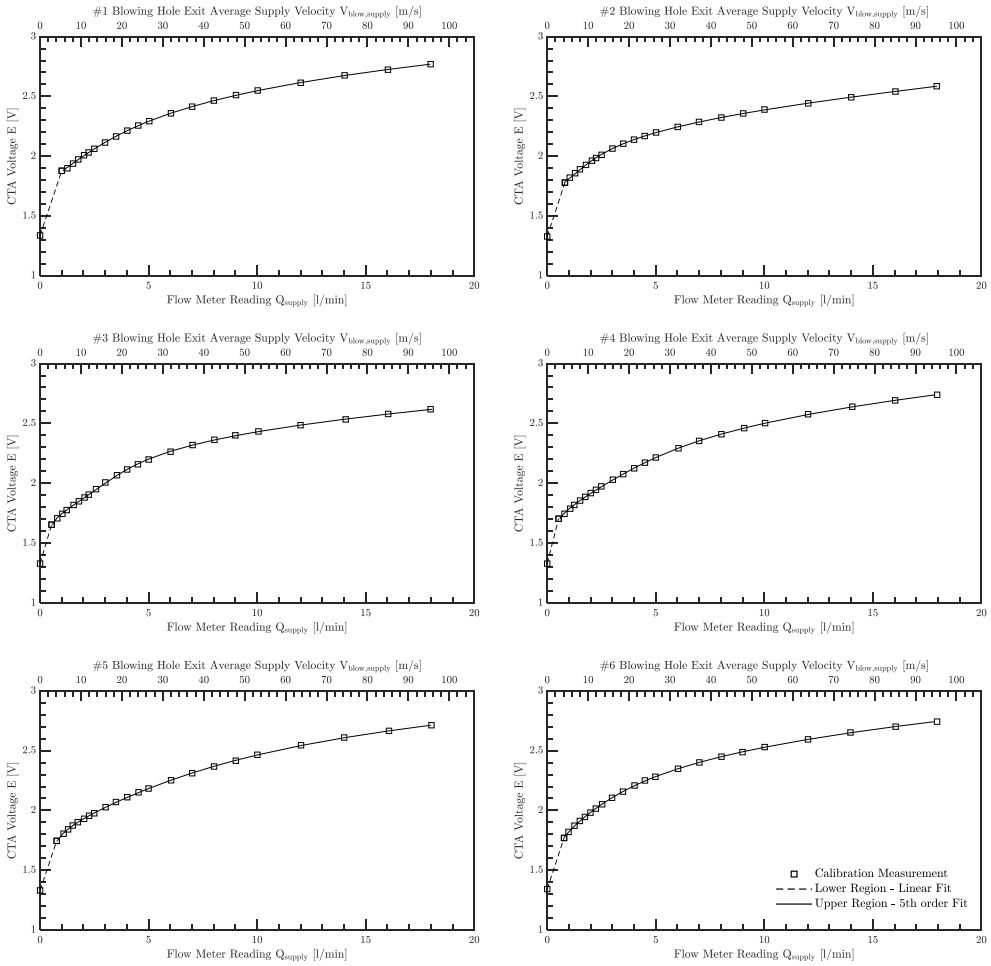

Figure 6.1: Steady air supply vs. CTA voltage calibration curves of all blowing holes: Flow meter reading (bottom X-axis), corresponding bleed hole exit average supply velocity (top X-axis).

6.1.2 Stage 2: Sample Periodic Blowing Profiles

Periodic blowing profiles obtained during Stage 2 measurements for blowing hole #1 are shown for excitation frequencies of $f_c = 2$ and 10 Hz in Figure 6.2, and for $f_c = 20$ and 32 Hz in Figure 6.3. The plots have been constructed such that the left columns indicate the generated control signals in the time domain, and the right columns show the blowing velocity response. For each frequency setting, results of the duty cycle values of $DC = 25\%$ and 50% are presented. The valve is capable of transmitting the duty cycle parameter, for which the sensitivity behavior is discussed in subsequent sections. As demonstrated in both sample figures, the hot wire response represents a fluctuating distribution for each frequency at the valve on state. These fluctuations define the upper and lower bounds of the active state mean blowing velocity, assessed as a root mean square level in the blowing velocity sensitivity evaluation. No filtering was applied to the blowing velocity distribution except for TF1. The results show that the desired frequency is achieved with a high level of repeatability, with the square shape preservation being evident across all frequencies. Although increasing the frequency beyond moderate levels, e.g. 20 Hz, might slightly affect the accuracy of the square waveform, the spectral content remains well maintained. Synchronous signal acquisition results indicate that the hot wire signal exhibits an approximate delay of 0.04 seconds (40 milliseconds) relative to the input signal. This delay does not appear to depend on waveform parameters and can likely be attributed to factors such as the electrical interface, tubing length, and associated transport delay. Given the total blowing piping length of approximately 72 cm and the mean blowing velocity (discussed in the following section), the estimated transport time for a single blowing wave is around 21 milliseconds, suggesting that this is the primary contributor to the response delay observed in the experiments. Considering the valve switching times (on and off) detailed in previous sections, which are much shorter than the overall system response delay for the tested frequency range, a static gain in the range of 12 to 14 dB is observed at low frequencies. This observation implies that the system may be particularly responsive to steady or slowly changing inputs in a dynamic reactive feedback flow control setup, especially due to the long tubing required in the system. The majority of studies referenced in the introduction utilize similar fast-switching valves integrated within the aerodynamic model body,

positioned close to the blowing outlets to take advantage of larger test section and model sizes. In the present work, a similar approach is taken to develop a generic experimental setup for various aerodynamic surfaces using fast-switching valves. The delay estimations described above confirm that characterization steps should be carefully conducted for each specific aerodynamic surface, rather than focusing solely on the valve itself, to ensure accurate performance prior to experiments. In this study, a parametric feedforward control actuation is implemented to determine whether the system is influenced by potential amplification due to the observed static gain. To address this, the sensitivity of the response signals is thoroughly investigated in the following sections, considering both excitation frequency and duty cycle.

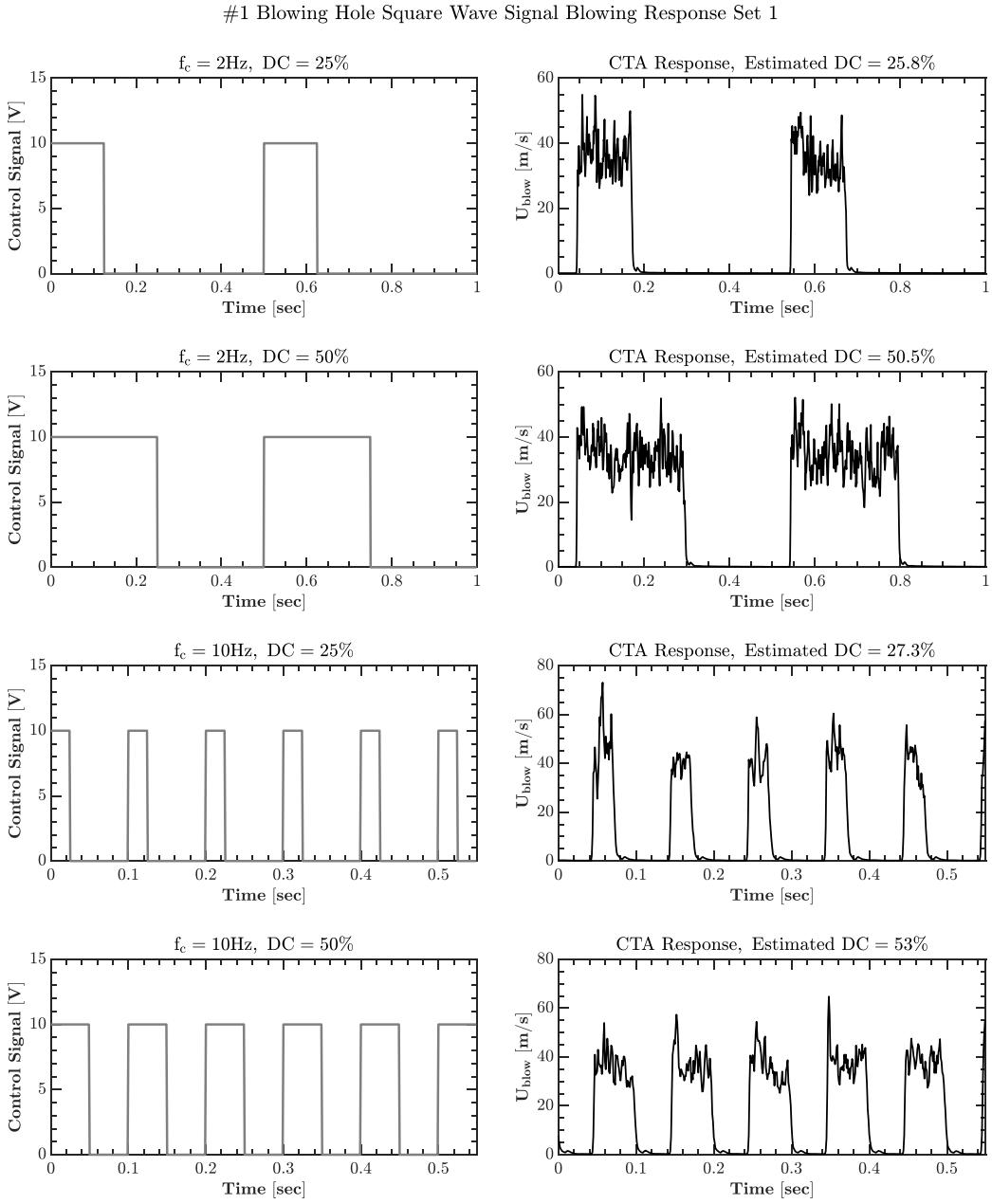

Figure 6.2: Sample square wave control signal and CTA response measurements for #1 blowing hole: $f_c = 2$ and 10 Hz, $DC = 25\%$ and 50%.

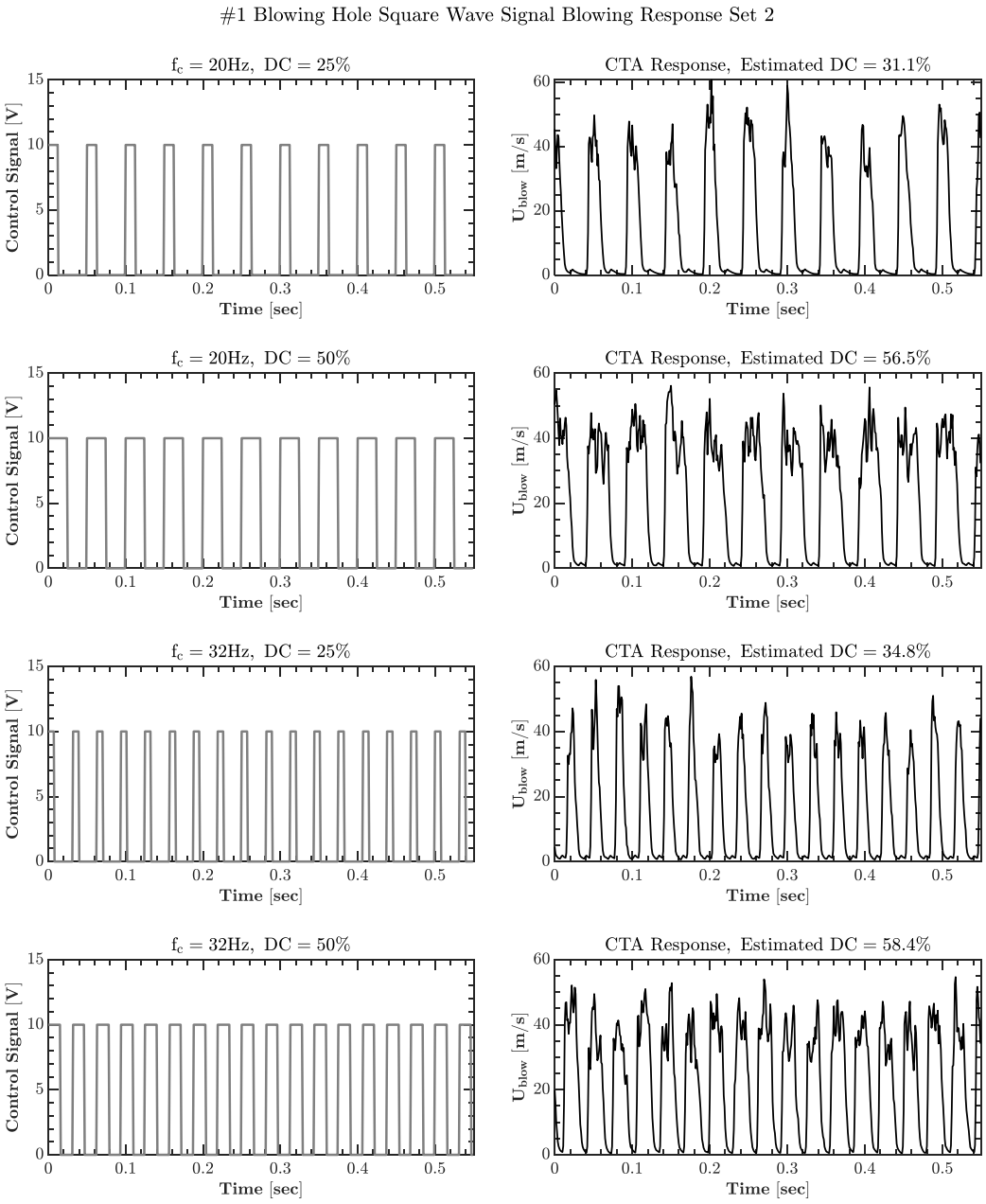

Figure 6.3: Sample square wave control signal and CTA response measurements for #1 blowing hole: $f_c = 20$ and 32 Hz, $DC = 25\%$ and 50%.

6.1.3 Variation of Mean Blowing Velocity with Excitation Frequency

Considering the operating principle of the active flow control setup described in the methodology section, it is important to investigate the effect of the excitation frequency on blowing velocity under fixed supply conditions. For that purpose, periodic velocity profiles obtained for each hole were investigated for varying control frequencies. The results are presented in Figures 6.4, 6.5, and 6.6 for the forward, middle, and aft stations, respectively. Each figure is organized such that the left graphs show results for $DC = 25\%$, while the right graphs display results for $DC = 50\%$. This allows for a comparison of blowing velocity responses at different duty cycles for each station. To quantify deviations in the average periodic blowing velocity ($\overline{U}_{\text{blow}}$) from the reference steady blowing velocity ($\overline{U}_{\text{blow,ref}} = 34$ m/s with a momentum coefficient setting of $C_\mu = 1\%$), reference steady blowing velocity lines are included in the plots.

Results of the forward station, given in Figure 6.4, show that, at duty cycle setting $DC = 25\%$, both sides represent similar behavior. Starting from $f_c = 1$ Hz, the valve on state mean velocity increases up to $f_c = 6 - 7$ Hz with a 0.8 m/s per Hz increase rate with respect to reference steady blowing velocity $\overline{U}_{\text{blow,ref}}$. Further increase in excitation frequency up to $f_c = 20$ Hz does not yield a considerable change; instead, it exhibits a trend of convergence. Beyond this frequency, a slight decrease in velocity is observed. This trend is also reflected in the root mean square (RMS) values of the valve on state mean velocity distribution for both sides. For blowing hole #1, the minimum RMS value is approximately $\overline{U}_{\text{blow,rms}} = 4.5$ m/s at the lowest frequency of $f_c = 1$ Hz and the maximum value is around $\overline{U}_{\text{blow,rms}} = 7.5$ m/s at $f_c = 20$ Hz. The blowing hole #2 exhibits slightly higher fluctuations; the minimum value is around $\overline{U}_{\text{blow,rms}} = 5.5$ m/s at a frequency of $f_c = 1$ Hz, and the maximum value is observed around $\overline{U}_{\text{blow,rms}} = 8.2$ m/s at $f_c = 20$ Hz. When the distributions $DC = 50\%$ are considered, for both blowing holes, the valve on state mean velocity represents an increasing trend up to $f_c = 14 - 15$ Hz with a 0.24 m/s per Hz increasing rate with respect to $\overline{U}_{\text{blow,ref}}$, whereas further increase in frequency does not exhibit considerable change. Compared to $DC = 25\%$ setting, RMS values are slightly reduced for $DC = 50\%$, with blowing hole #2 still showing slightly higher

fluctuations than #1.

Considering the results for the middle station, plotted in Figure 6.5, the deviation of the valve on state mean velocity is very limited for both blowing holes 3 and 4 at both duty cycle settings. The maximum difference with the reference steady blowing velocity $\overline{U}_{\text{blow,ref}}$ is around 2 m/s for both blowing holes. The deviations are mainly observed around the frequency range of $f_c = 5 - 15$ Hz. Similar to the forward blowing holes, velocity fluctuations at the valve open state are slightly reduced at DC = 50%. For blowing hole 3, the maximum value is observed around $\overline{U}_{\text{blow,rms}} = 7.8$ m/s and 6.8 m/s for DC = 25% and 50%, respectively. Whereas for blowing hole 4, the maximum value is observed around $\overline{U}_{\text{blow,rms}} = 6.3$ m/s and 5.5 m/s, respectively.

Results of the aft blowing holes indicated in Figure 6.6 are found to be quite similar to the results of the forward blowing holes. For DC = 25%, the valve on state mean velocity represents an increasing trend up to $f_c = 6 - 7$ Hz, then tends to exhibit a converged trend around $\overline{U}_{\text{blow}} = 39$ m/s for both blowing holes up to $f_c = 20$ Hz. Whereas for DC = 50%, the valve on state mean velocity represents an increasing trend up to $f_c = 15 - 16$ Hz with a 0.26 m/s per Hz increasing rate relative to $\overline{U}_{\text{blow,ref}}$. As with the other stations, DC = 50% represents slightly lower fluctuations compared to DC = 25%, with both blowing holes 5 and 6 showing similar fluctuation levels.

The response of blowing velocity to excitation frequency was similar for both the forward and aft stations, where higher excitation frequencies led to increased deviations from the reference steady blowing condition. While the middle station also displayed this trend, the deviations were noticeably less pronounced. This discrepancy could stem from differences in section lengths within the overall piping layout or potential variations in valve performance due to manufacturing tolerances.

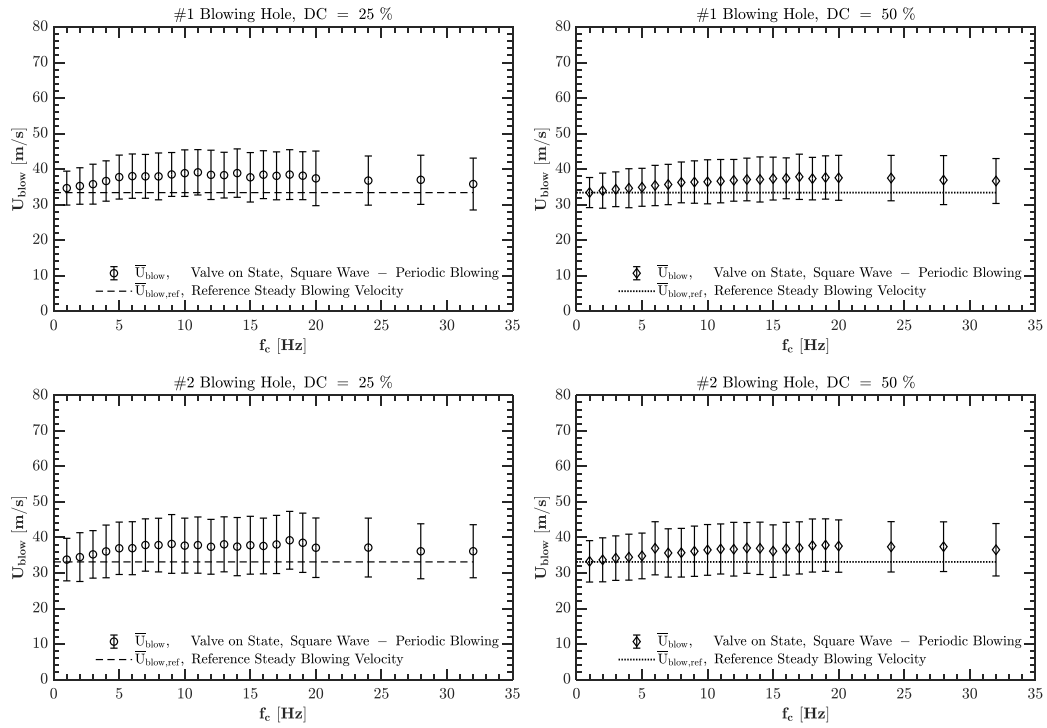

Figure 6.4: Variation of periodic blowing mean velocity at valve on (duty) state for #1 and #2 FWD blowing holes: $f_c = 1$ – 32 Hz and $DC = 25\%$, 50%.

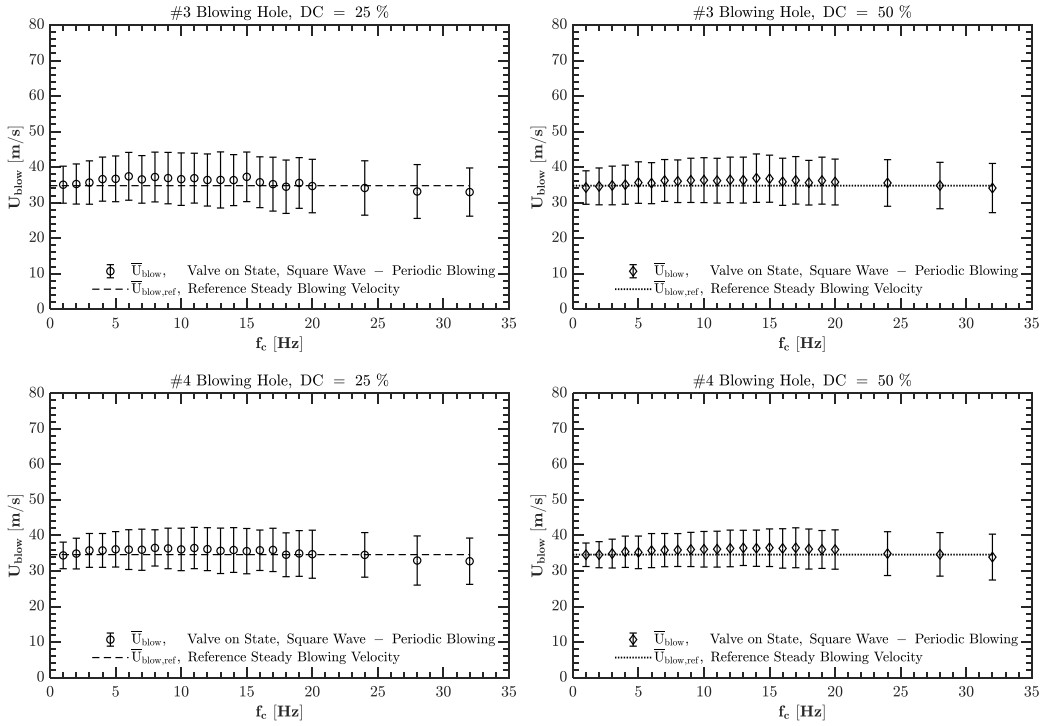

Figure 6.5: Variation of periodic blowing mean velocity at valve on (duty) state for #3 and #4 MID blowing holes: $f_c = 1$ – 32 Hz and $DC = 25\%$, 50%.

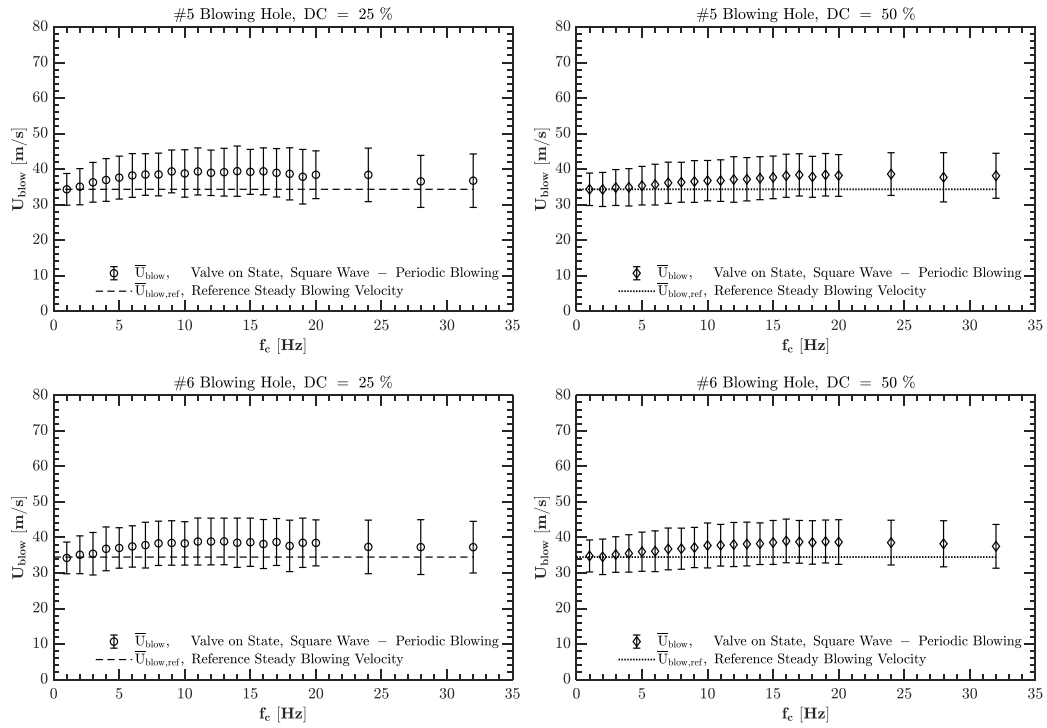

Figure 6.6: Variation of periodic blowing mean velocity at valve on (duty) state for #5 and #6 AFT blowing holes: $f_c = 1$ – 32 Hz and $DC = 25\%$, 50%.

6.1.4 Variation of Duty Cycle with Excitation Frequency

In addition to quantifying the potential variation in the valve on state mean velocity with respect to excitation frequency, it is also crucial to consider the variation in the duty cycle, as it directly impacts the actual momentum rate applied to the flow field. As discussed in the introduction, accurately estimating the effective momentum relies on evaluating the active state of the actuation element. Therefore, all velocity profiles measured in the current study were analyzed to estimate the duty cycle responses of each station based on Eqn. 6.2, the initial and final crossing instants of each pulse were determined using the mid-level reference process described in the methodology section, and the duty cycle was averaged over n.

$$DC = \frac{1}{n}\sum_{i=1}^{n}\frac{t_{\text{final cross},i} - t_{\text{init cross},i}}{t_{\text{init cross},i+1} - t_{\text{init cross},i}} \tag{6.2}$$

Figure 6.7 illustrates the estimated duty cycle values at each blowing hole individually for both control signal settings of DC = 25% and 50%. When analyzed collectively, each station typically shows an increasing duty cycle trend with increasing excitation frequency, and for each hole, a linear fit can be implemented. Table 6.2 provides the linear fit coefficients for each hole. Considering the responses of all stations, the deviation with respect to the commanded duty cycle signal is higher in the middle station, where at the maximum excitation frequency $f_c = 32\,\text{Hz}$, 19% and 18% differences are observed for DC = 25% and 50%, respectively. For forward and aft holes, deviations are limited compared to middle holes. At forward holes, the maximum deviation at maximum excitation frequency $f_c = 32\,\text{Hz}$ is 10% and 9% for DC = 25% and 50%, respectively, whereas at aft holes these deviations are about 10% for both DC values.

Considering the results of each station individually, the agreement between the holes is quite similar for the middle and aft holes. However, there is a slight deviation between holes #1 and #2 at the forward station, as can be inferred from the coefficients presented in Table 6.2. Although all blowing lines were kept the same length, as detailed in the methodology section, to ensure consistent losses, the lines differ only in their aerodynamic surface based on their positions according to the wing layout as detailed in Table 3.8. These results suggest that the duty cycle response appears to be a quite sensitive parameter due to possible factors including installation, excitation line geometry, length, geometric tolerances, and and potential variations in valve performance due to manufacturing tolerances. Considering the dynamics of a regular square wave signal, as the excitation frequency increases, the durations of the open and close states commanded by the control signal decrease asymptotically. Due to both the signal dynamics and inherent system delay, the transport of a single pulse is affected by the proximity of subsequent pulses and the overall travel length. Therefore, an increase in frequency is likely responsible for deviations in pulse shape, which consequently impacts the duty cycle. Despite this sensitivity, the agreement between holes at each station is generally satisfactory. This implies that once a calibration is performed covering the entire response of the aerodynamic surface's active flow control geometry, proper signal conditioning can be performed prior to actual wind tunnel measurements for duty cycle control.

Table 6.2: Duty cycle response linear fit coefficients.

		DC = 25%		DC = 50%	
STA	**Hole #**	**a**	**b**	**a**	**b**
FWD	#1	0.33	24.5	0.29	49.9
	#2	0.25	24.9	0.20	49.8
MID	#3	0.62	24.2	0.52	49.6
	#4	0.61	24.6	0.59	49.2
AFT	#5	0.32	24.7	0.28	49.7
	#6	0.30	24.6	0.24	49.8

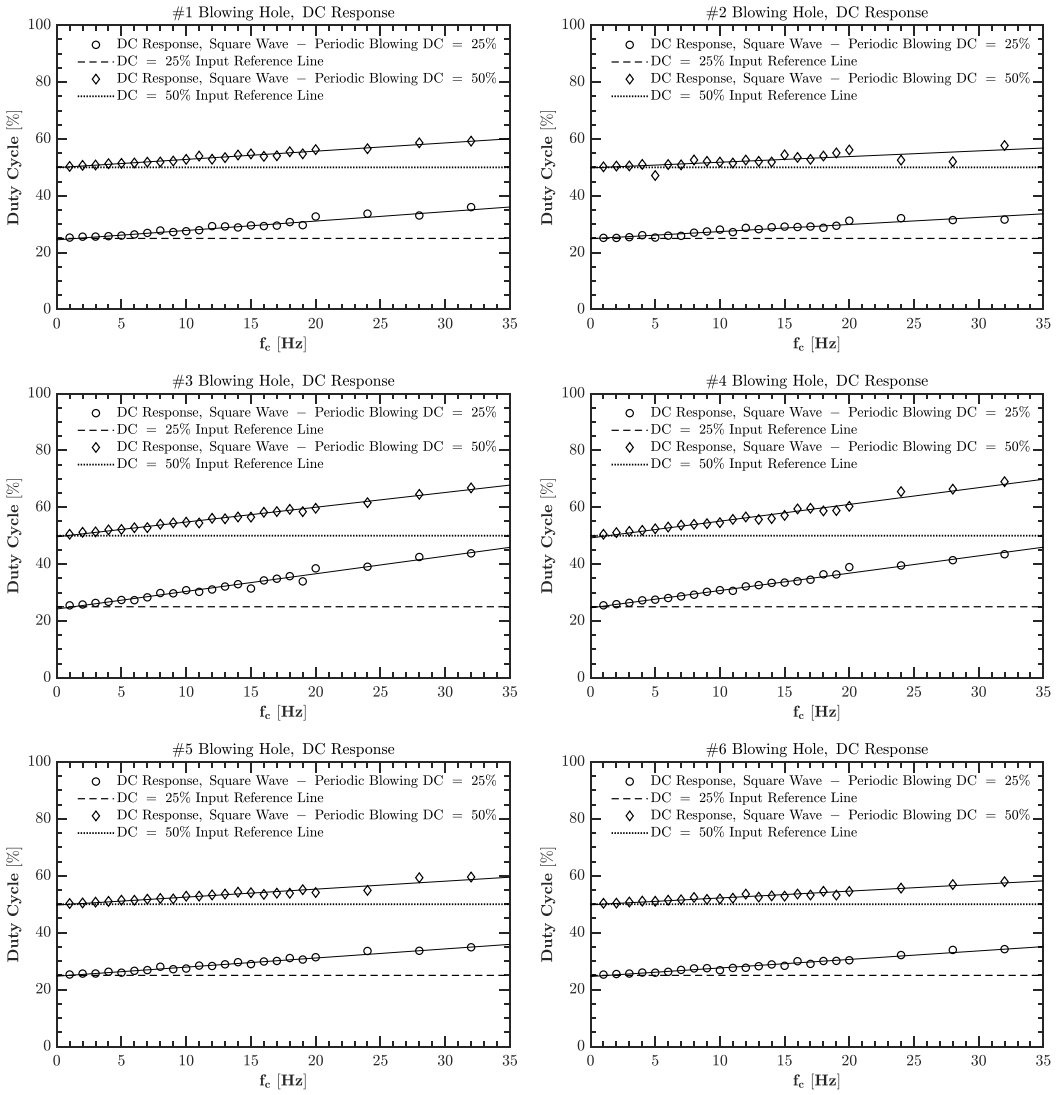

Figure 6.7: Variation of duty cycle response for all blowing holes with frequency $f_c = 1 - 32$ Hz.

6.1.5 Effect of Excitation Frequency for Different Momentum Coefficient Setting

Since all previous evaluations were performed to estimate the deviations of blowing velocity and duty cycle at a fixed momentum setting, the response of the system at different momentum coefficient settings, including $C_\mu = 2\%$ and 3%, is also investigated at blowing hole #3 for representative purposes at excitation frequencies of $f_c = 1, 4, 8, 12, 16,$ and 24 Hz with a duty cycle setting of DC = 50%. Figure 6.8 illustrates the effect of excitation frequency on the valve on state mean blowing velocity and, consequently, on the momentum coefficient at three different regulator settings corresponding to maximum reference momentum C_μ values. The results show that for all momentum coefficient settings, the deviation characteristics are very similar, indicating that at different momentum coefficient ranges of interest, the system response might be very similar for varying excitation frequencies. For both momentum coefficient settings $C_\mu = 2\%$ and 3%, the maximum difference in valve on state mean blowing velocity is observed at $f_c = 24$ Hz, which is about 2 m/s and 3.5 m/s respectively, in a decreasing trend.

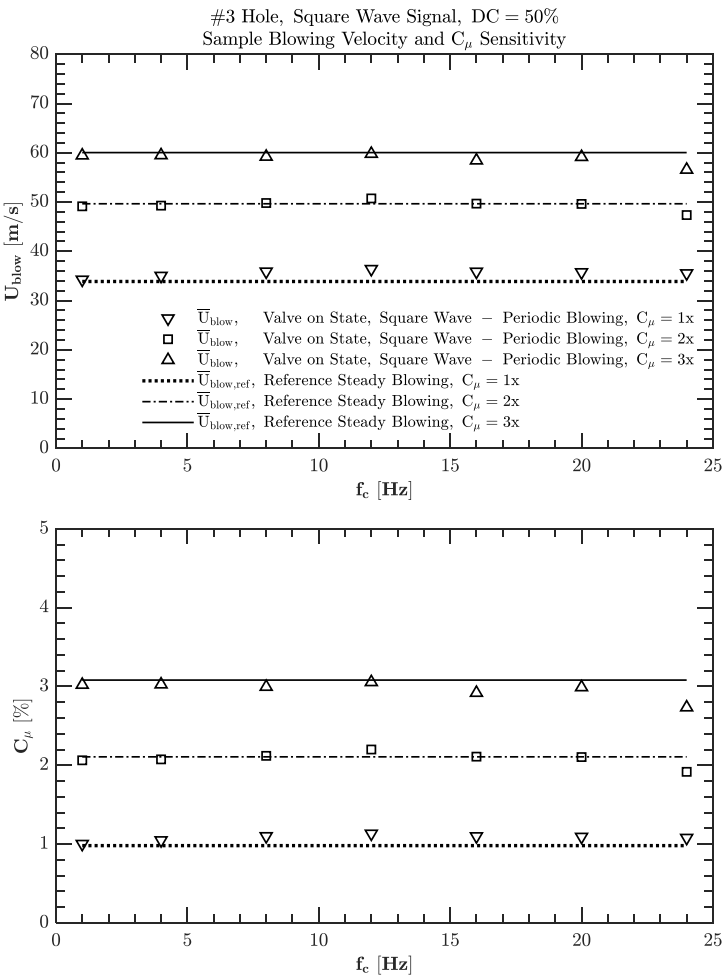

Figure 6.8: Sample sensitivity of periodic blowing mean velocity and momentum coefficient C_μ at valve on (duty) state for #1 blowing hole at three different constant regulator settings: 1x, 2x, and 3x.

6.2 Conclusions

The current chapter presents the in-situ characterization of an in-house active flow blowing control setup based on fast-switching solenoid valves. Measurements were conducted on a sample nonslender delta wing with a 45-degree sweep angle, which features six blowing holes symmetrically distributed at three stations along the leading edges. This setup was used to comprehensively assess the response characteristics of the flow control system before conducting actual aerodynamic wind tunnel experi-

ments. A two-stage calibration scheme was implemented. First, the in-situ calibration of the hot wire anemometry system was completed. Second, the responses for different flow control scenarios in the form of a periodic square wave were acquired for an excitation frequency range of $f_c = 1 - 32$ Hz and duty cycle values of DC = 25% and 50% at tunnel off conditions. Additionally, the sensitivity of different momentum coefficient settings was investigated. Based on the combined assessments from these characterization experiments, the following conclusions can be drawn:

- The in-situ calibration approach effectively estimates the periodic blowing response by accurately capturing the spectral content, particularly when the blowing hole geometry is comparable in size to the hot wire probe. For all blowing holes, a typical hot wire response was obtained using the well-known steady flow supply, referred to as the first transfer function (TF1). This response was used to extract periodic velocity profiles and perform characterization steps through data analysis. A key advantage of this in-situ calibration scheme is that, despite variations in calibration coefficients among different blowing holes, the agreement among blowing stations in terms of the trend wise behavior is found to be satisfactory. Additionally, agreement within each station in terms the symmetrical behavior is also found consistent.

- The response of the blowing velocity to excitation frequency is found to be similar for forward and aft stations in that an increase in excitation frequency results in deviation from the reference steady blowing setting. In contrast, for the middle station, these deviations are quite limited.

- The duty cycle response for all stations shows a linear variation with increasing frequency. At the maximum tested frequency, the maximum variation in DC is approximately 10% for the forward and middle stations. In contrast, for the middle blowing holes, the deviations are more significant, with the estimated maximum difference reaching about 19%.

- For different regulator settings aimed at greater steady momentum coefficient values $C_\mu = 2\%$ and 3%, the deviation behavior of the valve-on state mean blowing velocity relative to the steady reference blowing velocity with increasing excitation frequency is found to be quite similar to the behavior observed at

$C_\mu = 1\%$ setting.

- A major loss in blowing piping due to the total length, coupled with possible minor losses (including junctions, diameter changes, and bends), results in a considerable acoustic transport delay in the CTA response compared to the excitation signal. When combined with potential electrical delays, the systematic system response delay is observed to be on the order of 40 milliseconds. This indicates that the overall system dynamics exhibit slower characteristics compared to the valve's individual response dynamics. Such behavior is crucial to consider when designing reactive feedback active flow control systems, as the system response might amplify low-frequency excitation. Minimizing the response delay is essential to mitigate this effect.

In order to report the effectiveness of active flow control blowing systems accurately, the actual momentum injected during flow control actuation should be well identified, thus a systematic relation with aerodynamic flow conditions can be established. The results indicate that characterizing such an in-house active flow control system based on fast-switching pneumatic valve actuation is valuable for understanding the sensitivity of blowing response to control parameters including excitation frequency, duty cycle, and momentum coefficient. Factors such as blowing hole geometry and pipeline installation layout are quite critical and are believed to affect the blowing response characteristics. The in-situ calibration approach appears to be a useful and cost-effective tool when the blowing hole size is comparable to sensor dimensions, as mentioned, thus enabling monitoring of the periodic blowing content. Additionally, the procedures described can be beneficial for designing closed-loop active flow control systems, as they enable the creation of valve calibration charts for each control parameter.

CHAPTER 7

CONTROL OF FLOW STRUCTURES ON A NONSLENDER DELTA WING UTILIZING PERIODIC BLOWING

In the present study, the effect of periodic blowing applied through the leading edges on the flow structures of a 45° swept delta wing is investigated. The experiments were conducted in a low-speed wind tunnel using surface pressure and aerodynamic force measurements. Periodic blowing excitation was performed using an in-house active flow control setup based on a fast-switching valve, characterized via in situ hot-wire measurements. Two different waveforms, namely regular square wave and burst-modulated (BM) square wave, were tested with an effective total momentum coefficient range of $0.25\% \leq C_{\mu,\text{eff,total}} \leq 0.68\%$, in comparison to no actuation and steady blowing cases ($0.25\% \leq C_{\mu} \leq 1\%$) for the angle of attack range of $0° \leq \alpha \leq 30°$ at a Reynolds number of Re $= 9 \times 10^4$. For both regular and BM mode square waves, the carrier signal was tested for a non-dimensional excitation frequency range of $1 \leq f_c \leq 64$ Hz at two different duty cycle settings of DC$_c = 25\%$ and 50%. In the BM mode, the carrier signal was modulated with a modulating signal of $1 \leq f_m \leq 3$ Hz with a fixed duty cycle DC$_m = 50\%$. The results indicate that aerodynamic force measurements reveal that periodic blowing significantly improves lift stall and moment stability characteristics, allowing lift stall up to $\alpha \approx 22°$ with an accompanying increase in the maximum lift coefficient value.

Before the aerodynamic measurements are presented, the overall system response for the maximum momentum coefficient, $C_{\mu,\text{max}}$, and the effective momentum coefficient, $C_{\mu,\text{eff}}$, was calculated. Equation 7.1 [62] represents the effective momentum coefficient obtained by multiplying the maximum momentum coefficient by the duty cycle values. The following equations, 7.2 and 7.3, were used to estimate the total system

momentum coefficient values based on the measured blowing velocity and duty cycle response values.

$$C_{\mu,\text{eff}} = C_{\mu,\max} \times DC_c \tag{7.1}$$

$$C_{\mu,\max,\text{total}} = \sum_{i=1}^{6} C_{\mu,\max,\text{i}} \tag{7.2}$$

$$C_{\mu,\text{eff,total}} = \sum_{i=1}^{6} (C_{\mu,\max,\text{i}} \times DC_{c,i}) \tag{7.3}$$

The results, presented in Figure 7.1, show the total maximum and effective momentum coefficient estimations as a function of the investigated excitation frequency range of $1 \leq f_c \leq 32$ Hz. For the total maximum momentum coefficient value with a commanded duty cycle setting of $DC_c = 25\%$, a maximum deviation in overall system response of approximately 0.24% was observed around an excitation frequency of $f_c = 11$ Hz, beyond which the trend slightly reversed. In the case of a commanded duty cycle setting of $DC_c = 50\%$, an increasing trend was exhibited by the maximum momentum coefficient up to $f_c = 19$ Hz, where the maximum deviation was around 0.2%.

Regarding the total effective momentum coefficient, which represents the actual momentum injected into the flow field, the trends for both duty cycle settings were found to be quite similar across varying excitation frequencies. Both settings exhibited an increasing trend up to an excitation frequency of $f_c = 20$ Hz, after which stabilization occurred. The maximum deviation in the total effective momentum coefficient for the commanded duty cycle setting of $DC_c = 25\%$ was around 0.14% during this stabilized behavior, whereas a deviation of approximately 0.18% was noted for the duty cycle setting of $DC_c = 50\%$. It should be noted that this figure serves as an overall system characterization indicator for the commanded settings and investigated characterization range, which should be considered while evaluating the aerodynamic measurements. In the aerodynamic measurements, the settings outside this excitation frequency range was also performed and discussed as well.

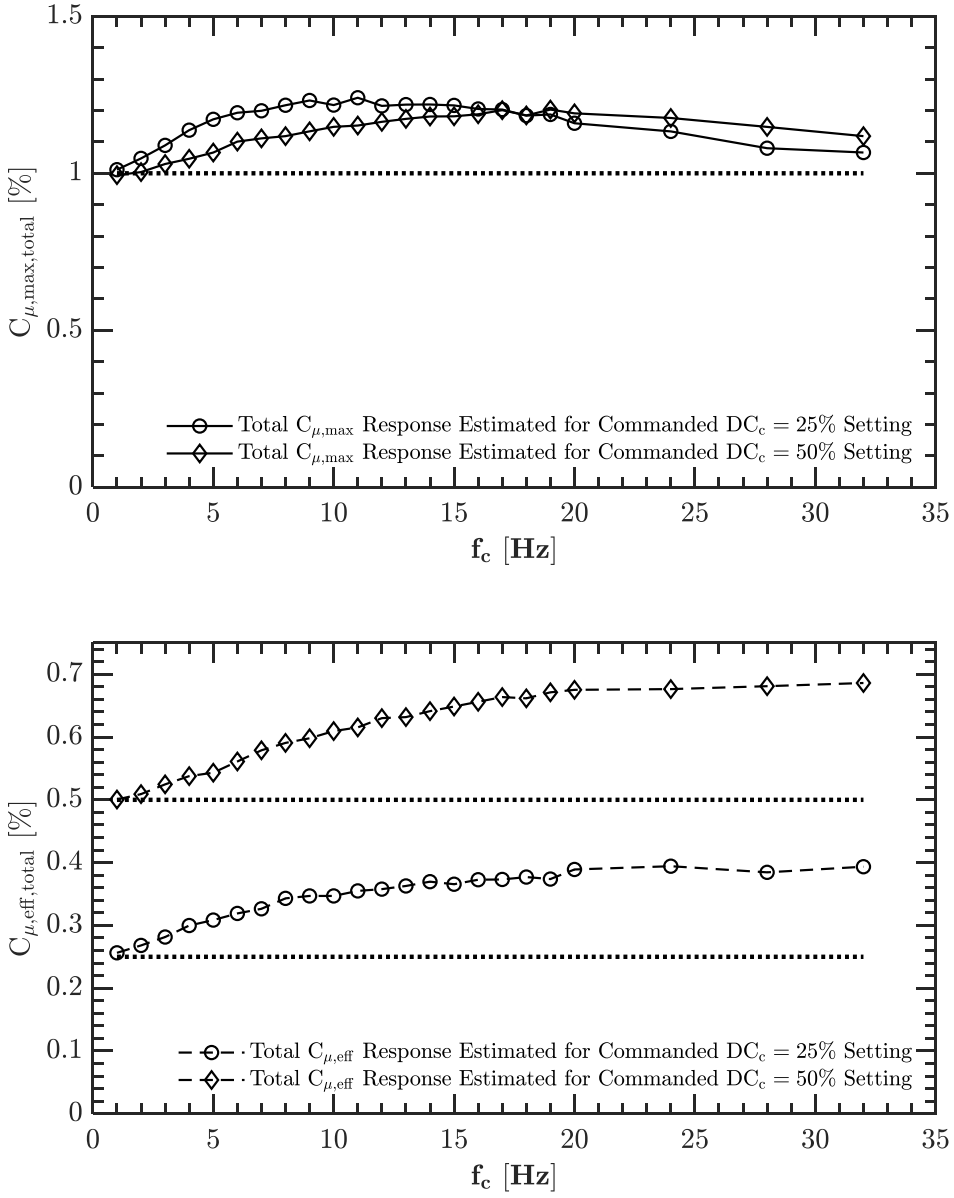

Figure 7.1: Overall calculated maximum $C_{\mu,\max}$ and effective $C_{\mu,\text{eff}}$ momentum coefficient response in comparison to commanded settings.

7.1 Results and Discussions

7.1.1 Surface Pressure Measurements

7.1.1.1 Effect of the Periodic Blowing with Regular Square Waveform Pattern

The effect of periodic blowing in the form of a regular square wave pattern on the flow structure is characterized by surface pressure measurements at a Reynolds number of $Re = 9 \times 10^4$ for four different angles of attack: $\alpha = 12°$, $16°$, $17°$, and $21°$. Figures 7.2, 7.3, 7.4, and 7.5 show the negative pressure coefficient $-C_p$ distributions for regular square wave periodic blowing actuation at varying frequencies for two different duty cycle values, $DC_c = 25\%$ and $DC_c = 50\%$, measured at a dimensionless chordwise station $x/C = 0.5$.

Each figure is constructed using the same approach, with the upper chart representing the results for $DC_c = 25\%$ and the bottom chart representing the results for $DC_c = 50\%$. Considering the size of the experimental matrix for the effect of the excitation frequency f_c, each tested case is represented by a line designated with a color which scaled in jet color bar of MATLAB from blue to red for the excitation frequency range of $0 \leq f_c \leq 64$ Hz. For comparison purposes, cases with no blowing control (black continuous lines), steady blowing $C_\mu = 1\%$ (black dashed lines), steady blowing $C_\mu = 0.5\%$ (black dash-dotted lines), and steady blowing $C_\mu = 0.25\%$ (black dotted lines)are also added to the chart, where applicable. Color bar designation along with no control and steady blowing cases are given in a legend placed at the top of each figure where applicable.

For the angle of attack $\alpha = 12°$, the effect of the excitation frequency ranging from $1 \leq f_c \leq 32$ Hz at a commanded maximum momentum coefficient value of $C_{\mu,\max} = 1\%$ is presented in comparison to the no control and steady blowing conditions with $C_\mu = 1\%$ in Figure 7.2. The no control case exhibits a typical hump-like pattern, which is recognized as the footprint of the vortical flow structure on the wing surface, with the highest peak value occurring at $y/S = 0.58$. For both duty cycle settings, an increase in excitation frequency results in a corresponding increase in the suction peak pressure. This effect is slightly more pronounced for the case of $DC_c = 50\%$

compared to $DC_c = 25\%$. The trend of $-C_p$ for steady blowing with $C_\mu = 1\%$ also indicates an increase in suction pressure peak, potentially moving outward. In the reattachment region observed through the inboard plane around $y/S = 0.35$, characterized by the minimum $-C_p$ value, the implementation of periodic blowing modifies the trend slightly, whereas steady blowing tends to deteriorate reattachment in that region.

For the angle of attack $\alpha = 16°$, the footprint of the vortical structure remains evident in the no control case, with a suction peak region identified around $y/S = 0.50$. The implementation of periodic blowing results in a significant improvement in the $-C_p$ distribution, with an observable increase in suction peak pressure and an outward movement towards $y/S = 0.58$. For $DC_c = 25\%$, the suction peak pressure increases from 9.4% to 42% as the excitation frequency ranges from $f_c = 1$ Hz to $f_c = 64$ Hz. In the case of $DC_c = 50\%$, the improvement is even more pronounced, with the suction peak pressure increasing from 20.2% to 44.4%. For both duty cycle settings, the reattachment region is favorably modified. With steady actuation, the increase in the momentum coefficient enhances the effects of steady blowing. The improvement achieved with steady blowing at $C_\mu = 1\%$ can be matched by regular square wave actuation with a commanded $DC_c = 50\%$ and $f_c = 32$ Hz, which results in an actual total effective momentum coefficient value of $C_{\mu,\text{eff,total}} = 0.65\%$, significantly lower than that observed in the steady case. Furthermore, increases in excitation frequency can also surpass the effects achieved through steady actuation.

Considering the results for the angle of attack $\alpha = 17°$, the footprint of the vortical structure is slightly diminished in the no control case, with a suction peak region observed around $y/s = 0.42$. The implementation of periodic blowing continues to yield significant improvements in the $-C_p$ distribution, with a noticeable increase in suction peak pressure and an outward movement towards $y/S = 0.50$ to $y/S = 0.58$. For $DC_c = 25\%$, the suction peak pressure increases from 16% to 56% as the excitation frequency ranges from $f_c = 1$ Hz to $f_c = 64$ Hz. For $DC_c = 50\%$, the improvement is slightly greater, with the suction peak pressure increasing from 29% to 69%. Similar to the results for $\alpha = 16°$, the increase in the momentum coefficient enhances the effects of steady blowing. For both commanded duty cycle settings, the effects of steady blowing with momentum coefficient values of 0.25% and 0.5% can

be matched and even surpassed by periodic blowing at moderate excitation frequencies, considering the total effective momentum coefficients.

When the angle of attack is increased further to $\alpha = 21°$, the pressure coefficient distribution exhibits a completely flat behavior, clearly indicating the loss of the vortical flow behavior. This phenomenon is associated with entering the stall region, as indicated by the performed force measurements. For both commanded duty cycle settings, an increase in excitation frequency leads to a slight systematic increase in the pressure coefficient value. When the excitation frequency is raised to higher settings, specifically for 24 Hz $\leq f_c$, a recovery in pressure distribution begins to manifest, which is not observed in any of the steady blowing cases.

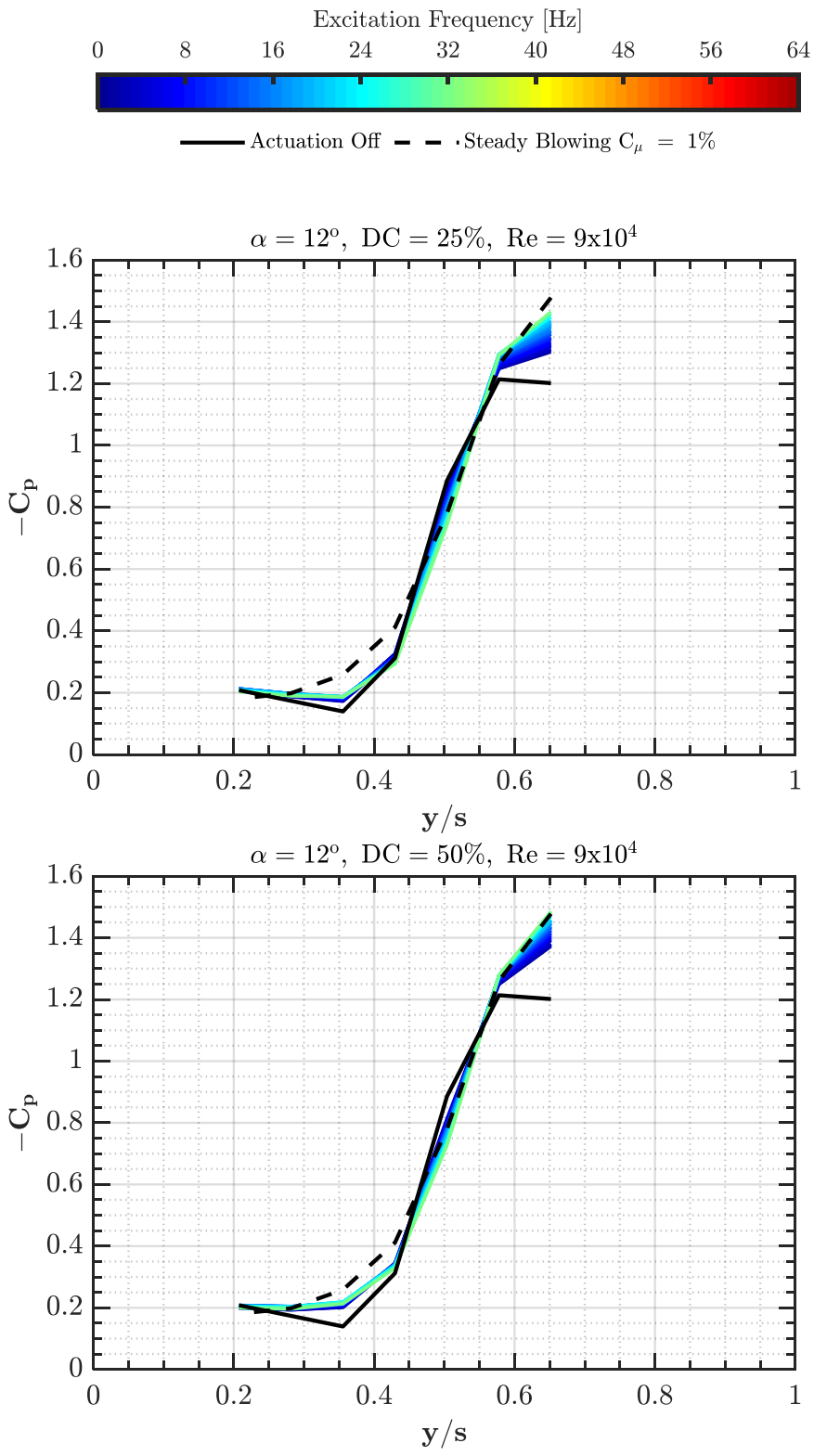

Figure 7.2: $-C_p$ distribution at half span for regular square wave blowing ($f_c = 1-32$ Hz, $DC_c = 25, 50\%$, $C_{\mu,\max} = 1\%$) in comparison to steady blowing cases ($C_\mu = 1\%$) at $\alpha = 12°$, $Re = 9 \times 10^4$.

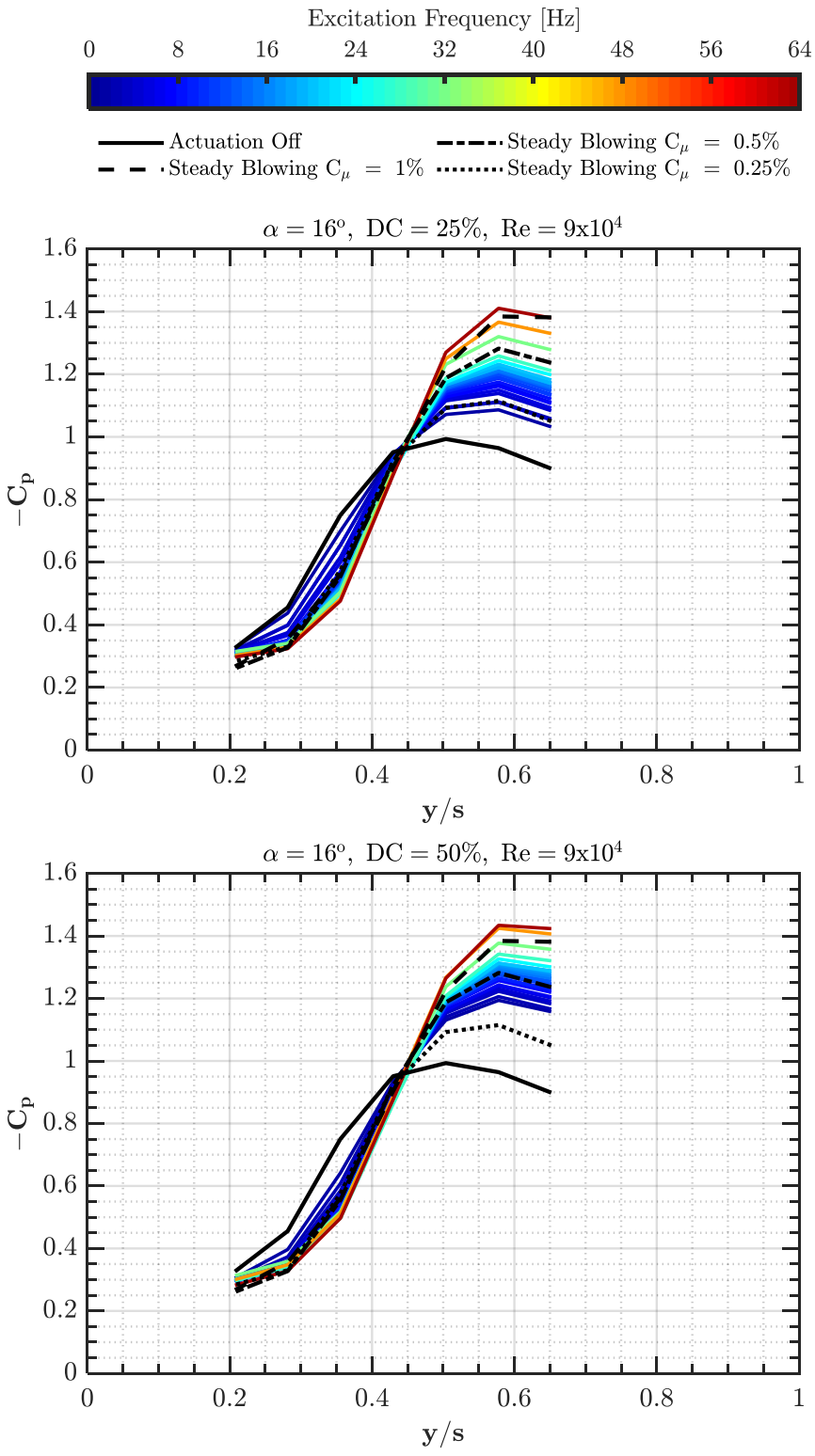

Figure 7.3: $-C_p$ distribution at half span for regular square wave blowing ($f_c = 1-64$ Hz, $DC_c = 25, 50\%$, $C_{\mu,\max} = 1\%$) in comparison to steady blowing cases ($C_\mu = 0.25\%, 0.5\%, 1\%$) at $\alpha = 16°$, $Re = 9 \times 10^4$.

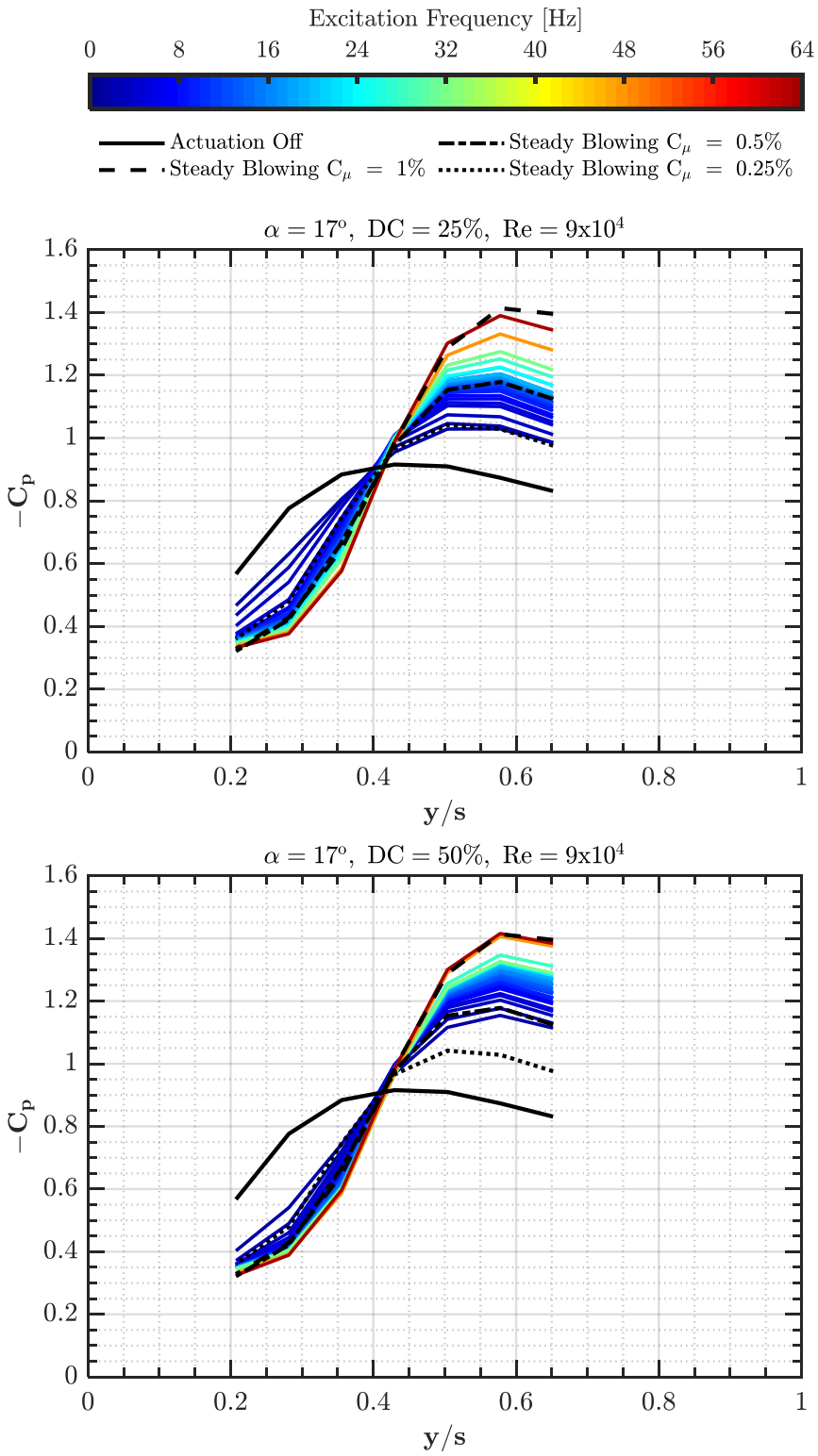

Figure 7.4: $-C_p$ distribution at half span for regular square wave blowing ($f_c = 1-64$ Hz, $DC_c = 25, 50\%$, $C_{\mu,\max} = 1\%$) in comparison to steady blowing cases ($C_\mu = 0.25\%, 0.5\%, 1\%$) at $\alpha = 17°$, $Re = 9 \times 10^4$.

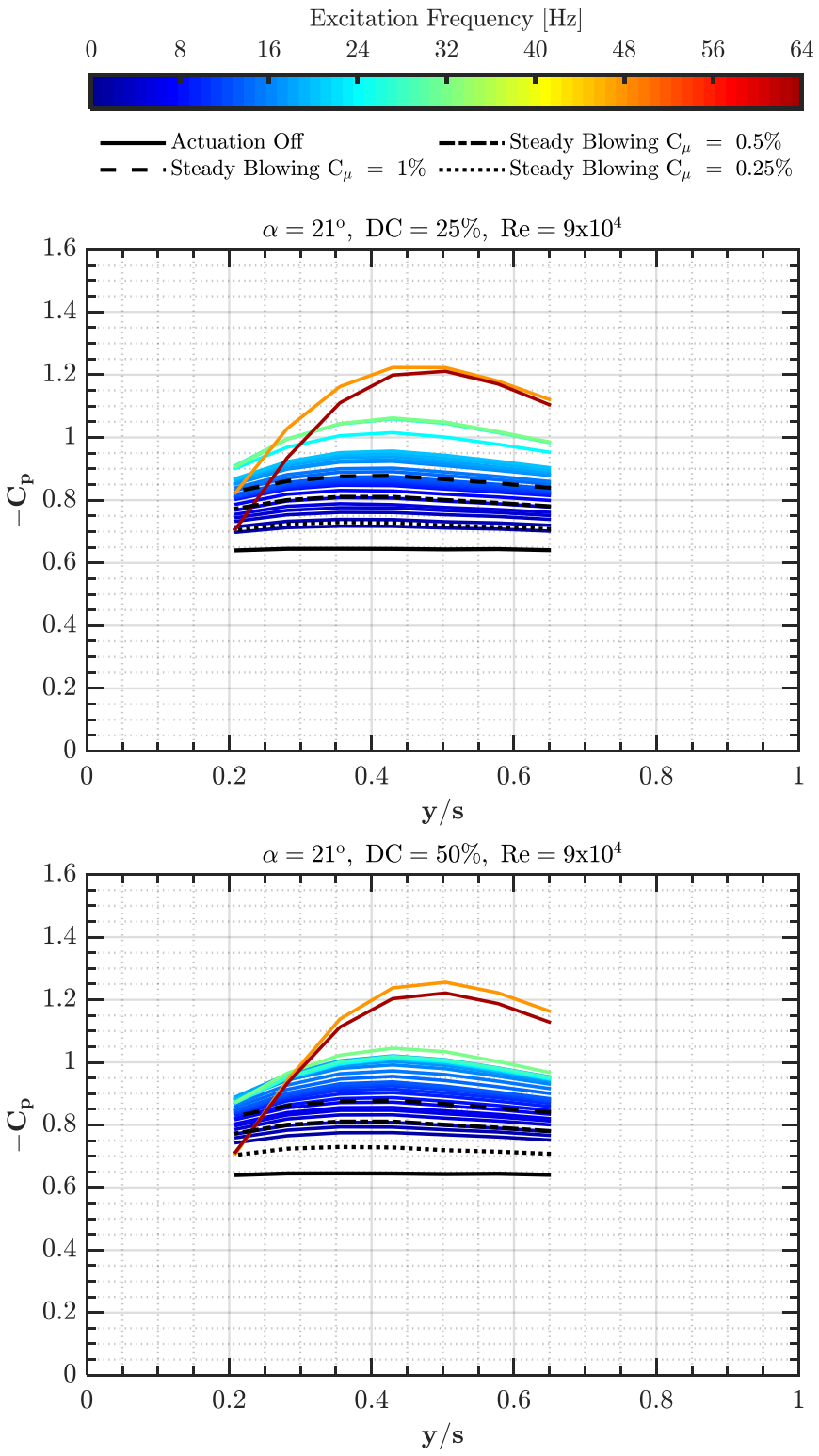

Figure 7.5: $-C_p$ distribution at half span for regular square wave blowing ($f_c = 1-64$ Hz, $DC_c = 25, 50\%$, $C_{\mu,\max} = 1\%$) in comparison to steady blowing cases ($C_\mu = 0.25\%, 0.5\%, 1\%$) at $\alpha = 21°$, $Re = 9 \times 10^4$.

7.1.1.2 Effect of the Periodic Blowing with Burst Modulated Square Waveform Pattern

The effect of periodic blowing in the form of a burst-modulated square wave pattern on the flow structure is characterized by surface pressure measurements at a Reynolds number of $Re = 9{\times}10^4$ for four different angles of attack: $\alpha = 12°$, $16°$, $17°$, and $21°$. Considering the results of the applied technique on surface pressure measurement comprehensively, only charts for $16°$ are shown in the current chapter for representative purposes. Figure 7.6 shows the negative pressure coefficient $-C_p$ distributions for burst-modulated square wave periodic blowing actuation at varying frequencies for two different carrier signal duty cycle values, $DC_c = 25\%$ and $DC_c = 50\%$, and one modulating signal duty cycle value, $DC_m = 50\%$, measured at a dimensionless chordwise station $x/C = 0.5$.

The figure is constructed with a total of six charts, three on each side. The left three charts represent the results for $DC_c = 25\%$ for modulating frequencies $f_m = 1$, $f_m = 3$, and $f_m = 4$ Hz, respectively, from top to bottom. The right three charts represent the results for $DC_c = 50\%$ with the same sequence. As in regular square wave blowing charts, the excitation frequency f_c for each tested case is represented by a line designated with a color that scales from blue to red for the excitation frequency range of $0 \leq f_c \leq 64$ Hz. For comparison purposes, cases with no blowing control (black continuous lines), steady blowing $C_\mu = 1\%$ (black dashed lines), steady blowing $C_\mu = 0.5\%$ (black dash-dotted lines), and steady blowing $C_\mu = 0.25\%$ (black dotted lines) are also included in the charts.

Considering the results for $DC_c = 25\%$, a very similar distribution is obtained for each modulating frequency case. With the injection of the burst-modulated square wave blowing, a recovery in the suction peak pressure coefficient value is observed, where an increase in the carrier signal frequency enhances this benefit. It should be noted that with the activation of the modulating frequency, the total effective momentum coefficient is decreased by a factor of the modulating duty cycle DC_m. Considering the commanded modulating signal excitation frequency values in the context of duty cycle response, no significant change is expected as per the characterization results. Thus, the total effective momentum coefficient in this case is

only half of the values attained in regular square wave blowing excitation. From this perspective, the total effective momentum coefficient for these cases ranges between $0.15\% \leq C_{\mu,\text{eff,total}} \leq 0.2\%$, as can be calculated from Figure 7.1. The effect obtained with steady excitation with $C_\mu = 0.25\%$ momentum coefficient values can be exceeded, whereas the effect of $C_\mu = 0.5\%$ can be achieved with burst-modulated blowing excitation by increasing the carrier frequency with lesser effective momentum coefficient values.

For $DC_c = 50\%$, a very similar improvement trend as in the cases of $DC_c = 25\%$ is observed for each modulating frequency case. The total effective momentum coefficient for these cases ranges between $0.27\% \leq C_{\mu,\text{eff,total}} \leq 0.35\%$, as can be calculated from Figure 7.1 by multiplying the factor $DC_m = 50\%$. The effect obtained with steady excitation with $C_\mu = 0.25\%$ momentum coefficient values can be exceeded, whereas the effect of $C_\mu = 0.5\%$ can be achieved with burst-modulated blowing excitation by increasing the carrier frequency with slightly lesser effective momentum coefficient values.

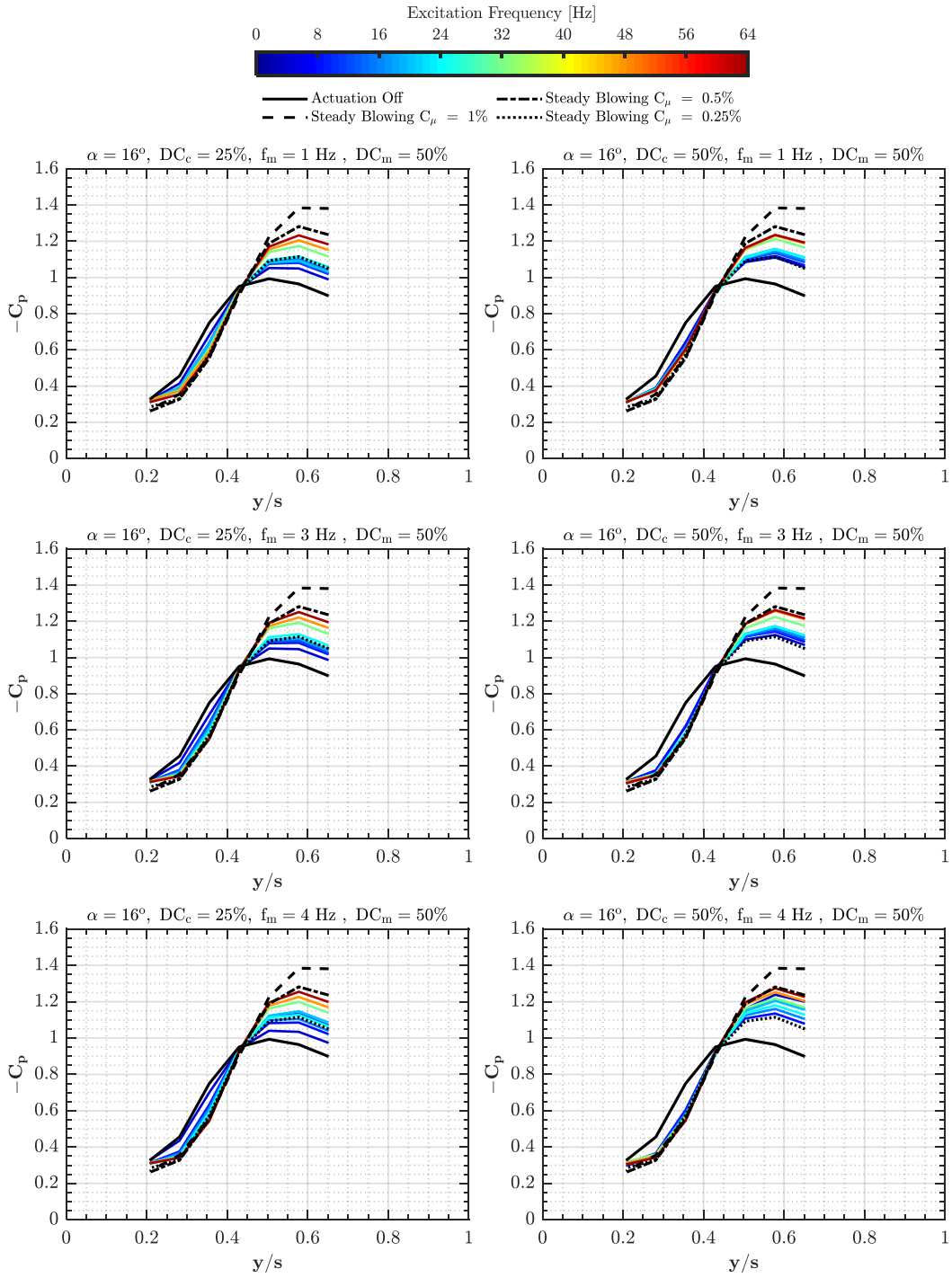

Figure 7.6: $-C_p$ distribution at half span for burst modulated square wave blowing ($f_c = 4, 8, 12, 16, 20, 24, 32, 48, 64$ Hz, $DC_c = 25, 50\%$, $f_m = 1, 3, 4$ Hz, $DC_m = 50\%$, $C_{\mu,\max} = 1\%$) in comparison to steady blowing cases ($C_\mu = 0.25\%, 0.5\%, 1\%$) at $\alpha = 21°$, $Re = 9 \times 10^4$.

7.1.1.3 Analysis of Surface Pressure Measurements: Temporal Behavior and Spectral Content

The surface pressure measurements have been primarily utilized to report the mean behavior at each measurement location. Despite the detailed investigation not being possible due to significant acoustic damping associated with the pneumatic tubing length between the pressure scanner and wing models, it is still considered that the temporal behavior and spectral content analysis of pressure data would provide valuable insights into the contribution of periodic blowing. For that purpose, the root mean square (RMS) and the one-sided power spectral density of the pressure coefficient is discussed for regular square wave blowing cases representatively.

RMS distributions for the surface pressure coefficient are given in Figure 7.7 and Figure 7.8 for $\alpha = 16°$ and $\alpha = 21°$ respectively, utilizing the following Eqn. 7.4.

$$C_{p,\text{RMS}} = \frac{p_{\text{RMS}}}{p_{\text{dyn}}} \tag{7.4}$$

Both figures are constructed using the same approach utilized in C_p charts. For the angle of attack $\alpha = 16°$, the no-control case represents RMS values varying between 0.05 and 0.1, with the peak value observed around $y/S = 0.36$. Considering the results of $DC_c = 25\%$ cases, periodic blowing alters the RMS distribution considerably, particularly at $y/S = 0.36$ and $y/S = 0.65$. The outboard station represents higher fluctuations, which decrease with increasing frequency. For the steady blowing cases, a slight decrease in RMS distribution is observed. Very similar observations are valid for the results of $DC_c = 50\%$ regular square wave blowing cases.

For the angle of attack $\alpha = 21°$, the no-control case represents an RMS distribution that does not show significant variation across the measured span, with values around 0.06 to 0.1. Considering the results of $DC_c = 25\%$ cases, starting with the lowest tested frequency $f_c = 1$ Hz, a considerable shift in the distribution appears, which decreases with increasing frequency up to $f_c = 24$ Hz. A further increase in frequency shows a reversal in behavior, and variations across the span start to appear. Very similar observations are valid for the results of $DC_c = 50\%$ cases.

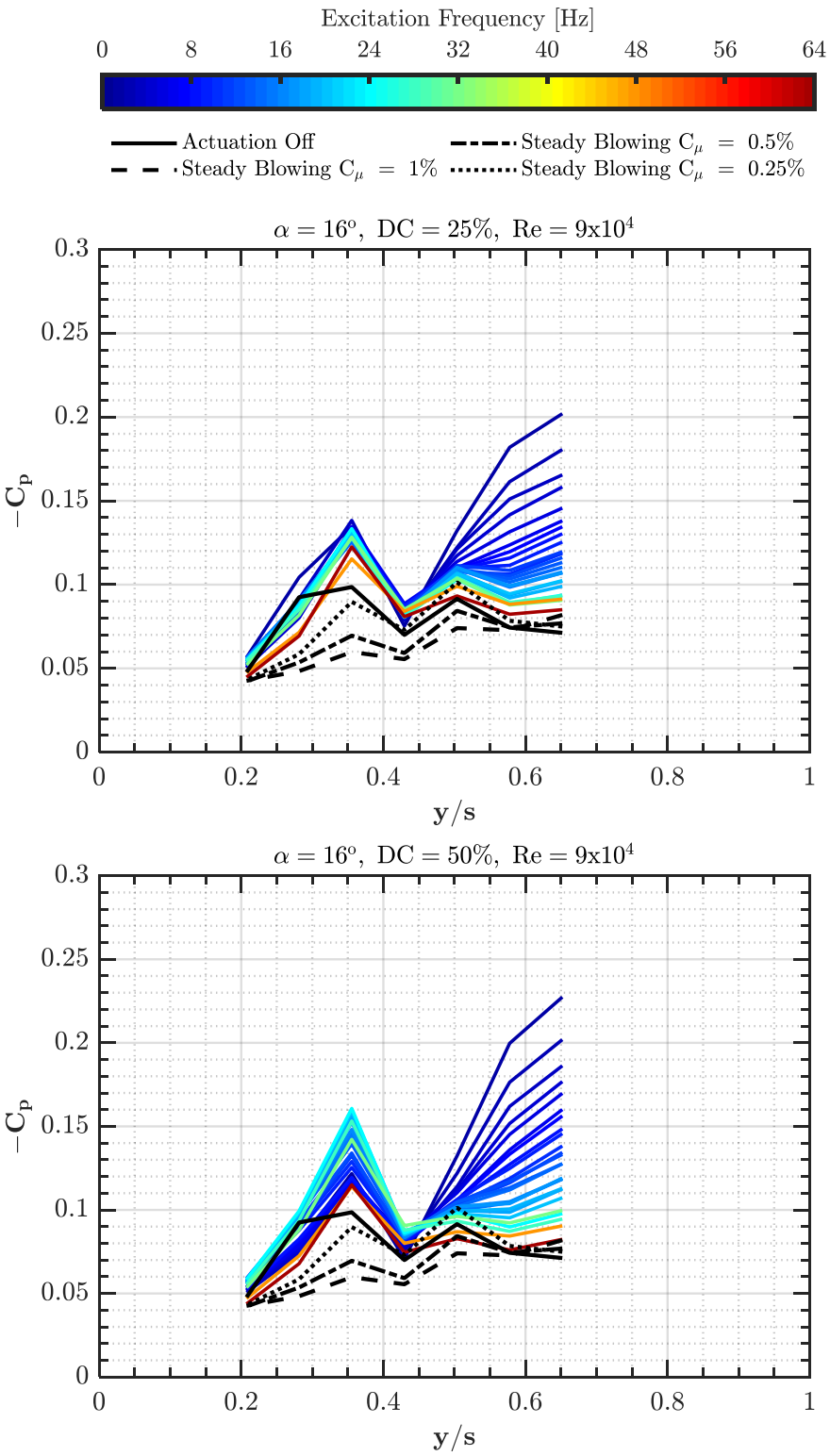

Figure 7.7: RMS of C_p distribution at half span for regular square wave blowing ($f_c = 1 - 64$ Hz, $DC_c = 25, 50\%$, $C_{\mu,\max} = 1\%$) in comparison to steady blowing cases ($C_\mu = 0.25\%, 0.5\%, 1\%$) at $\alpha = 16°$, $Re = 9 \times 10^4$.

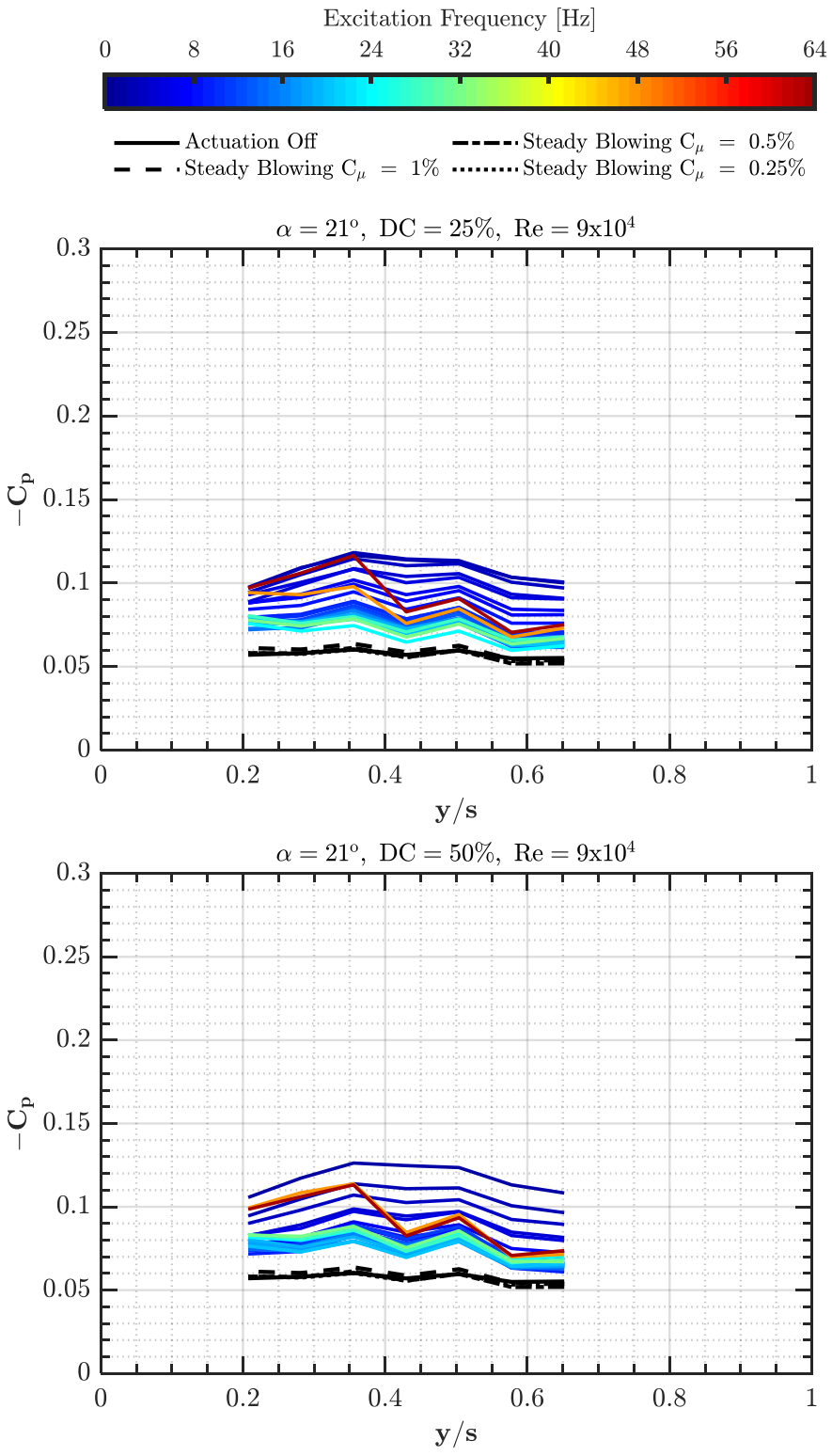

Figure 7.8: RMS of C_p distribution at half span for regular square wave blowing ($f_c = 1 - 64$ Hz, $DC_c = 25, 50\%$, $C_{\mu,\max} = 1\%$) in comparison to steady blowing cases ($C_\mu = 0.25\%, 0.5\%, 1\%$) at $\alpha = 21°$, $Re = 9 \times 10^4$.

The one-sided power spectral density (PSD) of the surface pressure coefficient is estimated using the Fast Fourier Transform (FFT) and is represented in Figure 7.9 at $\alpha = 16^{\circ}$ for $DC_c = 25\%$ regular square wave periodic blowing cases of representative excitation frequencies $f_c = [4, 10, 20, 32]$. For comparison purposes, no control and steady blowing with $C_\mu = 1\%$ cases are also added to the charts. Each condition is represented with a three-dimensional plot where the x-axis represents the frequency estimate, the y-axis represents the spanwise location of pressure tabs, and the z-axis represents the one-sided PSD.

Considering the results for the no-control case, no distinct frequency is observed for all measurement tabs, which is also valid for the steady blowing case. The effect of the periodic excitation is barely observed for all represented cases in the spectral domain. Smaller frequencies exhibit higher spectral content at outboard locations, whereas this behavior shifts inboard with increasing excitation frequency. This observation is quite in line with the aforementioned discussions made with RMS distributions. Considering the z-axis of each plot for spectral content, the order of magnitude is significantly smaller compared to mean C_p distributions.

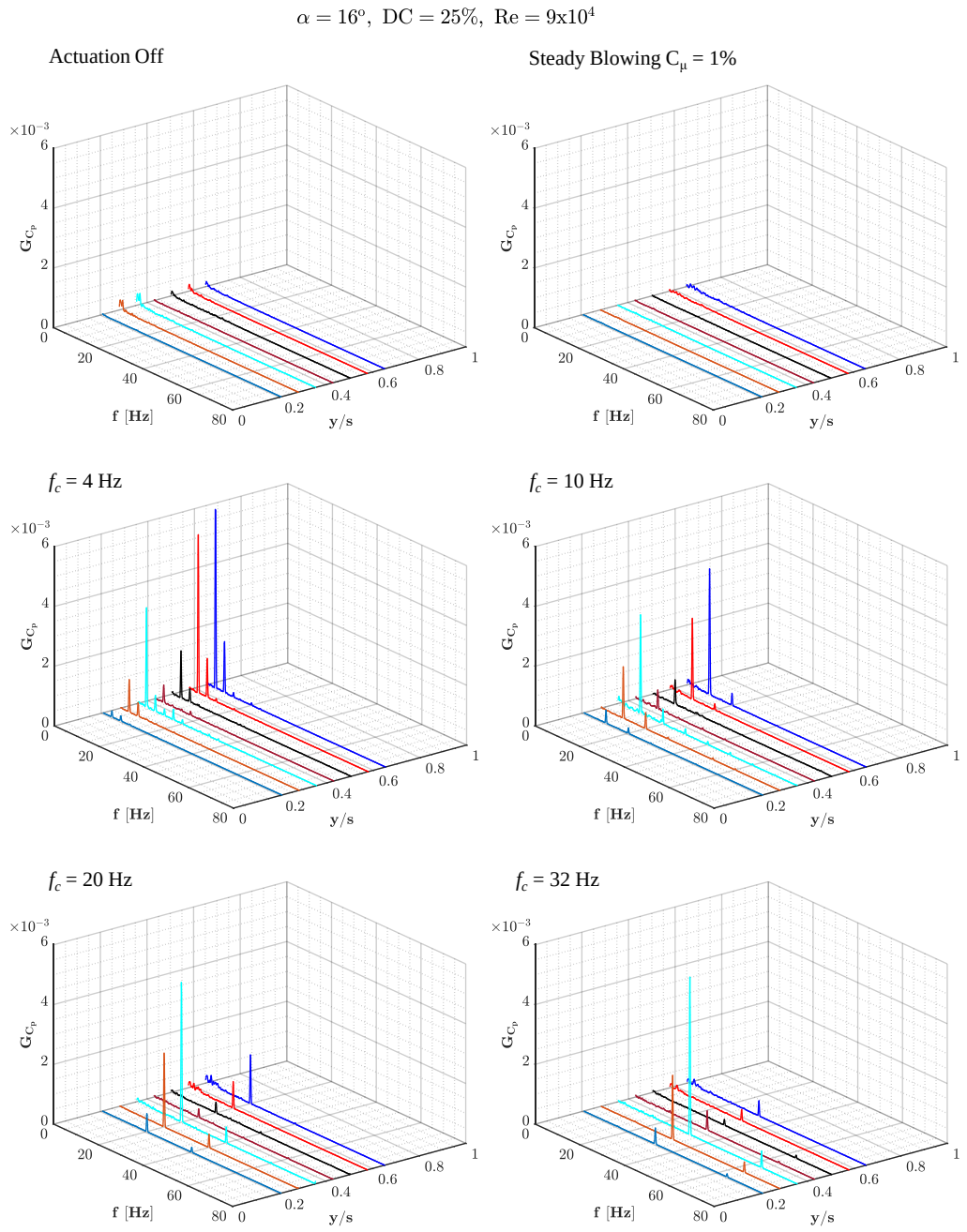

Figure 7.9: One sided power spectral density of C_p distribution at half span for regular square wave blowing ($f_c = [4, 10, 20, 32]$ Hz, $DC_c = 25\%$, $C_{\mu,\max} = 1\%$) in comparison to steady blowing ($C_\mu = 1\%$) at $\alpha = 16°$, $Re = 9 \times 10^4$.

7.1.2 Aerodynamic Force and Moment Measurements

7.1.2.1 Effect of Tubing

As explained in Chapter 3 in detail, the blowing flow is supplied to the wing model using flexible plastic pneumatic tubings. Prior to starting aerodynamic measurements, spot check experiments were performed to investigate the effect of the tubing on the force balance system, assuming that flexible tubes could create additional tension or bending in the mounting strut. For this purpose, measurements were taken for both connected and disconnected tubing cases during no blowing actuation conditions. Figure 7.10 shows the distributions of drag coefficient C_D, lift coefficient C_L, lift-to-drag ratio C_L/C_D, and pitching moment coefficient C_M at the trailing edge as a function of the angle of attack range $0^\circ \leq \alpha \leq 30^\circ$.

Considering the results of the drag coefficient distribution shown in the top left chart of Figure 7.10, the inclusion of the pneumatic tubing causes a systematic increase in the overall distribution with a very similar trend over the entire angle of attack range, as expected. For lift and pitching moment coefficient distributions, the effect of the tubing appears to be minor, with a very slight deviation in the post-stall regime. The systematic shift in the drag distribution also results in degradation in the lift-to-drag coefficient. Reporting the effect of the tubing is considered an initial step before discussing the effect of periodic blowing on force measurements. In the following sections, results of the periodic excitation include the effect of the tubing, and comparisons should be considered for the baseline case with no actuation, including the tube connections.

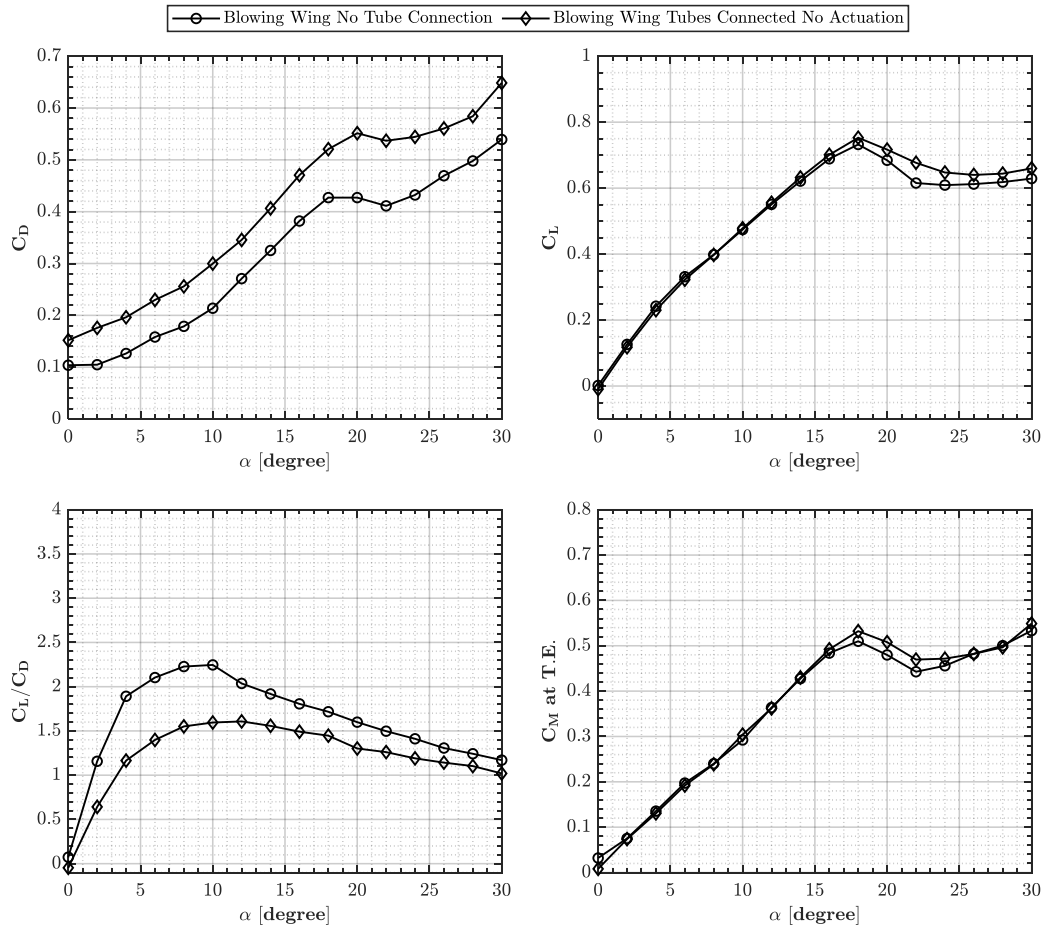

Figure 7.10: Distributions of drag coefficient C_D, lift to drag ratio C_L/C_D, lift coefficient C_L, and pitching moment coefficient at trailing edge C_M: effect of tubing connection for blowing wing at Re $= 9 \times 10^4$.

7.1.2.2 Effect of the Periodic Blowing with Regular Square Waveform Pattern

In Figure 7.11 and 7.12, distributions of drag coefficient C_D, lift coefficient C_L, lift to drag ratio C_L/C_D and pitching moment coefficient C_M at the trailing edge are given as a function of angle of attack for regular square wave periodic blowing cases of carrier duty cycle values of $DC_c = 25\%$ and $DC_c = 50\%$ respectively a function of the angle of attack range $0° \leq \alpha \leq 30°$.For comparison purposes, cases with no blowing control (black continuous lines), and steady blowing $C_\mu = 1\%$ (black dashed lines) are also added to the charts in each figure. As mentioned earlier in the text, since

the effect of the higher frequencies were found more favorable in surface pressure measurement, $f_c = [20, 28, 32, 48]$ Hz excitation frequencies are investigated at commanded duty cycle values of $DC_c = [25, 50]\%$. These cases are also represented with continuous lines having same color scale used in pressure coefficient charts with respect to f_c.

Considering the results of the drag coefficient distribution shown in the top left chart of Figure 7.11 for $DC_c = 25\%$, periodic and steady blowing actuation does not generate additioal drag in the range of $0° \leq \alpha \leq 18°$. Beyond $\alpha = 18°$, the no control case indicates a settled C_D distribution up to $\alpha = 24°$, whereas further increase in angle of attack up to $\alpha = 28°$ results in linear increase in C_D. In this region, for periodic blowing cases the trend observed with no control case is shifted upwards with increasing excitation frequency which also observed for steady blowing case. The results presented for $DC_c = 50\%$ in Figure 7.12 also represent very similar behavior.

Considering the lift coefficient distribution shown in the top right chart of Figure 7.11, the no control case demonstrates typical stall characteristics around $\alpha = 18°$ with $C_{L,\text{max}} = 0.75$, beyond which a considerable loss is observed. The lift curve slope, representing the so-called linear regime, is slightly modified in the presence of periodic blowing, becoming apparent beyond $\alpha = 6°$. A significant increase in the stall angle, accompanied by an improvement in the maximum lift coefficient, is observed with regular square wave periodic blowing. For carrier excitation frequencies of $f_c = 20$, $f_c = 28$, and $f_c = 32$ Hz, the stall angle is observed around $\alpha = 20°$ with a similar maximum lift coefficient value of $C_{L,\text{max}} = 0.80$ to 0.81. Further increasing the excitation frequency to $f_c = 48$ Hz delays the stall angle up to $\alpha = 22°$, with $C_{L,\text{max}} = 0.85$. Beyond the stall angles for each tested case, increasing the excitation frequency results in an increase in the lift coefficient distribution. The results of the steady blowing case with $C_\mu = 1\%$ also delay the stall angle up to $\alpha = 20°$ with a similar lift value, though the behavior with increasing attack angle is slightly less favorable compared to periodic actuation cases. The results presented for $DC_c = 50\%$ in Figure 7.12 also demonstrate very similar behavior. It should also be noted that in the linear regime, increasing the duty cycle further modifies the distribution, resulting in patterns very similar to those observed with steady blowing cases.

To discuss the aerodynamic performance of the periodic blowing technique, the lift-to-drag ratio C_L/C_D is shown in the bottom left charts of Figures 7.11 and 7.12. The increase in the lift coefficient under blowing conditions appears to compensate for the increase in the drag coefficient. Thus, all the conditions exhibit very similar behavior across the entire angle of attack range.

In the bottom right charts of Figures 7.11 and 7.12, the variation of the pitching moment coefficient C_M at the trailing edge (T.E.) as a function of angle of attack is represented. For the no control case, the linear positive slope extends up to $\alpha = 18^\circ$ and becomes negative beyond that angle, which can be considered the moment stall angle. When periodic blowing cases are investigated, the slope appears to be very similar in the linear regime, with a slight modification observed in the angle of attack range $6^\circ \leq \alpha \leq 12^\circ$. With periodic blowing, the moment stall angle can be delayed up to $\alpha = 20^\circ$ to 22° with increasing excitation frequency. The decay of the pitching moment can also be decreased beyond the stall angle with periodic blowing. Considering the results of steady blowing actuation with $C_\mu = 1\%$, the linear regime slope is maintained with a slight upward shift, and the moment stall can be delayed up to $\alpha = 20^\circ$.

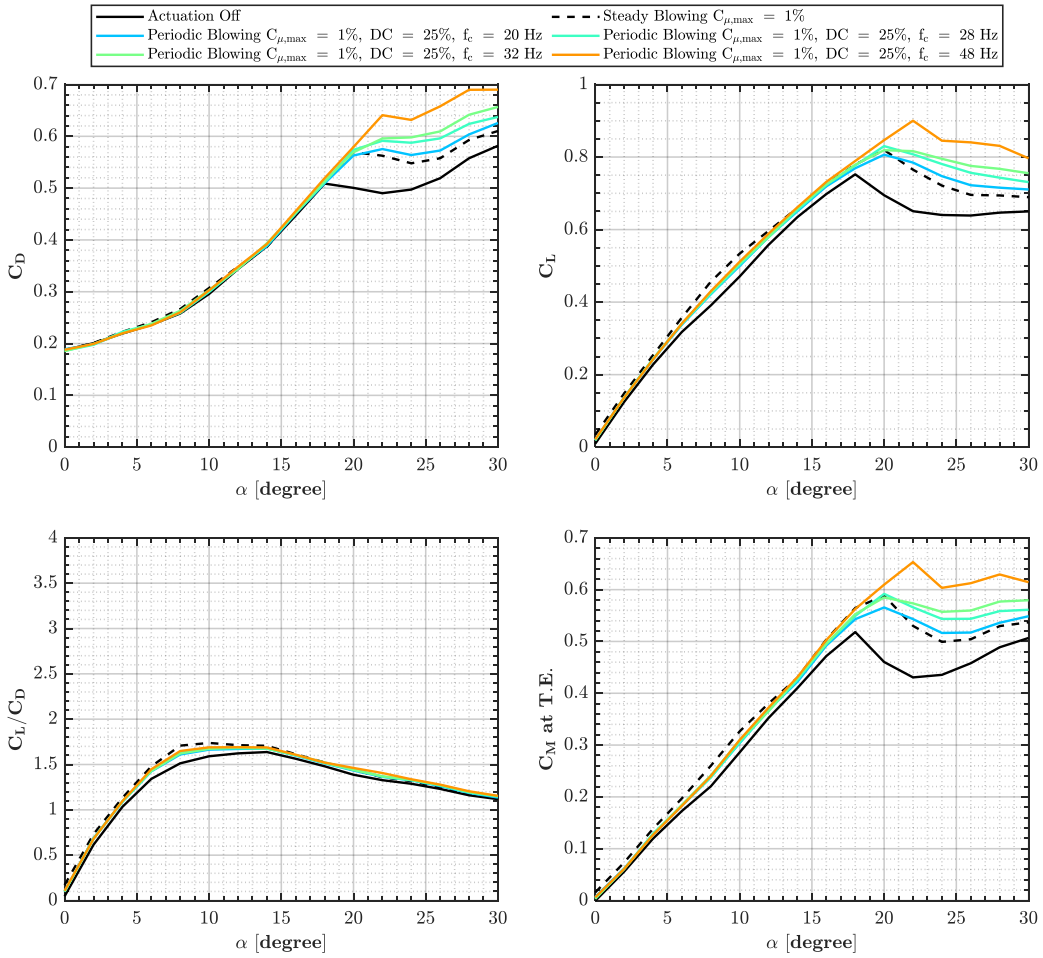

Figure 7.11: Distributions of drag coefficient C_D, lift to drag ratio C_L/C_D, lift coefficient C_L, and pitching moment coefficient at trailing edge C_M: regular square wave blowing ($f_c = [20, 28, 32, 48]$ Hz, $DC_c = 25\%$, $C_{\mu,\max} = 1\%$) in comparison to steady blowing cases ($C_\mu = 1\%$), at $Re = 9 \times 10^4$.

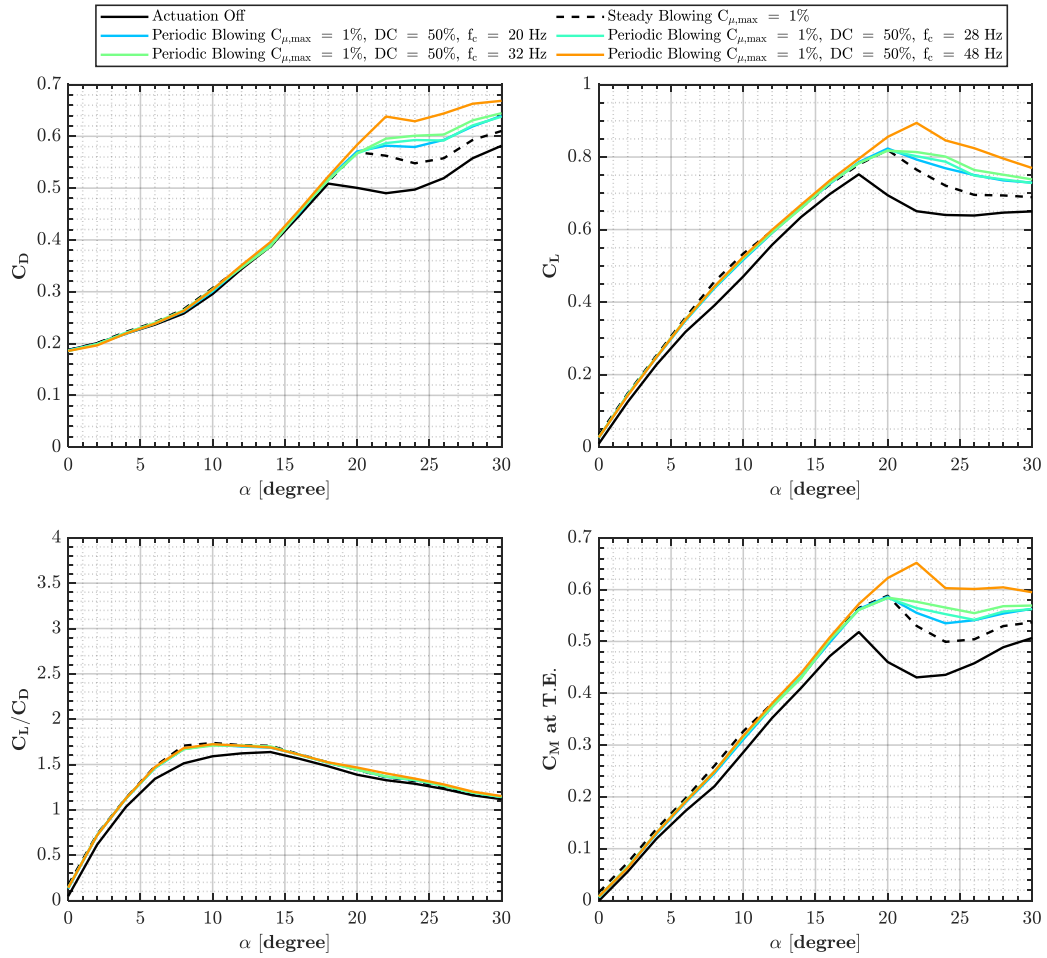

Figure 7.12: Distributions of drag coefficient C_D, lift to drag ratio C_L/C_D, lift coefficient C_L, and pitching moment coefficient at trailing edge C_M: regular square wave blowing ($f_c = [20, 28, 32, 48]$ Hz, $DC_c = 50\%$, $C_{\mu,\max} = 1\%$) in comparison to steady blowing cases ($C_\mu = 1\%$), at $Re = 9 \times 10^4$.

7.1.2.3 Effect of the Periodic Blowing with Burst Modulated Square Waveform Pattern

In Figure 7.13, the distributions of drag coefficient C_D, lift coefficient C_L, lift-to-drag ratio C_L/C_D, and pitching moment coefficient C_M at the trailing edge are given as a function of angle of attack for burst modulated square wave periodic blowing cases with carrier duty cycle values of $DC_c = 25\%$ over the angle of attack range $0° \leq \alpha \leq 30°$. For comparison purposes, cases with no blowing control (black continuous

lines) and steady blowing $C_\mu = 1\%$ (black dashed lines) are also included in the force and moment coefficient charts. As in the regular square wave blowing cases, since the effect of the higher frequencies was found to be more favorable in surface pressure measurements, excitation frequencies of $f_c = [20, 28, 32, 48]$ Hz are investigated at a commanded carrier duty cycle value of $DC_c = 50\%$. For the modulating signal, only the modulating frequency of $f_m = 3$ Hz is presented here with a duty cycle setting of $DC_m = 50\%$. Since no significant difference with modulating frequency was observed, the results for $f_m = 4$ Hz are presented in Appendix C.

Similar to the regular blowing cases, similar improvement characteristics are observed for burst modulated excitation with very similar stall delay characteristics in the lift and pitching moment distributions. As discussed earlier, the total effective momentum coefficient is almost half of the cases tested with regular blowing. The results indicate that the effect of the reduced momentum injection is apparent in drag modification at high angles of attack. The improvement in the post-stall regime obtained with steady blowing can be achieved and even exceeded with periodic blowing, which is also observed for the pitching moment beyond the stall region.

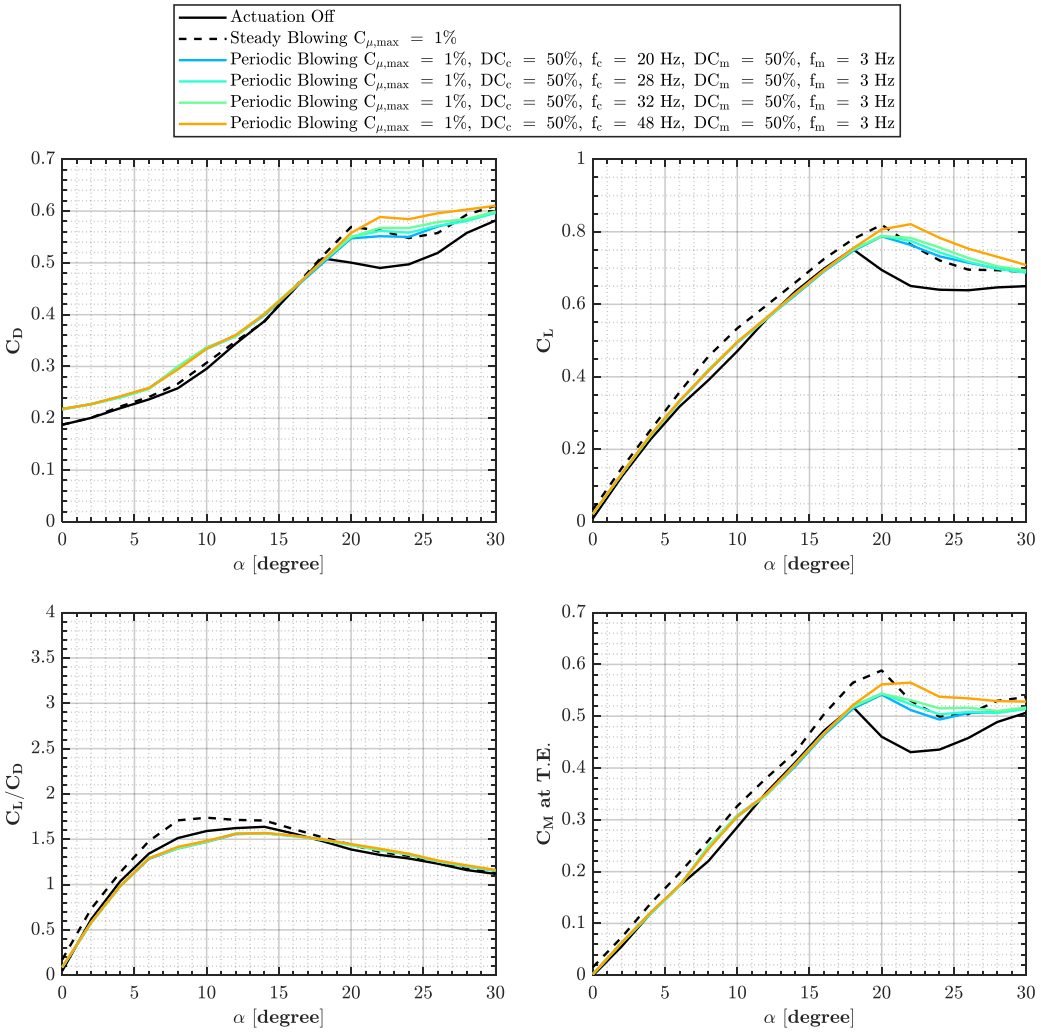

Figure 7.13: Distributions of drag coefficient C_D, lift to drag ratio C_L/C_D, lift coefficient C_L, and pitching moment coefficient at trailing edge C_M: burst modulated square wave blowing ($f_c = [20, 28, 32, 48]$ Hz, $DC_c = 50\%$, $f_m = 3$ Hz, $DC_m = 50\%$, $C_{\mu,\text{max}} = 1\%$) in comparison to steady blowing cases ($C_\mu = 1\%$), at $Re = 9 \times 10^4$.

7.2 Conclusions

The current chapter presents the effects of periodic blowing, applied in both regular and burst-modulated square wave forms, on the flow structures of a non-slender delta wing with a sweep angle $\Lambda = 45°$ using quantitative measurement techniques,

including surface pressure and aerodynamic force measurements. The experiments were performed in a low-speed wind tunnel at Reynolds numbers $Re = 9 \times 10^4$ for the angle of attack range of $0^\circ \leq \alpha \leq 30^\circ$. Considering the collective evaluations of the surface pressure coefficient distributions and aerodynamic force measurements, the principal findings are as follows:

1. With a regular square wave blowing pattern, significant improvements can be obtained in surface pressure coefficient distribution even at high angles of attack, where an increase in excitation frequency and duty cycle enhances the impact of the technique.

2. With a burst-modulated square wave blowing pattern, the total effective momentum coefficient is reduced by almost half, and lower additional frequency content can be injected into the flow field. Although considerable improvements can be achieved in surface pressure coefficient distributions, they are limited compared to regular square wave patterns.

3. With proper signal conditions, the effects on surface pressure measurements obtained using steady blowing actuation can be matched and even exceeded with periodic blowing actuation at lower effective momentum coefficient values.

4. Aerodynamic force measurements reveal that periodic blowing applied through the leading edges significantly improves the lift stall and moment stability characteristics, allowing lift stall up to $\alpha \approx 22^\circ$ with an accompanying increase in the maximum lift coefficient value. Additionally, pitching moment characteristics are significantly altered, delaying the moment stall and reducing the decay characteristics beyond that angle, which provides additional control power in the pitch axis. The application of periodic blowing results in an increase in drag coefficient C_D, but the improvement in lift coefficient prevents any degradation in C_L/C_D performance. The improvement obtained with steady blowing, particularly in the stall region, can be significantly exceeded with periodic excitation.

To conclude, the results suggest that periodic blowing excitation is successful in manipulating the aerodynamic behavior and cross-flow surface pressure distributions,

allowing significant improvements in lift and stability characteristics and considerable recoveries in the flow field. Such a technique shows potential for effective use in designing active blowing systems, particularly targeting the stall and stability characteristics of non-slender delta wing planforms.

CHAPTER 8

CONCLUSIONS AND RECOMMENDATIONS

This investigation focuses on the characterization and effects of passive and active flow control techniques on the flow structures of a 45° swept nonslender delta wing. Such planforms serve as simplified representatives of unmanned combat air vehicles (UCAVs), offering numerous advantages, including high maneuverability, agility, and a favorable structural-weight-to-take-off-weight ratio. As the transition from conceptual design to operational vehicles accelerates, concerns regarding performance, efficiency, and stability have become central to the aerospace community. Delta wing planforms may experience degradation in aerodynamic performance due to complex flow physics during critical flight phases, such as landing, takeoff, and maneuvering at high pitch and yaw rates. These phases often involve high angles of attack and sideslip, conditions under which delta wings can exhibit deteriorated performance due to unsteady flow and three-dimensional surface separation. Despite the complexity of these flow structures, there remains a limited body of research investigating the flow physics associated with nonslender wings.

In the passive flow control component of this study, the effects of a novel bleeding geometry design featuring a nozzle cross-section intended to enhance bleeding momentum were examined. Furthermore, a method for estimating the passive bleeding momentum coefficient was developed based on surface pressure measurements, utilizing the Bernoulli equation and a loss coefficient. In the active flow control segment, the study investigates the impact of periodic blowing in the form of square waves applied through the leading edges. Prior to these measurements, a comprehensive characterization of the flow control system was performed using in-situ approaches to test and construct calibration charts for each control parameter.In the present series

of investigations, a combination of experimental approaches, including surface pressure measurements, hot wire anemometry, force measurements, and particle image velocimetry (PIV), have been employed.

8.1 Passive Bleeding Flow Control

8.1.1 Passive Bleeding Momentum Estimation

Considering the combined assessments from the two-stage calibration effort and wind tunnel measurements, the principal findings are summarized as follows:

- In the initial stage, a typical hot wire response was obtained for the well-known bleed slot exit via supply flow at tunnel-off settings, referred to as the first transfer function (TF1). This function is used for simultaneous pressure tap and hot wire comparisons and characterization steps.
- During Stage 2 of the characterization scheme, the bleed exit velocity, exhibited a linear relationship with increasing upstream velocity. This measurement overestimated the exit conditions compared to the hot wire response, which represents the local actual measurements. The systematic parabolic relationship between the two estimation methods of bleed exit velocity indicates the need for computing a correction loss coefficient, where consistent loss behavior was observed across the tested calibration range.
- When the average across-slot loss coefficient was applied in actual wind tunnel tests, surface pressure taps effectively estimated the bleed slot flow responses at different aerodynamic regimes, including the linear maximum lift and stall onset regions, based on the angle of attack.

Overall, the results suggest that surface pressure taps, positioned near the bleeding slot inlets and outlets on a nonslender delta wing, can effectively estimate the across-slot momentum coefficients once a controlled calibration scheme is implemented. The systematic approach and observed behaviors are valuable for characterizing the

effectiveness of passive bleeding flow control concerning measured aerodynamic performance.

8.1.2 Passive Bleeding Flow Control With Nozzle Type Slots

Considering the comprehensive evaluations of the surface pressure coefficient distributions, surface velocity fields, and aerodynamic force measurements, the principal findings are summarized as follows:

- The introduction of nozzle bleeding slots effectively mitigates or modifies the three-dimensional surface separation on the baseline wing model, particularly near stall incidences, thereby promoting favorable reattachment. This is evidenced by the increases in surface normal positive vorticity contours, axial positive streamwise velocity contours, and recoveries in $-C_p$ distribution. Even at higher angles of attack ($\alpha = 20^\circ$), velocity field results demonstrate that the dominance of flow reversal can be controlled with nozzle slots. Specifically, CR075 significantly deflects and relocates the focal point of the three-dimensional surface separation, resulting in a considerable increase in positive streamwise velocity.

- Aerodynamic force measurements indicate that the nozzle bleeding slots notably enhance lift stall and moment stability characteristics. CR075, in particular, delays the lift stall by approximately $\Delta\alpha \approx 6^\circ$, accompanied by an increase in the maximum lift coefficient. Additionally, the pitching moment characteristics are significantly altered, preventing moment stall and replacing it with a constant distribution at high angles of attack.

In conclusion, the results suggest that the proposed passive nozzle bleeding slots effectively manipulate the surface flow field by preventing or modifying three-dimensional surface separation, thereby improving lift and stability characteristics. Despite an increase in drag distribution, this technique shows potential for effective application in the design of an active bleeding system, particularly targeting the stall and stability characteristics of nonslender delta wing planforms.

8.2 Periodic Blowing Active Flow Control

8.2.1 Characterization of Active Flow Control System

Based on the combined assessments obtained from characterization experiments for the in-house active flow control system, the following conclusions can be drawn:

- The in-situ calibration approach effectively estimates the periodic blowing response by accurately capturing the spectral content, particularly when the blowing hole geometry is comparable in size to the hot wire probe. A key advantage of this in-situ calibration scheme is that, despite variations in calibration coefficients among different blowing holes, the agreement within each station is found to be quite satisfactory.
- The response of the blowing velocity to excitation frequency is found to be similar for forward and aft stations, such that an increase in excitation frequency results in deviations from the reference steady blowing setting. In contrast, for the middle station, these deviations are quite limited. The duty cycle response for all stations shows a linear variation with increasing frequency. At the maximum tested frequency, the maximum variation in DC is approximately 10% for the forward and middle stations, whereas, for the middle blowing holes, the deviations are more significant, with the estimated maximum difference reaching about 19%.
- For different regulator settings aimed at greater steady momentum coefficient values ($C_\mu = 2\%$ and 3%), the deviation behavior of the valve-on state mean blowing velocity relative to the steady reference blowing velocity with increasing excitation frequency is found to be quite similar to the behavior observed at the $C_\mu = 1\%$ setting.

To report the effectiveness of active flow control blowing systems accurately, the actual momentum injected during flow control actuation should be well identified, thus establishing a systematic relation with aerodynamic flow conditions. The results indicate that characterizing such an in-house active flow control system based on fast-switching pneumatic valve actuation is valuable for understanding the sensitivity of

blowing response to control parameters, including excitation frequency, duty cycle, and momentum coefficient. Factors such as blowing hole geometry and pipeline installation layout are critical in this characterization.

8.2.2 Periodic Blowing Active Flow Control

Considering the comprehensive evaluations of the surface pressure coefficient distributions and aerodynamic force measurements, the principal findings are as follows:

- Employing a regular square wave blowing pattern leads to significant improvements in the surface pressure coefficient distribution, even at high angles of attack. An increase in excitation frequency and duty cycle enhances the efficacy of this technique. Conversely, utilizing a burst-modulated square wave blowing pattern reduces the total effective momentum coefficient by the modulating duty cycle ratio, thereby introducing lower additional frequency content into the flow field.
- Under optimal signal conditions, the effects on surface pressure measurements achieved using steady blowing actuation can be matched or even surpassed with periodic blowing actuation at lower effective momentum coefficient values.
- Aerodynamic force measurements indicate that periodic blowing through the leading edges significantly enhances lift stall and moment stability characteristics. This method allows lift stall up to $\Delta\alpha \approx 4 - 5^{\circ}$ with an accompanying increase in the maximum lift coefficient. Additionally, pitching moment characteristics are significantly modified, delaying the moment stall and reducing the decay characteristics beyond that angle, thus providing additional control power in the pitch axis.

In conclusion, the results suggest that periodic blowing excitation is effective in manipulating aerodynamic behavior and cross-flow surface pressure distributions, resulting in substantial improvements in lift and stability characteristics and significant recoveries in the flow field. This technique demonstrates potential for effective application in the design of reactive active blowing systems, particularly targeting the stall

and stability characteristics of nonslender delta wing planforms.

8.3 Recommendations for Future Work

Based on the aforementioned discussions and conclusions associated with employed passive and active flow control techniques presented in the current study, the following extensions and items can suggested and employed as future works:

- The passive bleeding momentum estimation technique can be applied to various bleeding geometries, including nozzle-type bleeding slots. This characterization approach is valuable for designing closed-loop flow control schemes, utilizing passive bleeding technique effectiveness charts and on-off valve actions with appropriate pressure sensor correlations across different flow regimes. Furthermore, to enhance the practicality of the technique, computational fluid dynamics (CFD) modeling, once compared and validated against the proposed scheme, can be employed to estimate the momentum coefficients of passive bleeding on diverse aerodynamic surfaces in advance.
- Experiments utilizing additional measurement techniques, such as particle image velocimetry (PIV) and laser Doppler anemometry (LDA), oriented in the cross-sectional planes of the bleeding geometry, can provide a detailed understanding of the interaction between the bleeding flow and the surface flow field.
- To the best of the authors' knowledge, this is the first study investigating the effect of nozzle-type bleeding slots on delta wings. These slots have proven to be highly effective in altering the flow structure of nonslender planforms. The sensitivity of design parameters, including slot thickness, is critical for achieving favorable outcomes with this technique. The effect of this technique could be even more pronounced on slender delta wings, which potentially exhibit higher suction characteristics due to the pressure difference between the pressure and suction sides. Additionally, slot positioning that aligns with the vortex core axis may further enhance the effectiveness of the technique.
- Once the flow control effectiveness of nozzle-type bleeding slots is assessed for a specific aerodynamic surface, a detailed parameter sensitivity study can be

conducted. Such a study would not only help identify the optimal geometry for a fixed design but also aid in developing active bleeding systems with variable contraction ratios at different phases of flight, based on a closed-loop control algorithm.

- Considering the wind tunnel and model dimensions, fast switching valves were required to be positioned to be outside the wind tunnel and blowing content shall be conveyed using pneumatic tubing. This was one of the key factors requiring the comprehensive characterization of the active flow control system which is believed to be decreasing the performance of the blowing system that prevents implementation of very high frequencies maintaining the input signal profile due to the travel time of the excitation flow. In the literature it is observed that usage of such valves on aerodynamic flow control studies exhibit a significant growth. Larger wind tunnel facilities with larger model scales are offering the installation of these valves into the model geometry itself thus assuring minimum loss due to tube installation. With that perspective similar characterization approach can be employed on single valve response with different exit tubing lengths.

- The interaction of the periodic blowing with the complex flow structures can be better understood performing phase locked particle image velocimetry measurements particularly in various cross flow planes for different angles of attacks. In addition to blowing flow control system characterization charts, such an insight coupled with surface pressure measurements would be very helpful in designing closed loop flow control schemes.

- The effect of the excitation frequency is quite apparent in aerodynamic investigations, thus improving or designing active flow control systems based on fast switching valves, synthetic jet actuators (SJAs), piezoelectric devices to achieve very high frequencies up to 200-300 Hz would be further topics to investigate effect of higher contents which has very rarely studied for nonslender delta wings.

- Given the wind tunnel and model dimensions, it was necessary to position the fast-switching valves outside the wind tunnel, with the blowing content con-

veyed via pneumatic tubing. This setup necessitated a comprehensive characterization of the active flow control system, as the travel time of the excitation flow is believed to reduce the system's performance, thereby preventing the implementation of very high frequencies while maintaining the input signal profile. Literature shows a significant increase in the use of such valves in aerodynamic flow control studies. Larger wind tunnel facilities with larger model scales offer the advantage of integrating these valves directly into the model geometry, minimizing losses due to tube installation. A similar characterization approach can be applied to assess the response of a single valve with different exit tubing lengths.

- The interaction of periodic blowing with complex flow structures can be better understood through phase-locked particle image velocimetry (PIV) measurements, particularly in various cross-flow planes at different angles of attack. Coupled with surface pressure measurements, these insights, along with blowing flow control system characterization charts, would be invaluable for designing closed-loop flow control schemes.

- The effect of excitation frequency is quite pronounced in aerodynamic investigations. Improving or designing active flow control systems based on fast-switching valves, synthetic jet actuators (SJAs), and piezoelectric devices to achieve very high frequencies up to 200-300 Hz would be a promising area for further research. This aspect has been rarely studied for nonslender delta wings, and exploring it could provide valuable insights into the effects of higher frequency content.

REFERENCES

[1] I. Gursul, R. Gordnier, and M. Visbal, "Unsteady Aerodynamics of Nonslender Delta Wings", *Progress in Aerospace Sciences*, vol. 41, no. 7, pp. 515–557, 2005,

[2] I. Gursul, "Vortex Flows on UAVs: Issues and Challenges", eng, *Aeronautical Journal*, vol. 108, no. 1090, pp. 597–610, 2004,

[3] I. Gursul and Z. Wang, "Flow Control of Tip/Edge Vortices", *AIAA Journal*, vol. 56, no. 5, pp. 1731–1749, May 2018,

[4] M. Gad-El-Hak and R. F. Blackwelder, "The Discrete Vortices from a Delta Wing", *AIAA Journal*, vol. 23, no. 6, pp. 963–962, 1985,

[5] W. H. J. Wentz and D. L. Kohlman, "Vortex Breakdown on Slender Sharp-Edged Wings", *Journal of Aircraft*, vol. 8, no. 3, pp. 156–161, 1971,

[6] I. Gursul, G. Taylor, and C. Wooding, "Vortex flows over fixedwing micro air vehicles. AIAA 2002-0698", *40th AIAA Aerospace Sciences Meeting & Exhibit*, 2002.

[7] R. E. Gordnier and M. R. Visbal, "Compact Difference Scheme Applied to Simulation of Low-Sweep Delta Wing Flow.", *AIAA Journal*, vol. 43, no. 8, pp. 1744–1752, 2005,

[8] G. S. Taylor, T. Schnorbus, and I. Gursul, "An Investigation of Vortex Flows Over Low Sweep Delta Wings", *33rd AIAA Fluid Dynamics Conference and Exhibit*, no. June, pp. 1–13, 2003.

[9] G. Taylor, Z. Wang, E. Vardaki, and I. Gursul, "Lift Enhancement over Flexible Nonslender Delta Wings", *AIAA Journal*, vol. 45, no. 12, pp. 2979–2993, 2007,

[10] A. Çelik, C. Çetin, and M. M. Yavuz, "Effect of passive bleeding on flow structure over a nonslender delta wing", *AIAA Journal*, vol. 55, no. 8, pp. 2555–2565, 2017,

[11] W. H. Wentz Jr. and D. L. Kohlman, "Wind tunnel investigations of vortex breakdown on slender sharp-edged wings", *NASA Contractor Report*, vol. 98737, 1969.

[12] M. V. Ol and M. Gharib, "Leading-Edge Vortex Structure of Nonslender Delta Wings at Low Reynolds Number", *AIAA Journal*, vol. 41, no. 1, pp. 16–26, 2003,

[13] B. Yaniktepe and D. Rockwell, "Flow Structure on a Delta Wing of Low Sweep Angle", *AIAA Journal*, vol. 42, no. 3, pp. 513–523, 2004,

[14] M. Elkhoury and Z. Nakad, "Surface Streamlines and Normal-to-Plane Motion Adjacent to a Delta-Wing Planform", *Journal of Aircraft*, vol. 46, no. 4, pp. 1440–1444, 2009,

[15] K. W. Mangler and J. H. B. Smith, "A Theory of the Flow Past a Slender Delta Wing with Leading Edge Separation", *Proceedings of the Royal Society of London A: Mathematical, Physical and Engineering Sciences*, vol. 251, no. 1265, pp. 200–217, May 1959.

[16] A. G. Parker, "Aerodynamic characteristics of slender wings with sharp leading edges - A review", *Journal of Aircraft*, vol. 13, no. 3, pp. 161–168, 1976,

[17] D. Rockwell, "Three-Dimensional Flow Structure on Delta Wings at High Angle-of-Attack - Experimental Concepts and Issues", in *31st Aerospace Sciences Meeting*, ser. Aerospace Sciences Meetings, American Institute of Aeronautics and Astronautics, Jan. 1993.

[18] M. Ozgoren, B. Sahin, and D. Rockwell, "Vortex Structure on a Delta Wing at High Angle of Attack", *AIAA Journal*, vol. 40, no. 2, pp. 285–292, 2002,

[19] R. C. Nelson and A. Pelletier, "The Unsteady Aerodynamics of Slender Wings and Aircraft Undergoing Large Amplitude Maneuvers", *Progress in Aerospace Sciences*, vol. 39, no. 2-3, pp. 185–248, 2003,

[20] I. Gursul, "Review of Unsteady Vortex Flows over Slender Delta Wings", *Journal of Aircraft*, vol. 42, no. 2, pp. 299–319, 2005,

[21] C. Breitsamter, "Unsteady Flow Phenomena Associated with Leading-Edge Vortices", *Progress in Aerospace Sciences*, vol. 44, no. 1, pp. 48–65, 2008,

[22] M. Menke and I. Gursul, "Unsteady nature of leading edge vortices", *Physics of Fluids*, vol. 9, no. 10, pp. 2960–2966, Oct. 1997,

[23] W. Jin-Jun and Z. Wang, "Experimental Investigations on Leading-Edge Vortex Structures for Flow over Non-Slender Delta Wings", *Chinese Physics Letters*, vol. 25, no. 7, pp. 2550–2553, 2008,

[24] P. B. Earnshaw and J. A. Lawford, "Low-Speed Wind-Tunnel Experiments on a Series of Sharp-Edged Delta Wings", *Aeronautical Research Council, Reports and Memoranda*, no. 3424, 1964.

[25] I. Gursul, Z. Wang, and E. Vardaki, "Review of Flow Control Mechanisms of Leading-Edge Vortices", *Progress in Aerospace Sciences*, vol. 43, no. 7-8, pp. 246–270, 2007,

[26] N. M. Williams, Z. Wang, and I. Gursul, "Active Flow Control on a Nonslender Delta Wing", *Journal of Aircraft*, vol. 45, no. 6, 2008,

[27] M. Gad-El-Hak and R. F. Blackwelder, "Control of the Discrete Vortices From a Delta Wing", *AIAA Journal*, vol. 25, no. 8, pp. 1042–1049, 1987,

[28] I. Gursul and W. Xie, "Origin of Vortex Wandering over Delta Wings", *Journal of Aircraft*, vol. 37, no. 2, pp. 348–350, Mar. 2000,

[29] M. M. Yavuz, M. Elkhoury, and D. Rockwell, "Near-Surface Topology and Flow Structure on a Delta Wing", *AIAA Journal*, vol. 42, no. 2, pp. 332–340, 2004,

[30] M. V. Lowson, "Visualization measurements of vortex flows", *Journal of Aircraft*, vol. 28, no. 5, pp. 320–327, May 1991,

[31] O. K. Rediniotis, H. Stapountzis, and D. P. Telionis, "Periodic vortex shedding over delta wings", *AIAA Journal*, vol. 31, no. 9, pp. 1555–1562, Sep. 1993,

[32] J. M. Delery, "Aspects of vortex breakdown", *Progress in Aerospace Sciences*, vol. 30, no. 1, pp. 1–59, Jan. 1994,

[33] O. Lucca-Negro and T. O'Doherty, "Vortex breakdown: A review", *Progress in Energy and Combustion Science*, vol. 27, no. 4, pp. 431–481, 2001,

[34] H. Werlé, "Quelques Résultats Expérimentaux Sur les Ailes en Flèche, aux Faibles Vitesses, Obtenus en Tunnel Hydrodynamique", *La Recherche Aéronautique*, 1954.

[35] G. S. Taylor and I. Gursul, "Buffeting Flows over a Low-Sweep Delta Wing", *AIAA Journal*, vol. 42, no. 9, pp. 1737–1745, 2004,

[36] E. C. Polhamus, "Predictions of vortex-lift characteristics by a leading-edge suction analogy", *Journal of Aircraft*, vol. 8, no. 4, pp. 193–199, 1971,

[37] M. Lee and C.-M. Ho, "Lift Force of Delta Wings", *Applied Mechanics Reviews*, vol. 43, no. 9, pp. 209–221, Sep. 1990,

[38] J. J. Miau, K. T. Kuo, W. H. Liu, S. J. Hsieh, J. H. Chou, and C. K. Lin, "Flow developments above 50-deg sweep delta wings with different leading-edge profiles", *Journal of Aircraft*, vol. 32, no. 4, pp. 787–794, Jul. 1995,

[39] B. Yaniktepe and D. Rockwell, "Flow Structure on Diamond and Lambda Planforms : Trailing Edge Region", *AIAA Journal*, vol. 43, no. 7, 2005.

[40] M. Gad-el-Hak, "Flow Control: The Future", *Journal of Aircraft*, vol. 38, no. 3, pp. 402–418, 2001,

[41] J. J. Wang and S. F. Lu, "Effects of leading-edge bevel angle on the aerodynamic forces of a non-slender 50° delta wing", *The Aeronautical Journal*, vol. 109, no. 1098, pp. 403–407, Aug. 2005,

[42] A. McClain, Z.-J. Wang, E. Vardaki, and I. Gursul, "Unsteady Aerodynamics of Free-to-Roll Nonslender Delta Wings", in *45th AIAA Aerospace Sciences Meeting and Exhibit*, Reston, Virigina: American Institute of Aeronautics and Astronautics, Jan. 2007, ISBN: 978-1-62410-012-3.

[43] T. Goruney and D. Rockwell, "Flow Past a Delta Wing with a Sinusoidal Leading Edge: Near-Surface Topology and Flow Structure", *Experiments in Fluids*, vol. 47, no. 2, pp. 321–331, 2009,

[44] H. Chen, C. Pan, and J. Wang, "Effects of Sinusoidal Leading Edge on Delta Wing Performance and Mechanism", *Science China Technological Sciences*, vol. 56, no. 3, pp. 772–779, 2013,

[45] H. Chen and J. J. Wang, "Vortex Structures for Flow over a Delta Wing with Sinusoidal Leading Edge", *Experiments in Fluids*, vol. 55, no. 6, pp. 1–9, 2014,

[46] A. Çelik and M. M. Yavuz, "Effect of Edge Modifications on Flow Structure of Low Swept Delta Wing", *AIAA Journal*, vol. 54, no. 5, pp. 1789–1797, 2016,

[47] B. Gülsaçan, G. Şencan, and M. M. Yavuz, "Effect of thickness-to-chord ratio on flow structure of a low swept delta wing", *AIAA Journal*, vol. 56, no. 12, pp. 4657–4668, 2018,

[48] M. Sharifi Ghazijahani and M. M. Yavuz, "Effect of thickness-to-chord ratio on aerodynamics of non-slender delta wing", *Aerospace Science and Technology*, vol. 88, pp. 298–307, May 2019,

[49] L. W. Traub and S. F. Galls, "Effects of Leading- and Trailing-Edge Gurney Flaps on a Delta Wing", *Journal of Aircraft*, vol. 36, no. 4, pp. 651–658, Jul. 1999,

[50] M. D. Buchholz and J. Tso, "Lift Augmentation on Delta Wing with Leading-Edge Fences and Gurney Flap", *Journal of Aircraft*, vol. 37, no. 6, pp. 1050–1057, Nov. 2000,

[51] D. I. Greenwell, "Gurney Flaps on Slender and Nonslender Delta Wings", *Journal of Aircraft*, vol. 47, no. 2, pp. 675–681, Mar. 2010,

[52] L. W. Traub and S. M. Chandrashekar, "Experimental study on the effects of wing sweep on Gurney flap performance", *Aerospace Science and Technology*, vol. 55, pp. 57–63, Aug. 2016,

[53] K. Kestel, B. Ramazanlı, and M. M. Yavuz, "Control of flow structure over a non-slender delta wing using passive bleeding", *Aerospace Science and Technology*, vol. 106, p. 106 136, 2020,

[54] A. M. Mitchell, D. Barberis, P. Molton, and J. Delery, "Oscillation of Vortex Breakdown Location and Blowing Control of Time-Averaged Location", *AIAA Journal*, vol. 38, no. 5, pp. 793–803, 2000,

[55] S. Guillot, E. Gutmark, and T. Garrison, "Delay of Vortex Breakdown over a Delta Wing via Near-Core Blowing", *AIAA Paper*, no. 315, 1998.

[56] J. S. Hong, Z. Z. Celik, and L. Roberts, "Effects of leading-edge lateral blowing on delta wing aerodynamics", *AIAA Journal*, vol. 34, no. 12, pp. 2471–2478, Dec. 1996,

[57] M. Zharfa, I. Ozturk, and M. M. Yavuz, “Flow Structure on Nonslender Delta Wing: Reynolds Number Dependence and Flow Control”, *AIAA Journal*, vol. 54, no. 3, pp. 880–897, 2016,

[58] S. McCormick and I. Gursul, “Effect of Shear-Layer Control on Leading-Edge Vortices”, *Journal of Aircraft*, vol. 33, no. 6, pp. 1087–1093, 1996.

[59] H. E. Helin and C. W. Watry, “Effects of Trailing-Edge Jet Entrainment on Delta Wing Vortices”, *AIAA Journal*, vol. 32, no. 4, pp. 802–804, 1994,

[60] M. M. Yavuz and D. Rockwell, “Control of Flow Structure on Delta Wing with Steady Trailing-Edge Blow”, *AIAA Journal*, vol. 44, no. 3, pp. 493–501, 2006,

[61] E. Vardaki, I. Gursul, G. S. Taylor, and P. Student, “Physical Mechanisms of Lift Enhancement for Flexible Delta Wings”, *AIAA paper*, no. January, pp. 1–13, 2005.

[62] C. Çetin, A. Çelik, and M. M. Yavuz, “Control of flow structure over a nonslender delta wing using periodic blowing”, *AIAA Journal*, vol. 56, no. 1, pp. 90–99, 2018,

[63] A. Buzica, J. Bartasevicius, and C. Breitsamter, “Experimental investigation of high-incidence delta-wing flow control”, *Experiments in Fluids*, vol. 58, no. 9, p. 131, Sep. 2017,

[64] W. Gu, O. Robinson, and D. Rockwellf, “Control of Vortices on a Delta Wing by Leading-Edge Injection”, *AIAA Journal*, vol. 32, no. 10, pp. 2134–2135, 1994,

[65] Y. Guy, J. Morrow, and T. Mclaughlin, “Control of Vortex Breakdown on a Delta Wing by Periodic Blowing and Suction”, *37th AIAA Aerospace Sciences Meeting and Exhibit*, 1999.

[66] C. H. Kuo and N. Y. Lu, “Unsteady Vortex Structure over Delta-Wing Subject to Transient Along-Core Blowing”, *AIAA Journal*, vol. 36, no. 9, pp. 1658–1664, 1998,

[67] A. Kölzsch and C. Breitsamter, “Vortex-Flow Manipulation on a Generic Delta-Wing Configuration”, *Journal of Aircraft*, vol. 51, no. 5, pp. 1380–1390, 2014,

[68] A. Buzica and C. Breitsamter, “Pulsed Blowing Interacting with a Leading-Edge Vortex”, *Aerospace*, vol. 7, no. 1, p. 4, Jan. 2020,

[69] D. Greenblatt, Y. Kastantin, C. N. Nayeri, and C. O. Paschereit, “Delta-Wing Flow Control Using Dielectric Barrier Discharge Actuators”, *AIAA Journal*, vol. 46, no. 6, pp. 1554–1560, Jun. 2008,

[70] R. Nelson, T. Corke, C. He, *et al.*, “Modification of the Flow Structure over a UAV Wing for Roll Control”, in *45th AIAA Aerospace Sciences Meeting and Exhibit*, Reston, Virigina: American Institute of Aeronautics and Astronautics, Jan. 2007, ISBN: 978-1-62410-012-3.

[71] J. Tan, Z. Wang, and I. Gursul, “Passive Poststall Flow Control on Nonslender Delta Wings Using Flags”, *AIAA Journal*, vol. 62, no. 3, pp. 989–1005, Mar. 2024,

[72] L. W. Traub, “Effects of Plain and Gurney Flaps on a Nonslender Delta Wing”, *Journal of Aircraft*, vol. 56, no. 2, pp. 469–480, Mar. 2019,

[73] X. Zhang, Z. Wang, and I. Gursul, “Control of multiple vortices over a double delta wing”, *47th AIAA Fluid Dynamics Conference, 2017*, no. June, pp. 1–27, 2017.

[74] A. Yıldırım, “Numerical Investigation of Flow Control Strategies on Delta Wings”, *Middle East Technical University*, Sep. 2019.

[75] G. Günacar, “Effect of Blowing Pattern Through Leading Edge on Flow Structure of 45 Degree Swept Delta Wing”, *Middle East Technical University*, Sep. 2016.

[76] N. Wood and L. Roberts, “Control of vortical lift on delta wings by tangential leading-edge blowing”, *Journal of Aircraft*, vol. 25, no. 3, pp. 236–243, Mar. 1988,

[77] S. Phillips, C. Lambert, and I. Gursul, “Effect of a Trailing-Edge Jet on Fin Buffeting Introduction”, *Journal of Aircaft*, vol. 40, no. 3, pp. 590–599, 2003,

[78] Q. Deng and I. Gursul, “Vortex Breakdown over a Delta Wing with Oscillating Leading Edge Flaps”, *Experiments in Fluids*, vol. 23, no. 4, pp. 347–352, 1997,

[79] H. Yang and I. Gursul, “Vortex Breakdown Over Unsteady Delta Wings and Its Control”, *AIAA Journal*, vol. 35, no. 3, pp. 571–574, 1997,

[80] E. Vardaki, Z. Wang, and I. Gursul, “Flow Reattachment and Vortex Re-formation on Oscillating Low-Aspect-Ratio Wings”, *AIAA Journal*, vol. 46, no. 6, pp. 1453–1462, 2008,

[81] M. Casper, P. Scholz, J. Colman, J. M. Di Leo, S. Delnero, and M. Camocardi, “Comparison of Aerodynamic Effects Promoted by Mechanical and Fluidic Miniflaps on an Airfoil NACA 4412”, *Applied Aerodynamics*, 2012.

[82] R. Gupta and P. J. Ansell, “Closed-loop trailing-edge separation control system using empirical mode decomposition”, *AIAA Journal*, vol. 56, no. 1, pp. 121–131, 2018,

[83] S. Löffler, M. Thieme, B. Steinfurth, and J. Weiss, “Wind-Tunnel-in-the-Loop Exploration and Optimization of Active Flow Control Parameters”, *AIAA Journal*, pp. 1–13, Sep. 2024,

[84] S. Düssler, F. Siebert, and A. Bauknecht, “Coandă-Type Flow Actuation for Load Alleviation”, *Journal of Aircraft*, vol. 59, no. 5, pp. 1303–1319, 2022,

[85] Z. Wu and H. Choi, “Modification of flow behind a circular cylinder by steady and time-periodic blowing”, *Physics of Fluids*, vol. 33, no. 11, 2021,

[86] C. P. Hühne and P. Scholz, “Active flow control to improve the outer-wing performance during take-off”, *53rd AIAA Aerospace Sciences Meeting*, no. January, pp. 1–13, 2015.

[87] S. Abdolahipour, M. Mani, and A. Shams Taleghani, “Experimental Investigation of Flow Control on a High-Lift Wing Using Modulated Pulse Jet Vortex Generator”, *Journal of Aerospace Engineering*, vol. 35, no. 5, pp. 1–18, 2022,

[88] S. Abdolahipour, M. Mani, and A. Shams Taleghani, “Parametric study of a frequency-modulated pulse jet by measurements of flow characteristics”, *Physica Scripta*, vol. 96, no. 12, 2021,

[89] B. Steinfurth and J. Weiss, “Efficiency Enhancement in Active Separation Control Through Optimizing the Duty Cycle of Pulsed Jets”, *AIAA Journal*, vol. 60, no. 12, pp. 6566–6580, 2022,

[90] M. Pipan and N. Herakovič, “Volume flow characterization of PWM-controlled fast-switching pneumatic valves”, *Strojniski Vestnik/Journal of Mechanical Engineering*, vol. 62, no. 9, pp. 543–550, 2016,

[91] F. Ternoy, J. Dandois, F. David, and M. Pruvost, “Flow Control: the Renewal of Aerodynamics? Overview of Onera Actuators for Active Flow Control”, *Journal AerospaceLab*, no. 6, pp. 1–14, 2013.

[92] C. Çetin, “Control Of Flow Structure On Low Swept Delta Wing Using Unsteady Leading Edge Blowing”, *Middle East Technical University*, Jun. 2016.

[93] G. Koçak, “Effect of Ground on Flow Structure of Non-Slender Delta And Reverse Delta Wings”, *Middle East Technical University*, Jan. 2023.

[94] M. Raffel, C. E. Willert, F. Scarano, C. J. Kähler, S. T. Wereley, and J. Kompenhans, *Particle Image Velocimetry*. Cham: Springer International Publishing, 2018, ISBN: 978-3-319-68851-0.

[95] A. J. Wheeler and A. R. Ganji, *Introduction to Engineering Experimentation*. 2010, ISBN: 0131742760.

[96] F. Jørgensen, “How to measure turbulence with hot-wire anemometersa practical guide”, *Dantec Dynamics*, p. 3244, 2002,

[97] M. M. Yavuz and D. Rockwell, “Identification and Control of Three-Dimensional Separation on Low Swept Delta Wing”, *AIAA Journal*, vol. 44, no. 11, pp. 2805–2811, 2006,

Appendix A

WING MODELS

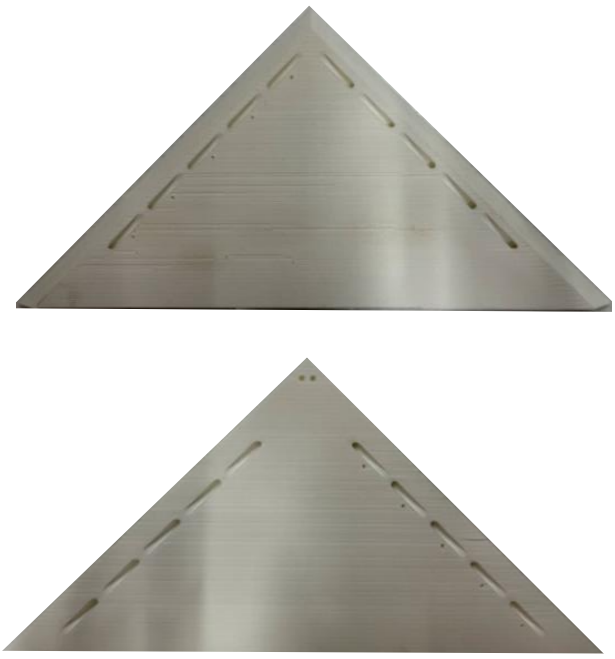

Figure A.1: Back bleed B18 wing equipped with surface pressure measurement taps at the proximity of bleeding slots ($\Lambda = 45°$, $t/C = 5.9\%$).

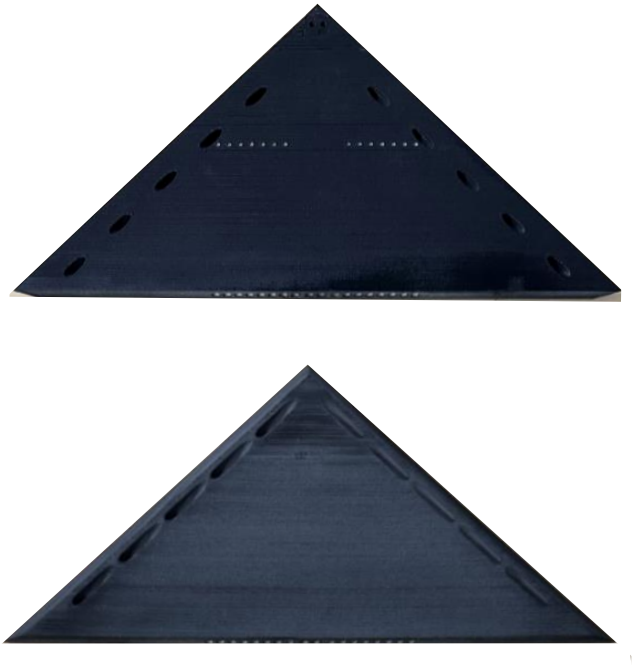

Figure A.2: Nozzle bleed wing wide CR050 ($\Lambda = 45°$, $t/C = 5.9\%$).

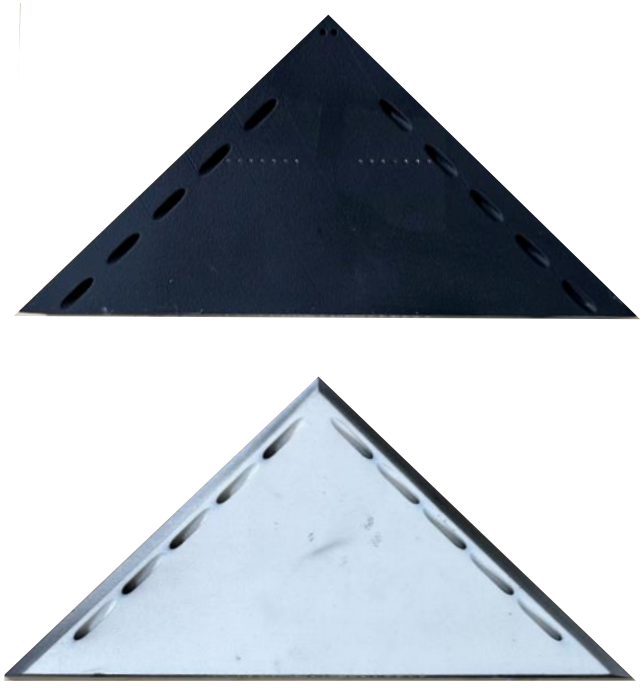

Figure A.3: Nozzle bleed wing wide CR075 ($\Lambda = 45°$, $t/C = 5.9\%$).

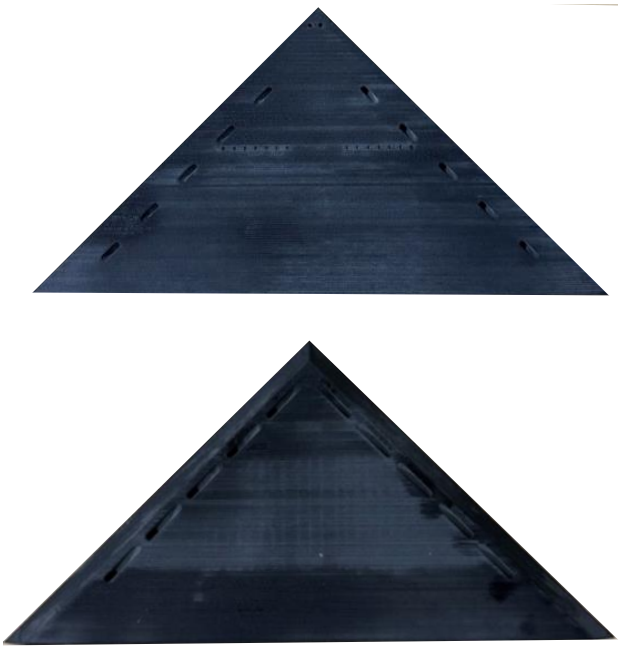

Figure A.4: Nozzle bleed wing narrow CR050 forward ($\Lambda = 45°$, $t/C = 5.9\%$).

Figure A.5: Nozzle bleed wing narrow CR050 rear ($\Lambda = 45°$, $t/c = 5.9\%$).

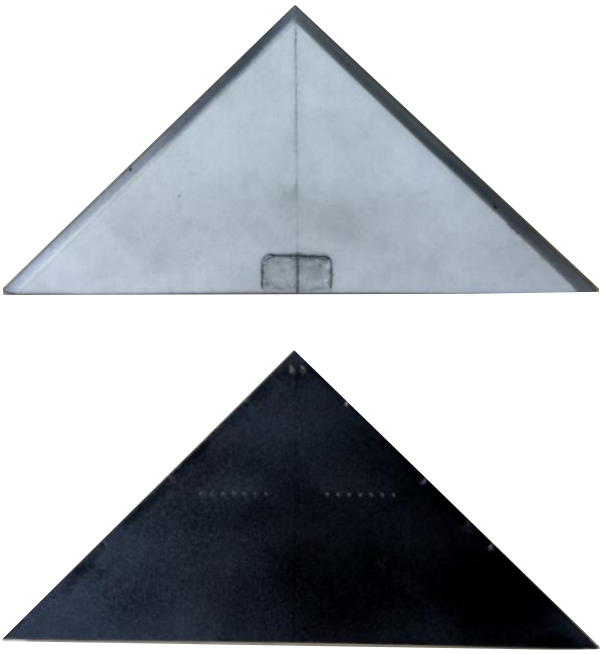

Figure A.6: Blowing wing ($\Lambda = 45°, t/c = 5.9\%$)

Appendix B

NOZZLE TYPE BLEEDING SLOTS PRESSURE MEASUREMENTS

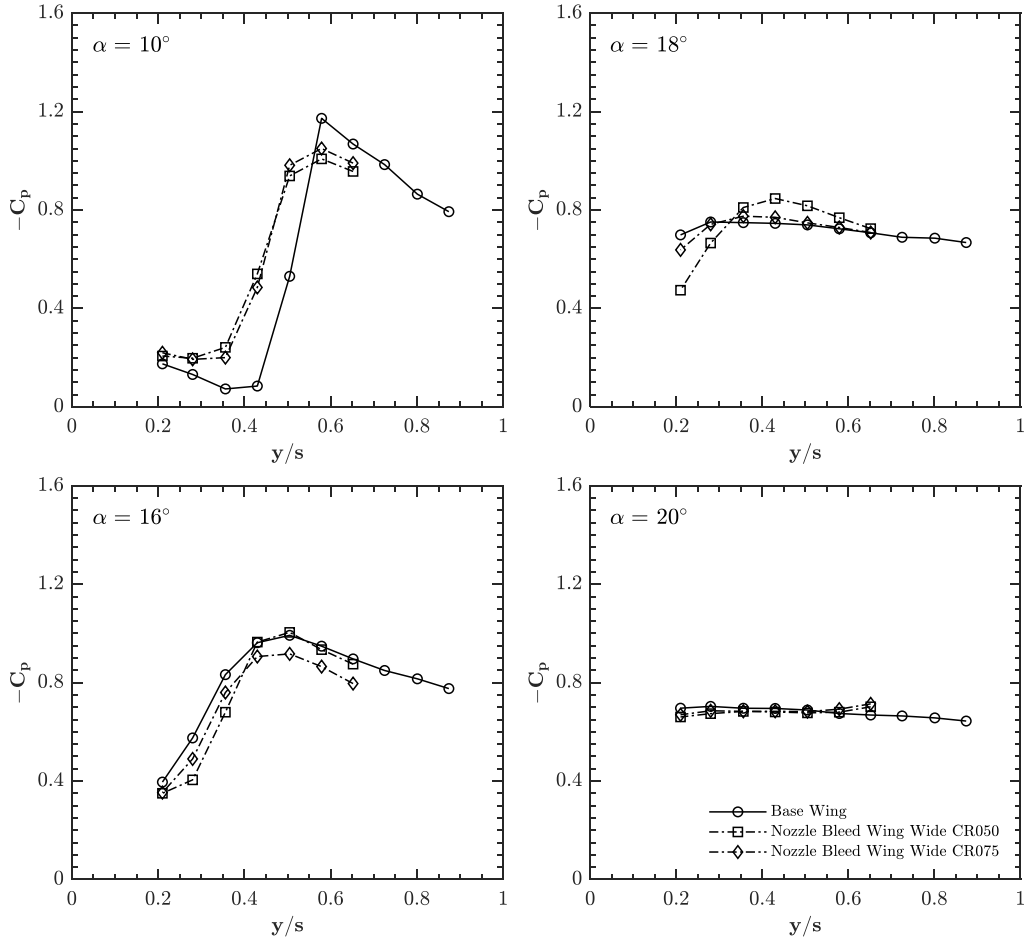

Figure B.1: $-C_p$ distribution at half span for base wing, nozzle bleed wing wide CR050, and nozzle bleed wing wide CR075 at angles of attack $\alpha = 10°$, $\alpha = 16°$, $\alpha = 18°$, and $\alpha = 20°$ at Re $= 3.5 \times 10^4$.

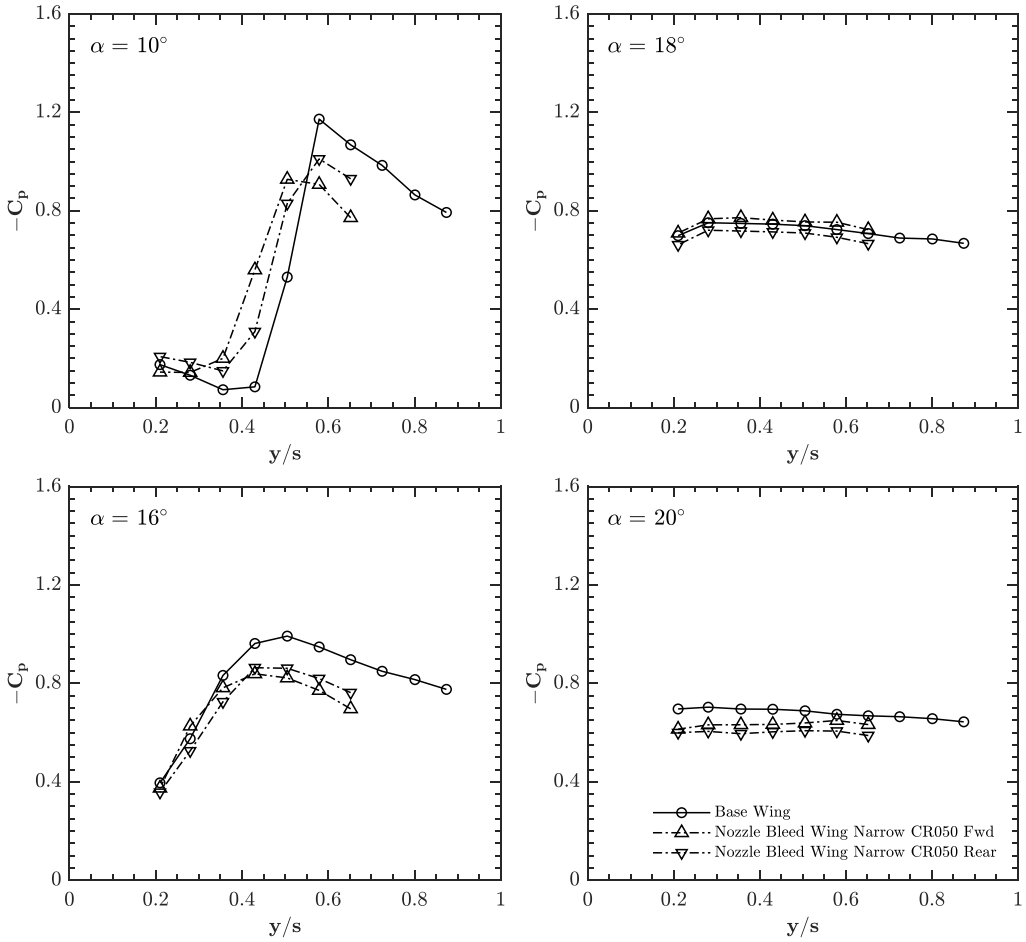

Figure B.2: $-C_p$ distribution at half span for base wing, nozzle bleed wing narrow CR050 forward, and nozzle bleed wing narrow CR050 rear at angles of attack $\alpha = 10°$, $\alpha = 16°$, $\alpha = 18°$, and $\alpha = 20°$ at Re $= 3.5 \times 10^4$.

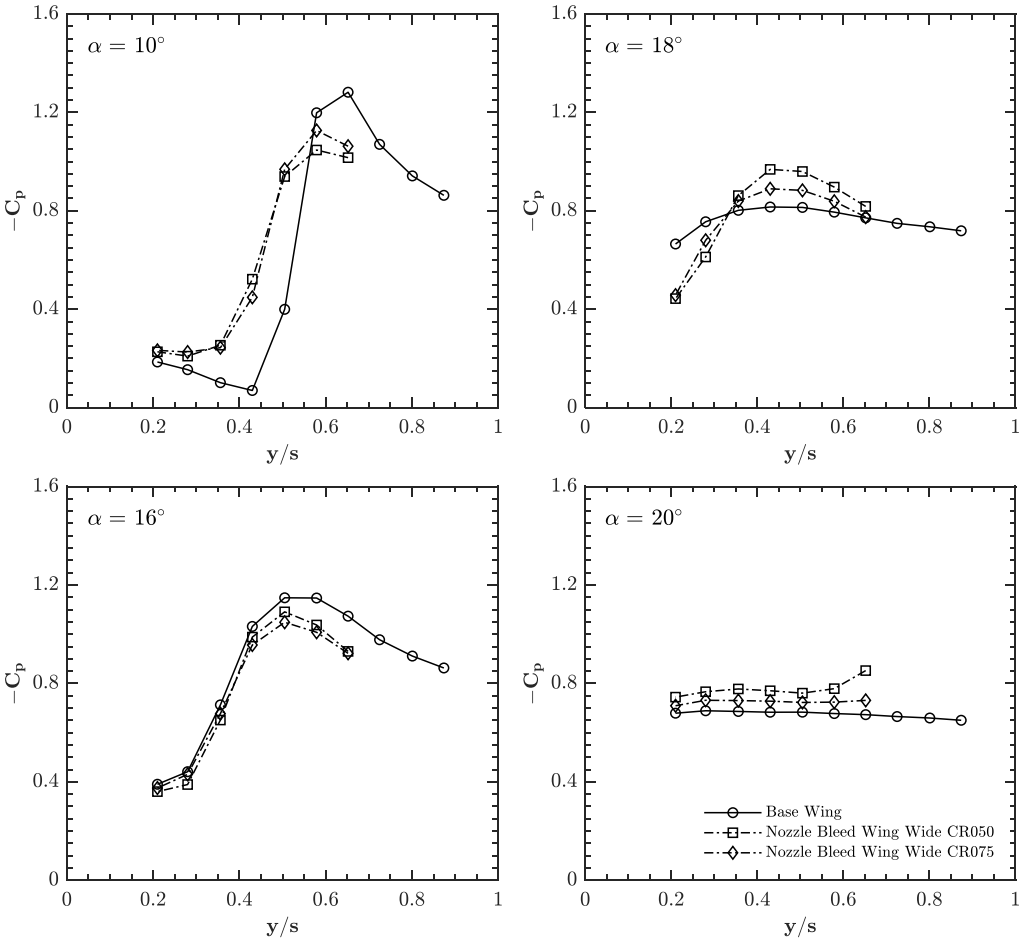

Figure B.3: $-C_p$ distribution at half span for base wing, nozzle bleed wing wide CR050, and nozzle bleed wing wide CR075 at angles of attack $\alpha = 10°$, $\alpha = 16°$, $\alpha = 18°$, and $\alpha = 20°$ at Re $= 7.5 \times 10^4$.

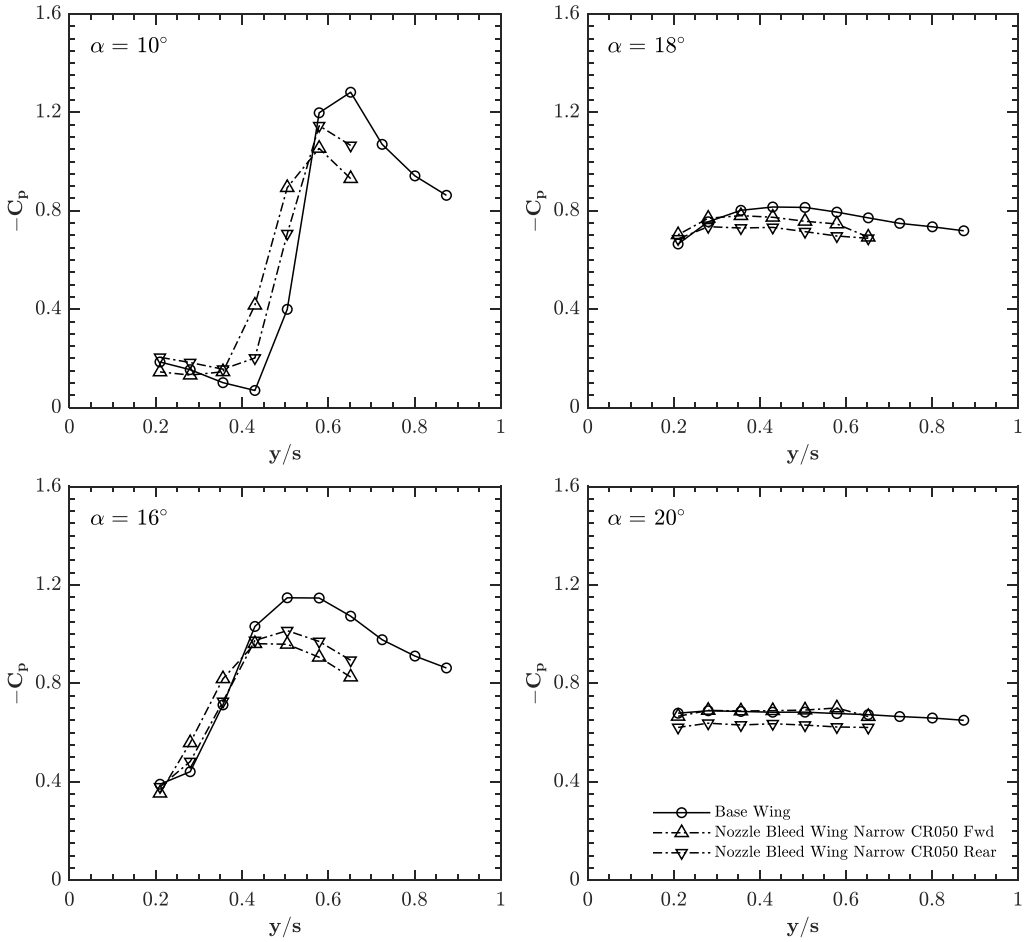

Figure B.4: $-C_p$ distribution at half span for base wing, nozzle bleed wing narrow CR050 forward, and nozzle bleed wing narrow CR050 rear at angles of attack $\alpha = 10°$, $\alpha = 16°$, $\alpha = 18°$, and $\alpha = 20°$ at Re $= 7.5 \times 10^4$.

Appendix C

EFFECT OF THE PERIODIC BLOWING WITH BURST MODULATED SQUARE WAVEFORM PATTERN: SURFACE PRESSURE MEASUREMENTS, FORCE MEASUREMENTS

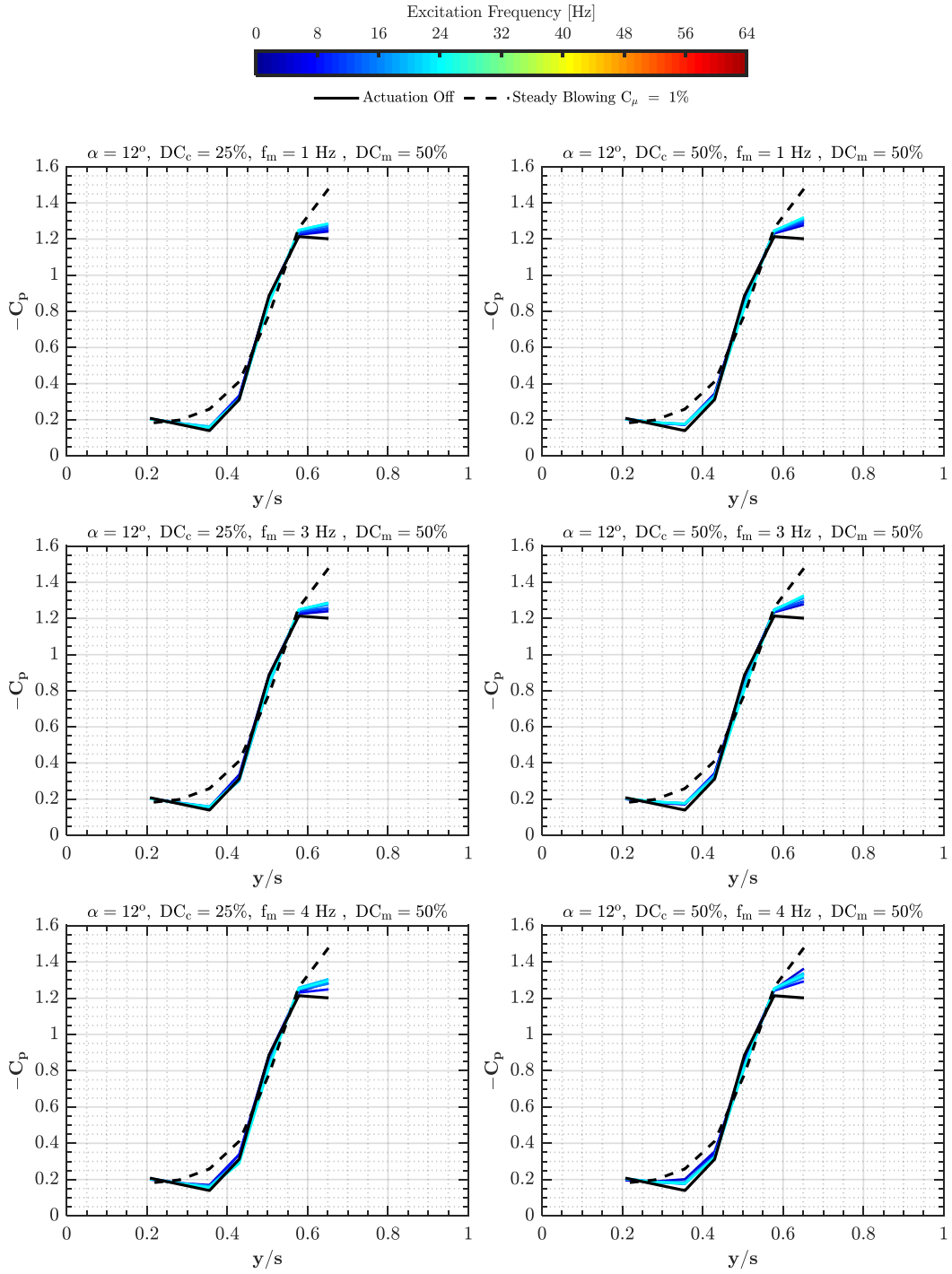

Figure C.1: $-C_p$ distribution at half span for burst modulated square wave blowing ($f_c = 4, 8, 12, 16, 20, 24$ Hz, $DC_c = 25, 50\%$, $f_m = 1, 3, 4$ Hz, $DC_m = 50\%$, $C_{\mu,\text{max}} = 1\%$) in comparison to steady blowing cases ($C_\mu = 1\%$) at $\alpha = 12°$, $Re = 9 \times 10^4$.

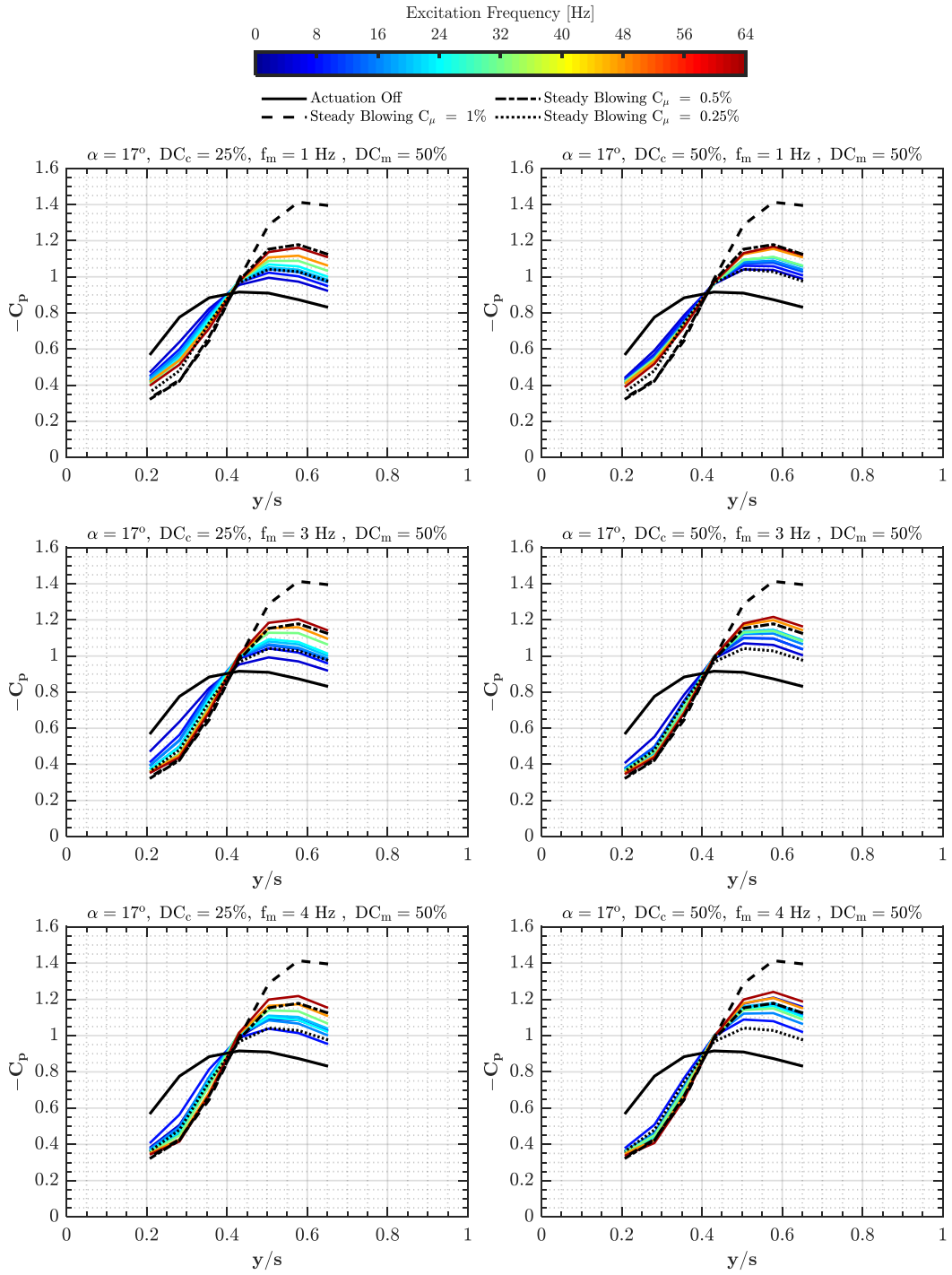

Figure C.2: $-C_p$ distribution at half span for burst modulated square wave blowing ($f_c = 4, 8, 12, 16, 20, 24, 32, 48, 64$ Hz, $DC_c = 25, 50\%$, $f_m = 1, 3, 4$ Hz, $DC_m = 50\%$, $C_{\mu,\text{max}} = 1\%$) in comparison to steady blowing cases ($C_\mu = 0.25\%, 0.5\%, 1\%$) at $\alpha = 21°$, $Re = 9 \times 10^4$.

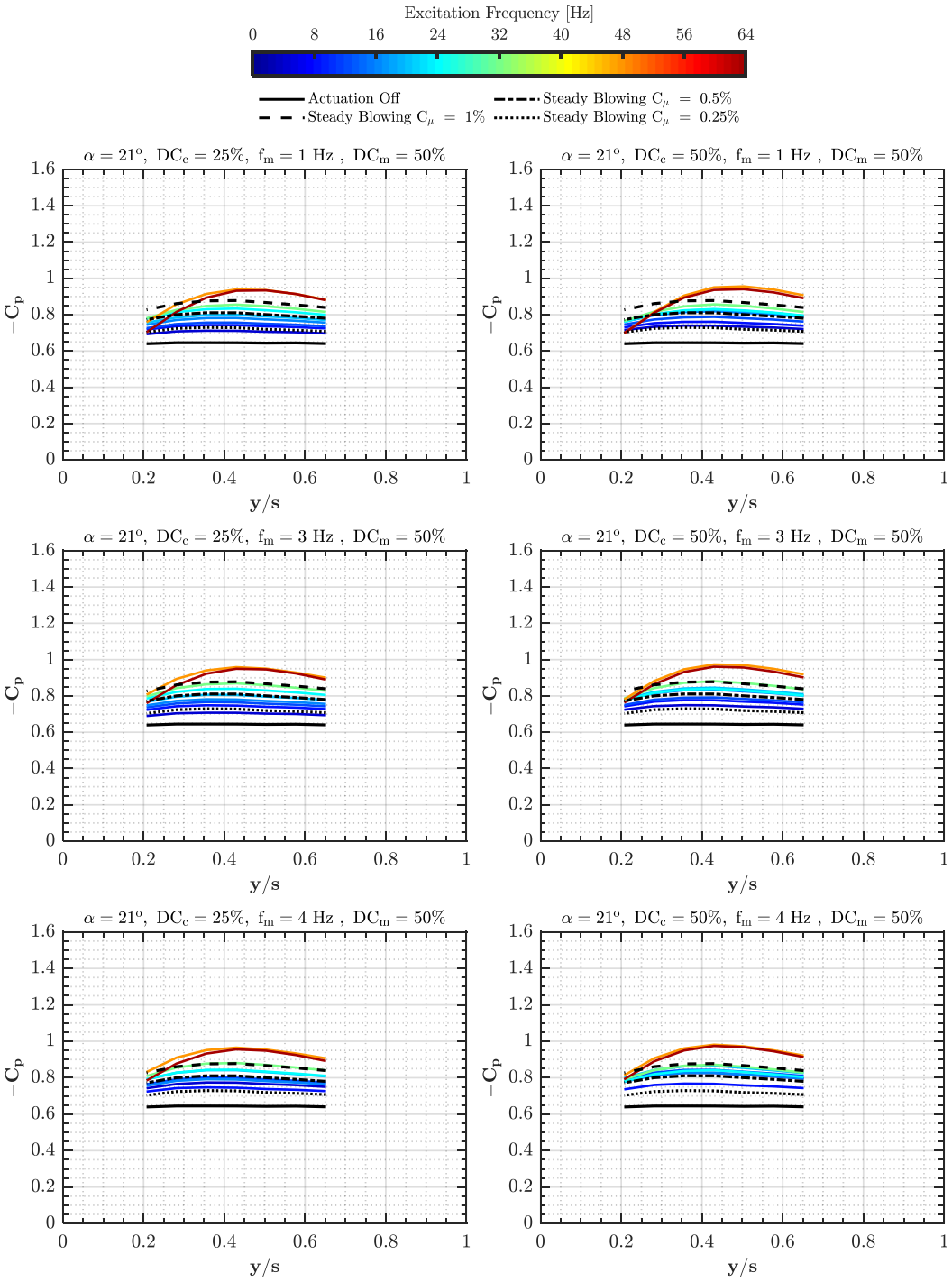

Figure C.3: $-C_p$ distribution at half span for burst modulated square wave blowing ($f_c = 4, 8, 12, 16, 20, 24, 32, 48, 64$ Hz, $DC_c = 25, 50\%$, $f_m = 1, 3, 4$ Hz, $DC_m = 50\%$, $C_{\mu,\max} = 1\%$) in comparison to steady blowing cases ($C_\mu = 0.25\%, 0.5\%, 1\%$) at $\alpha = 21°$, $Re = 9 \times 10^4$.

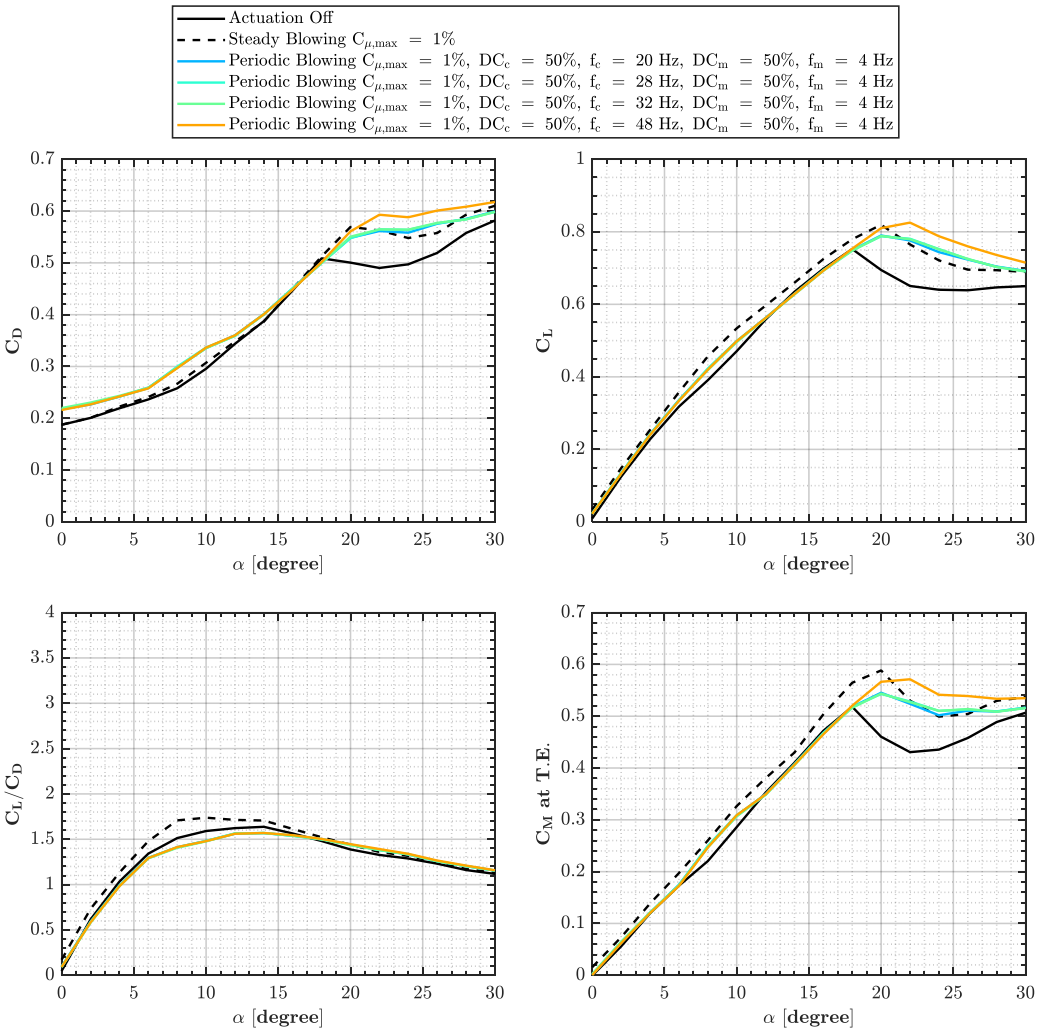

Figure C.4: Distributions of drag coefficient C_D, lift to drag ratio C_L/C_D, lift coefficient C_L, and pitching moment coefficient at trailing edge C_M: Burst modulated square wave blowing ($f_c = [20, 28, 32, 48]$ Hz, $DC_c = 50\%$, $f_m = 4$ Hz, $DC_m = 50\%$, $C_{\mu,\text{max}} = 1\%$) in comparison to steady blowing cases ($C_\mu = 1\%$), at $Re = 9 \times 10^4$.

CURRICULUM VITAE

Surname, Name: Çetin, Cenk

CONTACT INFORMATION

Address: Mechanical Engineering Department, METU
E-mail:

EDUCATION

Ph.D. September 2018 – November 2024
Middle East Technical University - Mechanical Engineering Department, Ankara, Turkey
Thesis: "Control Of Leading Edge Vortex And Three-Dimensional Surface Separation On A Non-Slender Delta Wing Using Passive And Active Techniques"
(CGPA: 3.29/4.00)

M.Sc. September 2014 – June 2016
Middle East Technical University - Mechanical Engineering Department, Ankara, Turkey
Thesis: "Control Of Flow Structure On Low Swept Delta Wing Using Unsteady Leading Edge Blowing"
(CGPA: 3.5/4.00)

B.Sc. September 2007 – June 2012
Gaziantep University - Mechanical Engineering Department, Gaziantep, Turkey
(CGPA: 3.58/4.00)

EXPERIENCE

Flight Physics IPT Leader at T625 GÖKBEY February 2024 – Present
Helicopter Division, Turkish Aerospace Industries Inc., Ankara, Turkey

Lead Design Engineer at Flight Mechanics November 2018 – February 2024
Helicopter Division, Turkish Aerospace Industries Inc., Ankara, Turkey

Researcher at Opaque Flow Project October 2017 – October 2018
Multiphase Systems, Process and Energy Department, Delft University of Technology, Delft, the Netherlands

Research - Teaching Assistant October 2014 – October 2017
Mechanical Engineering Department, Middle East Technical University, Ankara, Turkey

Third Lieutenant August 2013 – July 2014
Turkish Air Force, Turkey

Research - Teaching Assistant September 2012 – July 2013
Mechanical Engineering Department, Gaziantep University, Gaziantep, Turkey

JOURNAL PUBLICATIONS

1. **Çetin, C.**, Yavuz, M. M. "Comprehensive Characterization of a Pneumatic Active Flow Control System Using In-Situ Hot Wire Calibration." *Flow Measurement and Instrumentation*, First Revision Received on October 21, 2024, Under Review, 2024.

2. **Çetin, C.**, Yılmaz, O., Yavuz, M. M. "Control of Flow Structures on Nonslender Delta Wing Utilizing Nozzle-Type Bleeding Slots." *AIAA Journal*, 62(10), 4017-4027, 2024.

3. **Çetin, C.**, Yavuz, M. M. "Method Development for Estimation of Bleed Momentum Coefficient Using Surface Pressure Measurements and In Situ Hot Wire Calibration." *Flow Measurement and Instrumentation*, 97, 102603, 2024.

4. Öztürk, İ., **Çetin, C.**, Yavuz, M. M. "Effect of Fan and Shroud Configurations

on Underhood Flow Characteristics of an Agricultural Tractor." *Engineering Applications of Computational Fluid Mechanics*, 13(1), 506-518, 2019.

5. **Çetin, C.**, Çelik, A., Yavuz, M. M. "Control of Flow Structure over a Nonslender Delta Wing Using Periodic Blowing." *AIAA Journal*, 56(1), 90-99, 2018.

6. Çelik, A., **Çetin, C.**, Yavuz, M. M. "Effect of Passive Bleeding on Flow Structure over a Nonslender Delta Wing." *AIAA Journal*, 55(8), 2555-2565, 2017.

CONFERENCE PUBLICATIONS

1. **Çetin, C.**, Yılmaz, O., Yavuz, M. M. "Genişletilmiş Bir Aktif Akiş Kontrol Sistem Tasarimi Ve Karakterizasyonu." In *X. Ulusal Havacılık ve Uzay Konferansı UHUK, September 18-20 2024, Ankara, Turkey*, Paper No: 2024-133.

2. **Çetin, C.**, Koçak, G., Yavuz, M. M. "Yeni Bir Pasif Akıtma Tasarımı ile Düşük Ok Açılı Delta Kanat Akışının Kontrolü." In *IX. Ulusal Havacılık ve Uzay Konferansı UHUK, September 14-16 2022, İzmir, Turkey*, Paper No: 2022-041.

3. **Çetin, C.**, Şansal, K., Çalışkan, A., Kargın, V. "Modelling of Atmospheric Turbulence in Inhouse Rotorcraft Simulation Tool: Characterization and Comparison." In *48th European Rotorcraft Forum ERF, September 6-8 2022, Winterthur, Switzerland*, Paper No: 063.

4. Yavuz, M. M., Celik, A., **Cetin, C.**, "Control of Flow Structure on Non-Slender Delta Wing: Bio-inspired Edge Modifications, Passive Bleeding, and Pulsed Blowing." In *69th Annual Meeting of the APS Division of Fluid Dynamics, Volume 61 Number 20, H7 10, November 20-22 2016, Portland, Oregon.*

5. Çelik, A., **Çetin, C.**, Yavuz, M. M. "Düşük Ok Açılı Delta Kanat Üzerindeki Akışın Pasif Akıtma Yöntemiyle Kontrolü." In *VI. Ulusal Havacılık ve Uzay Konferansı UHUK, September 28-30 2016, Kocaeli, Turkey*, Paper No: 2016-085.

6. Çelik, A., **Çetin, C.**, Yavuz, M. M. "Kenar Değişikliklerinin Düşük Ok Açılı Delta Kanat Üzerindeki Akış Yapılarına Etkileri." In *VI. Ulusal Havacılık ve*

Uzay Konferansı UHUK, September 28-30 2016, Kocaeli, Turkey, Paper No: 2016-084.

7. **Çetin, C.**, Celik, A., Yavuz, M. M. "Düşük Ok Açılı Delta Kanat Akışının Zamana Bağlı Üfleme Tekniği ile Kontrolü." In *VI. Ulusal Havacılık ve Uzay Konferansı UHUK, September 28-30 2016, Kocaeli, Turkey*, Paper No: 2016-071.